THE UNIVERSITY *of* EDINBURGH

Synthesis and Properties of $CaFe_3O_5$ and Related Materials

Ka Hou (Jacky) Hong

A Thesis submitted for the degree of Doctor of Philosophy

The University of Edinburgh

2019

DECLARATION

I declare that this Thesis was composed solely by myself and all the work contained herein is my own except where explicitly stated otherwise. This work has not been submitted for any other degree of professional qualification. Part of this work has been published, as detailed in the Publications section.

Ka H. Hong

14th February 2019

LAY SUMMARY

Minerals that are made up of transition metals and oxygen play an important role in everyday life. The physical, electrical and magnetic properties that these materials exhibit allow them to be used in a wide variety of applications, such as electronic circuit boards, magnetic data-storage devices, battery cells and magnetic levitation technology used for transportation purposes. The demand for these electronic and magnetic materials has been continuously increasing with advancements in modern technology and this driving force has made the study of transition metal oxides one of the most active and intensively researched areas in materials science.

The properties of a material originate from how electrons interact with each other within the structure. These interactions are dependent on the chemical composition of the material and the arrangement of the atoms in the structure. The work in this explores the magnetic, electronic and structural properties of new members of the recently discovered MFe$_3$O$_5$ system. The synthesis of CaFe$_3$O$_5$ was carried out at 1100 °C, with results showing an electronic phase separation when the material is cooled below room temperature. The separation gives rise to two phases of the same structure with different electronic and magnetic properties. High-pressure synthesis techniques were

employed in the synthesis of $MnFe_3O_5$, $CoFe_3O_5$ and $NiFe_3O_5$, using pressures that exceed 10 GPa (over 100000 times atmospheric pressure) and temperatures over 1200 °C. Multiple magnetic transitions were observed in these materials when cooled below ~30 °C, which result in different magnetic states at different temperatures.

ABSTRACT

The iron oxide family has become one of the most intensively studied transition metal oxide systems since the discovery of the Verwey transition in magnetite (Fe_3O_4) in 1939. The ground state structure of Fe_3O_4 was only recently solved and revealed a complex charge and orbital ordered arrangement with weak Fe-Fe bonding interactions giving rise to trimerons, linear orbital molecule clusters of three Fe ions. A closely related phase, Fe_4O_5, was recently discovered and was found to undergo incommensurate charge order that led to the formation of dimeron and trimeron like groups at low temperature. Apart from Fe_4O_5, very little study has been carried out on this system. This Thesis explores different analogues of $M^{2+}Fe_3O_5$ (with M = Ca, Mn, Co and Ni). Physical property measurements and diffraction techniques were used to study the ground state structures of these mixed Fe^{2+}/Fe^{3+} valence state phases, to investigate the charge, spin and orbital ordering phenomena that are involved.

The M^{2+} = Ca analogue, $CaFe_3O_5$, was synthesised using the ceramic method at ambient pressure. Diffraction studies reveal an electronic phase separation when cooled below a magnetic transition at 302 K, where the high-temperature paramagnetic phase separates into two phases with different electronic and

antiferromagnetic ordering. One of the phases has charge ordered Fe^{2+}/Fe^{3+} with trimeron formation and the other has a charge averaged structure with infinite chains of orbital molecules.

High-pressure ceramic methods were used to synthesise $M^{2+}Fe_3O_5$ phases with small M^{2+} cations (M = Mn, Co and Ni). $MnFe_3O_5$ was synthesised at a pressure of 10 GPa. Magnetisation studies show a rich variety of magnetic states when cooled below 350 K. Spin order of the Fe cation site is observed below 350 K and result in antiferromagnetism. A second transition at 150 K marks the Mn spin order that leads to spin canting of some of the Fe spins and ferrimagnetism. A further magnetic transition at 60 K, driven by charge ordering of Fe^{2+} and Fe^{3+}, results in further spin reorientation and an enhancement in the magnetisation of $MnFe_3O_5$. The crystal structure of $MnFe_3O_5$ remains in the space group *Cmcm* within the investigated temperature range of 5-400 K.

The $CoFe_3O_5$ phase was stabilised under 12 GPa of pressure. A neutron diffraction study shows Co/Fe cation disorder in $CoFe_3O_5$. Similar to $MnFe_3O_5$, an antiferromagnetic transition is observed near room temperature, at 300 K, from the spin order of the octahedral sites. The triangular prismatic site is magnetically ordered when cooled below 100 K and leads to the spin of the octahedral site to cant and ferrimagnetism. $CoFe_3O_5$ shows semiconducting behaviour, with a negative magnetoresistance effect of 5 % at 125 K. The charge of $Fe^{2+/3+}$ in $CoFe_3O_5$ remains disordered down to 5 K. The absence of

charge order is likely due to the strong exchange interactions between the cations in the octahedral sites along the *a* axis.

An even higher pressure was used to synthesise $NiFe_3O_5$. Structure and property studies show an antiferromagnetic transition at ~275 K that marks the spin order of the octahedral sites in $NiFe_3O_5$. This is followed by an incommensurate magnetic ordering below ~150 K. A further magnetically ordered states is observed at ~20 K, where the spin of the three cation sites are ordered antiferromagnetically and propagate through the lattice with a *k*-vector of [½ ½ 0].

ACKNOWLEDGEMENTS

I would like to start by expressing my gratitude to my Prof. J. Paul Attfield for being such an amazing Ph.D supervisor. I would like to thank him for giving me the opportunity to be part of his group. He has provided me with an enormous amount of support and guidance throughout the past four years. I would like to thank all the Attfield group members for their help and support throughout the past few years. I particularly need to thank Dr James Cumby, Dr Angel Arevalo-Lopez, Dr Elena Solana Madruga, Dr Elise Pachoud, Dr Alexander J. Browne, Dr Paul M. Sarte, Dr Graham McNally and Dr Giuditta Perversi for their assistance in the laboratory and with my research. Many thanks to James for his work on Density Functional Theory calculations in this Thesis and for proofreading some of the chapters. I would also like to thank him for the time he spent mentoring me. Alex was the first person I met after joining the Attfield group and has taught me more than I can list here, particularly solid-state synthesis and GSAS. A massive thanks to Alex for proofreading a large part of this Thesis as well! Angel, Graham and Elena have spent hours and hours of their time teaching me the beauty of high-pressure synthesis and FullProf.

A special thanks to Paul Sarte who was both my colleague in Paul's group and my flatmate. Sarte has provided me both academic and mental support in the past few years and he is a good academic role model to look up to.

I would like to thank Dr Gary Nichol (University of Edinburgh) for his assistance with the thermogravimetric analysis that was carried out on one of the materials studied in this Thesis.

The synchrotron and neutron diffraction work described in this Thesis would not have been possible without the amazing assistance provided by facility local contacts and beamline scientists, particularly: Dr Mauro Coduri (European Synchrotron Radiation Facility), Dr Clemens Rita (Institut Laue-Langevin), Dr Andy Fitch (European Synchrotron Radiation Facility) and Dr Pascal Manuel (ISIS). Mauro has spent a lot of his own time helping us carrying out synchrotron diffraction experiments for almost all the high-pressure samples described in this work.

I would also like to thank Prof. Yuichi Shimakawa and his research group in Kyoto, Japan for the collaboration on one of the projects in this Thesis. I need to thank all his group members, particularly Dr Takashi Saito, Dr Midori Estefani Amano Patino, Dr Fabio Denis Romero and Xabier Martinez de Irujo Labalde.

All the work described in this thesis would not have been possible without the financial support from the European Research Council and Japan Society for the Promotion of Science; as well as Engineering and Physical Sciences Research Council and Science, Technology Facilities Council, the European

Synchrotron Radiation Facility and Institut Laue-Langevin for the provision of beamtimes.

Finally, I would like to thank my family, particularly my Dad, my Mum and my sister for their mental and financial support. A big special thanks to my fiancée, Jurgita Peciulyte, who has been very supportive in the past few stressful yet cheerful years and has been doing her best to help, especially in times when life did not go as expected. She also proofread part of this Thesis, particularly this part.

Another family to thank is the Team Peffer Bank (Rozi, Dr Eszter Fazekas, Gyuri Svachulay and Jurgita) who have provided great support to my writing through food and routine gatherings.

CONTENTS

Chapter 1. Introduction

1.1. Transition Metal Oxides

Transition metal oxides (TMOs) find a wide range of applications due to the fascinating electronic and magnetic properties they possess. These applications include electronic circuit boards, magnetic data-storage devices, battery cells and many more examples that play important roles in both everyday uses and cutting-edge technological applications. The advancements in modern technology provide a strong driving force for the research of TMOs, making them one of the most intensively studied classes of materials in the past few decades.

The behaviour of the valence *d*-orbital electrons from the cations in TMOs give rise to the unique physical properties of the materials. These *d*-electrons are strongly correlated with one another. Their mobility in an extended lattice structure is determined by their kinetic energy and Coulomb repulsion energy, which can result in electrons varying from being from fully delocalised (metallic behaviour) to completely localised at the cation sites (insulators). The *d*-electrons in TMOs are often found on the border between localised and delocalised behaviour. As a consequence of that, different electronic states with different physical properties are often found to have similar energies, making these systems very sensitive to perturbations. Small changes, such as in temperature, pressure and composition, can lead to one phase becoming more favourable than another and result in a phase transition. In some systems,

the energy difference between two or more electronic states is so small that multiple phases can coexist under the same physical conditions and give rise to exotic physical properties. A well-known example of that is the colossal magnetoresistance observed in manganite perovskites, where electronic phase separation results in a charge ordered insulating phase with ferromagnetic behaviour and an antiferromagnetic metallic phase. The coexistence of the two phases give rise to the strong magnetoresistance of these materials.[1,2,3]

1.2. Electronic Degrees of Freedom

The study of TMO systems usually involves solving their ground state structures, which reveals the fundamental electronic interactions in their extended structures. Ground states are established when thermal energy is removed from the system. In such states, the valence *d*-electrons in TMO systems are generally found to be localised at their corresponding cation sites, due to the strong electron correlation. The electronic structure can therefore be determined by the electron configurations of the cations. The fundamental properties of electrons give rise to the charge, orbital and spin degrees of freedom and when the degrees of freedom of different cation sites are correlated, an ordered electronic state is established.

The charge degree of freedom describes the mobility of *d*-electrons in a system. Charge ordering can occur in TMOs that consist of cations with multiple

oxidation states. The transition would result in the charges that are delocalised over all the cation sites in the lattice becoming localised at certain crystallographic sites, giving a particular site a set oxidation state. The occurrence of charge ordering is usually accompanied by a reduction in the electrical conductivity of the materials, due to the localisation of electrons.

The transition metals in TMOs experience crystal field effects from their interactions with the coordinating oxygen anions. In octahedral geometry, the five *d*-orbitals are split into two groups with degenerate crystal field potentials – the e_g and t_{2g} orbitals. The e_g group consists of the d_{z^2} and the $d_{x^2-y^2}$ orbitals, which have the symmetries that are directed at the O^{2-} and are higher in crystal field energy compared to the d_{xy}, d_{xz} and d_{yz} orbitals in the t_{2g} group. Asymmetrically filled degenerate *d*-orbitals have an orbital degree of freedom, where the degeneracy of orbitals can be broken through a Jahn-Teller distortion to gain crystal field stabilisation energy, as described in **Figure 1.1A**.[4]

TMOs with cations that have unpaired electrons have a spin degree of freedom, which gives them a magnetic moment. At high temperature these spins in the extended lattice have random orientations, due to random motions induced by thermal energy. Such a state is described as paramagnetic. Materials in the paramagnetic state can be magnetised in the presence of an external field, which aligns the spins antiparallel to the applied field. When the thermal energy is removed from a paramagnetic system, the spins from different cation sites can correlate with each other through exchange interactions to form

magnetically ordered states. The magnetic exchange mechanisms between cations can be described by the Goodenough-Kanamori rules[5,6,7] Direct exchange can occur between magnetic cations when the separation distance in between them is sufficiently close. Such interactions generally favour an antiparallel spin alignment with no net magnetic moment - antiferromagnetism. The magnetic behaviour in TMOs is often found to be governed by strong superexchange interactions, where the relation of the spin orientations of magnetic cation sites is determined by the M-O-M angle (180° favours antiferromagnetism, and 90° favours ferromagnetism, where the spins align in parallel with one and the other as shown in **Figure 1.1B**). In the case when there is an uneven number of antiparallel spins, such as in magnetite,[8,9] or in a canted antiferromagnet, the magnetic behaviour is described as ferrimagnetic.

If more than one degree of freedom is possessed by a system, they can couple to each other. The electronic degrees of freedom can also couple to those of the lattice, and in such a case, the electronic ordering may be accompanied by a lattice distortion. An example of a TMO that exhibits coupled electronic-lattice ordered states is $La_{0.5}Ca_{0.5}MnO_3$, a manganese-based perovskite that exhibits cooperative long-range charge, spin, orbital and lattice orderings.[10]

(A)

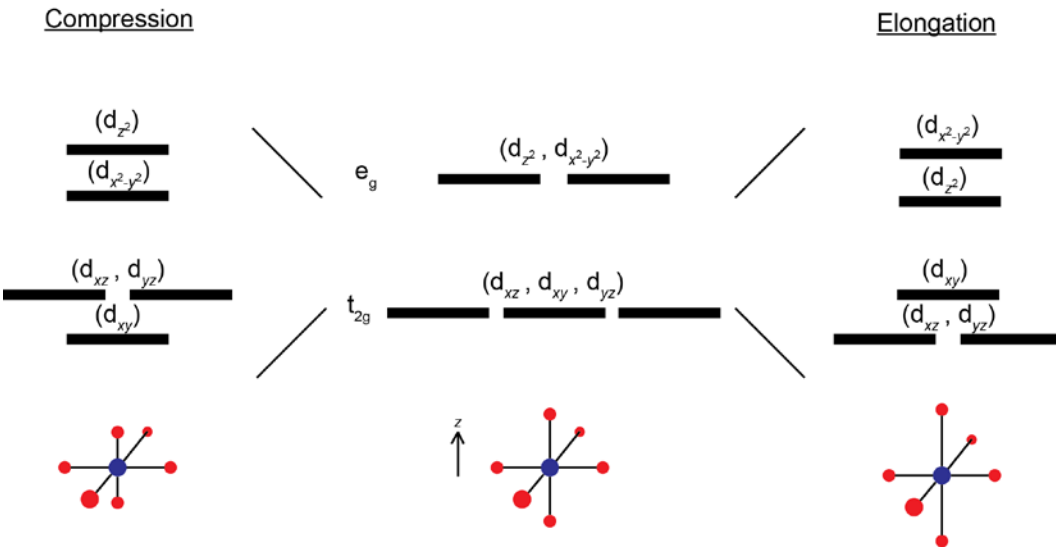

(B)

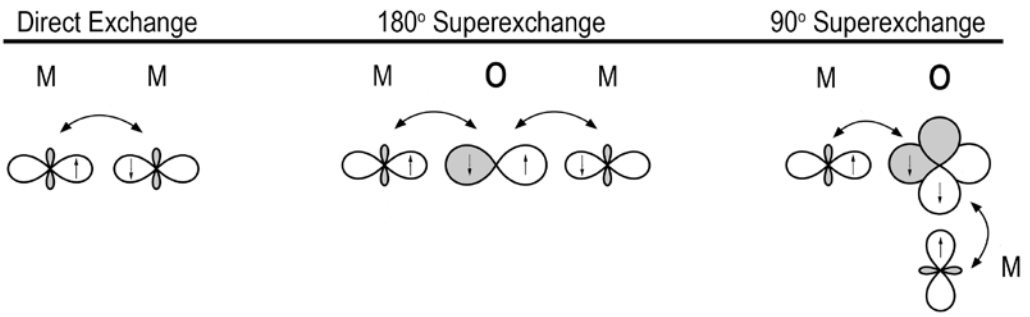

Figure 1.1 (A) Degeneracy in the t_{2g} and e_g orbitals can be removed through a Jahn-Teller distortion and results in octahedral compression (left) and elongation (right). The type of distortion an octahedron favours is dependent on the electronic configuration of the coordinated cation (blue).[4] (B) Direct exchange and M-O-M superexchange interactions in different geometries. Direct exchange between two magnetic cation sites favours an antiferromagnetic alignment due to the Pauli exclusion principle, as such a configuration allows the electrons to hop between the neighbouring sites. Whereas for neighbours with parallel spins, the mobility of the electrons is suppressed. Superexchange applies to cation sites that are separated by an oxygen, which allows the *d*-electrons to hop to neighbouring sites. As indicated in the figure, 180° M-O-M angles favours the cations on each side having antiparallel spins, and 90° degrees geometry gives rise to ferromagnetic configurations. Figure reproduced from reference 7.

1.3. Orbital Molecules

$La_{0.5}Ca_{0.5}MnO_3$ and many other manganite perovskites display long range electronic ordering across the crystal structure. Direct interactions between cations in these perovskites are not possible due to the large separation distances between the cations. However, in systems where the cation-cation distances are sufficiently short and the t_{2g} orbitals of the neighbouring cations are directed at each other, weak direct metal to metal interactions can occur. These direct interactions are stabilised via the delocalisation of t_{2g} electrons between local neighbours to form clusters of covalently-bond 'molecules' across the lattice.[11] For the electrons to be shared between multiple sites, their spin should be ordered, and the delocalisation of the electrons must obey the Pauli principle. The formation of these clusters of 'molecules' is associated with orbital ordering of the cations, which localises the *d*-electrons into specific t_{2g} orbitals such that they can interact with neighbouring cations, hence these clusters of molecules are known as orbital molecules.[12,13,14] The critical separation distance for different transition metal cations to interact with one another can be estimated using a model provided by J. Goodenough.[15]

1.3.1. Dimeric Orbital Molecules

Many of the reported orbital molecules are found in structures with edge-sharing octahedra, where the t_{2g} orbitals of different cations can interact across the short separation distance through the octahedron edges. One of the earliest reported cases of orbital molecules was found in the rutile-type

structure of VO_2.[16,17] Above 340 K, VO_2 adopts a tetragonal structure with one dimensional edge sharing VO_6 octahedra along the <001> direction, arranged with an equal distance between the cations along the chain. The V^{4+} ions are Jahn-Taller active and hence the *d*-electrons can be localised in the d_{xy} orbitals. When VO_2 is cooled below 340 K, a metal-insulator transition occurs, accompanied by crystal structural distortion that leads to alternating long and short (3.1 Å and 2.7 Å) V-V spacings. The lattice distortion allows the *d*-electrons to be shared between the close pairs and forms dimers along the chain.[18]

In the past few decades, many orbital molecule states have been reported in materials that adopt the spinel structure. Spinels have face-centred symmetry (space group $Fd\bar{3}m$), with a general chemical formula of AB_2X_4. There are two independent cation sites – A and B, and an anion site X. The A cation site forms AX_4 tetrahedra, whereas the B site has BX_6 octahedral coordination. Similar to VO_2, the octahedra are edge shared, therefore if the cations occupying the B site have a t_{2g} orbital degree of freedom, they can form orbital molecules. An example of that is the formation of Ti^{3+} dimers in the ground state structure of $MgTi_2O_4$.[19] $MgTi_2O_4$ undergoes a structural distortion at 260 K that changes the six equal Ti-Ti nearest neighbour separation distances such that some are either long (3.16 Å) or short (2.85 Å). In a similar manner as in VO_2, dimers are formed between the close Ti^{3+} pairs by sharing the single

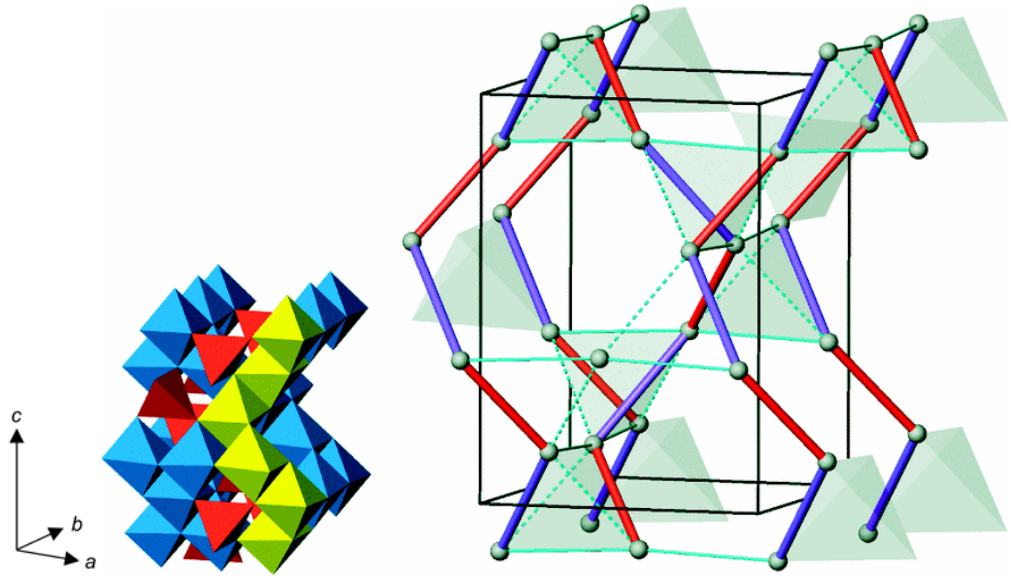

Figure 1.2 The formation of dimeric orbital molecules in the tetragonal structure of $MgTi_2O_4$ at 260 K. The short Ti-Ti distances are represented by the red bonds, where dimers are formed, with the purple bonds showing the longer separation distances. The inset to the left shows part of the spinel structure in the same orientation, with one of the helices highlighted in yellow. Figure reproduced from reference 19.

d-electron from each cation. The long and short Ti separations in $MgTi_2O_4$ form helices, leading to a chiral crystal structure, shown in **Figure 1.2**.

Orbital molecules can also form in systems with mixed valence cations. The non-integer charge of the cations give rise to a charge degree of freedom. Such a phenomenon can be found in $CuIr_2S_4$, where two cation environments (Ir^{4+} and Ir^{3+}) can be found at the B site of the spinel.[20] The Ir cations in $CuIr_2S_4$ have low spin electronic configurations, where Ir^{4+} (t_{2g}^5) has an orbital degree of freedom and Ir^{3+} (t_{2g}^6) is Jahn-Teller inactive with fully filled t_{2g} orbitals. At high temperature, the charge is distributed evenly across the B sites and gives an overall Ir oxidation state of 3.5+. However, charge ordering of $Ir^{4+/3+}$ at 340 K leads to a metal-insulator transition and orbital ordering of Ir^{4+}. The orbital

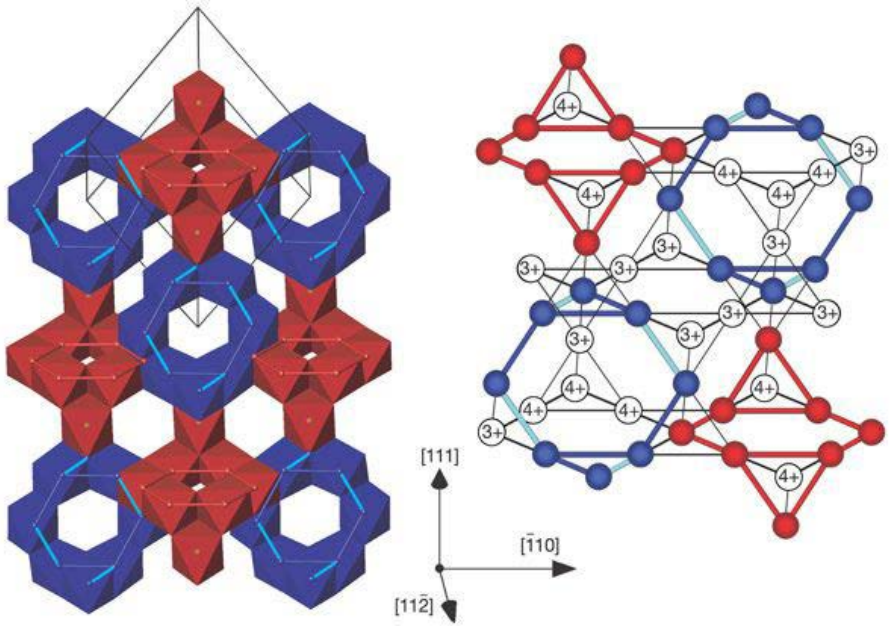

Figure 1.3 (Left) Crystal structure of $CuIr_2S_4$ at 50 K, with red and blue octahedra representing $Ir^{3+}O_6$ and $Ir^{4+}O_6$, respectively. Dimers of Ir^{4+}-Ir^{4+} are formed (as indicated by light blue bonds) below the charge and orbital ordering temperature of 340 K. (Right) formation of Ir_2^{8+} dimers lead to long and short Ir-Ir distances in the eight-membered Ir^{4+} rings. Figure reproduced from reference 20.

distortion of the Ir^{4+} site results in longer and shorter distances in the eight membered Ir ring structure and forms dimers. (**Figure 1.3**)

1.3.2. Large Orbital Molecules

Orbital molecules do not only exist in dimer forms, and larger orbital molecules were also reported. Triangular trimers are believed to form in $LiVO_2$ below the magnetic ordering temperature at T_C ~500 K. [21, 22] The transition is accompanied by a structural distortion and dramatic increase in the electrical resistivity of the material. It was claimed that the lattice ordering in $LiVO_2$ results in two close neighbours for each V^{3+}, each of which has two valence *d*-

electrons that can delocalise within a triangular trimer to form an orbital molecule. Another report of triangular trimers was found with the mixed valence vanadium oxide $BaV_{10}O_{15}$, where trimers are formed through the charge ordering of $V^{2+/3+}$ and the orbital degree of freedom possessed by V^{3+}.[23,24.25] (**Figure 1.4**) Trimeric orbital molecules also exist in linear geometry. One of the first reports of linear trimers was in the ground state structure of magnetite (Fe_3O_4),[12,13] which provided the solution to the long running mystery associated with the Verwey transition (as detailed in Section 1.4.1).[26]

Even larger orbital molecules were reported in 2006 by Y. Horibe, where V_7 heptamers are formed in AlV_2O_4 below 700 K.[27] However, a recent detailed study by A. Browne *et al.* revealed that the reported heptamers are actually pairs of trimers and tetramers, as shown in **Figure 1.5**, formed through a cubic to rhombohedral structural transition coupled with V^{2+} and V^{3+} charge ordering.[28] A follow-up study by Browne *et al.* showed that the Ga analogue of the vanadium oxide spinel system, GaV_2O_4, can be synthesised and also has

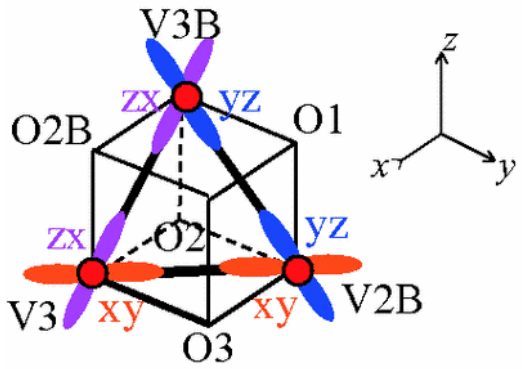

Figure 1.4 Triangular trimers in $BaV_{10}O_{15}$ at low temperatures. Trimers are formed from the overlapping of the three t_{2g} orbitals of the V2B, V3B and V3 sites, allowing the d-electrons from the three V^{3+} to delocalise within the cluster. Figure reproduced from reference 24 and 25.

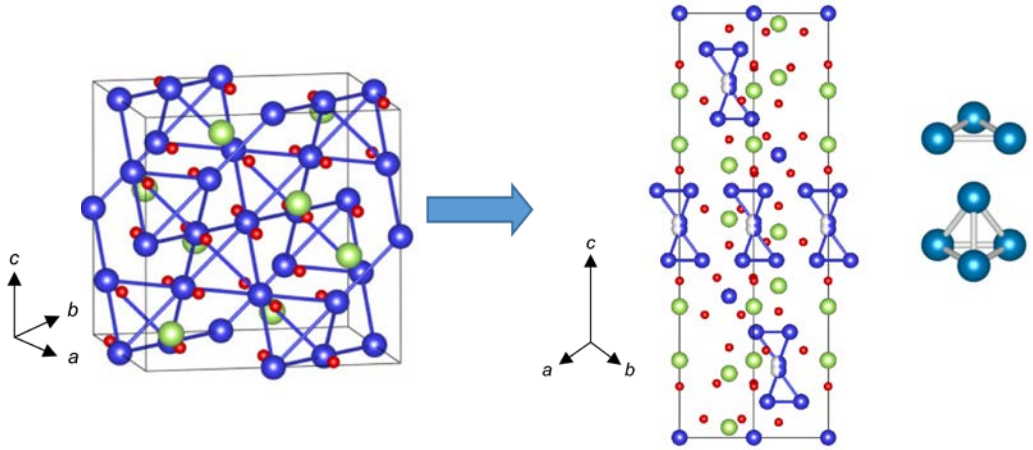

Figure 1.5 The rhombohedral distortion of AlV_2O_4 is accompanied by $V^{2+/3+}$ change and orbital orderings that lead to the formation of vanadium trimers and tetramers. Figure reproduced from reference 28.

V_3 and V_4 clusters, in a similar manner as in AlV_2O_4, when cooled below a charge ordering temperature of T_{CO} = 415 K.[29]

1.4. The $M^{2+}Fe_{n-1}O_{n+1}$ Ferrite System

Iron oxides are made up of two of the most abundant elements on Earth. This class of minerals plays an important role in the modern technological world. The properties possessed by many ferrites allow them to be use in a very wide variety of applications, such as in magnetic data storage and biosensing.[30,31,32,33] Iron oxides are also an abundant mineral under the surface of the Earth.[34,35] Being able to synthesise and study these materials in a laboratory, particularly those that are formed at high pressure, allows scientists to gain access to minerals that are previously inaccessible to due to

the depth they exist at. These studies would provide insights to the formation conditions and structural and electronic properties of these materials.

The iron oxide system is one of the most intensely studied areas in the solid-state field. And despite being one of the most commonly used and well-studied classes of minerals for decades, new discoveries are being made in the ferrite system every year; the ground state structure of one of the most well-known ferrites, magnetite, was only recently solved, and new members of the iron oxide family are being revealed every year.

1.4.1. Magnetite (*M* = Fe, *n* = 2)

Magnetite (Fe_3O_4) is the first ever discovered magnetic material, which gave rise to the word 'magnet'. It is one of the most common forms of iron oxide found on earth, alongside with hematite (Fe_2O_3). The structure of magnetite was first reported in 1915 by W. H. Bragg *et al.*.[36] It is one of the first crystal structures that was solved using x-ray diffraction.

Magnetite adopts the inverse spinel structure, with a chemical formula of $Fe^{3+}(Fe^{2+}Fe^{3+})O_4$. The tetrahedral site is occupied exclusively by iron ions with a 3+ oxidation state, whereas the octahedral site is populated with both Fe^{2+} and Fe^{3+} cations in a ratio of 1:1. Magnetite has a magnetic ordering temperature at T_C = 856 K. The system orders ferrimagnetically, which gives rise to its iconic permanent-magnet behaviour.[8,9] Magnetite is also known for its remarkable electrical conductivity, due to the presence of the minority spin

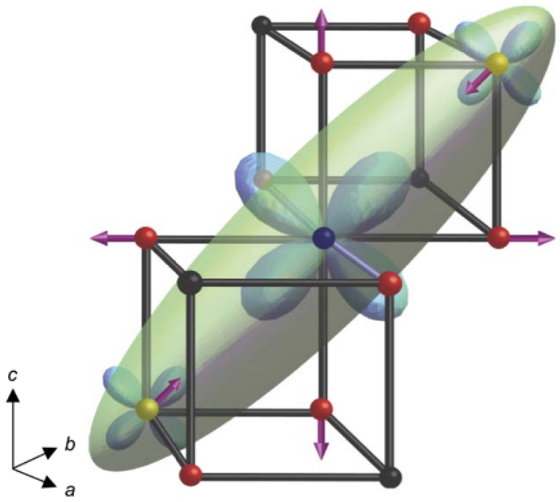

Figure 1.6 The formation of a trimeron between three iron B sites. Fe^{2+} is shown as blue sphere, with Fe^{3+} represented by yellow spheres and oxygen as red. The purple arrows show the atomic displacements due to the structural distortion. The d_{xy} orbitals through which the minority spin electron is delocalised between the three Fe ions is shown. Figure reproduced from reference 13.

electron of the Fe^{2+} ions, which can hop between edge sharing cation sites.[37] The ground state structure of magnetite was first reported in 1939 by E. J. W. Verwey, who observed a metal to insulator transition when cooling it below 120 K. The transition was named after the discoverer, as the Verwey transition. Subsequent reports proposed that the insulating behaviour resulted from the charge ordering of Fe^{2+} and Fe^{3+}, which suppresses the mobility of the minority spin electron. And such ordering would also lead the crystal structure to distort.[38] Numerous studies attempted to explain the nature of this transition.[39] Despite the original discovery being made decades ago, the ground state structure was only recently solved.[13,40] Diffraction experiments carried out on magnetite confirmed the occurrence of charge ordering at 120 K. The transition is accompanied by a structural distortion that leads to a lowering of the crystal symmetry from cubic to monoclinic. Orbital ordering of the Fe^{2+} sites localises

the minority spin electron into the d_{xy} orbital, which is directing at the d_{xy} orbitals of two Fe^{3+} nearest neighbours. The spin alignment allows the minority electron from the Fe^{2+} to delocalise over the Fe^{3+}-Fe^{2+}-Fe^{3+} trimer. This results in the formation of orbital molecules in the form of trimeric polarons known as trimerons, as shown in **Figure 1.6**.

1.4.2. Fe_4O_5 – The Parent Member of the $M^{2+}Fe_3O_5$ System

Fe_4O_5, a system closely related to magnetite, was recently discovered using high-temperature and high-pressure methods by B. Lavina *et al.*.[41] Fe_4O_5 is the parent member (with M = Fe) of the $M^{2+}Fe_3O_5$ system. Lavina's study showed that the Fe_4O_5 phase can be prepared under a pressure of 10 GPa at 1527 °C and the structure remains stable up to 30 GPa. Subsequent work has showed that a related series of Fe_nO_{n+1} homologues with larger n, such as Fe_5O_6, can be made at high pressures.[42,43,44]

Fe_4O_5 crystallises into an orthorhombic *Cmcm* cell with the $Sr_2Tl_2O_5$ type structure. The $Sr_2Tl_2O_5$ structure type is found to be adopted by all of the reported $M^{2+}Fe_3O_5$ members (as detailed in this Section and the Results Chapters 3 - 6 of this Thesis). This structure type was named after $Sr_2Tl_2O_5$, with its crystal structure revealed in 2005.[45,46] However, this *Cmcm* structure was actually first reported with the discovery of the Ca analogues of $M^{2+}Fe_3O_5$, $CaFe_3O_5$, in 1980.[47] There are four formula units in a *Cmcm* unit cell. The

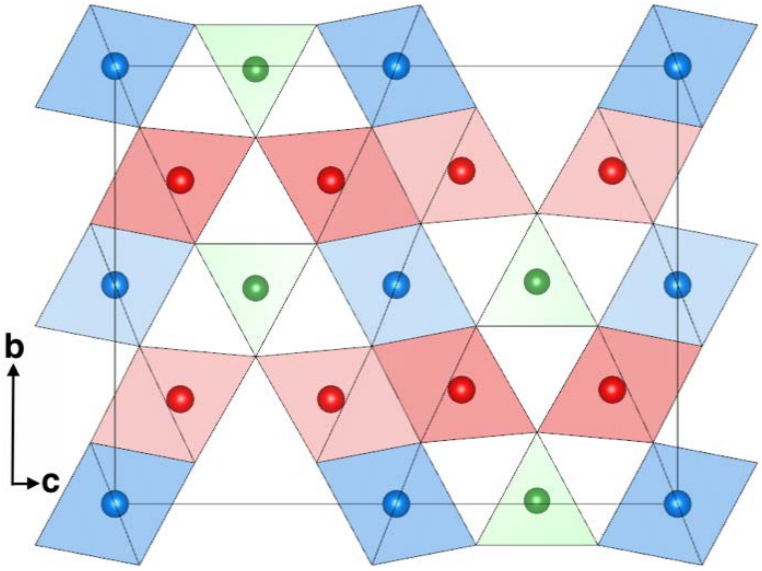

Figure 1.7 Projection of the *Cmcm* structure of $M^{2+}Fe_3O_5$, with M1 site octahedra shown in red, M2 site octahedra in blue, and M3 site triangular prisms in green. Oxygens are located at the corners of the polyhedra.

crystal structure consists of three crystallographically independent cation sites – two with octahedral coordination (referred to as M1 and M2 in this Thesis) and one triangular prismatic (M3), as shown in **Figure 1.7**. The M1 site has the Wyckoff position 8*f*, with a variable coordinate of (½, *y*, *z*) and Wyckoff position 4*a* for M2 at (0, 0, 0). The M3 site has coordinates of (0, *y*, ¼) and the Wyckoff position 4*c*. The three oxygen anion sites have Wyckoff positions and coordinates of 4*c* at (½, *y*, ¼) for O1 and 8*f* at (0, *y*, *z*) for O2 and O3. The crystallographic parameters of the MFe_3O_5 structure type is summarised in **Table 1.1**. In $M^{2+}Fe_3O_5$ structures the octahedral sites are occupied predominantly by Fe^{2+} and Fe^{3+} ions, forming edge-sharing FeO_6 octahedra in layers perpendicular to the *c* axis, whereas the large triangular prismatic site usually accommodates the M^{2+} species. However, in the case of where the

Table 1.1 MFe$_3$O$_5$ adopts the orthorhombic crystal structure ($a \neq b \neq c,\ \alpha = \beta = \gamma = 90°$), in the space group of Cmcm. Table summarises the atomic parameters for the MFe$_3$O$_5$ structure type.

Atoms	Wyckoff position	Atomic coordinates		
		x	*y*	*z*
M1	8*f*	½	*y*	*z*
M2	4*a*	0	0	0
M3	4c	0	*y*	¼
O1	4*c*	½	*y*	¼
O2	8*f*	0	*y*	*z*
O3	8*f*	0	*y*	*z*

M^{2+} is smaller than Fe^{2+} (as detailed in Chapters 5 and 6), cation disordering would be expected. The MO$_6$ triangular prisms share faces along the *a* axis, channelling through the layers of octahedra.

A detailed structural study of Fe_4O_5 published later by S. V. Ovsyannikov *et al.* confirmed that the triangular prismatic site in Fe_4O_5 is occupied exclusively by large Fe^{2+}, whereas the two octahedral sites consist of a mixture of Fe^{2+} and Fe^{3+} ions.[48] Fe_4O_5 exhibits antiferromagnetic behaviour at room temperature, with an estimated Fe spin ordering temperature T_N = 320 K. It displays semiconducting behaviour, with an electrical resistivity of ~0.018 Ω cm at room temperature and a charge activation energy of ~25 meV at ambient conditions, similar to that of magnetite (14 meV).[49] The high conductivity is likely due to the charge transfer between octahedral sites and the small conduction band gap. A dramatic increase in the resistivity of this material was reported at 150 K, with an increase of the activation energy to ~113 meV, similar to that of the Verwey transition found in magnetite. This change of the electrical properties of Fe_4O_5 originates from the charge order of Fe^{2+} and Fe^{3+} in the octahedral

sites at 150 K, which is accompanied by an incommensurate structural distortion. The lattice distortion, along with the orbital ordering of Fe^{2+}, leads to long and short Fe-Fe distances and forms clusters of spin aligned dimeric and trimeric orbital molecules, as shown in **Figure 1.8**. A second magnetic transition is also found in Fe_4O_5 below 90 K, where the spins of the Fe ions reorient to give rise to ferrimagnetism.

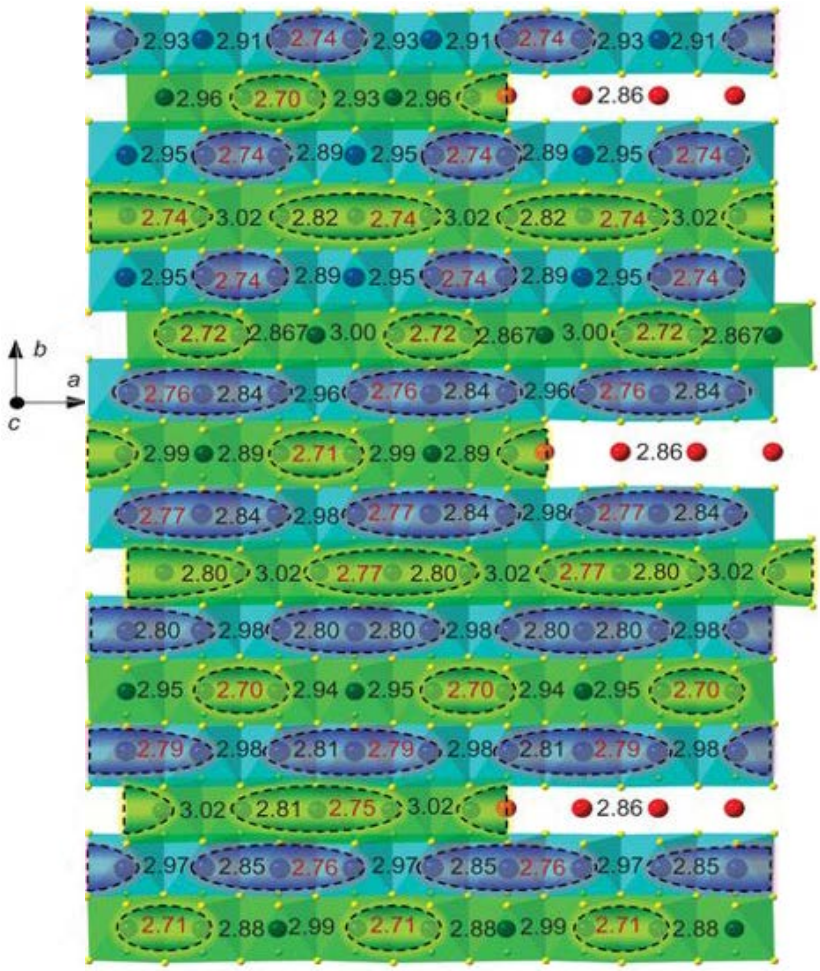

Figure 1.8 A cross section of the Fe_4O_5 crystal structure of at 4 K. The green and blue octahedra represent the M1 and M2 sites, respectively, that form edge sharing ribbons along the *a* axis. The M3 Fe site is shown as red spheres, respectively. The distances between the cation sites are shown in the figure. The shortening in the Fe-Fe distances lead to the formation of dimeric and trimeric orbital molecules in the low temperature structure of Fe_4O_5, as indicated by ellipsoids. Figure reproduced from reference 48.

Recent study by Ovsyannikov *et al.* revealed the low-temperature high-pressure phase diagram of Fe_4O_5.[50] The sensitivity of Fe_4O_5 to pressure has led to the discovery of several novel high-pressure phases of this system. These new phases form different charge ordered states when cooled below their ordering temperatures. Ovsyannikov's work demonstrates that the electronic properties in Fe_4O_5 can be tuned with the use of pressure, highlighting the complexity of the electronic behaviour of the $M^{2+}Fe_3O_5$ system.

1.4.3. $CaFe_{n-1}O_{n+1}$ (*M* = Ca) Analogues

The Ca analogues of the $M^{2+}Fe_{n-1}O_{n+1}$ system (with n = 4, 5 and 6) were reported by O. Evrard *et al.* in 1980.[47] This study showed that $CaFe_3O_5$, $CaFe_4O_6$ and $CaFe_5O_7$ can be synthesised using ceramic methods at ambient pressure. Initial phase characterisation indicated that $CaFe_3O_5$ adopts the same orthorhombic structure as Fe_4O_5, with Ca^{2+} occupying the triangular prismatic site that channels between the FeO_6 octahedra. With structural properties closely related to those of Fe_4O_5, complex electronic orderings of similar manners may be expected to be found in the Ca analogue. Despite the discovery of $CaFe_3O_5$ in 1980, no detailed study of this material has been made.

$CaFe_5O_7$ adopts a monoclinic $P2_1/m$ structure at room temperature. Recent reports showed an orthorhombic structure in the space group *Cmcm* above 360 K.[51,52] The 360 K orthorhombic to monoclinic transition is accompanied by an increase of the electrical resistivity and a change to the magnetic behaviour

of the system. The changes of physical properties, along with results obtained from bond valence sums and Mössbauer spectroscopy, implicated a coupled $Fe^{2+/3+}$ charge and spin ordering transition, similar to what was reported in Fe_4O_5. A second magnetic transition was also found at ~150 K, which led to an enhancement of the magnetic moment of $CaFe_5O_7$, resembling the spin reorientation transition observed in Fe_4O_5 at low temperatures that leads to ferrimagnetism.[48]

1.4.4. $Mg^{2+}_nFe^{2+}_{2-n}Fe_2O_5$ (*M* = Mg) Analogues

The Mg analogue of MFe_3O_5 was discovered in 2018, during the study of $Mg^{2+}_nFe^{2+}_{2-n}Fe_2O_5$ ($0.541(1) \leq n \leq 1.978(5)$) solid solutions.[53] Polycrystalline samples of $MgFe_3O_5$ and the related solid solutions were stabilised using high-pressure and high-temperature solid-state synthesis methods. Initial structural characterisation showed that phases with $0.541(1) \leq n \leq 1.978(5)$ have an orthorhombic structure in the space group *Cmcm*, isostructural to Fe_4O_5 and $CaFe_3O_5$.[41,47] The success in synthesising Fe_4O_5–$Mg_2Fe_2O_5$ solid solutions suggests that MFe_3O_5 phases with different M^{2+} species (besides Ca and Fe) can be synthesised and that solid solutions of Fe_4O_5–$M^{2+}_2Fe_2O_5$ may be prepared and studied. This would give rise to the possibility of tuning physical properties through chemical substitutions.

1.5. Aims of the Thesis

Fe_4O_5 displays exotic electronic ground states and it is currently the only member of the $M^{2+}Fe_3O_5$ family to have its structure studied in detail. The Ca analogue of the system has been discovered; however, studies of its structural and electronic behaviours have not yet been reported. Being isostructural with Fe_4O_5, $CaFe_3O_5$ is expected to exhibit exciting properties that are similar to those of its parent phase. The first part of this Thesis (Chapter 3) sets out to investigate the electronic properties of $CaFe_3O_5$ and to look for the formation of orbital molecules in the ground state structure of this material. The second part (Chapters 4-6) focuses on the discovery and characterisation of novel high-pressure phases of the $M^{2+}Fe_3O_5$ system, where small M^{2+} (M = Mn, Co and Ni) are stabilised in the *Cmcm* $M^{2+}Fe_3O_5$ structure using high-temperature and high-pressure solid-state synthesis techniques.

The aims of this Thesis were to:

- synthesise and study the Ca analogue of the $M^{2+}Fe_3O_5$ family,
- discover novel phases of the $M^{2+}Fe_3O_5$ system, by substituting M with transition metals that are electronically similar to Fe,
- study the structure and electronic properties of the novel phases,
- gain insights to the trends of and correlations between these phases,
- investigate the effect of the M^{2+} cation size and electronic properties on the structures and behaviours of MFe_3O_5 analogues.

1.6. References

1. E. Dagotto, T. Hotta, A. Moreo. *Phys. Rep.* **2001,** *344*,1–153.
2. M. Uehara, S. Mori, C. H. Chen, S. W. Cheong. *Nature* **1999,** *399*, 560–563.
3. Y. Tokura. *Rep. Prog. Phys.* **2006,** *69,* 797–851.
4. J. B. Goodenough. Magnetism and crystal structure in non-metals. *Massachusetts Inst Of Tech Lexington Lincoln Lab.* **1962,** 36.
5. J. B. Goodenough. *J. Phys. Chem. Solids* **1958,** *6*, 287-297.
6. J. Kanamori. *J. Phys. Chem. Solids* **1959**,*10*, 87-98.
7. E. Koch. *Autumn School on Correlated Electrons, Jülich* **2012,** *7*.
8. L. Néel. *Ann. Phys.* **1948,** *3*, 137-198.
9. C.G. Shull, E.O. Wollan, W.C. Koehler. *Phys. Rev. B* **1951,** *4,* 912–921.
10. P. G. Radaelli, D. E. Cox, M. Marezio, S. W. Cheong. *Phys. Rev. B* **1997,** *55*, 3015.
11. J. B. Goodenough. *Phys. Rev.*, **1960,** *117*, 1442–1451.
12. M. S. Senn, J. P. Wright, J. P. Attfield. *Nature*, **2012**, *481*, 173–176.
13. M. S. Senn, I. Loa, J. P. Wright, J. P. Attfield. *Phys. Rev. B*, **2012,** *85*, 125199.
14. J. P. Attfield. *APL Mater.* **2015,** *3,* 1–7.
15. J. B. Goodenough. *Magnetism and the Chemical Bond*, Wiley-Interscience, New York, **1963**.
16. J. B. Goodenough. *J. Solid State Chem.* **1970**, *3*, 490.
17. F. J. Morin. *Phys. Rev. Lett.* **1959,** *3,* 34.
18. K. D. Rogers. *Powder Diffr.* **1993,** *8*, 240–244.
19. M. Schmidt, W. Ratcliff, P. G. Radaelli, K. Refson, N. M. Harrison, S. W. Cheong, *Phys. Rev. Lett.* **2004,** *92*. 056402.

20. P. G. Radaelli, Y. Horibe, M. J. Gutmann, H. Ishibashi, C. H. Chen, R. M. Ibberson, Y. Koyama, Y. S. Hor, V. Kiryukhin, S. W. Cheong. *Nature* **2002,** *416,* 155–158.

21. H. F. Pen, J. Van Den Brink, D. I. Khomskii, G. A. Sawatzky. *Phys. Rev. Lett.* **1997,** *78,* 1323.

22. H. F. Pen, L. H. Tjeng, E. Pellegrin, F. M. F. de Groot, G. A. Sawatzky, M. A. van Veenendaal, C. T. Chen. *Phys. Rev. B - Condens. Matter Mater. Phys.* **1997,** *55,* 15500–15505.

23. T. Kajita, T. Kanzaki, T. Suzuki, J. E. Kim, K. Kato, M. Takata, T. Katsufuji. *Phys. Rev. B* ***2010,*** *81*, 060405(R).

24. K. Takubo, T. Kanzaki, Y. Yamasaki, H. Nakao, Y. Murakami, T. Oguchi, T. Katsufuji. *Phys. Rev. B* **2012,** *86*, 085141.

25. H. F. Pen, J. van den Brink, D. I. Khomskii, G. A. Sawatzky. *Phys. Rev. Lett.* **1997,** *78*, 1323.

26. E. J. W. Verwey. *Nature* **1939,** *144,* 327–328.

27. Y. Horibe, M. Shingu, K. Kurushima, H. Ishibashi, N. Ikeda, K. Kato, Y. Motome, N. Furukawa, S. Mori, T. Katsufuji*. Phys. Rev. Lett.* **2006,** *96,* 086406.

28. A. J. Browne, S. A. J. Kimber, J. P. Attfield. *Phys. Rev. Mater.* **2017,** *1,* 052003.

29. A. J. Browne, C. Lithgow, S. A. J. Kimber, J. P. Attfield *Inorg. Chem.* **2018,** *57 (5)*, 2815–2822.

30. G. Cordova, S. Attwood, R. Gaikwad, F. Gu, Z. Leonenko, *Nano Biomedicine and Engineering* **2014,** *6*, 31.

31. S. F. Hasany, N. H. Abdurahman, A. R. Sunarti, R. Jose. *Current Nanoscience* **2013,** *9*, 561.

32. J. Xie, S. Jon. *Theranostics* **2012,** *2*, 122.

33. S. Laurent, D. Forge, M. Port, A. Roch, C. Robic, L. Vander Elst, R. N. Muller. *Chem. rev.* **2008,** *108*, 2064.

34. J. Guignard, W. A. Crichton. *Mineral Mag*. **2014,** *78*, 361–371.

35. D. J. Frost, C. A. McCammon. *Annu. Rev. Earth Planet Sci.* **2008,** *36*, 389–420.

36. W. H. Bragg. *Nat*. **1915,** *95,* 561.

37. J. R. Drabble, T. D. Whyte, R. M. Hooper. *Solid State Commun.* **1971,** *9,* 275-278.

38. E. J. W. Verwey, P. W. Haayman, C. W. Romeijn. *J. Chem. Phys.* **1947,** *15,* 181.

39. S. Lee, A. Fursina, J. T. Mayo, C. T. Yavuz, V. L. Colvin, R. G. Sofin, I. V. Shvets, D. Natelson. *Nat. Mater.* **2008,** *7,* 130–133.

40. G. Perversi, J. Cumby, E. Pachoud, J. P. Wright, J. P. Attfield. *Chem. Commun.* **2016,** *52,* 4864–4867.

41. B. Lavina, P. Dera, E. Kim, Y. Meng, R. T. Downs, P. F. Weck, S. R. Sutton, Y. Zhao. *Proc. Natl. Acad. Sci. USA* **2011,** *108,* 17281–17285.

42. B. Lavina, Y. Meng. *Sci. Adv.* **2015,** 1, e1400260.

43. R. Myhill, D. O. Ojwang, L. Ziberna, D. J. Frost, T. B. Ballaran, N. Miyajima. *Contrib. Mineral. Petrol.* **2016,** *171*, 51.

44. Y. Garcia, G. Subias, J. *Phys. Condens. Matter* **2004,** *16,* R145.

45. M. Coutanceau, J.P. Doumerc, M. Chambon, J.C. Grenier, C. R. *Acad. Sci. Paris Ser. II* **1995,** *320,* 531.

46. P. Berastegui, S. Eriksson, S. Hull, F. J. García García, J. Eriksen. *Solid State Sci.* **2004,** *6,* 433–441.

47. O. Evrard, B. Malaman, F. Jeannot, *J. Solid State Chem.* **1980,** *35,* 112–119.

48. S. V. Ovsyannikov, M. Bykov, E. Bykova, K. Glazyrin, R. S. Manna, A. A. Tsirlin, V. Cerantola, I. Kupenko, A. V. Kurnosov, I. Kantor, A. S. Pakhomova, I. Chuvashova, A. I. Chumakov, R. Rüffer, C. McCammon, L. S. Dubrovinsky. *Nat. Chem.* **2016,** *8,* 501.

49. V. V. Shchennikov, S. V. Ovsyannikov, A. E. Karkin, S. Todo, Y. Uwatoko. *Solid State Commun.* **2009,** *149,* 759–762.

50. S. V. Ovsyannikov, M. Bykov, E. Bykova, K. Glazyrin, R. S. Manna, A. A. Tsirlin, V. Cerantola, I. Kupenko, A. V. Kurnosov, I. Kantor, A. S. Pakhomova, I.

Chuvashova, A. I. Chumakov, R. Rüffer, C. McCammon, L. S. Dubrovinsky. *Nat. Commun.* **2018,** *9,* 4142.

51. C. Delacotte, F. Hüe, Y. Bréard, D. Pelloquin. *Key Eng. Mater.* **2014,** *617,* 237−240.

52. C. Delacotte, F. Hüe, Y. Bréard, S. Hébert, O. Pérez, V. Caignaert, J. M. Greneche, D. Pelloquin. *Inorg. Chem.* **2014,** *53,* 10171–10177.

53. L. Uenver-Thiele, A. B. Woodland, N. Miyajima, T. B. Ballaran, D. J. Frost. *Contrib. Mineral. Petrol.* **2018,** *173,* 1−16.

Chapter 2. Experimental Techniques

2.1. Solid-State Synthesis

All the materials investigated in this Thesis are solids and were prepared using the ceramic method. The ceramic method is the most commonly used solid-state synthesis technique. Reactions of solids generally require a large activation energy, due to the low diffusion rate between reactants and the limitation of contact surface area.[1] Therefore, in order for the reaction to proceed, the solid reagents must be very well ground, mixed and packed together. And to overcome the high energy barrier for ionic diffusion, high-temperatures, and often high-pressures, are necessary.

2.1.1. Synthesis at Ambient Pressure

To prepare a sample for ceramic synthesis, powdered reactants are mixed together in stoichiometric ratios. It is essential to ensure the purity of the starting materials is high and they are dried before used so that the proportion of each component is accurate in the mixture. The powder mixture is then finely ground to form a homogenous mixture and pressed into pellets to maximise the rate of diffusion between reagents during the synthesis. All the samples described in this Thesis were ground manually using an agate mortar and pestle. The pellets were then heated in a box furnaces. The temperatures used for ceramic synthesis are generally above 500 °C and the duration of heating can range from hours to days, depending on the chemical species and the

quantity of sample. Due to the limitation of diffusion, samples may be reground, pellet-pressed and heated several times, for reaction completion to be reached.

As the formation of the high-temperature metastable product can be stabilised at high-temperature, and the outcome of the reaction can be influenced by altering the heating conditions and the sample environment. The atmosphere of a reaction can be controlled by passing a flow of gas through the tube furnace chamber. Inert gas, such as Ar (g) and N_2 (g) are used for reactions that are sensitive to air. To perform reduction or oxidation reactions, H_2 (g) and O_2 (g) (sometimes mixed with an inert gas to provide controls to the redox reaction) with a controlled flow rate are used. If the reactants involved are volatile or are highly sensitive to air, the reaction can be carried out under closed system. This can be achieved by sealing the reactants inside a quartz glass test tube under a vacuum condition before heating.[2] For example, Fe^0 can be oxidised to Fe^{3+} at temperatures as low as 260 °C in open atmosphere,[3] forming a more stable valence state of Fe. The use of vacuum conditions prevents the sample from air exposure that helps retaining the oxidation state and stoichiometric ratio of the final products, and hence minimises the formation of undesired products.

2.1.2. High-Pressure Synthesis

Ceramic synthesis can also be carried out under pressure to stabilise high-pressure and high-temperature metastable phases. High-pressure synthesis has become a very popular solid-state technique since 1955. The process was

first developed for the purpose of preparing synthetic diamonds. The potential of high-pressure synthesis has been dramatically widened and high-pressure materials has become one of the most popular areas in the solid-state field.

Pressure (P) can be defined by a simple relationship between force (F) and area (a), as demonstrated in **Equation 2.1**.

$$P = \frac{F}{a} \tag{2.1}$$

The amount of pressure an instrument can achieve is therefore limited by its loading force and the sample size. This can be illustrated by the simple piston-cylinder devices (**Figure 2.1**). Sample preparation in a piston-cylinder device involves loading a sample that is encapsulated into a tungsten carbide chamber. A tungsten carbide piston is then pressed onto the sample in the chamber to generate a high-pressure environment. These devices can

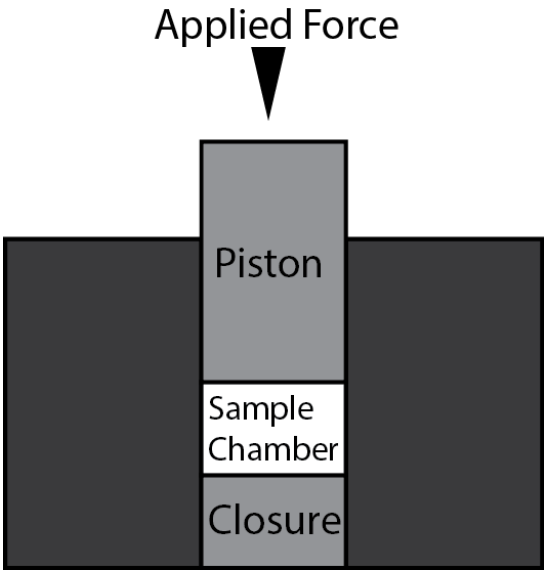

Figure 2.1 Schematic illustrating how pressure is generated using a simple piston-cylinder device. Figure reproduced from reference 5.

produce a large sample volume of approximately 100 mm^3 during one synthesis. However, only ~ 5 GPa of pressure can be achieved.[4] However, diamond anvil cells can generate pressures above 360 GPa, but with a sample size in the magnitude of a several μm^3.[5]

The high-pressure materials investigated in this Thesis require synthesis pressures from 10 GPa and in order to produce a good amount of sample under such pressure for characterisation (at least 50 mg of sample), a modified two-stage 6-8 Walker-type[6] multi-anvil press was used. The two-stage Walker-type module was invented by Walker and was modified by the press manufacturer Voggenreiter. The thickness of the steel ring in the press is double that of the original design, allowing the press to load up to 1000 tonnes of force. As described in its name, the press consists of two stages, where the first stage consists of six anvils that direct the applied force to the second stage. There are eight anvils in the second stage that allow the force to reach the sample at the centre equally from all directions. At each stage, the area the force is transferred to is smaller than the previous one, allowing the press to generate a very high-pressure. The setup is illustrated in a simple schematic diagram shown in **Figure 2.2**.

During high-pressure synthesis, the reactants are ground and mixed together. The mixture is pressed into a small platinum crucible that is lined with two thin layers of graphite for heating. The crucible is then placed inside a MgO octahedron, enclosed by eight tungsten carbide cubes (stage 2 of the press). The eight cubes form a split cube, with phyrophyllite placed on each side within

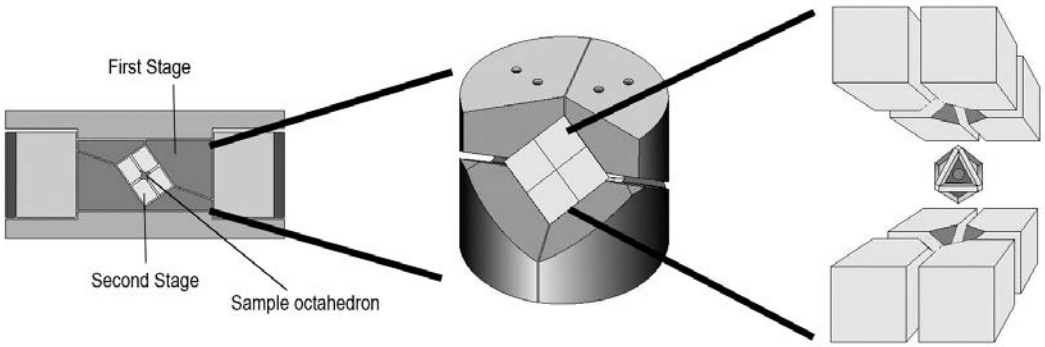

Figure 2.2 (Left) Schematic showing a cross section of the high-pressure press. (Middle) The carbide split cube is enclosed by the steel wedges. (Right) The sample octahedron sits in the middle of the eight tungsten carbide cubes.

the cubes for electrical insulation and force distribution. The split cube is then transferred onto the press chamber, enclosed by six hardened steel wedges (stage 1). A layer of mylar film is placed around the wedges, affixed with Polytetraflurooethane spray, for lubrication and electrical insulation. During heating, a current is passed through the graphite lining, which generates heat through the electrical resistance of graphite. At the end of the reaction, the sample is thermally quenched using the built-in water-cooling system. Quenching is essential in most high-pressure synthesis for trapping high-temperature and high-pressure metastable products. It also prevents the formation of thermodynamically favourable impurities during the process of cooling.

2.2. Diffraction Theory

The crystal and magnetic structure of the materials described in this Thesis were investigated using powder x-ray and neutron diffraction techniques. Diffraction is an elastic scattering process, where radiation is scattered by matter with no transfer of energy, and hence the energy of the incident wave is equal to that of the diffracted wave. The change in the wavevector from the incident (k_i) to the diffracted wave (k_f) upon scattering is defined as the scattering vector transfer Q and is expressed in **Equation 2.2**.

$$Q = k_f - k_i \tag{2.2}$$

2.2.1. Scattering from One Atom

X-ray and neutron radiation are generally used in diffraction experiments for obtaining structural information of solid-state materials, as their wavelengths are comparable to the atomic separation distance (generally in the order of Ångströms). X-rays and neutrons interact with atoms through different mechanisms:

X-rays are electromagnetic radiation and do not interact with the nuclei of atoms but can be scattered by the electron density that surrounds the atoms. The strength of the interaction between x-rays and an atom j is described by the form factor f_j, which is directly correlated with the atomic number of the atom. Hence, x-rays are not very sensitive to light elements. Due to the fact

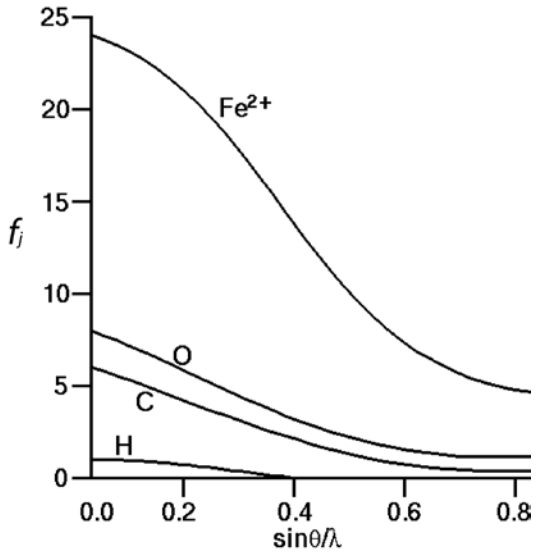

Figure 2.3 Evolution of x-ray scattering factor (f_j) of selected atoms over the scattering angle.[7]

that x-rays interact with the electron cloud of an atom, f_j corresponds to the Fourier transform of the electron density of the atom. The electron density decreases with the distance from the centre of the atom and the distribution can be described using a Gaussian function. Fourier transform of a Gaussian gives a narrower Gaussian, and therefore the f_j falls with the increase in scattering angle, as illustrated in **Figure 2.3**.[7]

Neutron radiation, on the other hand, is scattered by nuclei and the interaction strength b_j is independent of the atomic size. As the size of a nucleus is much smaller than the wavelength of the neutrons, nuclei are regarded as point scatterers. The distance that a nucleus can interact with the neutrons is the scattering length, which can differ significantly between atoms (**Figure 2.4**),[8] even between isotopes of the same element. Thus, neutrons can distinguish neighbouring elements on the periodic table, which is not possible for x-ray radiation, due to the similarity in electron density. Another advantage of

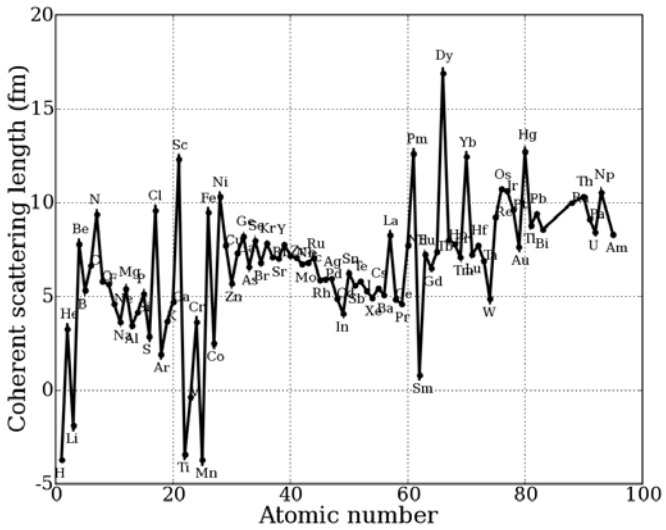

Figure 2.4 Neutron scattering length of elements in the periodic table.[8]

neutrons over x-rays is that oxygen diffracts x-rays poorly but has a large neutron scattering length. This is very useful for transition metal oxide systems, for obtaining accurate oxygen positions. As point scatterers have an isotropic interacting strength in all directions from the centre, along with the large difference in the size of nuclei and the wavelength of neutrons, the distribution of a nucleus in space gives a delta function. A delta function Fourier transforms to a horizontal line, hence b_j remains constant at any scattering angles.

Neutrons are charge neutral; hence they do not interact with electron density. However, each neutron carries an intrinsic magnetic moment with a spin ½ that allows neutrons to interact with matter that possesses a magnetic moment and gives rise to magnetic scattering. Just like x-ray form factors, the magnetic neutron form factors drop with the increase in scattering angle, and as such, magnetic reflections are only found in the low scattering angle region of a

diffraction pattern. Different from nuclear scattering, magnetic moments are axial vectors that have a magnitude and a direction. Therefore, the interactions between neutrons and magnetic atoms are highly anisotropic and the scattering cross section is dependent on the incident radiation and the moment of the atom. As a magnetic field is always at right angles to its direction, when a neutron is scattered by a magnetic component with a vector transfer Q, the moment of the component is always perpendicular to Q.

Although more structural information can be obtained from neutron diffraction compared to x-ray, using neutron also have disadvantages: neutron diffraction experiments require a much larger quantity of sample, due to the deeper penetration through materials. The restriction in sample size is particularly problematic for materials that can only be prepared in small quantities, such as high-pressure materials. Furthermore, neutron experiments can only be carried out in central facilities that can generate neutrons (as detailed in Section 2.2.6), and these experiments generally take a much longer time to organise and cost more to run than laboratory x-ray.

2.2.2. Scattering from a Lattice

2.2.2.1. Crystal and Magnetic Structure

The materials studied in this Thesis are crystalline, which means they contain a repeating arrangement of atoms that has translational symmetry in all three dimensions. The smallest unit with atoms that repeats in three dimensions to

make up the extended lattice is called a unit cell. The dimension and shape of a unit cell is defined by six lattice parameters – *a*, *b* and *c* for the length of its three edges; and α, β and γ for the angles. The relationship between the dimensions and angles, and the centring symmetry of the atoms in the cell can be described by one of the fourteen Bravais Lattices, as shown in **Figure 2.5**.[9] The atoms in a unit cell are defined by fractional coordinates (x, y and z) with respect to the origin of the cell. The atoms in the cells can be related to one another through symmetries, which can be described by symmetry operators, such as glide planes, screw axes and inversions. The combination of symmetry operators that can be applied to atoms and the fourteen Bravais

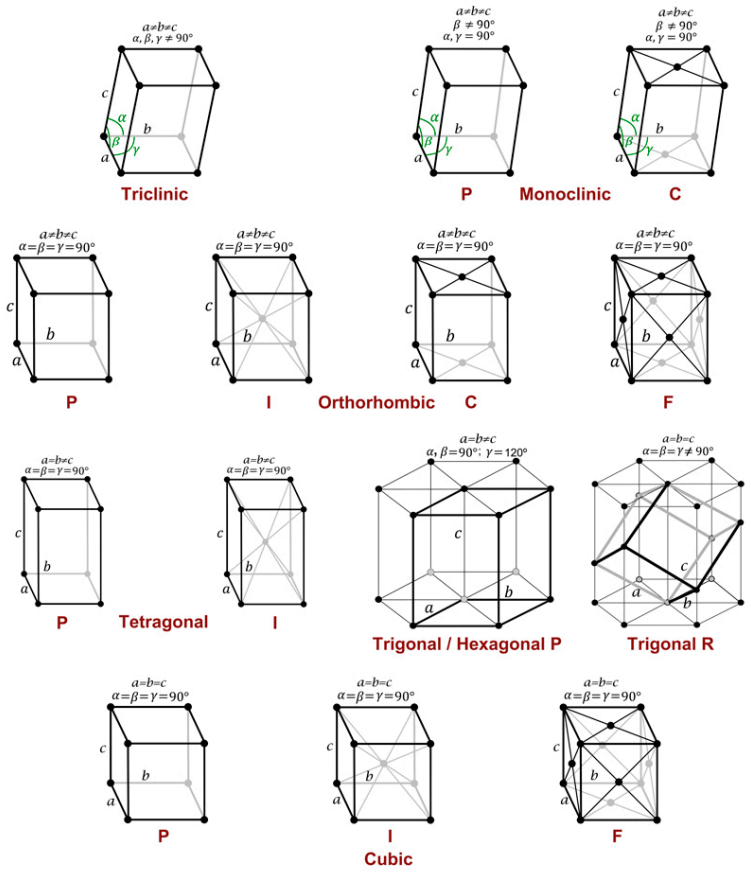

Figure 2.5 Fourteen Bravais Lattices, with centring symmetries labelled as P = primitive, C = *C*-centred, I = body-centred, F = face-centred.[9]

Lattices, gives rise to 230 possible space groups to describe crystal structures. All the materials described in this work have orthorhombic structures with a *Cmcm* space group. This means that they have lattice parameter relationships of $a \neq b \neq c$ and $\alpha = \beta = \gamma = 90°$, and have a *C*-centre symmetry, with mirror planes perpendicular to the *x* and *z* axis and a *c*-glide plane perpendicular to *y*.

The symmetry operations of magnetic moments of atoms in a unit cell are considered differently from those of the atomic position. As detailed in Section 2.2.1, magnetic moments are a vector that have a magnitude, as well as a direction. The position of these moments is given by the crystal space group. However, the direction of the moments can be changed by some symmetry operations, for example a mirror plane that is perpendicular to the moment can inverse its direction. All the combinations of symmetry operations in the 230 space groups gives rise to 1651 possible magnetic space groups, or often known as Shubnikov groups.[10] The number of potential magnetic structures of a system can be reduced using representation analysis. The analysis works by generating irreducible representations (IrReps), using the corresponding symmetry operators of the crystal space group and the atomic position to determine whether a moment would be parallel or antiparallel to the direction of the original moment after the symmetry operation. Each IrRep is made up of a set of basis vectors that represent the direction and magnitude of the magnetic moment for each crystallographic site. Magnetic representation analysis described in this Thesis were conducted using BasIreps in the FullProf Suite.[11]

The way magnetic moments propagate through a crystal unit cell is described by a propagation vector (*k*-vector). If the repetition of a magnetic cell is identical to the periodicity of the crystal unit cell, it has a *k*-vector of [0 0 0]. Magnetic unit cells with a period that is a rational fraction of the nuclear cell are said to be commensurate, otherwise, they are incommensurate.[12]

2.2.2.2. Bragg Diffraction

In 1913, during the investigation of the interactions between electromagnetic radiation with atoms, W. H. Bragg and his son discovered that the structure of crystalline materials can be determined using the diffraction of radiation.[13] Bragg *et al.* proposed that the periodic arrangement of atoms in crystalline gives rise to sets of infinite parallel planes of atoms that can act as diffraction gratings. Each set of these parallel planes is defined by Miller indices hkl. This notation describes the number of times a plane intercepts each axis in a unit cell. The distance that separates parallel planes with Miller indices of hkl is

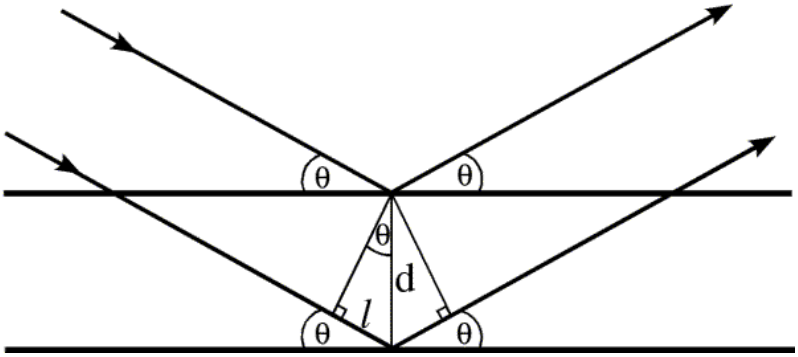

Figure 2.6 Diagram shows the radiation is reflected by two parallel atomic planes that are separated by distance *d*. The path length difference of the incident wave is labelled as *l*. The angle of the incident waves approaches (θ), in respect to the plane, is equal to that of the scattered wave. Figure reproduced from reference 13.

referred as d-spacing (d_{hkl}). As illustrated in **Figure 2.6**, incident radiation waves are reflected by the parallel atomic planes and the reflected waves are parallel to each other. However, the distances travelled by these parallel waves are differed by a path length difference after interacting with the atomic planes, which leads to a change in the phase of the reflected waves. In order for diffraction signals to be detected, the reflected waves must be in phase and interfere constructively, and thus the path length difference must be an integer n multiple of the radiation wavelength (λ), as described by Bragg's Law (**Equation 2.3**)

$$n\lambda = 2d \sin\theta \tag{2.3}$$

Where θ is the angle of the incident wave in respect to the atomic plane.

The d-spacings from each set of atomic planes in crystals are related to the lattice parameters. For orthorhombic systems, this relationship is given in **Equation 2.4**.

$$\frac{1}{{d_{hkl}}^2} = \frac{h^2}{a^2} + \frac{k^2}{b^2} + \frac{l^2}{c^2} \tag{2.4}$$

Thus, the lattice parameters of the material can be determined using the positions of the peaks in a diffraction pattern. Peak positions also provide symmetry information of the sample. Some of the reflections, from specific hkl planes, have no intensity, due to the crystal symmetry of the system. This is known as systematic absence. As these absent reflections are related to

specific symmetry operations, they can be used to determine the crystal symmetry of the system. For example, in a *C*-centred lattice, only reflections with both h and k odd or even are observed.

Diffraction patterns are usually presented as intensity against the scattering angle (θ). Intensity versus d or Q are often used for patterns that are collected using radiation of different λ or for time-of-flight data, as the d-spacing and Q are independent of λ. The relationships between θ, Q and d are expressed in **Equation 2.5**.

$$Q = \frac{2\pi}{d} = \frac{4\pi \sin\theta}{\lambda} \tag{2.5}$$

Whilst the diffraction peak position gives the lattice parameters of a crystalline sample, the intensity of each peak (I_{hkl}) provides information about the atomic arrangement of the atoms on the plane, as the intensity is related to the structure factor (F_{hkl}), as described in **Equation 2.6**.

$$I_{hkl} \propto |F_{hkl}|^2 \tag{2.6}$$

F_{hkl} is the summation of the contributions from all the atoms on the hkl plane. For x-ray, the F_{hkl} is described in **Equation 2.7**.

$$F_{hkl,\ \text{x-ray}} = \sum_i f_j e^{[2\pi i(hx_j+ky_j+lz_j)-\left(\frac{B_j \sin^2\theta}{\lambda^2}\right)]} \tag{2.7}$$

Where f_j is the form factor of which x-rays scattered by atom j at the atomic coordinates x_j, y_j and z_j. The isotropic thermal motions of atom j is described by the thermal factor B_j. The thermal factor is often presented in the form of the mean-squared displacement *U*. The relationship between *B* and *U* is defined by **Equation 2.8**:

$$B = 8\pi^2 U \tag{2.8}$$

In neutron scattering, the structural factor from nuclear (F_{nuc}) and magnetic (F_{mag}) contributions are independent from one another, as shown in **Equation 2.9** and **2.10**, respectively.

$$F_{\mathrm{nuc}} = \sum_i b_j e^{[2\pi i(hx_j+ky_j+lz_j)-\left(\frac{B_j \sin^2\theta}{\lambda^2}\right)]} \tag{2.9}$$

$$F_{\mathrm{mag}} = \sum_i p f_j q_j e^{[2\pi i(hx_j+ky_j+lz_j)-\left(\frac{B_j \sin^2\theta}{\lambda^2}\right)]} \tag{2.10}$$

Where p is the magnetic cross section, b_j and f_j are the form factors for neutron nuclear and magnetic scattering, respectively. As described in Section 2.2.1, the direction of vector transfer is important for magnetic scattering. Therefore, F_{mag} is dependent on the magnetic interaction vector q_j.

2.2.3. Powder Diffraction

Diffraction experiments can be carried out on single crystals, as well as on polycrystalline (powder) samples. Powder samples are made up of many small, randomly oriented crystals. The diffraction pattern produced by a single crystal consists of spots that are related to the symmetry and the orientation of the crystal, which allows the structure of the materials to be determined. In polycrystalline however, due the random orientation of the crystals, spots with the same scattering angle that are originated from different atomic planes cannot be distinguished from one another. Therefore, the diffraction signals are a superimposition of reflections from multiple atomic planes with the same $|hkl|$, forming sets of concentric rings, as shown in **Figure 2.7**.[12, 14] The overlapping of Bragg peaks results in a loss of structural information, such as lattice symmetry and atomic positions, that are essential for crystal structure-solution. This problem can be overcome by refining a structure model to fit to the obtained diffraction pattern using the Rietveld method, as described in Section 2.2.4. The use of powder samples also has advantages over single

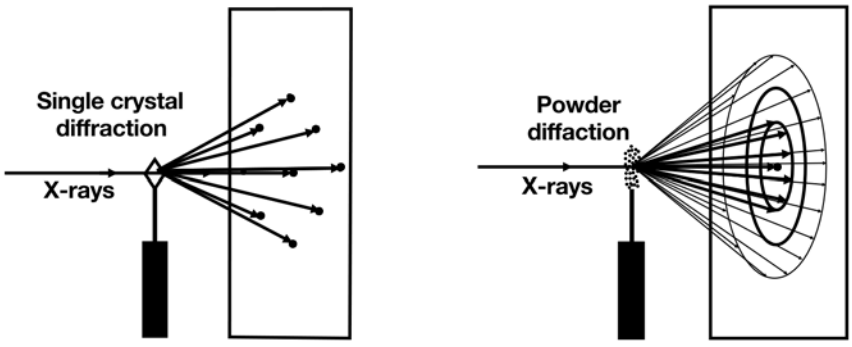

Figure 2.7 Diagram illustrates diffraction signals collected from (Left) a single crystal and (Right) polycrystalline sample.[14]

crystals, for example, it is very often easier to prepare powder sample for oxide-type materials, compared to single crystals. Furthermore, powder diffractometers generally have higher resolution, which can give more accurate structural information, more specifically, the lattice parameters.

2.2.4. Rietveld Refinement for Powder Diffraction

The Rietveld method was introduced in 1969.[15] It uses the least-squares method to refine a structure model against the powder diffraction pattern to extract crystal data. The Rietveld method is a structural refinement technique, but not a structure-solution method; it requires a starting structural model for an efficient fitting. Information such as the space group symmetry, approximate lattice parameters and atomic coordinates of the sample are needed.

To obtain structural information from powder diffraction data, the position, shape and intensity of each diffraction peak must be considered. With a known crystal symmetry, the Bragg peaks in a diffraction pattern can be indexed and assigned to the corresponding hkl values, using the Bragg's Law. The position of the diffraction peaks allows the lattice parameters of the sample to be determined. The intensity of the diffraction peaks primarily comes from the structure factor of the atoms on the relevant plane (as described by Equation 2.7, 2.9 and 2.10), however the intensity can also be influenced by other factors. For example, systematic absences can lead to decrease in intensity in diffraction peaks that have the same scattering angle. Other factors that are originated from the sample include: the absorption of incident radiation by the

sample, which changes the background intensity; the preferred orientation of crystals can result in a higher than normal intensity from certain sets of atomic planes; and the thermal motion of atoms, as described by Equation 2.8. The intensity of diffraction peaks can also be affected by instrumental factors, for example, the flux of the radiation and the polarisation of the beam.

Just like the intensity, the shape of diffraction peaks is influenced by the diffractometer and the powder sample. The peak profile of diffraction patterns collected using a constant wavelength can generally be described using the pseudo-Voigt function. The pseudo-Voigt profile is a convolution of Gaussian (**Equation 2.11**) and Lorentzian (**Equation 2.12**) functions, which can be expressed with Full-Width-at-Half-Maximum (FWHM) functions:

$$H_G = U\tan^2\theta + V\tan\theta + W \tag{2.11}$$

$$H_L = \frac{X}{\cos\theta} + Y\tan\theta \tag{2.12}$$

The H_G function (often known as the Caglioti Equation)[16] describes the Gaussian peak profile, with coefficients U, V and W that account for peak width, resulting from the resolution of the diffractometer. The Lorentzian term (H_L) accounts for the contributions from the sample. The first part of the H_L function describes the peak broadening associated with the size of the crystals in the powder sample. And as such, the average size of the crystals (P) can be calculated using the refined coefficient X in 0.01 degree-unit (**Equation 2.13**).

$$\mathrm{P} = \frac{18000\lambda}{\pi X} \tag{2.13}$$

The second term of the H_L function accounts for changes in the d_{hkl} values due to crystalline strain. The deviation in d_{hkl} can result in reduction in peak intensity and peak broadening, which lowers the resolution of the diffraction pattern.

The shape of the diffraction peaks collected using the time-of-flight method is asymmetrical, with a sharp leading front and a long tail. The leading edge originates from the pulse release of neutrons, which generate a rapid high flux upon release; and the tail comes from the slowing process where the moderator controls the energy of the neutrons. The asymmetrical peak is often described by the Ikeda-Carpenter function, which is a convolution of a Gaussian peak with a sharp front and a long tail edge.[30]

Determining all the F_{hkl} of a crystal system using powder diffraction data is very difficult, due to the overlapping of Bragg reflections. The Rietveld method overcomes this problem by dividing the diffraction pattern into many small steps (i), and the intensity (y_i) of each section is the background intensity ($y_{i\,back}$) added to the summation of all the reflections ($y_{i\,hkl}$) that have contribution to the section, as defined by **Equation 2.14**.

$$y_i = y_{i\,back} + \sum_{hkl} y_{i,hkl} \tag{2.14}$$

The difference in the intensity between the experimental pattern ($y_{i,obs}$) and the calculated model ($y_{i,calc}$) at each i is minimised, through refinement of the different parameters described earlier in this section, using the least-squares refinement method (**Equation 2.15**).

$$S_y = \sum_i w_i \, (y_{i,obs} - y_{i,calc})^2 \tag{2.15}$$

where w_i is a weighting factor, it is inversely proportional to the variance of S_y at each i and is generally equal to $\frac{1}{y_{i,obs}}$. The least-squares refinement can be evaluated using the profile factor (R_p), the weighted profile factor (R_{wp}) and the goodness-of-fit factor (χ^2), as illustrated in **Equations 2.16**, **2.17** and **2.18**, respectively.

$$R_p = \frac{\sum_i (y_{i,obs} - y_{i,calc})}{\sum_i (y_{i,obs})} \tag{2.16}$$

$$R_{wp} = \sqrt{\frac{\sum_i w_i (y_{i,obs} - y_{i,calc})^2}{\sum_i w_i (y_{i,obs})^2}} = \sqrt{\frac{S_y}{\sum_i w_i (y_{i,obs})^2}} \tag{2.17}$$

$$\chi^2 = \frac{S_y}{N - P + C} \tag{2.18}$$

χ^2 is calculated based on the fit and number of data points (N), refined parameters (P) and constraints (C). As the fit improves, the value of χ^2 tends towards 1, and the R-factors tend towards 0.

Diffraction patterns can also be fitted using a Le Bail fitting model.[17] The Le Bail method involves estimating the intensity of diffraction peaks using an arbitrary value, instead of the corresponding structure factors (F_{hkl}). Therefore, this fitting method does not require atomic information to fit diffraction data. The lattice parameters and peak shape functions can be refined to fit the diffraction peaks to the measured intensity.

In this research, refinements of the powder diffraction data using the Rietveld and Le Bail methods were carried using the General Structure Analysis System (GSAS) and the FullProf Studio.[11,18]

2.2.5. Bond Valence Sum and Magnitude of Jahn-Teller Distortion

With the atomic coordinates determined through Rietveld refinement, the valence state (V) of cations in TMOs can be calculated using the bond valence sum (BVS) method. BVS estimates the oxidation of the cation using the distances between the cation and the coordinated oxygens (d_i), as defined in **Equation 2.19**.

$$V_n = \sum_i e^{\left(\frac{d_n - d_i}{B}\right)} \tag{2.19}$$

Where d_n is the bond valance parameter for the metal with an assumed valence state of n and B is a global constant.[19] The materials described in this

Thesis are mixed-valance iron oxides, where intermediate valence states between Fe^{2+} and Fe^{3+} are possible. These intermediate valence states can be calculated using an interpolation between the estimates of the two nearest integer oxidation states (**Equation 2.20**).

$$V = \frac{L(V_H - V_L) - (H - L)V_L}{(V_H - V_L) - (H - L)} \tag{2.20}$$

Where H and L are the higher and lower oxidation states, respectively.[20]

BVS is a useful technique for probing charge ordering transitions in TMOs. Charge ordering of some cations, for example Fe^{2+} and Fe^{3+}, can result in orbital ordering (as detailed in Chapter 1). The magnitude of Jahn-Teller distortion (Q_{JT}) in a MO_6 octahedron geometry can be calculated from the difference between the average M-O distances along the z axis ($d_{\pm z}$) and the average of the ones along the x ($d_{\pm x}$) and y ($d_{\pm y}$) axis (**Equation 2.21**).[21]

$$Q_{\mathrm{JT}} = \frac{2(d_{+z} + d_{-z}) - (d_{+x} + d_{-x} + d_{+y} + d_{-y})}{2\sqrt{3}} \tag{2.21}$$

2.2.6. Sources and Instruments

2.2.6.1. X-ray

In in-house x-ray diffractometers, the x-rays are generally generated using x-ray tubes. These tubes are vacuum sealed and consist of an electron emitter

and a metal target. When a positive voltage is applied to the metal, the electrons accelerate towards the target. Upon impact, x-rays are generated through two mechanisms. Bremsstrahlung radiation results from the rapid deceleration of electrons at collision. It is relatively weak and consists of x-ray radiation from a broad range of energy. The second mechanism is due to the removal of electrons from the inner-shell of the metal target, which causes the relaxation of an electron from a higher energy shell to replace the hole. The process of relaxation emits energy that corresponds to the quantised energy difference between the two levels. The wavelength of x-rays produced by an x-ray tube is determined by the metal target.

Initial structural characterisation of the samples studied in this Thesis were carried out using a Bruker D2 Phaser Powder x-ray diffractometer. The D2 operates with a Bragg-Brentano geometry, with x-rays generated from a copper x-ray tube. Copper emits $K_{\alpha 1}$ and $K_{\alpha 2}$ radiation from 2*p* to 1*s* relaxation, with wavelengths of 1.54056 Å and 1.54439 Å, respectively. Most of the Cu K_{β} radiation (1.3923 Å) generated from 3*p* to 1*s* transition is absorbed by the Ni filter. During a measurement, the sample is evenly spread on top of a silicon flat plate that rotates the sample inside the diffractometer chamber.

In-house x-ray diffractometers are a fast and relatively cheap option for simple structural analysis, such as to confirm the formation of desired phases at the end of a reaction. They are however limited by their resolution and radiation flux (from metal target overheating). To carry out more sophisticated measurements synchrotron sources are needed.

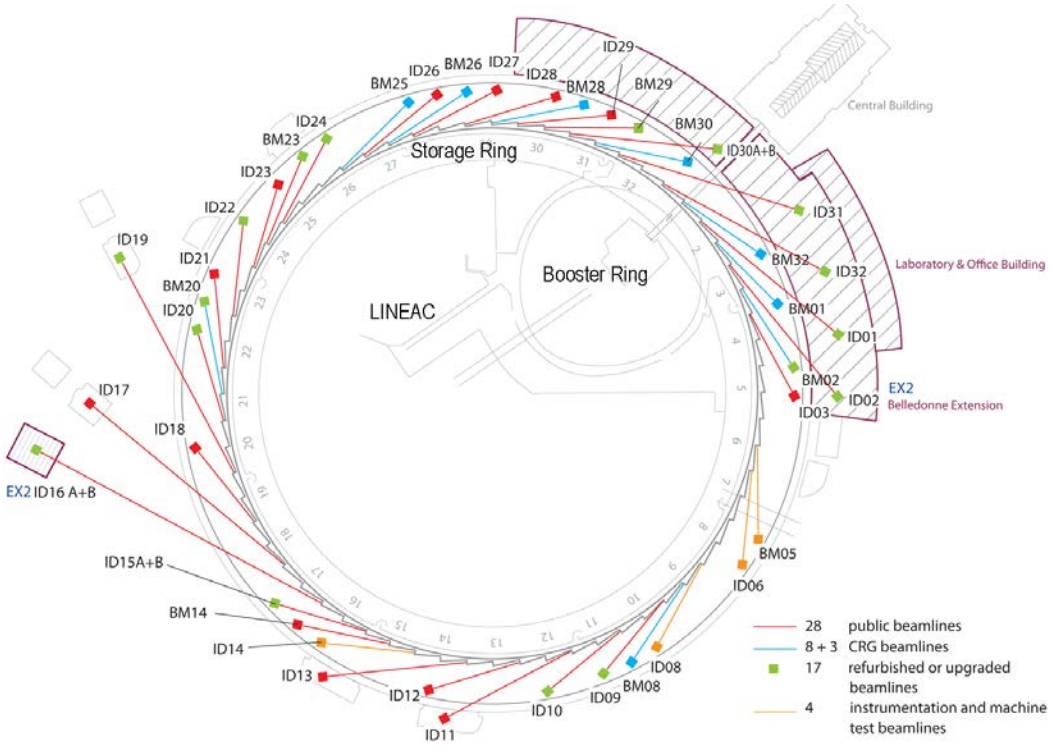

Figure 2.8 Floor plan of the European Synchrotron Radiation Facility, with beamlines that are built tangential to the storage ring.[23]

Synchrotron x-ray radiation is generated in particle accelerator facilities, where electrons are accelerated inside a ring.[22] The electrons are guided to follow a circular path. At the bends, as the electrons change direction, a beam of synchrotron radiation that is tangential to the circular path is emitted. At the European Synchrotron Radiation Facility (ESRF) in Grenoble, France (**Figure 2.8**),[23] electrons are accelerated using a linear accelerator (LINAC) until they reach 200 MeV. The electrons then enter a 300 m diameter booster synchrotron ring where they continue to speed up. When the electrons reach a final energy of 6 GeV, they are injected into an 844 m storage ring. The electrons are released from the booster ring every 50 ms, and inside the storage ring, the electrons travel at the speed of light under an ultra-high

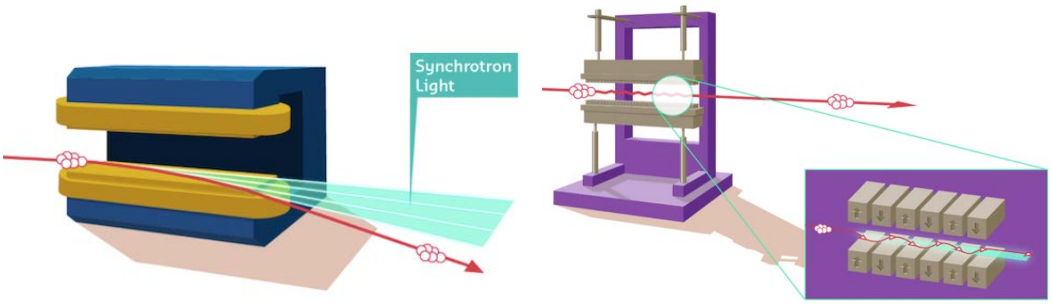

Figure 2.9 A bending magnet (Left) guides electrons to the direction that follows the orbit around the synchrotron ring. As electrons are deviated from their original path, the energy loss through the change of direction is emitted tangentially to the flight path. The radiation release consists of a broad range of continuous spectrum, from microwaves to x-rays. An undulator (Right), also known as an insertion device, is made up of an array of small magnets that forces the electron to a wavy trajectory. The radiation that is emitted at each bend overlaps and interferes constructively. This results in a more focused beam with wavelengths that can be more finely tuned, compared to the bending magnet.[24]

vacuum (10^{-9} mbar) for hours. The storage ring at the ESRF consists of 32 straight and curved alternating sections. Focusing magnets are placed at the linear section to keep the electrons close to the ideal path. Two types of magnets (bending magnets and undulators) are used at the bends to guide the electrons around the ring and generate synchrotron radiation during the process, as described in **Figure 2.9**.[24,25]

The crystal structural study of all the materials presented in this Thesis were carried out at the beamline ID22 at the ESRF. ID22 is a high resolution powder diffraction beamline (**Figure 2.10**).[26,27] The radiation arrives at ID22 through an undulator and passes through a channel cut Si 111 monochromator that selects the desired x-ray energy (6 – 90 keV). For standard experiments, powder samples are packed in glass/quartz capillaries and mounted onto a spinning stage. A liquid-helium cryostat or hot-air blower can be installed to

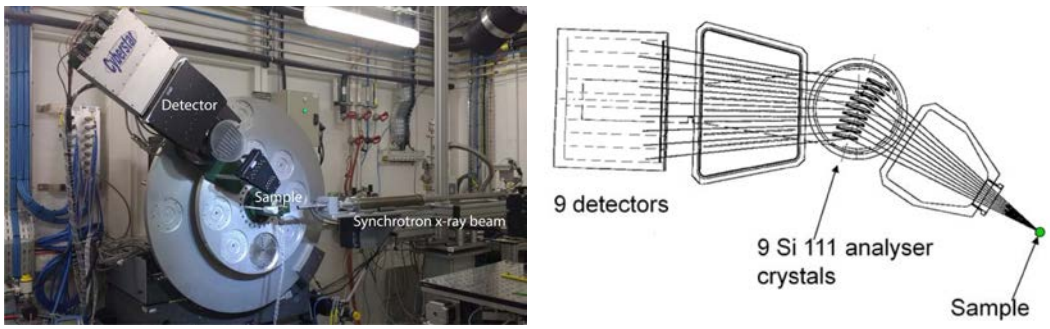

Figure 2.10 (Left) ID22 experiment hutch, with the synchrotron beam guided to the sample in the middle and diffraction signals are picked up by the Si 111 detectors that can rotate around the sample. Schematic of the detector (Right) shows the nine analyser crystals that direct the diffracted radiation to the corresponding detector.[26,27]

carry out measurements at temperatures with a range of 4 to 1223 K. In standard operation mode, ID22 uses a multianalyser stage detector, which consists of nine independent Si 111 analyser crystal detectors that are 2° apart, as detailed in **Figure 2.10**. The nine detectors work in parallel with one another to increase the efficiency of measurement and more importantly precisely define the angle of diffraction for high resolution experiments.[28]

2.2.6.2. Neutron

Neutrons, for scientific uses, are produced using nuclear fission reactors or through accelerator-based sources. Fission reactions involves splitting ^{235}U through ^{1}n absorption, which in turn produces high energy neutrons. The nuclear reaction is sustained by slowing down the neutrons released by colliding them with a moderator that controls the temperature of the neutrons. Some part of the neutron diffraction experiments in this Thesis were carried

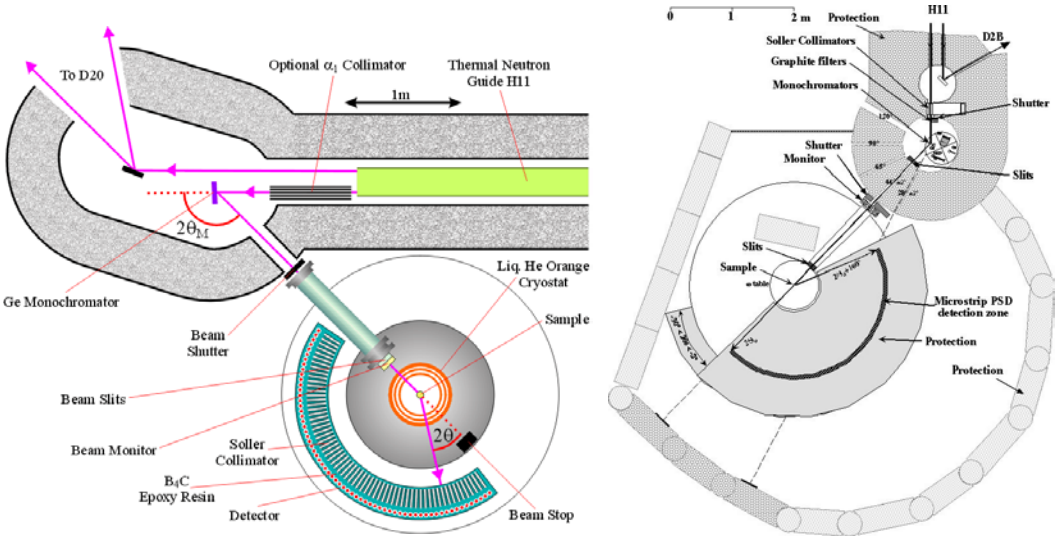

Figure 2.11 The D2B (Left) and D20 (Right) diffractometers at the ILL. Diagram shows neutrons are supplied to the two beamlines from the same neutron guide. Multiple monochromators are found in D20 for altering the wavelength of the neutron for suitable resolution/flux settings. Different components and the setup of the two diffractometers are labelled.[32,33]

out using the Institut Laue Langevin (ILL) reactor in Grenoble, France. This reactor operates with a thermal power of 58.3 MW and a raw neutron flux of 1.5×10^{15} s^{-1} cm^{-2}.[29,30] The high energy neutrons generated at the reactor are slowed down using a combination of moderators. The wavelength used by individual instruments is selected using crystal germanium monochromators, which focus the neutron beam at a specific energy. This process however leads to a dramatic reduction in the neutron flux that arrives at the sample.

Part of the work in this Thesis involved the use of the instruments D2B and D20 at the ILL. The two instruments operate from the same beam guide from the reactor. The neutron beam is divided into two parallel beams, with one used for D2B and the other for D20, as described in **Figure 2.11**.

D2B is a high-resolution diffraction beamline. The monochromator has a very high take-off angle of 135° that compensates the loss flux with the large mosaic spread. The diffraction signals are collected by the 128 detectors that rotate around the sample, covering a 2θ range of 5 to 165°. Cryogenic systems and furnaces can be installed in D2B that give it the ability to measure samples from 0.05 to 1000 K.[31,32]

D20 is an extremely high flux diffractometer (up to 9.8 x 10^7 $s^{-1}cm^{-2}$ in high intensity mode).[33] D20 is therefore capable of measuring small powder samples (down to ~ 50 mg), such as those prepared from high-temperature and high-pressure synthesis, where sample size is limited by the synthesis conditions. When the neutron beam arrives at D20, it is guided to one of the one of the 4 monochromators that selects the desired wavelength. The monochromatic neutron beam then enters one of the five take off ports, each of which offers different output resolutions. Lastly the beam reaches the sample and the diffracted neutrons are picked up by the microstrip detectors that covers an angular range of 2θ = 153.6˚. The sample chamber in D20 can host cryogenic systems that allow experiments to be carried out with a temperature range of 1.9 to over 1373 K.[34]

Self-sustaining reactors produce a constant flow of neutrons; however, the flux of reactor-based sources is limited by the heat generated during fission reactions. This limitation in neutron production can be circumvented by accelerator-based sources. These accelerator-based facilities generate neutrons via a process called spallation, which involves accelerating protons

towards a heavy target, where the collision of the two results in neutrons 'breaking off' from the nuclei of the target.

The ISIS Neutron and Muon Source (**Figure 2.12**) in the U.K. consists of a 40 m long LINAC used to accelerate H^- to 37 % of the speed of light.[35] At the end of the LINAC, the ions pass through a thin sheet of alumina foil that removes the electrons from the ions, leaving the protons to enter a 163 m circumference synchrotron ring. The protons continue to accelerate in the ring until they reach 84 % of the speed of light, where the proton beam is then extracted from the synchrotron and directed to collide with a tantalum-clad-tungsten target. The bombardment of the target by high energy protons (~800 MeV) results in polychromatic neutrons with extremely high energy. And like that of the neutrons produced from reactors, they are cooled to temperatures that correspond to wavelengths in the same magnitude of atomic separation distances using moderators. Neutrons are generated from accelerator-base

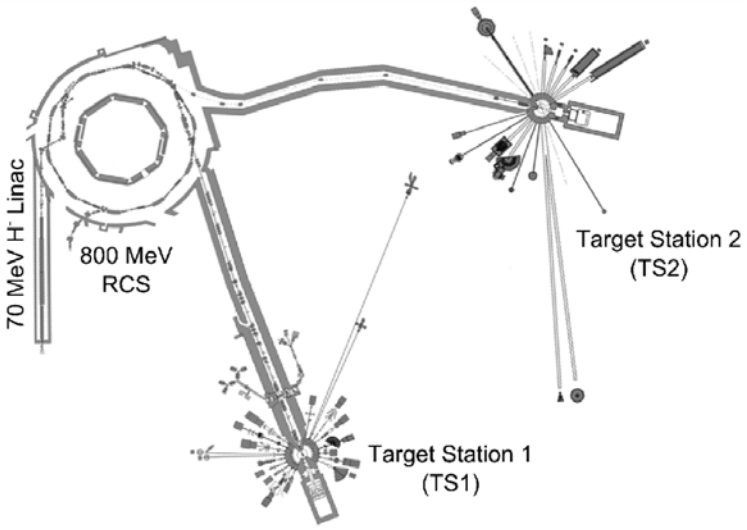

Figure 2.12 The ISIS Neutron and Muon Source has a 70 MeV LINAC that connects to a ~800 MeV synchrotron ring. The diagram shows the neutron beam is guided from the synchrotron ring to the two target stations (TS1 and TS2). Both target stations consist of a tantalum-clad-tungsten target. The WISH diffractometer is located at the TS2.[35]

facilities at a rate of 50 Hz, allowing an almost constant stream of neutron production at all time. Different from a fission facility, monochromators are not required to separate the polychromatic neutrons, instead time of flight techniques are employed by using the difference in the velocity of neutrons with different energy, as illustrated in **Equation 2.22**.

$$t = \frac{mL\lambda}{h} \tag{2.22}$$

Where t is the time for a neutron to travel a distance L and m is the mass of the neutron.[30] This separation method works as long as there is no overlapping between each neutron pulse. Although reactors produce a higher raw flux of thermal neutron, the use of monochromators limits the flux that arrives at the sample, to the point that is almost comparable to that of spallation sources. Another advantage of using spallation neutron sources is the availability of high energy neutrons that make high scattering angle measurements possible. This allows diffraction patterns of very small d-spacing to be collected.

WISH is a high flux and good resolution time-of-flight neutron diffractometer in ISIS TS2.[33] With its high flux capability, the crystal and magnetic structural characterisation of most of the high-pressure samples investigated in this Thesis was carried out on WISH. The high neutron flux of WISH allows it to measure samples down to 50 mg, with good resolution. Closed-circuit refrigerators can be installed in WISH for variable temperature measurements between 5 and 400 K. WISH can also host pressure cells for diffraction patterns to be collected at pressures.

(A)

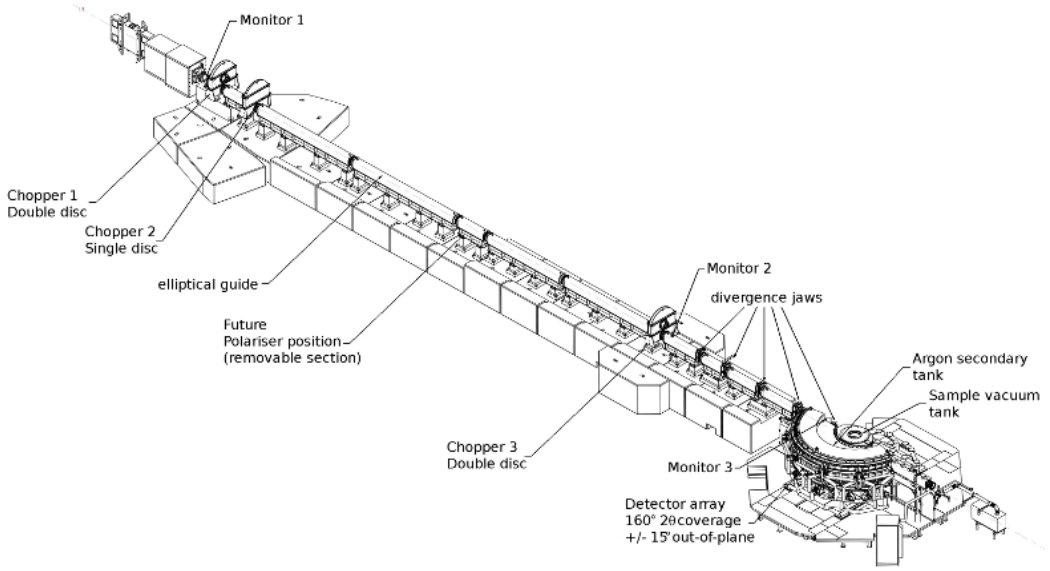

(B)

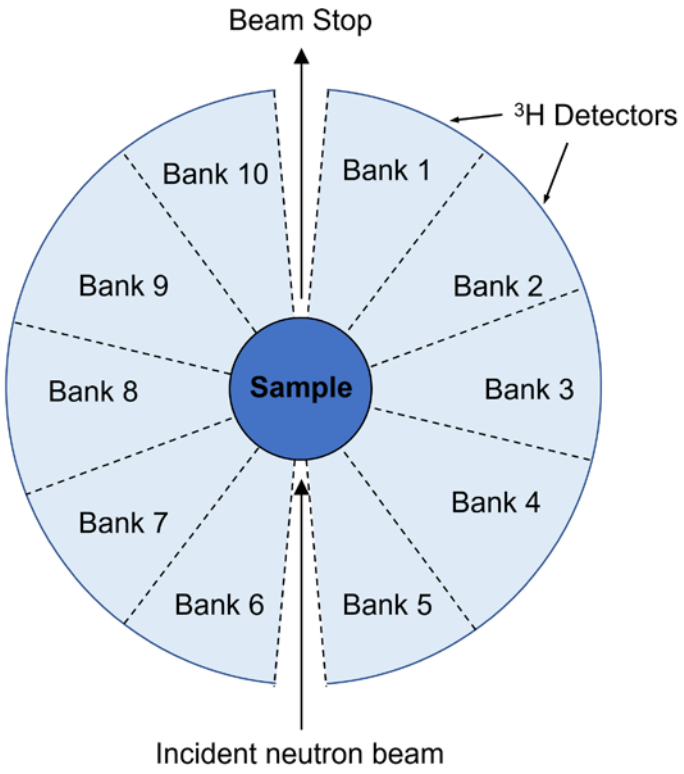

Figure 2.13 (A) WISH diffractometer with the neutron beam guide from ISIS TS2 target.[36] (B) Schematic diagram illustrating the layout of the ten ^{3}He detectors in WISH. Each bank of detector covers an angle of 32°.

WISH operates with a low pulse frequency of 10 Hz that allows neutrons of a very broad range of energy to pass through, and hence diffraction patterns with a wide d-range (from 0.7 to up to 50 Å) can be collected. There are five sets of piezoelectric slits for controlling the incident neutron beam for a desired resolution/flux, as shown in **Figure 2.13A**.[36] Ten banks of ^{3}He detectors are used in WISH, each of which covers an angle of 32° and no space in between, as illustrated in **Figure 2.13B**. Averages of histogram are taken from the banks of detector that are parallel to each other, e.g. bank 1 and 10, 2 and 9, 3 and 8, 4 and 7 or 5 and 6. In this Thesis, Rietveld refinement was carried out on the diffraction data collected from WISH by considering all the histograms simultaneously.

2.3. Magnetic Property Measurements

The magnetic properties of an atom are given by its unpaired electrons. All electrons have an intrinsic magnetic moment that comes from their spin angular momentum (S). The orbits of electrons that travel around the nucleus also gives rise to a magnetic moment from the orbital angular momentum (L). The orbital angular momentum depends on the orbital the unpaired electron is occupying. The spin and orbital angular momentums combine through spin-orbital coupling. The total angular momentum (J) of an atom is the summation of the spin-orbital momentums of all the unpaired electrons, and the total magnetic moment possessed by an atom (μ) can be expressed with **Equation 2.23**.

$$\mu = g\mu_{\mathrm{B}}\sqrt{J(J+1)} \tag{2.23}$$

Where μ_{B} is the Bohr magneton and g is the Landé g-factor (**Equation 2.24**).

$$g = \frac{3}{2} + \frac{S(S+1) - L(L+1)}{2J(J+1)} \tag{2.24}$$

In many TMOs, the orbital angular momentum is quenched, due to crystal field splitting that removes the degeneracy between different *d*-orbitals. In such cases, J is equal to S, and the effective magnetic moment (μ_{eff}) of these TMOs can be calculated from the spin angular momentum of the unpaired electrons (S), as illustrated in **Equation 2.25**.

$$\mu = 2\mu_{\mathrm{B}}\sqrt{\mathrm{S}(\mathrm{S}+1)} \tag{2.25}$$

Materials with paramagnetic behaviour contain unpaired electrons that are not correlated with each other. In the absence of an external magnetic field, the spins of these electrons have random orientation, due to their thermal motions. The application of a magnetic field (H) to a paramagnetic system can lead to magnetisation (M) by aligning the spins of the unpaired electrons with the field. The magnetic susceptibility (χ) of a material can therefore be expressed by **Equation 2.26**:

$$M = \chi H \tag{2.26}$$

As the spins are easier to be aligned when thermal energy is removed from the system, χ is inversely proportional to temperature, as described by the Curie Law (**Equation 2.27**).

$$\chi = \frac{C}{T} \tag{2.27}$$

The Curie Law describes systems that exhibit perfect paramagnetism. However, most materials have minor spin-interactions, even at their paramagnetic state. The spin exchange interactions between the electrons can be account for by adding a Weiss constant (θ) to the Curie Law and is commonly known as the Curie-Weiss Law (**Equation 2.28**).

$$\chi = \frac{C}{T - \theta} \tag{2.28}$$

A positive θ value indicates ferromagnetic interactions, whereas a negative value suggests antiferromagnetism. C is the Curie constant and is often used to calculate the effective magnetic moment of the material using the relationship shown in (**Equation 2.29**).

$$C = N\frac{N_{\mathrm{A}}{\mu_{\mathrm{B}}}^2{\mu_{\mathrm{eff}}}^2}{3k_{\mathrm{B}}} \tag{2.29}$$

where N is the number of magnetic atoms per formula unit, N_{A} is Avogadro's number and k_{B} is Boltzmann's constant.

As described in Section 1.2, spin interactions between magnetic ions can occur when thermal energy is removed from the system, and results in long range magnetic ordering below a critical temperature. The transition temperature is commonly known as the Curie (T_C) and Néel temperature (T_N) for ferromagnetic and antiferromagnetic orderings, respectively.

2.3.1. Magnetometer

The magnetic properties of a materials can be measured using a superconducting quantum interference device (SQUID) magnetometer. A SQUID consists of a ring made up of two superconducting components separated by thin layers of insulator, known as Josephson junctions.[37] The Cooper pairs from each side can tunnel through the insulator in between when they are phase coherent, allowing a supercurrent to flow through.[38] The current induces a magnetic field with a coherent magnetic flux. If this flux were to be disturbed, the two superconductors would be out of phase and result in a voltage across the junctions.

The magnetic property measurements described in this work were carried out using a Quantum Design Magnetic Property Measurement System (MPMS) XL, using the direct current mode. To prepare for an experiment, the sample is kept inside a gelatin capsule, enclosed by a plastic straw. The straw is then transferred into the MPMS chamber. During a measurement, the sample is moved through a set of superconducting pickup coils. The pickup coils are connected to the 'input' coils that are located on top of the Josephson junctions.

The movement of the magnetic sample through the pickup coils generates a current in the coil, which results in a magnetic field that passes to the input coils. The presence of an external field near the Josephson junctions changes the magnetic flux and hence produces a voltage that is proportional to the magnetisation of the sample. Measurements at the Quantum Design MPMS XL with the standard setup can be carried out with a temperature range of 2 to 400 K and an applied field of -7 to 7 T.

2.4. Electrical Properties Measurements

The electrical property of a sample changes with its surrounding environment. External factors, such temperature, pressure and magnetic field can alter how charges propagate through a material. Furthermore, electronic and structural transitions can often lead to changes in physical properties. The electrical resistivity of solid samples in this Thesis were investigated using a Quantum Design Physical Property Measurement System (PPMS). The Quantum Design PPMS allows measurements to be carried out between a temperature of 2 to 400 K and under a magnetic field up to 7 T. To prepare for measurements, the sample is setup using the four-terminal sensing method, also known as the four-probe method. The setup involves attaching four conducting wires in parallel to the surface of the sample using a conductive adhesive (such as silver paste). The two wires in the middle are connected to a voltmeter, whereas the outer two are connected to a current source. The current the flow across the sample is controlled by the current source and the

voltage drop due to the resistance is picked up by the voltmeter, providing more accurate readings of the sample.

Using the built-in superconducting magnet in the PPMS, the magnetoresistance (MR) of a material can be measured. MR is often presented as a percentage of change (**Equation 2.30**) in the resistance of a sample compared to a zero-field measurement (R_0):

$$MR\ (\%) = \frac{R_H - R_0}{R_0} \times 100\ \% \tag{2.30}$$

Where R_H is the resistance of the sample in the presence of a magnetic field H.

2.5. Mössbauer Spectroscopy

When a free nucleus absorbs or emits a gamma ray, it recoils to conserve the momentum. The loss of energy due to recoiling prevents resonance transmission to occur. In 1957, R. Mössbauer discovered that in extended lattice structures, the recoil energy is not transferred between atoms, but instead the whole lattice experiences the recoil effect as a phonon. As the mass of the lattice is in many magnitudes heavier than a single nuclei, the energy loss is negligible compared to the absorption and emitting energy, giving rise to recoilless resonance transmissions.[39] In order to establish resonance, the absorbed energy needs to match exactly with that emitted by the source. To study iron-based materials described in this Thesis, ^{57}Fe

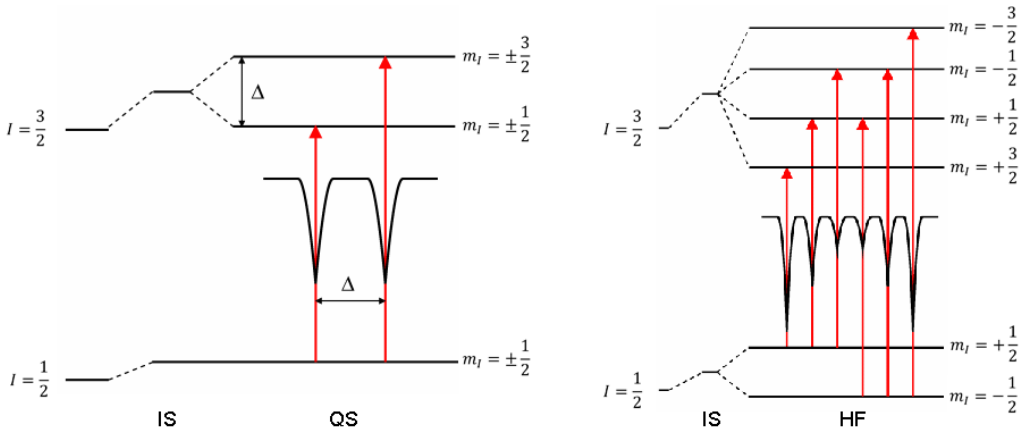

Figure 2.14 (Left) Isomer shift (IS) in the $I = \frac{1}{2}$ and $\frac{3}{2}$ energy levels and quadrupole splitting (QS) in the $I = \frac{3}{2}$ level, resulting in a doublet Mössbauer signal. (Right) Hyperfine magnetic splitting (HF) in the presence of a magnetic field, giving rise to a sextet signal. Figure reproduced from reference 41.

Mössbauer was used. ^{57}Fe Mössbauer source emits gamma radiation through the electron capturing of a ^{57}Co radioactive source.[40] During the decay to ground state ^{57}Fe, gamma rays with energy comparable to Fe nuclear excitation (E = 14.4 keV) is released.

Mössbauer spectroscopy provides information of the environment of atoms in a lattice by probing the energy of nuclear transitions. To detect these hyperfine interactions that are in the order of billionths of an electron volt, the gamma source is moved towards and away from the sample to create a tiny range of energy, using the Doppler effect. The motion of the source is at fractions of mm/s compared to the speed of the gamma rays (at the speed of light), allowing very subtle transitions to be detected.

The energy levels in a nucleus can be affected by its environment. Electric and magnetic fields experienced by the nuclei can result in shifting and splitting in the nuclear energy levels (**Figure 2.14**).[41]

- ISOMER SHIFT (IS): The *s*-electrons of an atom are often found at the nucleus. The size of a nucleus at its excited state is larger than when it is at the ground state, which means that there is more overlapping between the s-electrons and the excited nucleus. The overlapping can result in a shift in the resonance energy. Other electrons in the atoms can affect the *s*-electron, which indirectly impose an effect on the nucleus and shift the resonance energy. The change in energy is measured by comparing to a pure source, for example alpha-iron is used as a reference for ^{57}Fe Mössbauer spectra. The isomer shift is often used to determine the valence state of atom being investigated.
- QUADRUPOLE SPLITTING (QS): The charge distribution in nuclei with a nuclear spin quantum number $I > \frac{1}{2}$ is non-spherical and thus has a nuclear quadrupole moment. In systems with asymmetrical charge distributions, such as those originated from ligand arrangements, the energy level will be split by the asymmetrical electric field. In ^{57}Fe, the excited state has a $I = \frac{3}{2}$ and can be split into levels and gives rise to a doublet Mössbauer signal.
- HYPERFINE MAGNETIC SPLITTING (HF): For a nucleus with a spin of I has $2I + 1$ number of possible spin orientations. In the absence of a magnetic field, the energy levels of different spin orientations are equal. However, if a nucleus experiences a magnetic field, these energy levels will split due to dipole interaction. This is known as the Zeeman splitting. The splitting of the energy levels is proportional to the magnetic field experienced by the nucleus, and therefore can be used to study

the magnetic properties of a material. In ^{57}Fe, with the presence of a field, the ground state ($I = \frac{1}{2}$) is split into two levels ($M_I = \pm\frac{1}{2}$) and the excited state ($I = \frac{3}{2}$) is split into four levels ($M_I = \pm\frac{1}{2}\ and\ \pm\frac{3}{2}$), resulting in a sextet signal in a Mössbauer spectrum.

2.6. References

1. M. Hayward. in Comprehensive Inorganic Chemistry II (Second Edition): From Elements to Applications, *Elsevier, Oxford* **2013,** *vol. 2,* 417–453.

2. A. Wold, K. Dwight. Solid state chemistry: synthesis, structure, and properties of selected oxides and sulphides. *Springer Science & Business Media.* **2012**.

3. N. Bertrand, C. Desgranges, D. Poquillon, M. C. Lafont, D. Monceau. *Oxid. Met.* **2010,** *73,* 139–162.

4. H. Huppertz. *Zeitschrift Fur Krist.* **2004,** *219,* 330–338.

5. W. A. Bassett. *High Press. Res.* **2009,** *29,* 163–186.

6. D. Walker, M. A. Carpenter and C. M. Hitch. *Am. Mineral.* **1990,** *75,* 1020–1028.

7. http://pd.chem.ucl.ac.uk/pdnn/diff1/scaten.htm

8. V. F. *Sears Neutron News,* **1992**, *3*, No. 3, 29-37.

9. http://www.xtal.iqfr.csic.es/Cristalografia/parte_03_4-en.html

10. H. Watanabe, H. C. Po, A. Vishwanath. *Sci. Adv.* **2018,** *4,* 8.

11. J. Rodriguez-Carvajal. *Physica B.* **1993**, *192,* 55–69.

12. D. S. Sivia. Elementary Scattering Theory, *Oxford University Press.* **2011.**

13. W. H. Bragg. *Phys. Rev.* **1913,** *88,* 428.

14. https://www.monash.edu/rlo/assignment-samples/engineering/sample-engineering-lab-report

15. H. M. Rietveld. *J. Appl. Cryst.* **1969,** *2,* 65.

16. G. Caglioti, A. Paoletti, F. P. Ricci. *Nucl. Instruments,* **1958,** *3,* 223.

17. A. Le Bail. *Powder Diffr.* **2005,** *20,* 316.

18. A. C. Larson, R. B. Von Dreele. *Los. Alamos National Laboratory Report LAUR* **2004,** *748,* 86.

19. I. D. Brown. *J. Appl. Crystallogr.* **1996,** *29,* 479.

20. J. P. Attfield. *Solid State Sci.* **2006,** *8,* 861.

21. M. S. Senn, J. P. Wright, J. P. Attfield. *Nature* **2012,** *481,* 173.

22. The European Synchrotron Radiation Facility, The Purple Book: Science and Technology Programme 2008-2017, *The European Synchrotron Radiation Facility, Grenoble,* **2007.**

23. https://www.esrf.eu/about/press-room/intro-esrf-journalists

24. https://www.esrf.eu/about/synchrotron-science/synchrotron

25. https://www.esrf.eu/home/education/what-is-the-esrf/how-does-the-esrf-work.html

26. A. Fitch. Synchrotron Radiation and Neutrons ESRF, *Durham Diffraction school,* **2018.**

27. J. L. Hodeau, P. Bordet, M. Anne, A. Prat, A. N. Fitch, E. Dooryhée, G. Vaughan, A. Freund. *Proc. SPIE*, **1998,** *3448,* 353.

28. https://www.esrf.eu/id22/technical-description

29. The Institut Laue-Langevin, The Yellow Book: Guide to neutron research facilities at the ILL, Grenoble, **2008.**

30. S. M. Bennington, A. C. Hannon, S. E. Rogers. The ISIS Neutron and Muon Facility Neutron Training Course, *Didcot,* **2006.**

31. https://www.ill.eu/instruments-support/instruments-groups/instruments/d2b/descryption/instrument-layout/

32. http://pd.chem.ucl.ac.uk/pdnn/inst3/diff1.htm

33. T. C. Hansen, P. F. Henry, H. E. Fischer, J. Torregrossa, P. Convert, *Meas. Sci. Technol.* **2008,** *19,* 034001.

34. https://www.ill.eu/users/instruments/instruments-list/d20/description/instrument-layout/

35. The ISIS Neutron and Muon Source, Annual Review 2015, *Didcot,* **2015.**

36. https://www.isis.stfc.ac.uk/Gallery/WISH_layout_small.jpg

37. W. G. Jenks, S. S. H. Sadeghi, J. P. Wikswo, *J. Phys. D. Appl. Phys.* **1997,** *30,* 293.

38. B. D. Josephson, *Phys. Lett.* **1962,** *1,* 251.

39. T. E. Cranshaw, B. W. Dale, G. O. Longworth, C E Johnson. Mössbauer Spectroscopy and its Applications, *Cambridge Univ. Press: Cambridge,* **1985.**

40. B. Fultz, “Mössbauer Spectrometry” in Characterization of Materials. *John Wiley. New York.* **2011.**

41. M. E. Pandelia, N. Lanz, S. Booker, C. Krebs. *Biochim Biophys Acta.* **2015,** *1853,* 1395.

Chapter 3. Synthesis and Characterisation of $CaFe_3O_5$

3.1. Introduction

The iron oxide family is known for its rich electronic and magnetic properties and has been one of the most intensity studied systems of the last few decades. This is particularly true for mixed valence members, where the charge ordering of Fe^{2+} and Fe^{3+} is often coupled with spin, lattice and orbital ordering and results in complex electronic ground states. An example of that is Fe_3O_4, as detailed in Chapter 1, where $Fe^{2+/3+}$ charge order leads to the formation of trimerons below the Verwey transition.[1,2] A closely related system, $M^{2+}Fe_3O_5$ (with M^{2+} = Ca and Fe), was discovered in recent decades,[3,4] however only the parent of the system, Fe_4O_5, has been extensively studied, with reports showing dimer and trimer formation from $Fe^{2+/3+}$ incommensurate charge ordering, accompanied by spin reorientation.[5] The Ca analogue was first reported by Evrard, *et al.* in 1980.[3] The publication showed that $CaFe_3O_5$ and related Ca phases ($CaFe_4O_6$ and $CaFe_5O_7$) can be synthesised using ceramic methods. However, throughout the 35 years after the discovery, only the crystal structural behaviour of the $CaFe_5O_7$ phase was reported (as described in Chapter 1).[6] This chapter details the synthesis and characterisation of $CaFe_3O_5$. Diffraction techniques and physical property measurements were carried out to investigate the crystal structure, electrical and magnetic behaviour of $CaFe_3O_5$. Unlike the Fe analogue, the large Ca^{2+} cations in

$CaFe_3O_5$ are expected to be stabilised in the triangular prismatic site of the system at ambient pressure, as was described by Evrard. With similarity of the crystal structure to that of Fe_4O_5, similar spin and orbital ordering phenomena are likely to be found in $CaFe_3O_5$. However, the larger cation size of Ca^{2+} (1.00 Å) compared to Fe^{2+} (0.78 Å)[7] means a larger unit cell, which may lead to M-M and M-O-M exchange interactions that are different from the Fe analogue and may even result in the suppression of $Fe^{2+/3+}$ charge ordering and orbital molecule formation due to the increase in M-M distances.

3.2. Experimental and Results

3.2.1. Synthesis of $CaFe_3O_5$

$CaFe_3O_5$ was synthesised using $CaFe_2O_4$ as a precursor. $CaFe_2O_4$ was prepared through the ceramic technique with conditions detailed by Wan *et al*.[8] Stoichiometric quantities of $CaCO_3$ and Fe_2O_3 powders (1:1) were ground together using a mortar and pestle. The mixed powder was pressed with 5 tons of force into a pellet and was preheated at 850 °C for 4 hours in an alumina crucible, followed by regrinding, repelletting and reheating at 1100 °C for 12 hours. The x-ray diffraction pattern of the resulting sample was collected using a Bruker D2 Phaser diffractometer using a Cu K_α radiation source (a 15-minute scan of $5° \leq 2\theta \leq 70°$) to confirm the formation and the purity of $CaFe_2O_4$. A Rietveld fit to the diffraction pattern is shown in Figure 3.1. The Bragg reflections

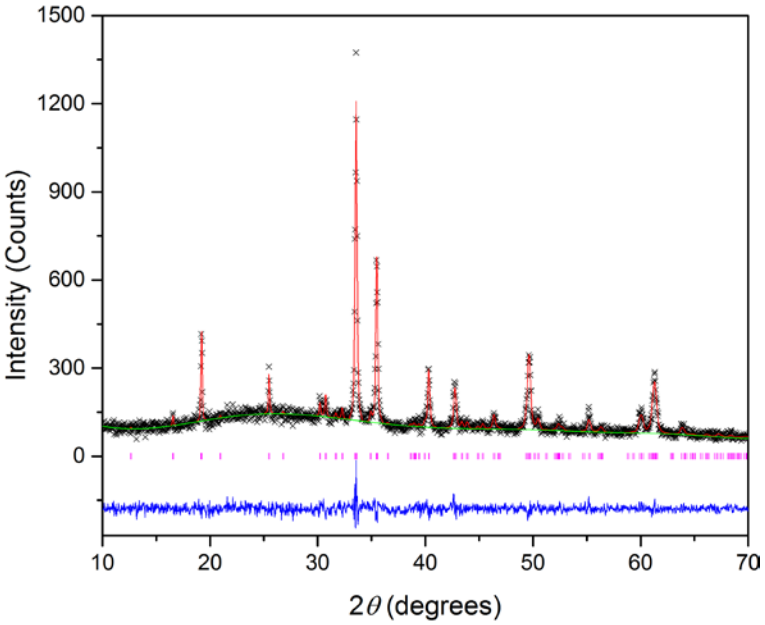

Figure 3.1 Rietveld fit of D2 Powder x-ray diffraction pattern $CaFe_2O_4$ obtained at room temperature (χ^2 = 1.22, R_{wp} = 9.93 %, R_p = 7.81 %).

were Rietveld fitted using GSAS [9] with the space group *Pnma*, with orthorhombic lattice parameters of *a* = 10.6992(19) Å, *b* = 9.2296(18) Å and *c* = 3.0205(4) Å and a cell volume of 298.27(13) Å^3, consistent to what was reported in the literature.[8] No trace of the starting materials or other impurities was observed in the x-ray diffraction data.

The synthesis of $CaFe_3O_5$ was carried out by mixing the prepared $CaFe_2O_4$ with Fe_2O_3 and Fe powders in a 1:⅓:⅓ ratio and pressed into a pellet. The pellet was placed into an alumina crucible and sealed in a quartz tube under vacuum conditions. The evacuated tube containing the mixture was then transferred into a high-temperature furnace. The heating duration was set to 12 hours and synthesis temperatures between 1000 and 1100 °C were explored. The resulting products were analysed using powder x-ray diffraction

Table 3.1 Synthesis conditions for $CaFe_3O_5$, and the % purity by weight of product determined by Rietveld refinement.

Sample	*T* (°C)	*t* (h)	Purity (%)	Impurities
1	1000	12	38(1)	$Ca_2Fe_2O_5$ (32%), Fe_3O_4 (30%)
2	1050	12	78(2)	$Ca_2Fe_2O_5$ (15%), $CaFe_5O_7$ (7%)
3	1100	12	100(0)	-

techniques, with diffraction patterns collected with the parameters described above for $CaFe_2O_4$ using the Bruker D2 Phaser. Details of the synthesis conditions and results are described in **Table 3.1**. Rietveld fits to the collected patterns from the sample synthesised at 1000 °C indicate the presence of $Ca_2Fe_2O_5$ and Fe_3O_4 impurities in the product, resulting in a purity of 38(1) % by weight of $CaFe_3O_5$. The purity of $CaFe_3O_5$ increased to 78(2) % at 1050 °C, with the rest of the composition made up of $Ca_2Fe_2O_5$ and $CaFe_5O_7$. A phase pure product was obtained at 1100 °C, with no trace of other phases observed in the x-ray diffraction pattern.

An x-ray diffraction pattern was recorded for the sample synthesised at 1100 °C using the D2 Phaser, with a 12-hour scan for $5° \leq 2\theta \leq 140°$. Rietveld refinement of the collected pattern, as shown in **Figure 3.2**, confirms that the $CaFe_3O_5$ sample adopts the orthorhombic $Sr_2Tl_2O_5$-type structure[10] with the space group *Cmcm* at room temperature, with Ca ions occupying the triangular prismatic site, just as was first reported by Evrard.[3] The room temperature lattice parameters were found to be a = 3.02862(7) Å, b = 10.0193(2) Å and c = 12.6226(3) Å, with a cell volume of 383.03(3) Å^3. The crystal structural

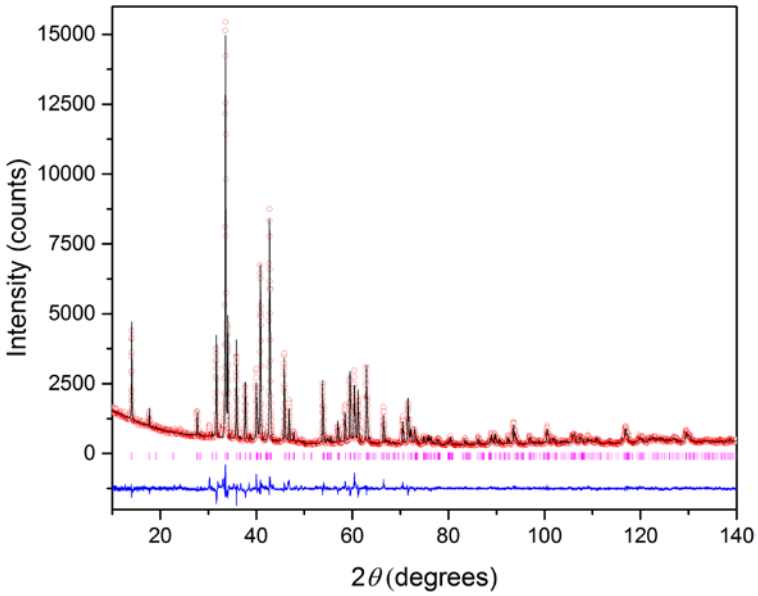

Figure 3.2 Rietveld fit of the 12-hour D2 powder x-ray diffraction pattern of $CaFe_3O_5$ obtained at room temperature ($\chi^2 = 2.85$, $R_{wp} = 6.6$ %, $R_p = 5.0$ %).

behaviour was studied using powder synchrotron x-ray and neutron diffraction, as described later in Section 3.2.4.

3.2.2. Thermogravimetric Analysis

The oxygen content in $CaFe_3O_5$ was studied using a thermogravimetric technique, with a Netzsch Jupiter STA 440 F1. 1.2119 mg of $CaFe_3O_5$ sample was transferred into an alumina crucible and then loaded into the sample chamber. The sample was heated in air at 10 °C min^{-1} to 900 °C, and then cooled back down to room temperature at the same rate. An x-ray diffraction pattern of the sample was taken after the analysis using the Bruker D2 Phaser (using Cu K_α/K_β radiation, for a 15 minutes scan of $5° \leq 2\theta \leq 70°$) to ensure all of the $CaFe_3O_5$ sample was oxidised. A refinement against the diffraction pattern was done using GSAS,[9] with all the reflections indexed with $Ca_2Fe_2O_5$

and Fe_2O_3 profiles, and no trace of $CaFe_3O_5$ was observed. The thermogravimetric analysis results, as shown in **Figure 3.3**, indicated a 2.789 % mass increase in the oxidised product, in agreement with the calculated value of 2.781% for the oxidation of $CaFe_3O_5$. This observation confirms that no oxygen deficiency is found in the synthesised sample of $CaFe_3O_5$.

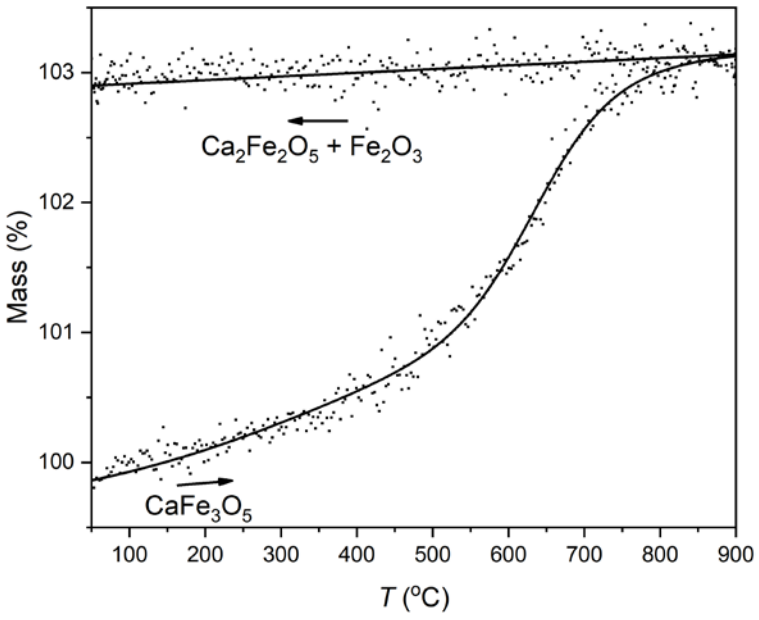

Figure 3.3 The change in percentage mass that occurs while heating the $CaFe_3O_5$ sample in air at 10 °C min^{-1} to 900 °C and then cooling at the same rate. Arrows indicate the direction of the measurement.

3.2.3. Magnetic and Physical Property Measurements of $CaFe_3O_5$

Magnetometry measurements were carried out using a 5.7 mg sample of $CaFe_3O_5$ using a Quantum Design MPMS XL SQUID magnetometer. The magnetic susceptibility was recorded on warming in zero field cooled (ZFC) and field cooled (FC) conditions between 2 and 400 K with an applied magnetic field of 1000 Oe. A plot of the magnetic susceptibility of $CaFe_3O_5$ against the measured temperature is shown in **Figure 3.4**. Similar behaviour was observed in both the ZFC and FC measurements. A sharp magnetic transition was found at T_M = 302 K, similar to the antiferromagnetic transition observed in Fe_4O_5 with a T_N = 320 K. Magnetisation versus field hysteresis loops were taken at 2, 230 and 300 K ($-7 \leq \mu_0 H$ (T) ≤ 7). As illustrated in **Figure 3.5**, the 300 K measurement showed an almost paramagnetic behaviour with a tiny moment of 0.004 μ_B per formula unit of $CaFe_3O_5$. The small moment was likely due to the fact that the measurement was recorded very close to the magnetic transition temperature of 302 K. At 230 K, a magnetic moment of 0.04 μ_B per formula unit was observed. The hysteresis loops showed little change between 230 K and 2 K. The loop at 2 K is slightly thinner, with a coercivity of 0.3 T, suggesting that the material is more responsive to the external field, and hence more ferromagnetic.

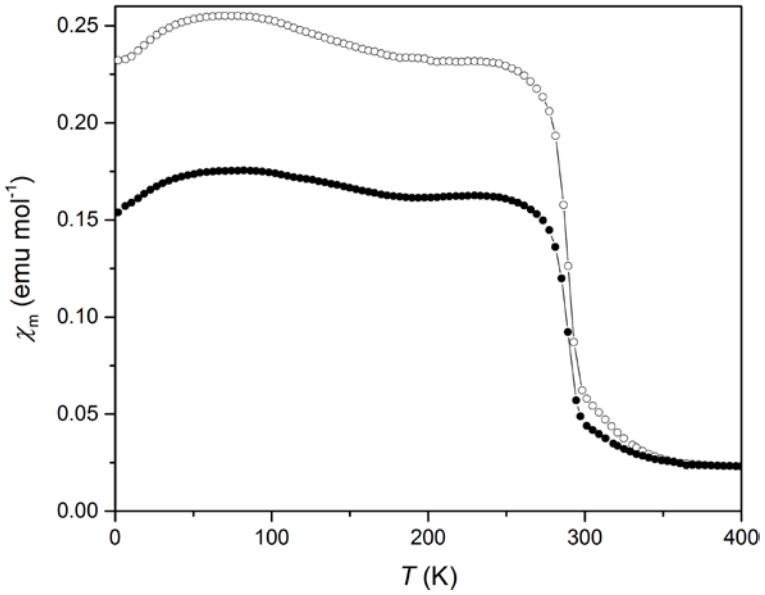

Figure 3.4 ZFC (closed symbols) and FC (open symbols) magnetic susceptibilities of $CaFe_3O_5$.

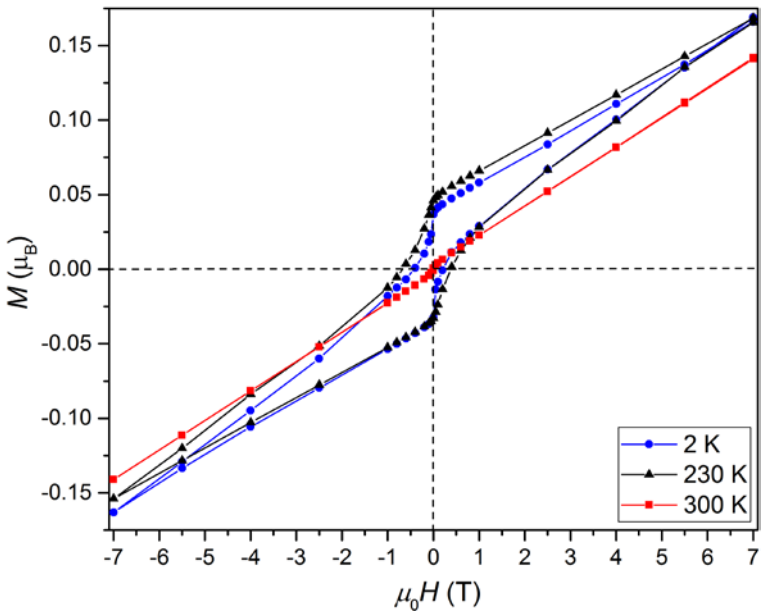

Figure 3.5 Magnetisation-field measurements of $CaFe_3O_5$ at 2, 230 and 300 K.

The electrical properties of $CaFe_3O_5$ were studied using a Quantum Design PPMS. A pellet of polycrystalline sample with a cross section and length of 0.0304 cm^2 and 0.33 cm, respectively, was used. The resistivity of the sample was measured between 180 and 400 K, as shown in **Figure 3.7.** $CaFe_3O_5$ shows semiconducting behaviour in the measured temperature range, with the resistivity of the sample decreasing with temperature. The resistance of the sample was found to be too great to be recorded by the PPMS below 180 K. A change in the slope of the resistivity was observed at the magnetic transition temperature (T_M = 302 K). By fitting the Arrhenius equation $\rho = A \exp(E_a/k_B T)$ to the two slopes, activation energies E_a of 0.61 eV and 0.26 eV below and above T_M, respectively, were calculated. The magnetoresistance of $CaFe_3O_5$ was studied using the same pellet by measuring its resistance against a looped external magnetic field of $-7 \leq \mu_0 H$ (T) ≤ 7 at 200 K. The MR vs $\mu_0 H$ hysteresis loop shown in **Figure 3.6** indicates a small magnetoresistance exhibited by the sample. This is likely to be reflecting the small net magnetisation of $CaFe_3O_5$.

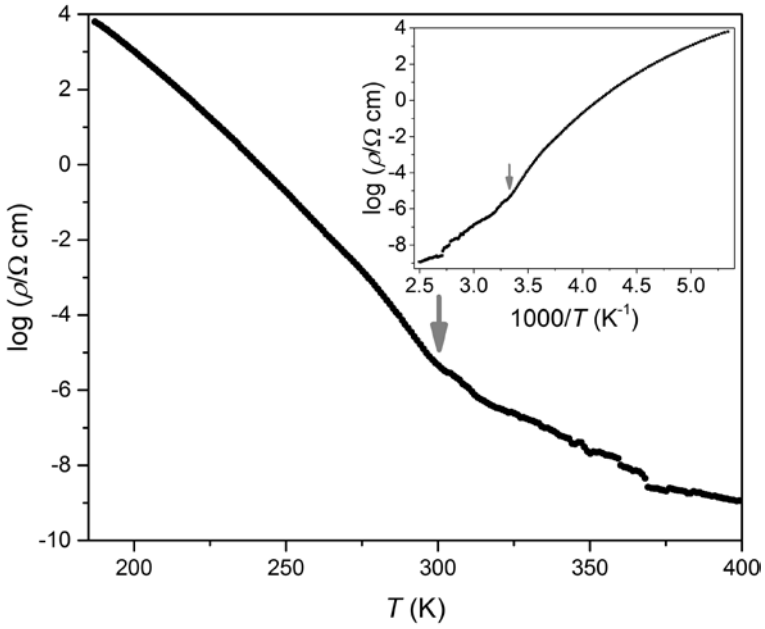

Figure 3.7 Log_{10} plot of the electrical resistivity of $CaFe_3O_5$ against temperature, with the discontinuity at 300 K marked. The inset in the top right shows the plot of the natural log of the resistivity against reciprocal temperature used to obtain the activation energies for electronic excitation below and above the transition temperature.

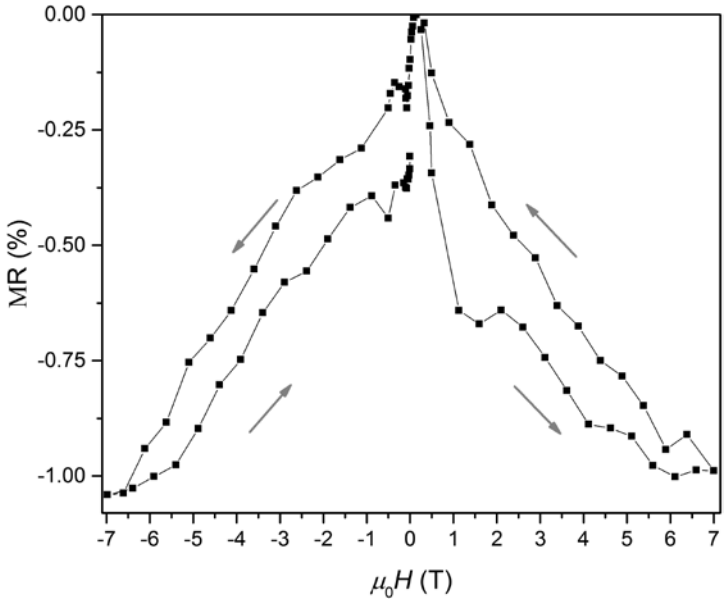

Figure 3.6 The magnetoresistance MR of $CaFe_3O_5$ measured at 200 K.

3.2.4. Diffraction Study of $CaFe_3O_5$

The crystal and magnetic structures of $CaFe_3O_5$ were studied using high resolution synchrotron x-ray and neutron diffraction techniques. Synchrotron diffraction data were collected at the ID22 beamline of the ESRF with an incident wavelength of 0.3999 Å. The sample was packed into a quartz capillary with an outer diameter of 0.7 mm. Diffraction data were collected, while spinning the sample, between 80 and 500 K using an Oxford Cryostream system with a hot air blower attachment.

Powder neutron diffraction experiments were carried out at the D2B beamline of the ILL with an incident wavelength 1.5940 Å, using a 5 g powder sample. The sample was packed into a vanadium can and diffraction patterns were collected at temperatures from 4 to 500 K (4 to 90 K using a helium cryostat and 90 to 500 K using a cryostream).

The diffraction patterns collected from the synchrotron and neutron diffraction experiments were refined using the FullProf Suite.[11] The peak shape was refined using a pseudo-Voigt profile, as described in Section 2.2.4. The background of the diffraction patterns is fitted using linear interpolation between a set of background points with refinable heights. The refined thermal parameters from the synchrotron data were found to be smaller than usual, which are likely due to the absorption of x-rays by the sample and quartz capillary. This also resulted in some unrealistic values (negative parameters) for the oxygen thermal factors, hence the thermal factors of the oxygen were constrained to be refined together. During the refinement of 80 and 100 K

synchrotron data, the thermal parameters of all the atoms were constrained to be refined together to obtain a coefficient that accounts for the thermal contributions of all the atoms. The refined crystallographic details from synchrotron x-ray and neutron diffraction patterns are summarised in **Table 3.2** to **Table 3.7.** Despite the use of thermal parameter constraints in the refinement of synchrotron data, the obtained structural parameters are consistent with those from neutron diffraction.

The Rietveld fits to the diffraction patterns obtained at 500 K from synchrotron and neutron diffraction data are shown in **Figure 3.8A** and **Figure 3.8B**, respectively. The results synchrotron showed a small amount [2.29(3) % by volume] of $Ca_2Fe_2O_5$ impurity present in the sample. The absence of $Ca_2Fe_2O_5$ reflections neutron data is likely due to the lower resolution pattern, compared to that of the synchrotron.

(A)

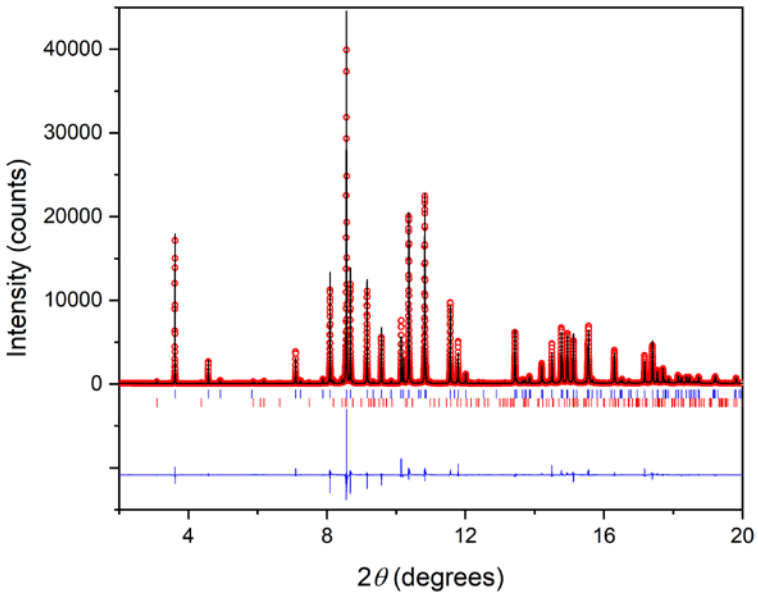

(B)

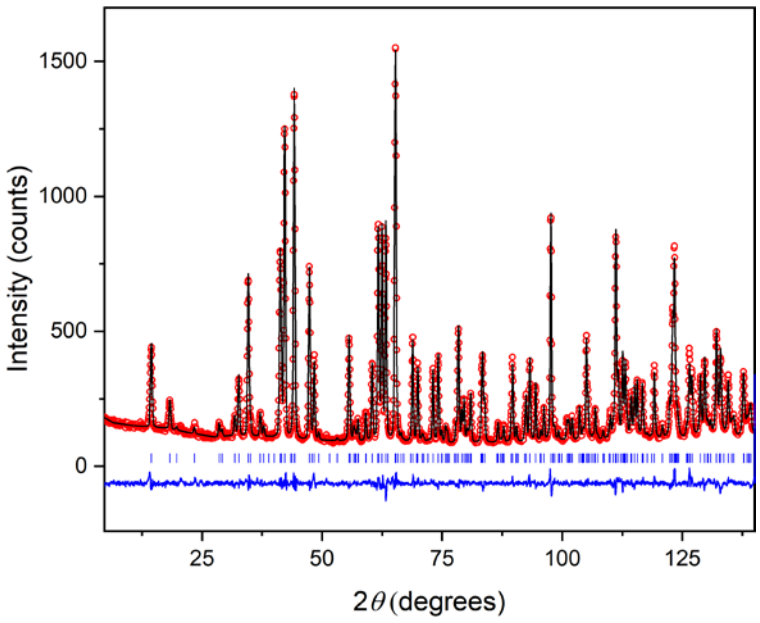

Figure 3.8 Rietveld fits to (A) synchrotron x-ray powder diffraction profiles for $CaFe_3O_5$ at 500 K, with blue tick marks indicating the $CaFe_3O_5$ phase and pink marks a 2.3(3) % by volume $Ca_2Fe_2O_5$ impurity, and (B) powder neutron diffraction profiles at 500 K, with structural phases indicated with blue tick marks.

The distribution of Ca and Fe ions over the three cation sites was investigated using the 500 K synchrotron and neutron diffraction patterns. The large difference of the electron densities of Ca and Fe, and their high neutron coherent scattering length contrast (4.70 fm for Ca and 9.45 fm for Fe)[12] , allows x-ray and neutron scattering to distinguish between the two and hence the occupancy of the sites could be refined. Both the x-ray and neutron results show that the two octahedral sites are occupied exclusively by Fe ions. These findings were consistent with the fact that Ca^{2+} ions are larger than $Fe^{2+/3+}$, therefore they are not likely to be found occupying the considerably smaller octahedral sites. (M-O distances are detailed in the crystallographic information in **Table 3.8** and **Table 3.9**) However, refinements of the trigonal prismatic site occupancy show Ca with a small amount of Fe [4.4(3) % by volume]. Consistent findings were obtained from the refined neutron diffraction data, which revealed that 4.0(8) % of the triangular prismatic site is occupied by Fe. The Ca/Fe occupancy of the trigonal prismatic site was fixed to the

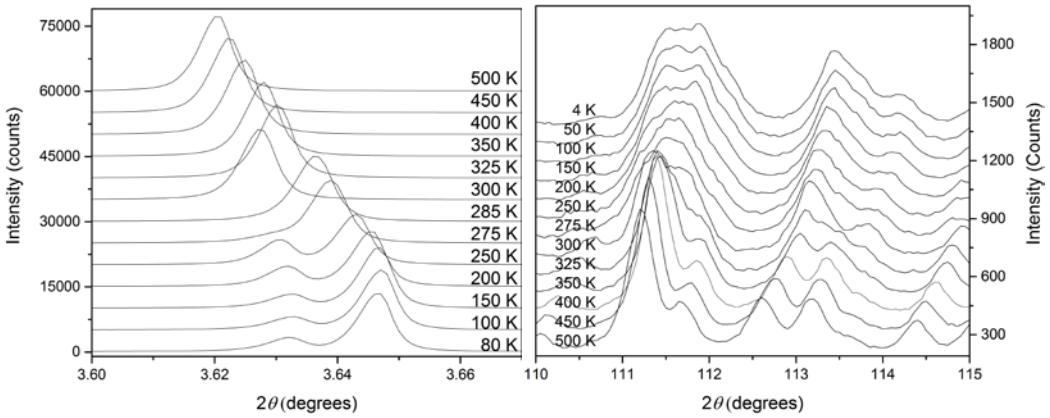

Figure 3.9 Evolution of diffraction peaks with temperature from x-ray (Left) and neutron (Right) diffraction. The splitting of the (002) reflection when cooled below the T_M = 302 K transition is illustrated in the plot on the left. The plot on the right shows the broadening and separation of some nuclear peaks.

refined 500 K values in the refinement profiles of patterns obtained below 500 K.

Diffraction patterns obtained below room temperature reveal long range phase separation as the diffraction peaks in both the synchrotron x-ray and neutron diffraction patterns broaden or split into two components below T_M. The diffraction patterns shown in **Figure 3.9** highlight the temperature evolution of certain Bragg reflections. The shift of the x-ray (002) peak to lower 2θ at 300 K evidenced a small bulk lattice distortion due to spin ordering before separation into two phases occurs at lower temperatures. Neutron diffraction data show that both of the low temperature phases become magnetically ordered at the same temperature, at T_M = 302 K. The magnetic peaks shown in **Figure 3.10** indicate that one phase has a magnetic propagation vector [½ 0 0] while for the other it is [0 0 0]. Details of the magnetic structures are

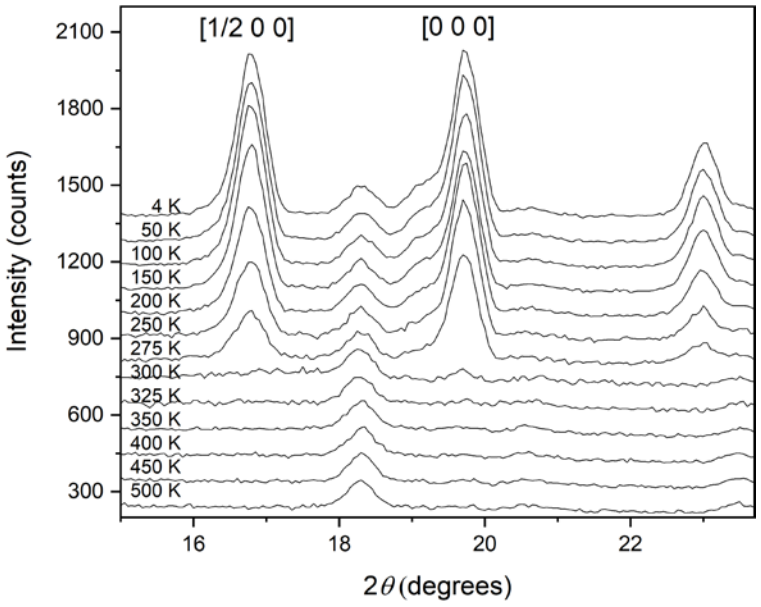

Figure 3.10 The appearance of the magnetic reflections with propagation vectors of [0 0 0] and [½ 0 0] that correspond to the two low temperature phases of $CaFe_3O_5$ below 302 K.

discussed later. Rietveld fits to the diffraction patterns obtained at 80 K from x-ray diffraction and 4 K from neutron diffraction (as shown in **Figure 3.11A** and **B**) show that the low temperature phases adopt the same *Cmcm* space group symmetry as the high-temperature phase (HT).

The temperature evolution of the refined lattice parameters from x-ray and neutron diffraction data are shown in **Figure 3.12A** and **B**, respectively. Anisotropic thermal expansion was observed when cooled below 350 K, just above the phase separation and T_M, suggesting possible strain and phase frustration in the HT phase near the transition temperature. The low temperature phase with a magnetic propagation vector of [½ 0 0] was found to have larger *b* and *c* lattice parameters and a smaller *a* in comparison to the other phase. However, both phases have similar cell volumes.

(A)

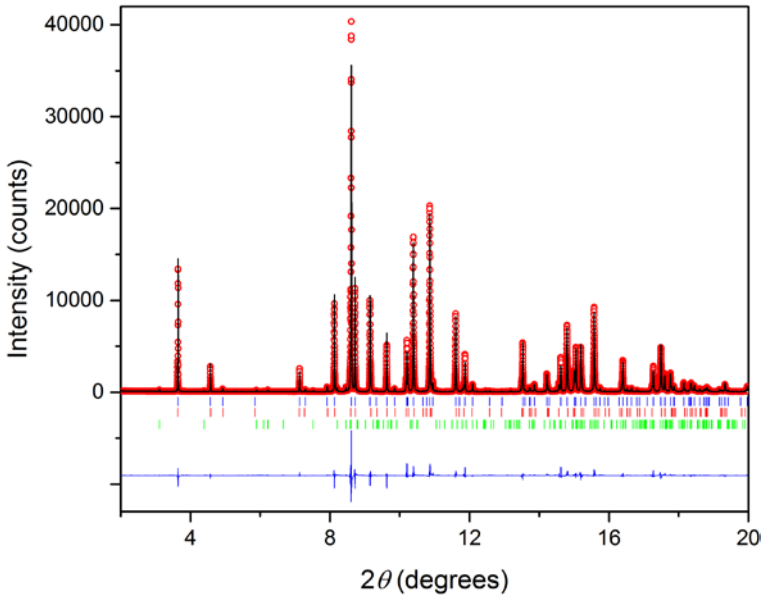

(B)

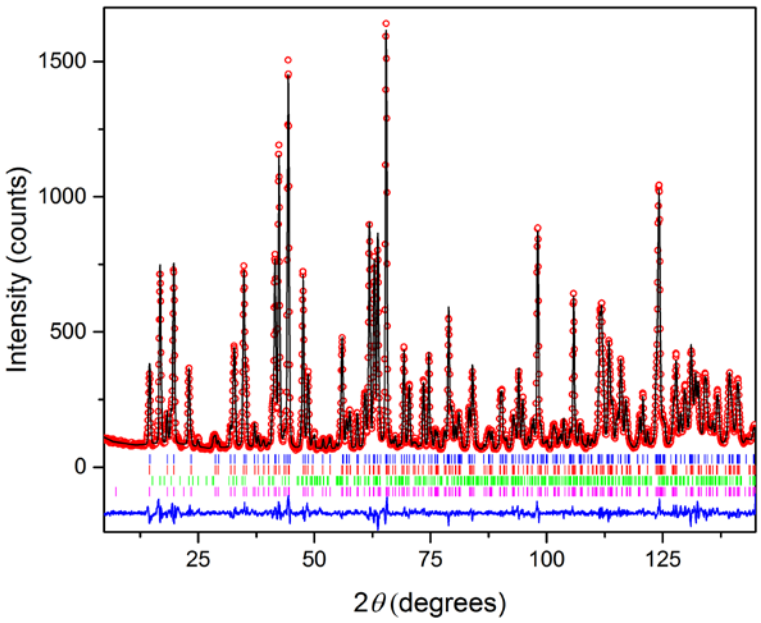

Figure 3.11 Rietveld fits to (A) synchrotron x-ray powder diffraction profiles for $CaFe_3O_5$ at 80 K, with blue and red tick marks indicating the two low temperature phases and green marks a 2.3% by volume $Ca_2Fe_2O_5$ impurity, and (B) powder neutron diffraction profiles at 4 K, with structural phases indicated with blue and red tick marks. The green and pink tick marks represent the magnetic phases with propagation vectors of [½ 0 0] and [0 0 0] respectively.

(A)

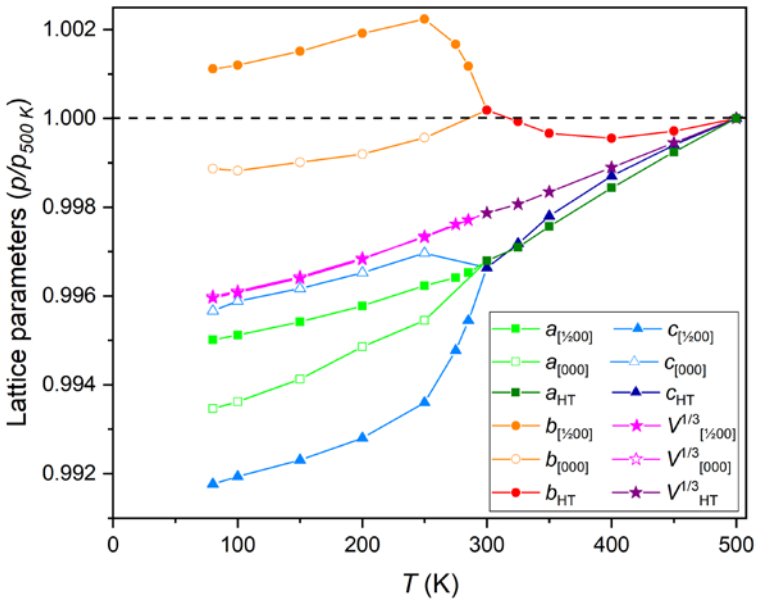

(B)

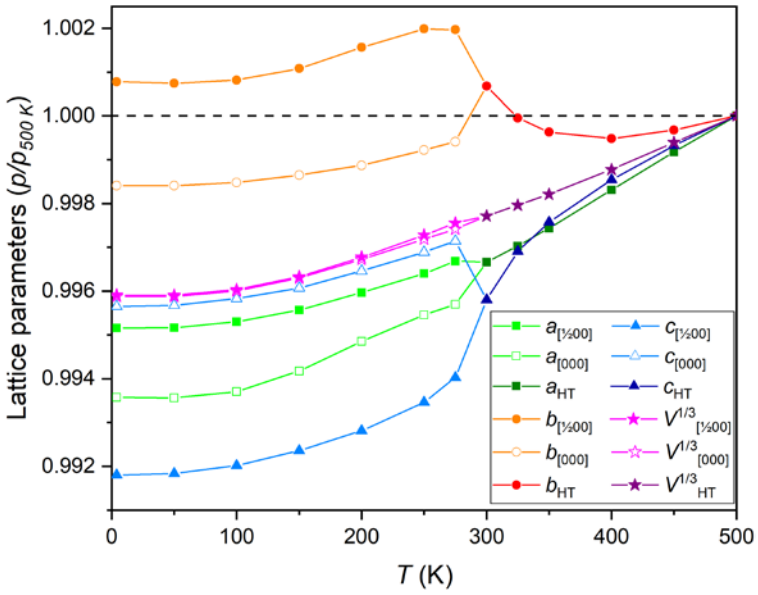

Figure 3.12 Changes in the lattice parameters relative to 500 K values obtained from (A) powder synchrotron x-ray diffraction data [$a_{500\ K}$ = 3.039972(2) Å, $b_{500\ K}$ = 10.016679(8) Å and $c_{500\ K}$ = 12.676256(10) Å] and (B) powder neutron diffraction ($a_{500\ K}$ = 3.03896(1) Å, $b_{500\ K}$ = 10.01355(5) Å and $c_{500\ K}$ = 12.67039(7) Å), from a single high temperature (HT) phase separated into two low temperature phases, with magnetic propagation vectors of [½ 0 0] and [0 0 0].

The refined phase fractions of the low-temperature $CaFe_3O_5$ phase with magnetic *k*-vector of [½ 0 0], using the synchrotron x-ray and neutron diffraction data, are shown in **Figure 3.13**. The results show the rise of the low-temperature phase when cooled below 300 K. Larger fractions were observed for the [½ 0 0] phase in both synchrotron x-ray and neutron results, suggesting that the structure with [½ 0 0] magnetic order is more thermodynamically stable compared to the other phase. It also indicated that the electronic phase separation in $CaFe_3O_5$ is an incomplete transformation from the HT phase to the [½ 0 0] ordered one, in a similar manner as the ferromagnetic to charge ordered states in manganite perovskites that led to phase-separated microstructures.[13,14,15] The thermodynamic stability of the two low temperature structures was studied using density functional theory calculations, as described later in Section 3.2.6. Furthermore, the refined phase fractions were found to be different in the results from the synchrotron x-ray and neutron

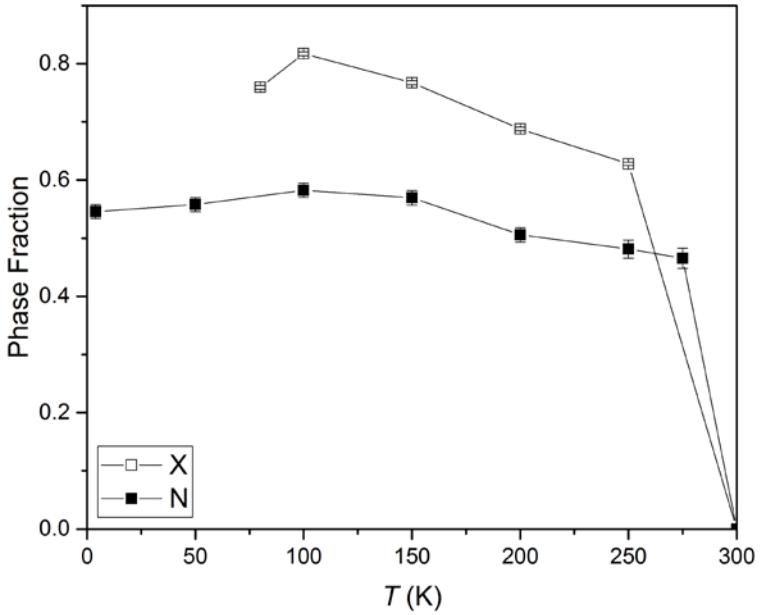

Figure 3.13 The phase fractions of the phase with propagation vector [½ 0 0], obtained from synchrotron (X) and neutron (N) diffraction data.

diffraction data, despite both diffraction experiments were carried from the same sample. This results suggested that the separation of the HT *Cmcm* phase is likely to be a strain-driven transition, resulting in into two phases similar in energy with the same lattice symmetry, and therefore the fraction of separation is dependent on the thermal history of the sample.

Table 3.2 Refined structural parameters of the two low-temperature phases of $CaFe_3O_5$, with magnetic propagation vectors of [½ 0 0] and [0 0 0], from synchrotron diffraction data at 80 and 100 K. Both phases adopt the orthorhombic structure in the space group of *Cmcm*. Estimated standard deviations in independent variables are shown in parentheses. Fe1 atoms are located at (0, *y*, *z*), Fe2 atoms with site symmetry 4*a* are located at (0, 0, 0), Ca1/Fe atoms at (0, *y*, ¼), O1 atoms at (0, *y*, ¼), O2 atoms at (0, *y*, z) and O3 atoms at (0, *y*, *z*). The occupancy of the Ca1 site was fixed to a Ca/Fe ratio of 0.044/0.956. * The thermal parameters for all the atoms are constrained to be refined together.

			T / K	80		100	
			Phase	[½ 0 0]	[0 0 0]	[½ 0 0]	[0 0 0]
Cell			*a* (Å)	3.02481(1)	3.02010(1)	3.02514(1)	3.02058(1)
			b (Å)	10.02784(1)	10.00535(2)	10.02869(1)	10.00493(2)
			c (Å)	12.57189(1)	12.62138(3)	12.57402(1)	12.62411(2)
			V (Å^3)	381.335(1)	381.382(2)	381.473(1)	381.509(1)
Fe1	8*f*	*y*		0.26558(2)	0.26641(8)	0.26557(2)	0.26646(10)
		z		0.11023(1)	0.11141(5)	0.11027(1)	0.11128(6)
Ca1/Fe	4*c*	*y*		0.51983(5)	0.51985(15)	0.51985(5)	0.51989(18)
O1	4*c*	*y*		0.19241(16)	0.19358(46)	0.19252(16)	0.19205(55)
O2	8*f*	*y*		0.64932(11)	0.64422(34)	0.64918(11)	0.64300(40)
		z		0.44702(8)	0.44955(25)	0.44724(8)	0.44970(30)
O3	8*f*	*y*		0.90321(12)	0.90646(32)	0.90347(12)	0.90539(38)
		z		0.13587(7)	0.13570(20)	0.13601(7)	0.13466(25)
			B_{iso} / Å^2 *	0.011(2)	0.047(9)	0.022(2)	0.112(10)
			R_p / %		9.4		10.0
			R_{wp} / %		11.0		11.9
			χ^2		11.3		13.0

Table 3.3 Refined structural parameters of the two low-temperature phases of $CaFe_3O_5$, with magnetic propagation vectors of [½ 0 0] and [0 0 0], from synchrotron diffraction data between 150 and 250 K. Both phases adopt the orthorhombic structure in the space group of *Cmcm*. Estimated standard deviations in independent variables are shown in parentheses. Fe1 atoms are located at (0, *y*, *z*), Fe2 atoms with site symmetry 4*a* are located at (0, 0, 0), Ca1/Fe atoms at (0, *y*, ¼), O1 atoms at (0, *y*, ¼), O2 atoms at (0, *y*, z) and O3 atoms at (0, *y*, *z*). The occupancy of the Ca1 site was fixed to a Ca/Fe ratio of 0.044/0.956. * The thermal parameters for all the atoms are constrained to be refined together.

			T / K		150		200		250
			Phase	[½ 0 0]	[0 0 0]	[½ 0 0]	[0 0 0]	[½ 0 0]	[0 0 0]
Cell			*a* (Å)	3.02604(1)	3.02213(1)	3.02715(1)	3.02433(1)	3.02853(1)	3.02614(1)
			b (Å)	10.03180(1)	10.00678(3)	10.03589(1)	10.00861(2)	10.03907(1)	10.01231(1)
			c (Å)	12.57874(1)	12.62772(3)	12.58504(1)	12.63224(2)	12.59515(1)	12.63783(2)
			V (Å^3)	381.847(1)	381.884(2)	382.335(1)	382.370(1)	382.938(1)	382.909(1)
Fe1	8*f*		*y*	0.26561(2)	0.26643(9)	0.26555(3)	0.26684(6)	0.26572(3)	0.26683(5)
			z	0.11027(1)	0.11135(5)	0.11029(2)	0.11142(4)	134416(2)	0.11136(3)
Ca1/Fe	4*c*		*y*	0.51995(5)	0.51994(16)	0.52018(5)	0.52038(11)	0.52030(6)	0.52057(10)
O1	4*c*		*y*	0.19250(16)	0.19285(48)	0.19240(17)	0.19275(35)	0.19204(19)	0.19296(30)
O2	8*f*		*y*	0.64910(11)	0.64395(35)	0.64927(12)	0.64294(25)	0.64868(13)	0.64277(21)
			z	0.44671(8)	0.45009(26)	0.44694(9)	0.44944(19)	0.44691(10)	0.44904(16)
O3	8*f*		*y*	0.90307(11)	0.90678(33)	0.90315(12)	0.90640(24)	0.90351(13)	0.90561(20)
			z	0.13599(7)	0.13513(21)	0.13561(8)	0.13536(16)	0.13548(8)	0.13514(14)
			B_{iso} / Å^2 (Fe1)	0.093(4)	0.039(15)	0.134(4)	0.105(11)	0.195(5)	0.174(10)
			B_{iso} / Å^2 (Fe2)	0.103(5)	0.106(20)	0.170(6)	0.161(15)	0.264(7)	0.226(13)
			B_{iso} / Å^2 (Ca1/Fe)	0.090(8)	0.069(30)	0.152(10)	0.138(22)	0.233(11)	0.241(19)
			B_{iso} / Å^2 (O)*	0.011(12)	0.009(38)	0.037(13)	0.050(28)	0.085(15)	0.099(25)
			R_p / %		9.5		9.5		9.6
			R_{wp} / %		11.3		11.2		11.2
			χ^2		11.7		10.9		10.9

Table 3.4 Refined structural parameters of the high temperature (HT) phase of $CaFe_3O_5$ in space group *Cmcm* from synchrotron diffraction data between 300 and 500 K using an Oxford Cryostream system. Estimated standard deviations in independent variables are shown in parentheses. Fe1 atoms are located at (0, *y*, *z*), Fe2 atoms with site symmetry 4*a* are located at (0, 0, 0), Ca1/Fe atoms at (0, *y*, ¼), O1 atoms at (0, *y*, ¼), O2 atoms at (0, *y*, z) and O3 atoms at (0, *y*, *z*). The occupancy of the Ca1 site was fixed to a Ca/Fe ratio of 0.044/0.956. * The thermal parameters for all the atoms are constrained to be refined together.

			T / K	300	325	350	400	450	500
			Phase						HT
Cell			*a* (Å)	3.03023(1)	3.03116(1)	3.03257(1)	3.03523(1)	3.03767(1)	3.03997(1)
			b (Å)	10.01855(1)	10.01597(1)	10.01331(1)	10.01220(1)	10.01382(1)	10.01669(1)
			c (Å)	12.63366(1)	12.64055(1)	12.64841(1)	12.65984(1)	12.66862(1)	12.67627(1)
			V (Å^3)	383.540(1)	383.768(1)	385.083(1)	384.723(1)	385.363(1)	385.998(1)
Fe1	8*f*	*y*		0.26602(2)	0.26609(2)	0.26611(2)	0.26617(2)	0.26626(2)	0.26630(2)
		z		0.11084(1)	0.11089(1)	0.11095(1)	0.11100(1)	0.11103(1)	0.11097(1)
Ca1/Fe	4*c*	*y*		0.52020(4)	0.52031(4)	0.52033(4)	0.52042(4)	0.52051(4)	0.52061(4)
O1	4*c*	*y*		0.19259(12)	0.19205(13)	0.19230(13)	0.19222(13)	0.19220(13)	0.19249(13)
O2	8*f*	*y*		0.64535(9)	0.64469(9)	0.64428(9)	0.64383(9)	0.64354(9)	0.64370(9)
		z		0.44851(7)	0.44861(7)	0.44876(7)	0.44887(7)	0.44894(7)	0.44916(7)
O3	8*f*	*y*		0.90484(9)	0.90462(9)	0.90476(9)	0.90487(9)	0.90501(9)	0.90501(9)
		z		0.13504(6)	0.13503(6)	0.13492(6)	0.13479(6)	0.13477(6)	0.13443(6)
			B_{iso} / Å^2 (Fe1)	0.256(3)	0.283(4)	0.319(10)	0.384(4)	0.439(4)	0.483(4)
			B_{iso} / Å^2 (Fe2)	0.356(5)	0.376(5)	0.414(5)	0.486(6)	0.559(6)	0.617(6)
			B_{iso} / Å^2 (Ca1/Fe)	0.349(7)	0.389(7)	0.441(18	0.522(8)	0.592(8)	0.742(10)
			B_{iso} / Å^2 (O)*	0.151(9)	0.175(9)	0.197(10)	0.232(10)	0.273(10)	0.296(10)
			R_p / %	10.7	10.8	10.9	10.9	11.0	11.1
			R_{wp} / %	12.2	12.4	12.5	12.5	12.6	12.6
			χ^2	11.5	12.4	12.3	12.0	11.9	11.7

Table 3.5 Refined structural parameters of the two low-temperature phases of $CaFe_3O_5$, with magnetic propagation vectors of [½ 0 0] and [0 0 0], from neutron diffraction data between 4 and 100 K. Both phases adopt the orthorhombic structure in the space group of *Cmcm*. Estimated standard deviations in independent variables are shown in parentheses. Fe1 atoms are located at (0, *y*, *z*), Fe2 atoms with site symmetry 4*a* are located at (0, 0, 0), Ca1/Fe atoms at (0, *y*, ¼), O1 atoms at (0, *y*, ¼), O2 atoms at (0, *y*, *z*) and O3 atoms at (0, *y*, *z*). The occupancy of the Ca1 site was fixed to a Ca/Fe ratio of 0.040/0.960.

			T / K	4		50		100
			Phase	[½ 0 0]	[0 0 0]	[½ 0 0]	[0 0 0]	[½ 0 0]	[0 0 0]
Cell			*a* (Å)	3.02425(3)	3.01944(3)	3.02425(3)	3.01940(3)	3.02467(2)	3.01984(4)
			b (Å)	10.02139(9)	9.99766(11)	10.02102(9)	9.99758(11)	10.02117(9)	9.99835(12)
			c (Å)	12.56654(10)	12.61533(15)	12.5693(10)	12.61564(15)	12.56926(10)	12.61759(16)
			V (Å^3)	380.857(6)	380.823(7)	380.855(6)	380.824(8)	381.007(6)	380.968(8)
Fe1	8*f*		*y*	0.2650(2)	0.2669(3)	0.2651(2)	0.2666(3)	0.2646(2)	0.2670(3)
			z	0.1104(1)	0.1113(2)	0.1103(1)	0.1111(2)	0.1102(1)	0.1112(2)
Ca1/Fe	4*c*		*y*	0.5201(5)	0.5193(7)	0.5199(5)	0.5201(7)	0.5206(5)	0.5201(8)
O1	4*c*		*y*	0.1925(4)	0.1913(6)	0.1927(4)	0.1915(7)	0.1926(4)	0.1910(7)
O2	8*f*		*y*	0.6504(3)	0.6409(6)	0.6504(3)	0.6406(6)	0.6200(3)	0.6408(6)
			z	0.4484(2)	0.4485(3)	0.4485(2)	0.4485(3)	0.4483(2)	0.4488(3)
O3	8*f*		*y*	0.9034(4)	0.9038(6)	0.9030(4)	0.9041(6)	0.9034(4)	0.9035(6)
			z	0.1357(2)	0.1356(3)	0.1358(2)	0.1357(3)	0.1360(2)	0.1358(3)
			B_{iso} / Å^2 (Fe1)	0.54(4)	0.56(6)	0.57(4)	0.57(6)	0.67(4)	0.58 (6)
			B_{iso} / Å^2 (Fe2)	0.72(5)	0.49(6)	0.67(5)	0.53(6)	0.74(5)	0.55(7)
			B_{iso} / Å^2 (Ca1/Fe)	0.60(9)	0.86(11)	0.56(9)	0.83(12)	0.79(9)	0.88(13)
			B_{iso} / Å^2 (O1)	0.52(8)	1.03(11)	0.46(7)	1.21(12)	0.65(8)	1.19(13)
			B_{iso} / Å^2 (O2)	0.65(6)	1.16(8)	0.67(5)	1.19(8)	0.79(5)	1.23(9)
			B_{iso} / Å^2 (O3)	0.62(6)	0.96(7)	0.63(5)	0.96(8)	0.77(5)	0.91(8)
			R_p / %		6.14		6.17		6.25
			R_{wp} / %		7.28		7.30		7.37
			χ^2		4.15		4.15		4.16

Table 3.6 Refined structural parameters of the two low-temperature phases of $CaFe_3O_5$, with magnetic propagation vectors of [½ 0 0] and [0 0 0], from neutron diffraction data between 150 and 175 K. Both phases adopt the orthorhombic structure in the space group of *Cmcm*. Estimated standard deviations in independent variables are shown in parentheses. Fe1 atoms are located at (0, *y*, *z*), Fe2 atoms with site symmetry 4*a* are located at (0, 0, 0), Ca1/Fe atoms at (0, *y*, ¼), O1 atoms at (0, *y*, ¼), O2 atoms at (0, *y*, *z*) and O3 atoms at (0, *y*, *z*). The occupancy of the Ca1 site was fixed to a Ca/Fe ratio of 0.040/0.960.

	T / K		150		200		250		275	
	Phase		[½ 0 0]	[0 0 0]	[½ 0 0]	[0 0 0]	[½ 0 0]	[0 0 0]	[½ 0 0]	[0 0 0]
Cell	*a* (Å)		3.02550(2)	3.02128(4)	3.02671(3)	3.02331(3)	3.02802(4)	3.02516(3)	3.02888(4)	3.02589(4)
	b (Å)		10.02440(9)	10.00006(12)	10.02924(10)	10.00226(10)	10.03344(13)	10.00573(10)	10.03326(13)	10.00767(11)
	c (Å)		12.57361(10)	12.62060(16)	12.57934(11)	12.62558(14)	12.58755(15)	12.63103(14)	12.59469(15)	12.63422(16)
	V (Å^3)		381.342(6)	381.306(8)	381.854(6)	381.797(7)	382.429(8)	382.328(7)	382.747(8)	382.591(8)
Fe1	8*f*	*y*	0.2649(2)	0.2669(3)	0.2648(2)	0.2672(2)	0.2649(3)	0.2675(3)	0.2651(3)	0.2670(3)
		z	0.1102(1)	0.1113(2)	0.1103(1)	0.1114(1)	0.1104(2)	0.1112(2)	0.1102(2)	0.1114(2)
Ca1/Fe	4*c*	*y*	0.5202(5)	0.5195(8)	0.5208(9)	0.5194(6)	0.5209(8)	0.5203(7)	0.5213(8)	0.5194(7)
O1	4*c*	*y*	0.1921(4)	0.1918(7)	0.1922(5)	0.1920(5)	0.1921(6)	0.1921(6)	0.1925(6)	0.1915(6)
O2	8*f*	*y*	0.6505(3)	0.6407(6)	0.6504(3)	0.6411(5)	0.6502(4)	0.6413(5)	0.6506(4)	0.6414(5)
		z	0.4482(2)	0.4487(3)	0.4483(3)	0.4485(3)	0.4486(3)	0.4488(3)	0.4487(3)	0.4484(3)
O3	8*f*	*y*	0.9031(4)	0.9039(6)	0.9035(4)	0.9042(5)	0.9046(6)	0.9035(5)	0.9040(5)	0.9030(6)
		z	0.1358(2)	0.1355(3)	0.1355(2)	0.1353(3)	0.1358(3)	0.1352(3)	0.1355(3)	0.1352(3)
B_{iso} / Å^2 (Fe1)			0.67(4)	0.62(6)	0.75(5)	0.66(5)	0.92(7)	0.67(6)	0.84(8)	0.76(7)
B_{iso} / Å^2 (Fe2)			0.82(5)	0.67(7)	0.90(6)	0.76(6)	1.16(8)	0.69(7)	1.08(9)	0.86(7)
B_{iso} / Å^2 (Ca1/Fe)			0.74(9)	0.98(13)	0.95(11)	0.96(11)	1.12(14)	1.07(12)	1.04(14)	1.01(13)
B_{iso} / Å^2 (O1)			0.60(8)	1.12(12)	0.69(9)	1.07(10)	0.63(11)	1.01(11)	0.70(12)	1.07(12)
B_{iso} / Å^2 (O2)			0.76(5)	1.25(8)	0.84(6)	1.22(7)	1.03(9)	1.16(8)	0.88(9)	1.30(9)
B_{iso} / Å^2 (O3)			0.75(5)	0.90(8)	0.74(6)	1.04(7)	0.95(8)	0.97(8)	0.85(9)	1.01(8)
R_p / %				6.17		6.42		7.68		7.90
R_{wp} / %				7.22		7.36		8.58		8.72
χ^2				3.87		3.81		2.47		2.40

Table 3.7 Refined structural parameters of the high temperature (HT) phases of $CaFe_3O_5$ at and above 300 K in space group *Cmcm* from neutron diffraction data. Estimated standard deviations in independent variables are shown in parentheses. Fe1 atoms are located at (0, *y*, *z*), Fe2 atoms with site symmetry 4*a* are located at (0, 0, 0), Ca1/Fe atoms at (0, *y*, ¼), O1 atoms at (0, y, ¼), O2 atoms at (0, *y*, *z*) and O3 atoms at (0, *y*, *z*). The occupancy of the Ca1 site was fixed to a Ca/Fe ratio of 0.040/0.960.

	T / K		300	325	350	400	450	500
	Phase							HT
Cell	*a* (Å)		3.02883(2)	3.02993(2)	3.03117(1)	3.03382(1)	3.03646(1)	3.03896(1)
	b (Å)		10.02037(7)	10.01307(6)	10.00983(5)	10.00837(5)	10.01028(5)	10.01356(5)
	c (Å)		12.61722(8)	12.63123(8)	12.63964(5)	12.65191(6)	12.66182(6)	12.67040(6)
	V (Å^3)		382.933(4)	383.218(4)	383.506(3)	384.158(3)	384.866(3)	385.571(3)
Fe1	8*f*	*y*	0.2657(1)	0.2660(1)	0.2658(1)	0.2659(1)	0.2660(1)	0.2661(1)
		z	0.1108(1)	0.1108(1)	0.1109(1)	0.1109(6)	0.1109(6)	0.1109(7)
Ca1/ Fe	4*c*	*y*	0.5191(3)	0.5194(3)	0.5203(3)	0.5201(3)	0.5200(3)	0.5202(3)
O1	4*c*	*y*	0.1923(2)	0.1924(2)	0.1920(2)	0.1920(2)	0.1921(2)	0.1921(2)
O2	8*f*	*y*	0.6468(2)	0.6456(2)	0.6452(2)	0.6443(2)	0.6440(2)	0.6437(2)
		z	0.4483(2)	0.4486(1)	0.4490(1)	0.4492(1)	0.4490(1)	0.4494(1)
O3	8*f*	*y*	0.9032(2)	0.9038(2)	0.9037(2)	0.9040(2)	0.9044(2)	0.9044(2)
		z	0.1654(1)	0.1353(1)	0.1353(1)	0.1351(1)	0.1351(1)	0.1349(1)
B_{iso} / Å^2 (Fe1)			0.80(3)	0.89(2)	0.93(2)	1.11(2)	1.26(3)	1.15(3)
B_{iso} / Å^2 (Fe2)			0.98(3)	1.08(3)	1.09(3)	1.16(3)	1.11(2)	1.28(3)
B_{iso} / Å^2 (Ca1/Fe)			1.06(6)	1.13(5)	1.19(5)	1.28(4)	1.38(4)	1.73(6)
B_{iso} / Å^2 (O1)			0.83(4)	1.01(4)	1.01(3)	1.07(4)	1.19(4)	1.28(4)
B_{iso} / Å^2 (O2)			1.12(4)	1.26(3)	1.29(3)	1.41(3)	1.52(3)	1.65(3)
B_{iso} / Å^2 (O3)			0.88(3)	0.98(3)	1.02(2)	1.11(3)	1.22(2)	1.32(3)
R_p / %			8.74	8.53	7.09	7.08	7.15	7.24
R_{wp} / %			9.45	9.07	7.66	7.57	7.64	6.64
χ^2			2.75	2.49	3.5	3.3	3.3	3.2

Table 3.8 Fe-O and Fe-Fe bond lengths /Å and BVSs obtained from powder synchrotron x-ray diffraction data, with mean values < >, shown for the high temperature (HT) phase of $CaFe_3O_5$ at 500 K and the separated low-temperature phases, with magnetic propagation vectors of [½ 0 0] and [0 0 0], at 80 K.

Bond	Distance		
	HT	[½ 0 0]	[0 0 0]
Ca1-O1 (x 2)	2.297(1)	2.298(1)	2.303(4)
Ca1-O3 (x 4)	2.407(2)	2.390(1)	2.376(3)
<Ca1-O>	2.370(1)	2.359(1)	2.352(1)
Fe1-O1	1.9113(6)	1.9042(8)	1.895(3)
Fe1-O2	2.245(1)	2.222(1)	2.230(4)
Fe1-O2 (x 2)	2.0986(8)	2.0407(8)	2.090(3)
Fe1-O3 (x 2)	2.0819(7)	2.0727(9)	2.083(3)
<Fe1-O>	2.0862(3)	2.0589(4)	2.079(1)
BVSs of Fe1	2.39(1)	2.64(1)	2.46(5)
Fe2-O2 (x 4)	2.1893(8)	2.2300(9)	2.183(3)
Fe2-O3 (x 2)	1.953(1)	1.965(1)	1.952(3)
<Fe2-O>	2.1105(4)	2.1415(4)	2.106(1)
BVSs of Fe2	2.22(1)	2.03(1)	2.25(4)
Fe1-Fe1, Fe2-Fe2	3.0400(1)	3.0248(1)	3.0201(1)
Fe2-Fe2(x 2)	3.2158(5)	3.1728(5)	3.209(1)
Fe1-Fe2(x 4)	3.1257(2)	3.1199(3)	3.1177(8)

Bond valence sums for each iron site were calculated using a standard method with linear interpolation to estimate mixed charge states between Fe^{2+} and Fe^{3+}.[16,17] The calculations were carried out for the two Fe sites using the refined M-O distances from x-ray and neutron diffraction data (**Table 3.8** and **Table 3.9** respectively). The temperature evolution of the BVSs of $CaFe_3O_5$ between 4 and 500 K is shown in **Figure 3.14A**. The results show that the Fe1 and Fe2 sites have BVSs of 2.42(2) and 2.19(2) respectively at 500 K, equivalent to formal charges of +2.75 and +2.50 when renormalised to the average of +2.67. The charge distribution is consistent with the Fe2 site being slightly larger than the Fe1 site, which makes the Fe2 site more preferable for the larger Fe^{2+} cation ions, hence the lower estimated site valence. A change in the charge distribution was observed below the 302 K magnetic and phase

Table 3.9 Fe-O and Fe-Fe bond lengths /Å and BVSs obtained from powder neutron diffraction data, with mean values < >, shown for the HT phase of $CaFe_3O_5$ at 500 K and the separated low-temperature phases, with magnetic propagation vectors of [½ 0 0] and [0 0 0], at 4 K..

Bond	Distance		
	HT	[½ 0 0]	[0 0 0]
Ca1-O1 (x 2)	2.295(3)	2.296(5)	2.288(7)
Ca1-O3 (x 4)	2.403(2)	2.296(5)	2.288(7)
<Ca1-O>	2.367(2)	2.359(4)	2.354(6)
Fe1-O1	1.912(1)	1.899(3)	1.907(4)
Fe1-O2	2.239(2)	2.205(4)	2.251(5)
Fe1-O2 (x 2)	2.096(2)	2.037(3)	2.106(5)
Fe1-O3 (x 2)	2.078(2)	2.077(4)	2.061(5)
<Fe1-O>	2.083(1)	2.055(1)	2.082(2)
BVSs of Fe1	2.41(2)	2.67(6)	2.44(8)
Fe2-O2 (x 4)	2.190(1)	2.231(3)	2.165(5)
Fe2-O3 (x 2)	1.961(2)	1.961(3)	1.962(5)
<Fe2-O>	2.113(1)	2.141(1)	2.097(2)
BVSs of Fe2	2.19(2)	2.03(4)	2.29(7)
Fe1-Fe1, Fe2-Fe2	3.039(1)	3.024(1)	3.019(1)
Fe2-Fe2(x 2)	3.213(2)	3.173(3)	3.205(4)
Fe1-Fe2(x 4)	3.126(1)	3.124(2)	3.111(3)

segregation transition. In the phase with magnetic propagation vector [½ 0 0], the Fe1 and Fe2 BVSs were found to diverge to very different values of 2.67(6) and 2.03(4) at 4 K, consistent with charge order (CO) of Fe^{3+} and Fe^{2+} respectively, whereas the coexisting phase with [0 0 0] magnetic order shows the opposite behaviour as the Fe1 and Fe2 BVSs converge to similar values of 2.44(8) and 2.29(7) at 4 K, indicating that the electronic states at the two sites are not significantly different, hence this phase is charge averaged (CA). Charge ordering observed in the CO phase can be explained by the change of the cation size, due to anisotropic thermal expansion. The Fe2 site is found to be much larger than the Fe1 site in the CO phase, and hence more likely to accommodate the larger Fe^{2+} cation, whilst in the CA phase similar Fe1 and Fe2 site sizes are observed.

(A)

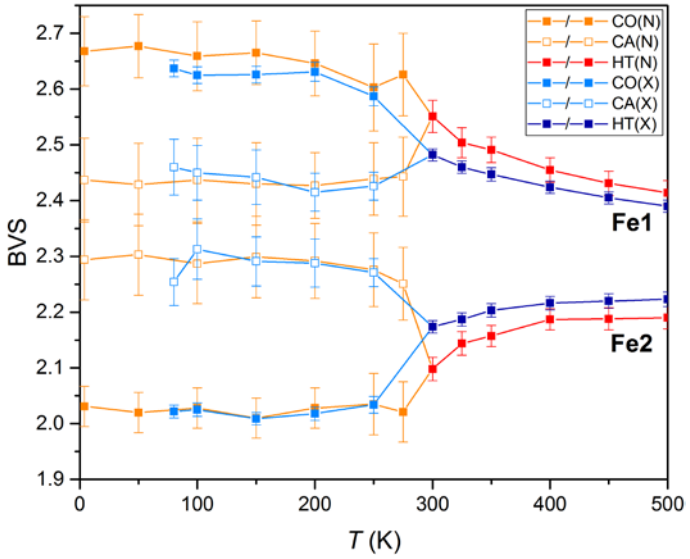

(B)

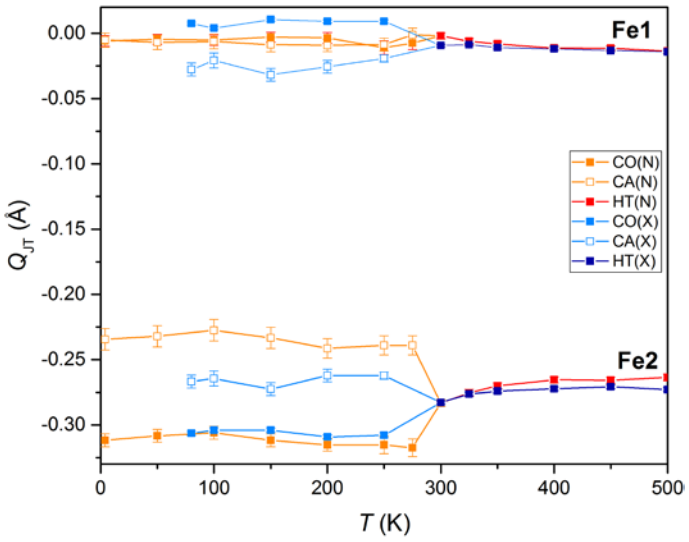

Figure 3.14 Temperature dependence of the (A) BVS and (B) Jahn-Teller distortion Q_{JT} of the two Fe sites in the HT, CO and CA phases, obtained from neutron (N) and synchrotron x-ray (X) diffraction data.

The Jahn-Teller distortion of the two Fe sites in the CO, CA and the HT phases was studied using the refined M-O distances obtained from synchrotron x-ray and neutron diffraction data. The changes in the Jahn-Teller distortion parameter Q_{JT} (detailed in Chapter 2) in $CaFe_3O_5$ are shown in **Figure 3.14B**. In the HT phase, the large negative Q_{JT} value (that corresponds to Jahn-Teller compression) observed in the Fe2 site was due to intrinsic distortions within the HT structure. However, the Q_{JT} of the Fe2 site becomes more negative for the CO phase below T_M = 302 K, consistent with the localisation of Fe^{2+} states. High spin Fe^{2+} ions are known to exhibit a Jahn-Teller distortion, due to their degenerate $3d^6$ electronic configuration. The t_{2g} degeneracy is lifted through tetragonal octahedral compression that results in the localisation of the minority spin electron and the gaining of crystal-field stabilisation energy. In keeping with the magnitude of the decrease of the Fe2 Q_{JT} in the CO phase, a comparable increase in Q_{JT} was observed in the Fe2 site in the CA phase, in

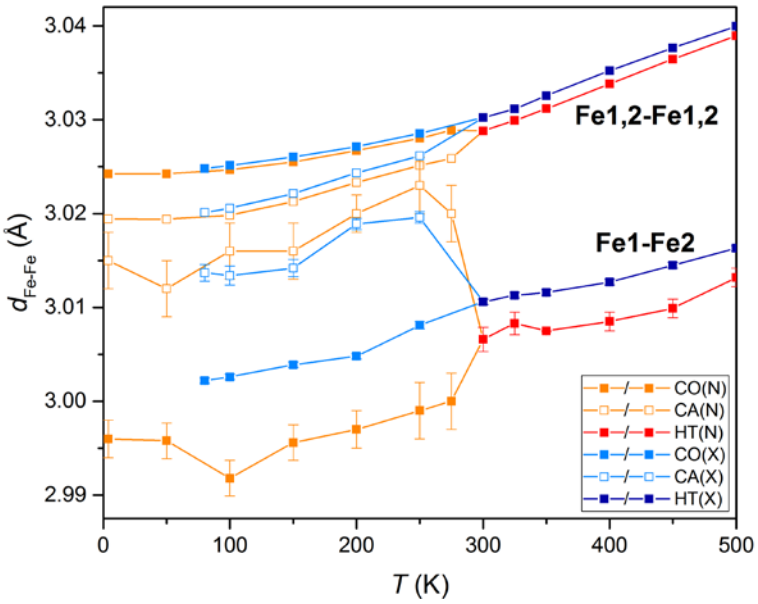

Figure 3.15 The evolution of the Fe1-Fe2 bonding distances with temperature, with the lattice parameter (Fe1,2-Fe1,2) as reference, obtained from neutron (N) and synchrotron x-ray (X) diffraction data.

keeping with the increase in site valence. The Jahn–Teller distortion at the Fe2 site in the CO phase leads to t_{2g} orbital ordering with the minority spin electron localised in the d_{xy} orbital. The d_{xy} orbital of Fe2 is in alignment with the edge sharing Fe1 neighbours, giving rise to the possibility of weak Fe1–Fe2–Fe1 bonding interactions in the CO phase, like that of the trimerons found in Fe_3O_4.[2] The claim of trimeron formation is further supported by the shortening of the distances in the Fe1–Fe2–Fe1 group. The temperature evolution of the Fe1-Fe2 distance between 4 and 500 K, obtained from synchrotron x-ray and neutron diffraction, is shown in **Figure 3.15**. An increase in the Fe1-Fe2 distance was observed in the CA phase in contrast to the decrease in the CO structure. **Figure 3.15** also shows that there is a slight shortening of the Fe1-Fe1 and Fe2-Fe2 distances in the CA structure, which may result in increased interactions between the magnetic cations along the *a* axis.

The magnetic structure of $CaFe_3O_5$ was studied using the neutron diffraction data. Magnetic irreducible representation analysis was carried out using BasIreps[11] for both the CO and CA phases, which have propagation vectors of [½ 0 0] and [0 0 0] respectively (**Table 3.10** and **Table 3.11**). A good fit to the 4 K diffraction data was obtained for each low temperature phase using the models shown in Figure 3.16. The magnetic structure of the CO phase was solved using magnetic operations Γ2ψ6 for Fe1 and Γ4ψ12 for Fe2, and Γ5ψ8 was used for both Fe1 and Fe2 sites (with negative coefficients for Fe2) in the CA phase. Both phases show antiferromagnetic behaviour. The small moment

Table 3.10 Irreducible representations (IrReps) and basis vectors (BV) for Fe1 and Fe2 spin order in the CO phase of $CaFe_3O_5$ at 4 K, with propagation vector [½ 0 0]. The magnetically independent atoms are Fe1 at (½, 0.2650, 0.1104) and Fe2 at (0, 0, 0). The symmetry related positions are generated by the operators 1: (*x*, *y*, *z*), 2: (*x*, *y*, -*z*+½), 3: (*x*, -*y*, *z*+½) and 4: (*x*, -*y*, -*z*). The structure was solved using $\Gamma 2\psi 6$ for Fe1 and $\Gamma 4\psi 12$ for Fe2.

IrReps	Γ_1			Γ_2			Γ_3			Γ_4		
BV	ψ_1	ψ_2	ψ_3	ψ_4	ψ_5	ψ_6	ψ_7	ψ_8	ψ_9	ψ_{10}	ψ_{11}	ψ_{12}
Atoms	m_x	m_y	m_z	m_x	m_y	m_z	m_x	m_y	m_z	m_x	m_y	m_z
Fe1_1	+	+	+	+	+	+	+	+	+	+	+	+
Fe1_2	+	-	-	+	-	-	-	+	+	-	+	+
Fe1_3	-	-	+	+	+	-	-	-	+	+	+	-
Fe1_4	-	+	-	+	-	+	+	-	+	-	+	-
Fe2_1	+			+				+	+		+	+
Fe2_2	-			+				-	+		+	-

Table 3.11 Irreducible representations (IrReps) and basis vectors (BV) for Fe1 and Fe2 spin order in the CA phase of $CaFe_3O_5$ at 4 K, with propagation vector [0 0 0]. The magnetically independent atoms are Fe1 at (0, 0.2669, 0.1113) and Fe2 at (0, 0, 0). The symmetry related positions are generated by the operators 1: (*x*, *y*, *z*), 2: (-*x*, -*y*, *z*+½), 3: (-*x*, *y*, -*z*+½) and 4: (*x*, -*y*, -*z*). The structure was solved using $\Gamma_5\psi_8$ for both Fe1 and Fe2 sites.

IrReps	Γ_1	Γ_2		Γ_3		Γ_4	Γ_5		Γ_6	Γ_7	Γ_8	
BV	ψ_1	ψ_2	ψ_3	ψ_4	ψ_5	ψ_6	ψ_7	ψ_8	ψ_9	ψ_{10}	ψ_{11}	ψ_{12}
Atoms	m_x	m_y	m_z	m_y	m_z	m_x	m_y	m_z	m_x	m_x	m_y	m_z
Fe1_1	+	+	+	+	+	+	+	+	+	+	+	+
Fe1_2	-	-	+	-	+	-	+	-	+	+	+	-
Fe1_3	-	+	-	-	+	+	+	-	-	+	-	+
Fe1_4	+	-	-	+	+	-	+	+	-	+	-	-
Fe2_1	+			+	+		+	+		+		
Fe2_2	-			-	+		+	-		+		

observed in the magnetisation measurements is likely to originate from a small canting of the antiferromagnetic spins that is too small to be refined. **Table 3.12** summarises the ordered moment of the Fe sites in $CaFe_3O_5$ between 4 and 300 K. The magnetic structure of the CO phase shows ferromagnetic alignment of the magnetic spins of the three Fe ions in the *bc* plane, as shown connected with black lines in **Figure 3.16.** This means that the minority spin

Table 3.12 The refined Fe moments in the CO and CA phases of $CaFe_3O_5$ between 4 and 300 K. The moments of the Fe1 and Fe2 sites were constrained to be equal.

Phases	4 K	50 K	100 K	150 K	200 K	250 K	275 K	300 K
CO	4.03(3)	3.98(3)	3.85(3)	3.70(3)	3.39(3)	2.86(4)	2.30(4)	0
CA	3.63(4)	3.68(4)	3.60(4)	3.40(4)	3.28(3)	3.02(3)	2.66(3)	0

electron from the central Fe^{2+} can hop to the two neighbouring Fe^{3+} sites, leading to bonding interactions. Trimeron formation requires Fe^{3+}–Fe^{2+}–Fe^{3+} charge order, orbital order at the central Fe^{2+} in the plane of the three atoms, ferromagnetic alignment of the three magnetic moments and shortening of the Fe–Fe distances within the trimeron. All these conditions are observed in the Fe1–Fe2–Fe1 units in the CO phase, thus confirming the trimeron ordering in the CO phase of $CaFe_3O_5$, however none of these were found in the CA structure. The infinite ferromagnetic chains found along the *a* axis in the CA phase, along with the shortening of Fe1-Fe1 and Fe2-Fe2 distances, suggests possible weak bonding interactions between the Fe ions in each chain. This

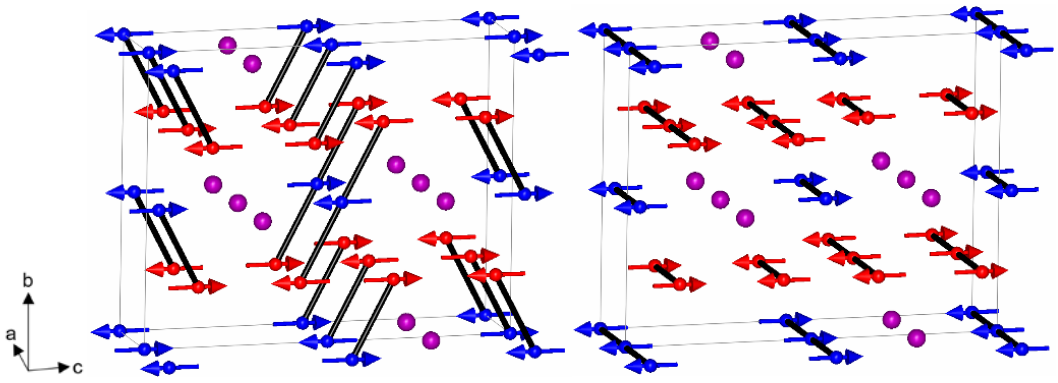

Figure 3.16 Magnetic structures for the two low temperature phases of $CaFe_3O_5$. Fe1/Fe2 spins are shown in red/blue and Ca ions in purple. (Left) Magnetic structure of the charge ordered (CO) phase $CaFe_3O_5$ with propagation vector [½ 0 0], with lines showing ferromagnetic order within trimerons. (Right) Magnetic structure of the charge averaged (CA) phase, with [0 0 0] propagation and lines showing the ferromagnetic chain parallel to the *a* axis.

could be the driving force that forms the charge averaged state, where the minority electrons from the Fe^{2+} are delocalised along the chain and lead to the suppression of $Fe^{2+/3+}$ charge order.

3.2.5. Mössbauer Spectroscopic Study

^{57}Fe Mössbauer spectroscopy confirms the change in valence states and the magnetic properties of the two independent Fe sites in $CaFe_3O_5$ from the HT structure to the two low temperature phases. The measurements were performed in transmission geometry with a constant-acceleration spectrometer using a ^{57}Co/Rh radiation source. The velocity scale and the isomer shift (IS) were determined using the relative values of *α*-Fe at room temperature. A powder sample of $CaFe_3O_5$ (100 mg) was placed into a 1.5 cm diameter coin-shaped capsule, made from a sheet of 40 μm thick ultra-pure aluminium foil. Spectra were recorded at 3.5 K (91 hours), 250 K (95 hours) and 375 K (70 Hours). Each obtained spectrum was fitted with Lorentzian functions using the least-squares method, as shown in **Figure 3.17**. Details of

Table 3.13 Mössbauer parameters for the two iron sites in $CaFe_3O_5$ at 3.5, 250 and 375 K.

T (K)	Phase	Site	IS (mm s^{-1})	HF (T)	QS (mm s^{-1})
3.5	CO	Fe1	0.54(1)	52.4(1)	-0.02(1)
		Fe2	1.02(1)	27.4(1)	-0.003(22)
250	CO	Fe1	0.47(1)	37.6(1)	-0.03(1)
		Fe2	0.96(1)	21.7(1)	-0.05(3)
	CA	Fe1	0.43(1)	43.6(2)	0.03(6)
		Fe2	0.80(1)	25.0(5)	-0.02(18)
375	HT	Fe1	0.43(1)	0	0.30(1)
		Fe2	0.60(1)	0	-0.23(5)

the obtained Mössbauer parameters are summarised in **Table 3.13**. The 375 K data confirm that $CaFe_3O_5$ is spin disordered above T_M = 302 K, with the presence of two doublets in a 2:1 abundance ratio representing the signals from the Fe1 and Fe2 sites respectively. ISs that are similar to the typical values for mixed valence Fe^{2+} and Fe^{3+} octahedral sites[18] were obtained for these two sites.

At 250 K, below the coupled magnetic and phase separation transition temperature, four sets of sextets are observed. These sextets are originated from the four crystallographically independent magnetic iron sites in the CO and CA phases (two Fe sites from each phase). The sextets are assigned to their Fe crystallographic sites using the 2:1 abundance ratio. ISs of 0.47(1)/0.96(1) are observed in the sextet pair with a larger abundancy (62(2) %) for the Fe1/Fe2 sites, confirming a Fe^{3+} valence state at the Fe1 site and a Fe^{2+} valence state at the Fe2 site.[18] More similar IS values were obtained for the other sextet pair with smaller abundancy (38(2) %) from the CA phase. These findings are consistent with the diffraction results detailed in Section 3.2.4, where a $Fe^{2+/3+}$ CO phase with a larger phase fraction coexists with a CA structure at 250 K. The slightly larger difference in the hyperfine magnetic splitting (HF) between the Fe1 and Fe2 sites in the CO phase is likely reflecting the charge distribution of the two sites.

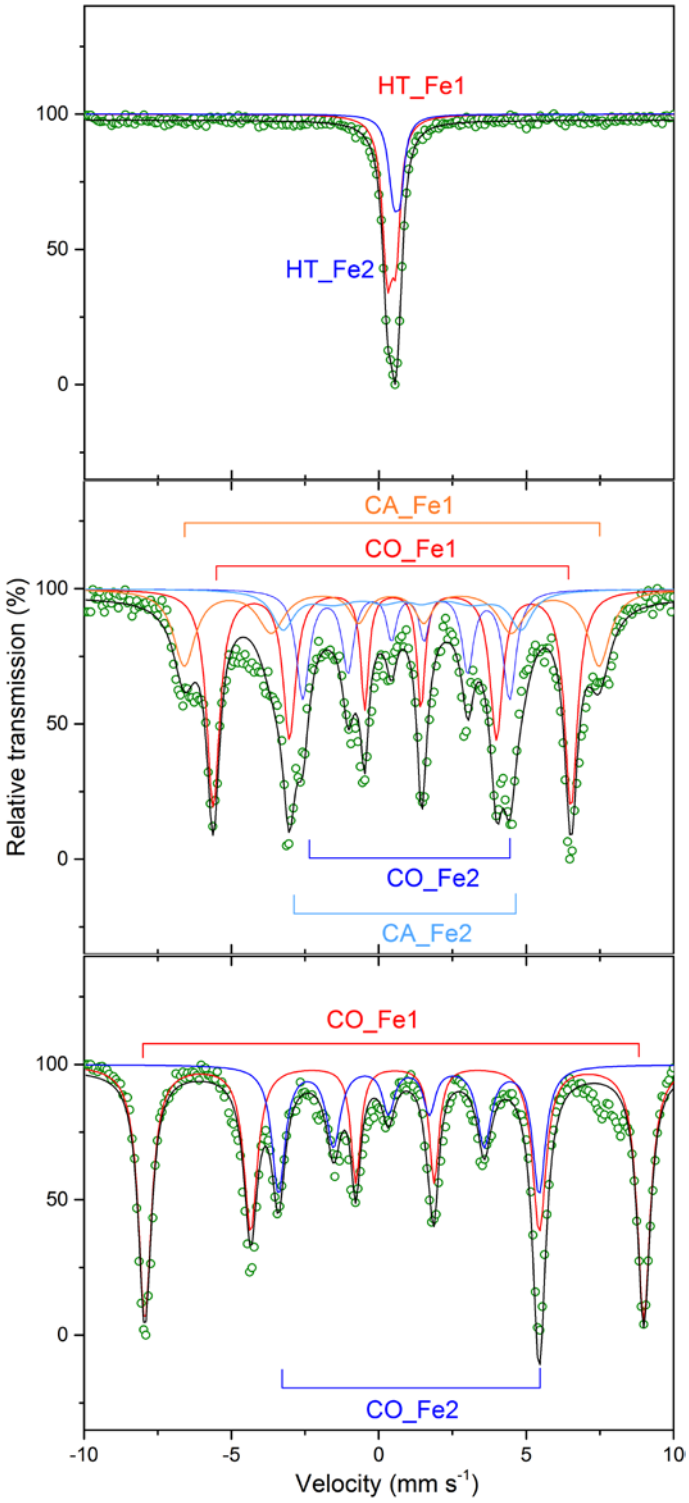

Figure 3.17 Mössbauer spectra of $CaFe_3O_5$ obtained at (top) 375 K, (Middle) 250 K and (bottom) 3.5 K, with green points representing the measured data and black lines showing the summed fit.

In keeping with the phase fraction trends observed in the diffraction data (**Figure 3.13**), the fraction of the CA phase at 3.5 K was a lot smaller than that of the CO phase such that its intensity could not be fitted. Two sextets were fitted to the 3.5 K data in a ratio of 2:1 for the Fe1 and Fe2 sites, with IS values corresponding to Fe^{3+} and Fe^{2+}. Just like in the 250 K data, a large HF is observed for the Fe1 site, consistent with the site valence state. The large associated errors obtained for the quadrupole splitting (QS) for the 3.5 and 250 K data are likely to result from the overlapping of sextets in the spectra.

3.2.6. Electronic Structure Calculations

DFT+U calculations were performed by Dr James Cumby to study the electronic structures of the low temperature phases of $CaFe_3O_5$. The calculations were carried out using CASTEP[19] (v16 and 17), with planewaves (650 eV cutoff) and on-the-fly pseudopotentials, within the Perdew, Burke and Ernzerhof (PBE) approximation to exchange and correlation. Band structures of the CO and CA phases were predicted; the use of small Hubbard *U* energy values results in a metallic charge averaged ground state for both phases, and at large values of *U* give rise to insulating charge ordered states. Values in the range of 2.0 < *U* (eV) < 4.0 simultaneously predict the charge averaged state

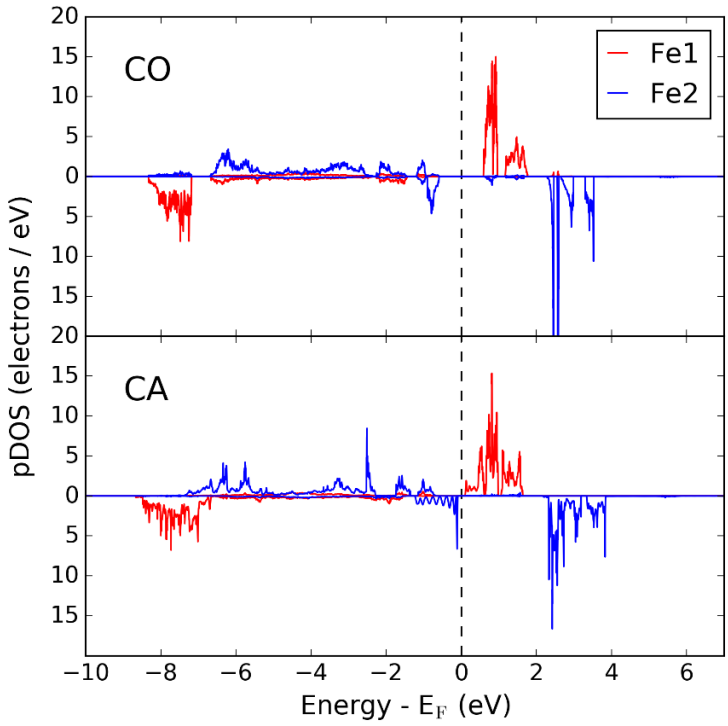

Figure 3.18 Partial density of states (pDOS) for Fe1 and Fe2 d-orbitals (arbitrary spin direction chosen) for the CO and CA phases, calculated with *U* = 3.4 eV.

Table 3.14 Bader charge and volume, Mulliken charge and spin, and total energies of the CO and CA phases of $CaFe_3O_5$ from band structure calculations with U = 3.4 eV.

	CO		CA	
	Fe1	Fe2	Fe1	Fe2
Bader Charge	1.85	1.51	1.83	1.55
Bader Volume ([Bohr radius]^3)	50	59	52	56
Mulliken Charge	1.04	0.86	1.01	0.91
Mulliken Spin (μ_B)	4.08	3.72	4.07	3.65
Total energy (eV)		-46328.588		-46327.893
Free energy (E – TS) (eV)		-46328.858		-46328.048

for the CA structure and the charge ordered state for the CO structure, and hence confirm that this range is realistic for Fe oxides. As illustrated in **Figure 3.18**, a bang gap at E_F = 0 eV is observed in the band structure of the CO phase, indicating an insulating like behaviour, whilst an almost continuous band is found in the CA structure. Band mixing between Fe1 and Fe2 can also be observed in the band structure of the CO phase in the region around -8 eV, which corresponds to the d_{xy} orbital and is attributed to trimeron bonding.

Bader charge analysis and Mulliken population analysis were carried out to investigate the charge, spin moment and the free energy of the iron sites in the CO and CA phases of $CaFe_3O_5$. The calculated Bader and Mulliken parameters at U = 3.4 eV for the two independent iron sites are summarised in **Table 3.14**. The results show a larger difference between the Fe1 and Fe2 charges and spins for the CO phase, compared to the CA, in keeping with the BVS results. The predicted Bader volume was also found to be consistent with the valence of the sites. Similar free energies were calculated for the two low temperature phases of $CaFe_3O_5$, which explains the coexistence of the two

ground states. The smaller free energy for the CO structure is likely the reason of its larger phase fraction observed in the diffraction experiments.

3.3. Conclusion

$CaFe_3O_5$ was synthesised using the ceramic method under ambient pressure conditions. The crystal structure of $CaFe_3O_5$ was confirmed by laboratory powder x-ray diffraction, with results showing an orthorhombic crystal structure in the space group *Cmcm*, just like the Fe analogue of the $M^{2+}Fe_3O_5$ system. The oxygen content of $CaFe_3O_5$ was investigated using TGA and the results confirmed no oxygen deficiency in the structure. Magnetisation studies reveal a magnetic transition at T_M = 302 K, with a small moment of 0.04 μ_B per formula unit of $CaFe_3O_5$ recorded at 230 K. Electrical resistivity measurements show semiconducting behaviour, with a small change in the resistivity slope observed near T_M.

Synchrotron x-ray and neutron diffraction experiments revealed long range electronic phase separation in $CaFe_3O_5$, where a single HT paramagnetic state separates into two distinct low temperature phases with different spin and electronic orders when cooled below 302 K. The two low temperature structures were found to be antiferromagnetically ordered, with different magnetic structures; one of the phases has $Fe^{2+/3+}$ CO associated with trimeron formation whilst the other phase is CA, stabilised by the ferromagnetic Fe chains along the *a* axis. DFT electronic structure calculations confirmed

that the energy difference of the two low temperature structures is very small, allowing them to coexist below 302 K. The different lattice strains of the two phases were likely to be introduced by the weak Fe–Fe bonding that results from the ferromagnetic orders.

The discovery of electronic phase separation coupled to $Fe^{2+/3+}$ charge and spin ordering in $CaFe_3O_5$ has resulted in a publication in Nature Communications (Long range electronic phase separation in $CaFe_3O_5$).[20]

3.4. References

1. E. J. W. Verwey. *Nature* **1939**, *144*, 327–328.

2. M. S. Senn, J. P. Wright, J. P. Attfield. *Nature* **2012**, *481,* 173–176.

3. O. Evrard, B. Malaman, F. Jeannot, *J. Solid State Chem.* **1980,** *35,* 112–119.

4. B. Lavina, P. Dera, E. Kim, Y. Meng, R. T. Downs, P. F. Weck, S. R. Sutton, Y. Zhao. *Proc. Natl. Acad. Sci. USA* **2011,** *108,* 17281–17285.

5. S. V. Ovsyannikov, M. Bykov, E. Bykova, K. Glazyrin, R. S. Manna, A. A. Tsirlin, V. Cerantola, I. Kupenko, A. V. Kurnosov, I. Kantor, A. S. Pakhomova, I. Chuvashova, A. I. Chumakov, R. Rüffer, C. McCammon, L. S. Dubrovinsky. *Nat. Chem.* **2016,** *8,* 501.

6. C. Delacotte, F. Hüe, Y. Bréard, S. Hébert, O. Pérez, V. Caignaert, J. M. Greneche, D. Pelloquin. *Inorg. Chem.* **2014,** *53,* 10171–10177.

7. R. D. Shannon. *Acta Cryst.* **1976,** *A32* 751-767.

8. R. Wan, C. Jia, W. Zhang. *J. Alloys Compd.* **2012,** *544,* 1–5.

9. A. C. Larson, R. B. Von Dreele. *Los. Alamos National Laboratory Report LAUR* **2004,** *748*, 86–748.

10. P. Berastegui, S. Eriksson, S. Hull, F. J. García García, J. Eriksen. *Solid State Sci.* **2004,** *6,* 433–441.

11. J. Rodriguez-Carvajal. *Physica B.* **1993** *192* ,55–69.

12. V. F. *Sears Neutron News* **1992**, *3*, No. 3, 29-37.

13. E. Dagotto, T. Hotta, A. Moreo, *Phys. Rep.* **2001,** *344*,1–153.

14. M. Uehara, S. Mori, C. H. Chen, S. W. Cheong. *Nature* **1999,** *399*, 560–563.

15. Y. Tokura. *Rep. Prog. Phys.* **2006,** *69,* 797–851.

16. J. P. Attfield, *Solid State Sci.* **2006**, *8*, 861–867.

17. I. D. Brown, *J. Appl. Crystallogr.* **1996**, *29*, 479–480.

18. F. Menil. *J. Phys. Chem. Solids*, **1985,** *46*, 763–789.

19. S. J. Clark, M. D. Segall, C. J. Pickard, P. J. Hasnip, M. I. J. Probert, K. Refson, M. C. Payne. *Z. Kristallogr*. **2005,** *220*, 567-570.

20. K. H. Hong, A. M. Arevalo-Lopez, J. Cumby, C. Ritter, J. P. Attfield. *Nat. Commun.* **2018,** *9,* 2975.

Chapter 4. High-Pressure Synthesis and Properties of $MnFe_3O_5$

4.1. Introduction

The "parent" of the MFe_3O_5 family, Fe_4O_5, was discovered using high-pressure solid-state methods,[1] as pressure is required to stabilise small cations, such as Fe^{2+} in the case of Fe_4O_5, at the triangular prismatic site in the *Cmcm* $CaFe_3O_5$-type structure, whilst $CaFe_3O_5$, with larger Ca^{2+} cations can be synthesised under ambient pressure, as described in Chapter 3. This chapter details the synthesis of $MnFe_3O_5$, a novel analogue of the MFe_3O_5 family (with $M = Mn^{2+}$), that is isostructural to Fe_4O_5. With the similarity in the ionic radius between high spin Mn^{2+} (0.83 Å) and Fe^{2+} (0.78 Å),[2] it was predicted that $MnFe_3O_5$ could be made using similar synthetic conditions as in Fe_4O_5, under high-temperature and pressure conditions.[1] Furthermore, high-pressure is known to stabilise Mn^{2+} in unusual coordination environments, for example, at the A cation sites of the ABO_3 perovskite structure in $MnVO_3$.[3]

In this chapter, the physical properties and structural behaviour of $MnFe_3O_5$ were explored using electrical and magnetic property measurement techniques, accompanied by x-ray and neutron diffraction, across a temperature range of 5 to 400 K. $MnFe_3O_5$ is a mixed valence system that consists of $Fe^{2+/3+}$, along with Mn^{2+}. The similar ionic radius and electron density between Fe^{2+} and Mn^{2+} suggested that $MnFe_3O_5$ would exhibit complex charge, spin and orbital ordering, like that of Fe_4O_5, and other closely

related materials as described in Chapter 1.[4,5,6] On the other hand, Mn^{2+} has a d^5 electronic configuration, which does not display the Jahn-Teller effect due to its non-degenerate electronic configuration. Therefore, the environment of the triangular prismatic site in $MnFe_3O_5$ would be different from the Fe analogue, which may result in a different Fe charge distribution. In addition, high spin Mn^{2+} does not have a minority-spin electron that can interact with neighbouring cations, therefore the formation of orbital molecules at the triangular prismatic sites, like that of Fe_4O_5, is not expected.[4]

4.2. Experimental and Results

4.2.1. Synthesis of $MnFe_3O_5$

$MnFe_3O_5$ was synthesised using high-pressure and high-temperature solid-state synthesis techniques, as described in Section 2.1.2. Powders of MnO and Fe_3O_4 in a 1:1 ratio were ground together using a mortar and pestle to form a homogeneous mixture. The powder mixture was then packed into a Pt capsule and loaded inside the two-stage Walker-type module. The synthesis conditions were explored, with a fixed starting pressure of 10 GPa and a temperature range between 1200 and 1300 °C tested. The duration of heating was set to 20 minutes. A total of thirteen batches of $MnFe_3O_5$ were made and the synthesis records are summarised in **Table 4.1**. Phase confirmation was carried out using powder x-ray diffraction. Diffraction patterns of each batch of the high-pressure products were collected using a Bruker D2 Phaser

Table 4.1 Synthesis conditions of each batch of the $MnFe_3O_5$ sample.

Sample	*P* (GPa)	Set *T* (°C)	Experiment notes	Phase(s)
#1	10	1250	Blowout with pressure dropped by 30 tons.	$MnFe_3O_5$ + Pt
#2	10	1250	Blowout with pressure dropped by 12.5 tons.	$MnFe_3O_5$ + Pt + unidentified impurities
#3	10	1250		$MnFe_3O_5$ + Pt + unidentified impurities
#4	10	1300	sample melted	-
#5	10	1250		$MnFe_3O_5$ + Pt + unidentified impurities
#6	10	1200		$MnFe_3O_5$ + Pt
#7	10	1200	Blowout with pressure dropped by 40 tons.	$MnFe_3O_5$ + Pt + unidentified impurities
#8	10	-	Heating control failed to start up.	$MnFe_3O_5$ + Pt + unidentified impurities
#9	10	1200		$MnFe_3O_5$ + Pt
#10	10	1250		$MnFe_3O_5$ + Pt + unidentified impurities
#11	10	1200		$MnFe_3O_5$ + Pt
#12	10	1200		$MnFe_3O_5$ + Pt
#13	10	1200		$MnFe_3O_5$ + Pt

diffractometer using a Cu K_α radiation source (15 minutes scans of $5° \leq 2\theta \leq 70°$). A stacked plot of the diffraction patterns of all the synthesised samples is shown in **Figure 4.1**. Each of the collected patterns was Rietveld fitted using GSAS for phase confirmation and initial characterisation.[7] The preferred orientation of the sample in the flat plate geometry of the D2 diffractometer is accounted for using the Modified March's function.

Rietveld refinement to the powder x-ray diffraction pattern of sample #1 (**Figure 4.2**) shows the synthesised $MnFe_3O_5$ sample to be consistent with the *M*Fe_3O_5 structure type. The Bragg peaks from the collected x-ray data were

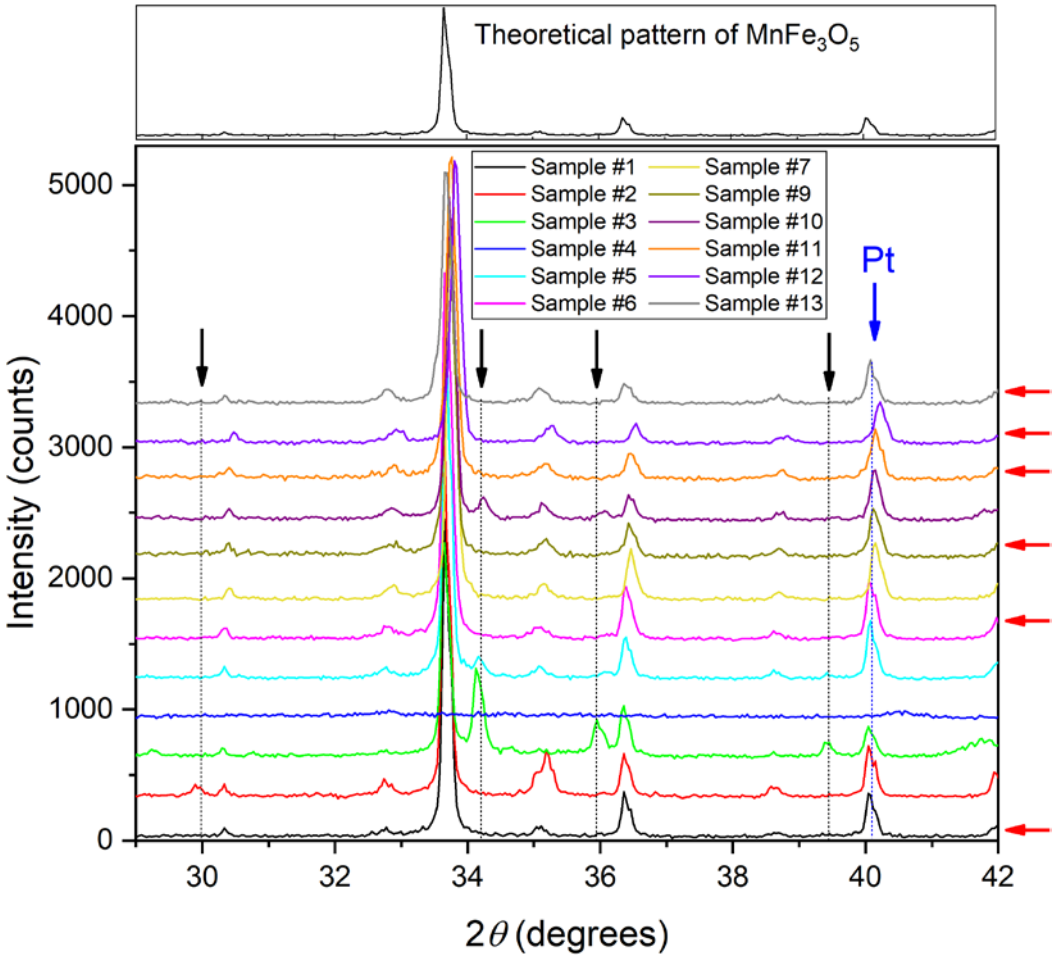

Figure 4.1 Diffraction patterns collected from samples of $MnFe_3O_5$, with a theoretic pattern from a pure $MnFe_3O_5$ sample shown above. Black arrows indicate the impurity reflections from several unidentified high-temperature high-pressure phases and the presence of Pt, overlapping with reflections from $MnFe_3O_5$ is indicated by the blue arrow. No trace of impurity (except for the small amount of Pt) were found in sample #1, #6, #9, #11-13 (indicated with red arrows).

indexed with a unit cell of *Cmcm*, isostructural to Fe_4O_5, with orthorhombic lattice parameters of a = 2.9137(1) Å, b = 9.8565(7) Å, and c = 12.6143(6) Å, with a cell volume of 362.52(4) $Å^3$ at room temperature. The lattice parameters are found to be larger than those for Fe_4O_5,[1] consistent with the relative ionic radii of Mn^{2+} and Fe^{2+}. A small amount of platinum (1.1(1) % by weight) is also observed in the diffraction pattern. The platinum originated from the capsule

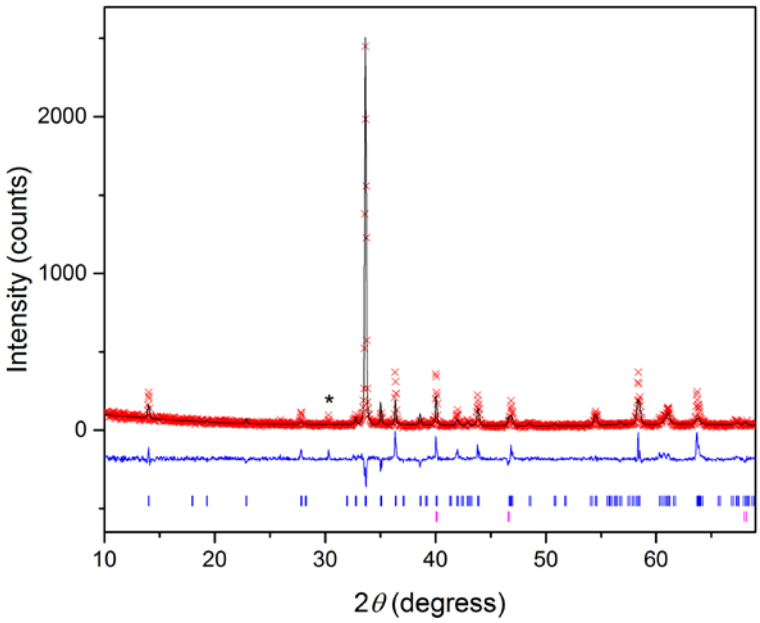

Figure 4.2 Rietveld refinement of sample #1 powder x-ray diffraction data obtained at room temperature using the D2 diffractometer, with upper tick marks representing the $MnFe_3O_5$ phase and lower as Pt. (χ^2 = 2.86, R_{wp} = 21.96 %, R_p = 16.54%) Asterisk marks the observable K_β reflection.

used in the high-pressure synthesis. However, no trace of starting materials or other impurities is observed.

Heating of the sample was carried out using graphite heaters, with the temperature controlled through an applied current through the heaters. Sample #1 was prepared with a set temperature of 1250 °C. During the process of heating, one of the tungsten carbide anvils in the press broke, which led to a sudden drop in pressure by 30 tons. As a consequence of that, the pressure and temperature of the sample is lower than the set point and, in this case, coincidentally results in a phase pure sample. However, using the same reaction temperature for sample #2, #3 and #5 led to the formation of several unidentified high-pressure impurities, as shown **Figure 4.1**, with impurity reflections indicated by black arrows. It is also noted that the reaction mixture

melted when heated above 1250 °C, as observed in sample #4 with a set temperature of 1300 °C. By lowering the heating temperature to 1200 °C, a phase pure product of $MnFe_3O_5$ can be obtained. There are other factors that can affect the synthesis conditions, such as the quality of the graphite used for heating and the alignment of the anvils in the press, that could lead to the sample being over/under-heated and -pressurised and result in impurities in the final product. This was observed in sample #10, where a higher than expected electrical current was passed to the heaters and led to an increase in temperature by 50 °C and hence the formation of impurities.

4.2.2. Property Measurements

Magnetometry measurements were carried out on sample #1 (11.4 mg) with a Quantum Design MPMS XL Superconducting Quantum Interference Device (SQUID) magnetometer. The magnetic susceptibility was recorded on warming in zero field cooled (ZFC) and field cooled (FC) conditions between 2 and 400 K with an applied magnetic field of 5000 Oe. The temperature evolution of the magnetic susceptibility of $MnFe_3O_5$ (**Figure 4.4**) shows a susceptibility maximum at 350 K, indicating an antiferromagnetic transition. A broad magnetic susceptibility upturn observed below 150 K evidences a ferro- or ferri-magnetic transition. The divergence between the zero-field cooled and field cooled susceptibilities at ~60 K marks a further magnetic ordering at low temperature. The results are in agreement with those reported on Fe_4O_5, with T_N = 320 K, charge ordering at 150 K and spin rearrangement at 85 K.[4]

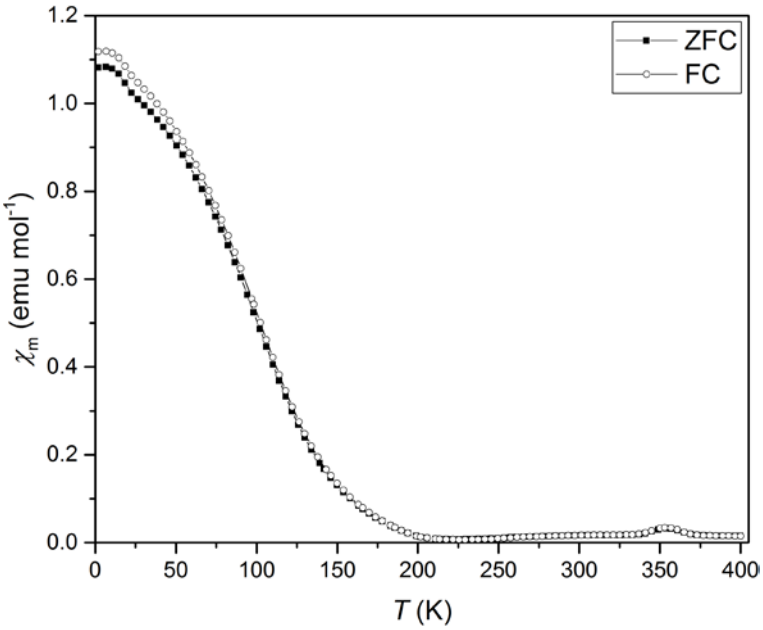

Figure 4.4 The magnetic susceptibility of $MnFe_3O_5$ measured in zero field cooled (ZFC) and field cooled (FC) conditions between 2 and 400 K.

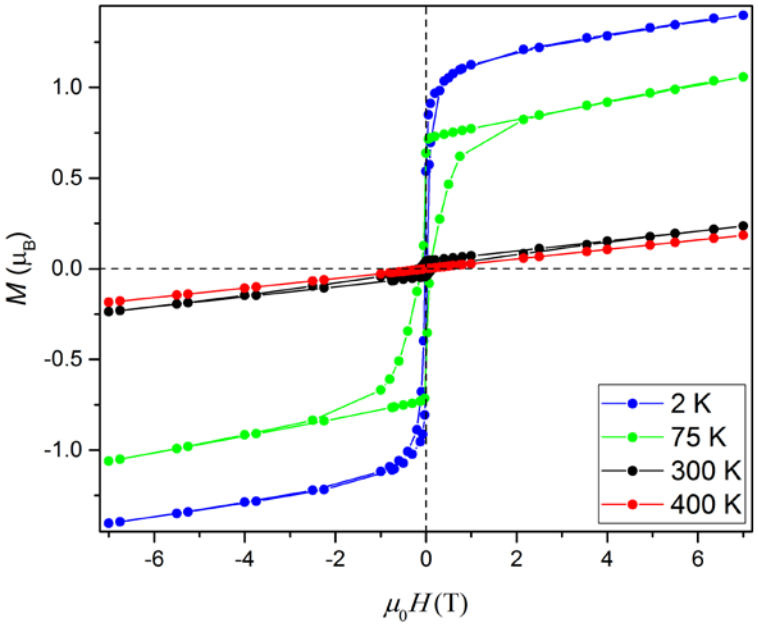

Figure 4.3 Magnetisation versus field hysteresis loops (-6.5 ≤ $\mu_0 H$ (T) ≤ 6.5) recorded at 2, 75, 300 and 400 K.

Magnetisation versus field hysteresis loops were taken on the same sample at 2, 75, 300 and 400 K (-6.5 ≤ $\mu_0 H$ (T) ≤ 6.5), as shown in **Figure 4.3**. The 400 K measurement indicates paramagnetic behaviour, with the magnetisation of the sample increasing linearly with the external field. A small moment of 0.025 μ_B per $MnFe_3O_5$ formula unit, with a coercivity of 0.18 T, is observed at 300 K. The weak ferromagnetic component observed here could be due to traces of a magnetic impurity such as Fe_3O_4, below the limit of x-ray detection. The 75 K data confirms the change to ferrimagnetism when cooled below 300 K, with a saturated magnetic moment of 0.72 μ_B per formula unit and a coercivity of 0.10 T. The increase in the saturated moment observed at 2 K confirms the low temperature magnetic transition at 60 K found in the magnetic susceptibility versus temperature measurements. The 2 K magnetisation results show a moment of 1.12 μ_B per formula unit and a small coercivity of 0.03 T.

The electrical resistivity of $MnFe_3O_5$ was studied using a Quantum Design Physical Property Measurement System (PPMS). A polycrystalline pellet from $MnFe_3O_5$ sample #13, with a cross section of 0.0001 cm^2 and a length of 0.045 cm, was used. The measurements were carried out on warming and the results show that $MnFe_3O_5$ displays semiconducting behaviour, with the resistivity increasing when cooled from 380 to 260 K (**Figure 4.5**). The resistance of the sample was too great to be measured below 260 K. The insert of Figure 4.5 shows two linear regions in the plot of log(resistivity) versus inverse temperature, with a change of slope near 285 K. Fitting of the Arrhenius equation to the two linear regions gives the activation energy E_a as 210 meV

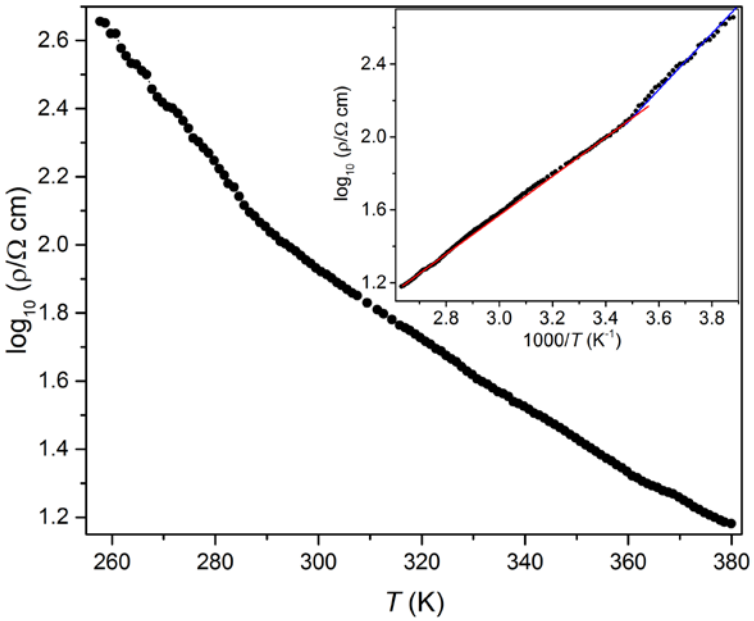

Figure 4.5 Logarithmic plot of the electrical resistivity of $MnFe_3O_5$ measured between 260 and 380 K, with inset showing the plot against reciprocal temperature. The red and blue lines show the Arrhenius fits above and below 285 K.

above and 280 meV below the 285 K crossover. This temperature does not match any of the observed magnetic transition temperatures and may correspond to a change from defect-dominated to intrinsic bandgap conduction.

4.2.3. Synchrotron X-ray Diffraction Study of $MnFe_3O_5$

High resolution powder synchrotron x-ray diffraction data were collected on sample #1 at the ID22 beamline of the ESRF. The synchrotron x-ray incident wavelength was calibrated to 0.39994 Å. The sample was packed into a glass capillary with an outer diameter of 0.3 mm. Diffraction data were collected on warming, using a liquid helium cryostat system between 13 and 120 K and using an Oxford Cryostream system between 90 and 400 K. The obtained

diffraction patterns were Rietveld-fitted using the FullProf Suite.[8] The peak shape was refined using a pseudo-Voigt profile, as described in **Section 2.2.4**. The background of the diffraction patterns is fitted using linear interpolation between a set of background points with refinable heights. **Figure 4.6** shows the refined diffraction pattern at 300 K, lattice parameters of a = 2.92018(1) Å, b = 9.87800(4) Å, and c = 12.64108(6) Å, and a cell volume of 364.639(3) Å^3. The small deviation from the lattice parameter obtained from the D2 diffractometer could be resulted from the systematic errors associated with the D2 diffractometer and the difference in the sample environment. The intensity of some of the diffraction peaks in the synchrotron data are different from those obtained from the D2 diffractometer. This is likely due to the effect of preferred orientation from the different diffractometer geometry, as described in Section 4.2.1.

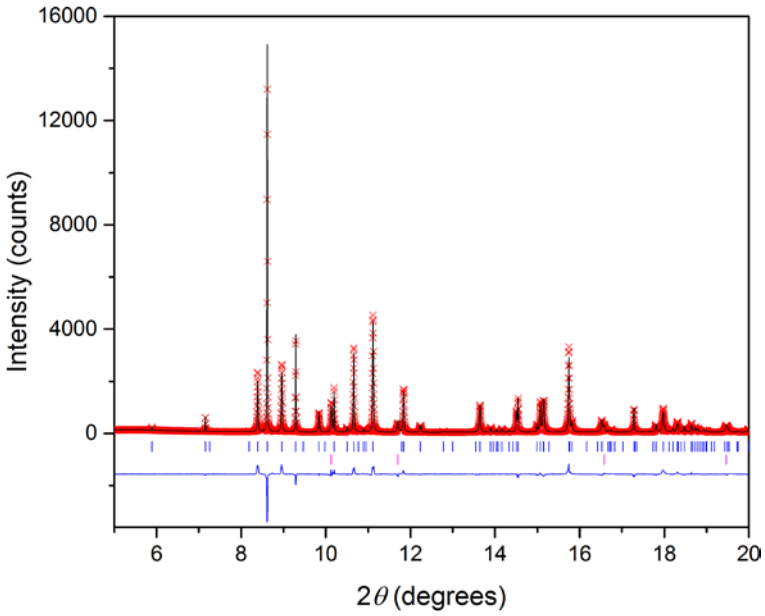

Figure 4.6 Rietveld fit to synchrotron powder diffraction profiles for $MnFe_3O_5$ at 300 K, with upper tick marks indicating the $MnFe_3O_5$ phase and lower for residual platinum (1.67(1) % by volume) from the sample container used during high-pressure-temperature synthesis. (χ^2 = 5.35, R_{wp} = 9.66 % and R_p = 8.58 %)

The change in the lattice parameters and cell volume of $MnFe_3O_5$ between 13 and 400 K are shown in **Figure 4.7**. Between 90 and 120 K the plot shows the overlapping of data collected with the liquid helium cryostat system and Oxford cryostream. Anisotropic thermal expansion is observed upon cooling below 350 K, with the *a* and *c* components contracting whilst *b* expands. The onset of the anisotropic behaviour is close to the 350 K magnetic ordering transition, and thus the lattice distortion appears to be magnetostrictive. Another discontinuity in the lattice parameters and volume is found at 60 K, where the divergence between the zero-field cooled and field cooled magnetisation measurements was observed (**Figure 4.4**). However, no long-range structural distortion is found down to 13 K. The cell volume of $MnFe_3O_5$ decreases with temperature, and changes in the slope of the cell volume are also observed around 350 and 60 K. Details of the refined crystal structure model of $MnFe_3O_5$ from synchrotron x-ray diffraction patterns obtained between 13 and 400 K are summarised in **Table 4.2** to **Table 4.5**. The refined thermal parameters from the synchrotron data were found to be smaller than usual, which are likely due to the absorption of x-rays by the sample. This also resulted in some unrealistic thermal factors (negative parameters) for the cation and anion sites, hence the thermal factors of all the atoms were constrained to be refined together to obtain a coefficient that accounts for their thermal.

The refined metal-oxygen and metal-metal bond distances at 13 and 400 K are shown in **Table 4.6**. The average Mn–O bond length was found to be greater than that for the two Fe sites, suggesting that the former site is occupied principally by Mn^{2+}, as the ionic radii of high spin Mn^{2+} (0.83 Å) is larger than that of Fe^{2+} (0.78 Å) and Fe^{3+} (0.65 Å).[9] However, it was not possible to refine the Fe/Mn populations of the cation sites directly using the x-ray data given the very similar electron densities of the two elements.

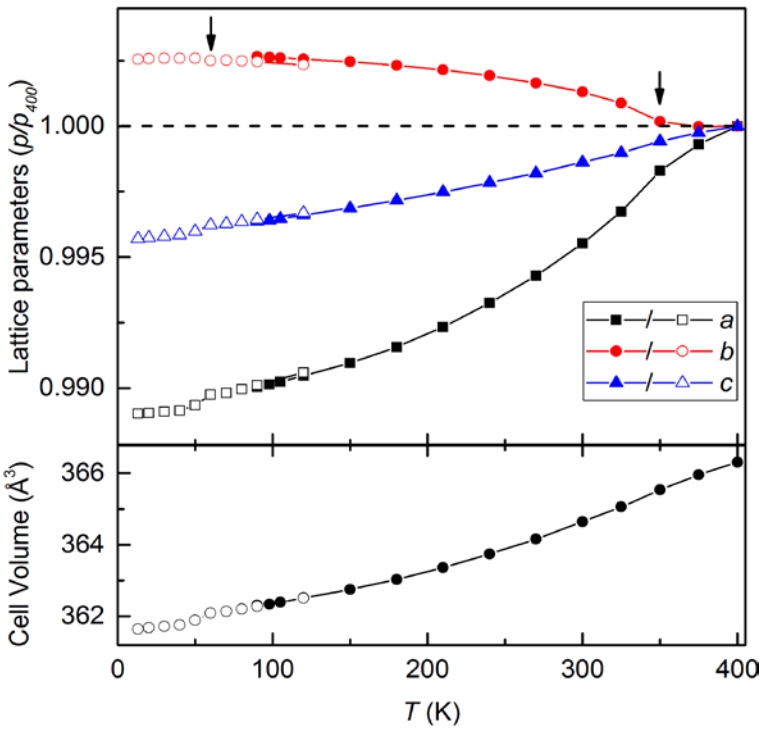

Figure 4.7 Changes in the lattice parameters and cell volume of $MnFe_3O_5$ between 13 and 400 K, using values obtained from refined powder synchrotron x-ray diffraction patterns. Data were obtained using a helium cryostat (opened symbols) for the low temperature region and an Oxford cryostream between 90 and 400 K (closed symbol). Arrows indicate the anisotropic thermal expansion at 350 K and discontinuities in the lattice parameters at 60 K.

Table 4.2 Refined structural parameters of $MnFe_3O_5$ in space group *Cmcm* from synchrotron x-ray diffraction data between 13 and 50 K using a liquid helium cryostat system. Estimated standard deviations in independent variables are shown in parentheses. Fe1 atoms are located at (½, *y*, *z*), Fe2 atoms with site symmetry 4*a* are located at (0, 0, 0), Mn atoms at (0, *y*, ¼), O1 atoms at (½, *y*, ¼), O2 atoms at (0, *y*, z) and O3 atoms at (0, *y*, *z*). * The thermal parameters for all the atoms are constrained to be refined together.

			T / K	13	20	30	40	50
Cell			*a* (Å)	2.90111(2)	2.90121(2)	2.90134(2)	2.90148(2)	2.90208(2)
			b (Å)	9.89021(4)	9.89049(4)	9.89059(4)	9.89061(4)	9.89070(4)
			c (Å)	12.60411(6)	12.60471(6)	12.60531(6)	12.60597(6)	12.60782(6)
			V (Å^3)	361.645(3)	361.684(3)	361.721(3)	361.758(3)	361.890(3)
Fe1	8*f*		*y*	0.23709(5)	0.23714(5)	0.23717(5)	0.23713(5)	0.23717(5)
			z	0.11527(4)	0.11527(4)	0.11527(4)	0.11533(4)	0.11834(4)
Mn	4*c*		*y*	0.48627(7)	0.48627(7)	0.48631(7)	0.48627(7)	0.48631(8)
O1	4*c*		*y*	0.32523(32)	0.32567(32)	0.32521(32)	0.32510(32)	0.32450(34)
O2	8*f*		*y*	0.35916(24)	0.35937(24)	0.35930(24)	0.35917(24)	0.35913(25)
			z	0.04269(18)	0.04259(19)	0.04260(18)	0.04260(18)	0.04288(19)
O3	8*f*		*y*	0.09164(25)	0.09163(25)	0.09171(25)	0.09177(25)	0.09260(26)
			z	0.13989(16)	0.13981(16)	0.14002(16)	0.13976(16)	0.13938(17)
			B_{iso} / Å^2*	0.054(7)	0.006(6)	0.008(6)	0.013(6)	0.103(7)
			R_p / %	13.2	13.3	13.5	13.4	14.2
			R_{wp} / %	15.6	15.6	15.6	15.6	16.4
			χ^2	13.3	8.1	8.0	7.9	7.97

Table 4.3 Refined structural parameters of $MnFe_3O_5$ in space group *Cmcm* from synchrotron x-ray diffraction data between 60 and 120 K using a liquid helium cryostat system. Estimated standard deviations in independent variables are shown in parentheses. Fe1 atoms are located at (½, *y*, *z*), Fe2 atoms with site symmetry 4*a* are located at (0, 0, 0), Mn atoms at (0, *y*, ¼), O1 atoms at (½, *y*, ¼), O2 atoms at (0, *y*, z) and O3 atoms at (0, *y*, *z*). * The thermal parameters for all the atoms are constrained to be refined together.

			T / K	60	70	80	90	120
Cell			*a* (Å)	2.90324(2)	2.90346(2)	2.90387(2)	2.90431(2)	2.90573(2)
			b (Å)	9.88980(4)	9.88988(4)	9.88964(4)	9.88935(4)	9.88817(4)
			c (Å)	12.61082(6)	12.61131(6)	12.61227(6)	12.61344(6)	12.61656(7)
			V (Å^3)	362.088(3)	362.132(3)	362.202	362.280(3)	362.504(3)
Fe1	8*f*	*y*		0.23724(5)	0.23724(5)	0.23726(5)	0.23727(5)	0.23738(6)
		z		0.11530(4)	0.11531(4)	0.11517(4)	0.11522(4)	0.11513(4)
Mn	4*c*	*y*		0.48617(8)	0.48616(7)	0.48620(8)	0.48627(8)	0.48616(8)
O1	4*c*	*y*		0.32486(33)	0.32500(33)	0.32499(33)	0.32501(33)	0.32559(34)
O2	8*f*	*y*		0.35926(24)	0.35914(24)	0.35891(24)	0.35904(24)	0.35838(25)
		z		0.04328(18)	0.04352(18)	0.04337(18)	0.04355(18)	0.04382(19)
O3	8*f*	*y*		0.09307(25)	0.09311(25)	0.09369(25)	0.09333(25)	0.09313(26)
		z		0.13950(16)	0.13967(16)	0.13953(16)	0.13934(16)	0.13937(16)
			B_{iso} / Å^2*	0.034(7)	0.032(7)	0.056(7)	0.040(7)	0.076(8)
			R_p / %	13.7	13.5	13.6	13.1	13.3
			R_{wp} / %	15.7	15.6	15.8	15.5	15.9
			χ^2	7.64	7.43	7.53	11.5	9.94

Table 4.4 Refined structural parameters of $MnFe_3O_5$ in space group *Cmcm* from synchrotron x-ray diffraction data between 90 and 210 K using an Oxford Cryostream system. Estimated standard deviations in independent variables are shown in parentheses. Fe1 atoms are located at (½, *y*, *z*), Fe2 atoms with site symmetry 4*a* are located at (0, 0, 0), Mn atoms at (0, *y*, ¼), O1 atoms at (½, *y*, ¼), O2 atoms at (0, *y*, *z*) and O3 atoms at (0, *y*, *z*). * The thermal parameters for all the atoms are constrained to be refined together.

			T / K	90	98	105	120	150	180	210
Cell			*a* (Å)	2.90413(2)	2.90439(2)	2.90470(2)	2.90539(2)	2.90681(2)	2.90859(2)	2.91083(2)
			b (Å)	9.89136(5)	9.89098(5)	9.89077(6)	9.89039(6)	9.88937(6)	9.88801(6)	9.88629(6)
			c (Å)	12.61259(7)	12.61298(8)	12.61382(8)	12.61559(8)	12.61894(8)	12.62262(8)	12.62674(8)
			V (Å^3)	362.307(4)	362.336(4)	362.392(4)	362.514(4)	362.751(4)	363.028(4)	363.363(4)
Fe1	8*f*		*y*	0.23668(7)	0.23641(7)	0.23650(7)	0.23648(7)	0.23656(7)	0.23657(7)	0.23672(8)
			z	0.11522(5)	0.11526(5)	0.11524(5)	0.11528(5)	0.11525(5)	0.11520(5)	0.11515(5)
Mn	4*c*		*y*	0.48655(10)	0.48660(10)	0.48657(10)	0.48664(11)	0.48653(11)	0.48650(11)	0.48660(11)
O1	4*c*		*y*	0.32142(41)	0.32173(42)	0.32136(43)	0.32146(43)	0.32135(43)	0.32129(44)	0.32130(44)
O2	8*f*		*y*	0.35691(31)	0.35636(31)	0.35611(32)	0.35627(32)	0.35592(32)	0.35539(32)	0.35540(33)
			z	0.04536(23)	0.04524(24)	0.04521(24)	0.04539(24)	0.04525(24)	0.04499(25)	0.04489(25)
O3	8*f*		*y*	0.09230(32)	0.09249(32)	0.09251(33)	0.09226(33)	0.09236(33)	0.09241(33)	0.09233(34)
			z	0.14017(21)	0.13936(21)	0.13940(21)	0.13946(22)	0.13949(22)	0.13942(22)	0.13941(22)
			B_{iso} / Å^2*	0.035(9)	0.046(10)	0.055(10)	0.067(10)	0.082(10)	0.123(11)	0.142(11)
			R_p / %	12.0	12.3	12.7	12.7	12.6	12.8	13.0
			R_{wp} / %	13.8	14.2	14.5	14.6	14.6	14.8	15.0
			χ^2	16.3	15.7	17.1	17.6	17.4	17.6	17.6

Table 4.5 Refined structural parameters of $MnFe_3O_5$ in space group *Cmcm* from synchrotron x-ray diffraction data between 240 and 400 K using an Oxford Cryostream system. Estimated standard deviations in independent variables are shown in parentheses. Fe1 atoms are located at (½, *y*, *z*), Fe2 atoms with site symmetry 4*a* are located at (0, 0, 0), Mn atoms at (0, *y*, ¼), O1 atoms at (½, *y*, ¼), O2 atoms at (0, *y*, *z*) and O3 atoms at (0, *y*, *z*). * The thermal parameters for all the atoms are constrained to be refined together.

			T / K	240	270	300	325	350	375	400
Cell			*a* (Å)	2.91353(2)	2.91657(2)	2.92018 (1)	2.92375(2)	2.92831(2)	2.93129(2)	2.93332(2)
			b (Å)	9.88410(6)	9.88133(6)	9.89800(4)	9.87375(7)	9.86680(7)	9.86498(7)	9.86510(7)
			c (Å)	12.63118(8)	12.63581(8)	12.64108(6)	12.64570(9)	12.65129(9)	12.65535(9)	12.65854(9)
			V (Å^3)	363.747(4)	364.158(4)	364.639(3)	365.061(4)	365.535(5)	365.957(5)	366.307(5)
Fe1	8*f*		*y*	0.23698(8)	0.23732(8)	0.23754(5)	0.23762(8)	0.23788(9)	0.23788(9)	0.23790(9)
			z	0.11513(5)	0.11511(5)	0.11511(3)	0.11505(6)	0.11504(6)	0.11491(6)	0.11496(6)
Mn	4*c*		*y*	0.48662(11)	0.48674(11)	0.48678(7)	0.48691(11)	0.48686(12)	0.48672(12)	0.48660(12)
O1	4*c*		*y*	0.32194(44)	0.32245(44)	0.32656(30)	0.32245(46)	0.32293(49)	0.32221(49)	0.32224(50)
O2	8*f*		*y*	0.35549(32)	0.35519(32)	0.35677(22)	0.35508(33)	0.35485(35)	0.35513(36)	0.35504(36)
			z	0.04495(25)	0.04495(25)	0.04664(17)	0.04466(26)	0.04482(27)	0.04503(27)	0.04485(27)
O3	8*f*		*y*	0.09183(34)	0.09131(34)	0.09357(23)	0.09117(35)	0.09167(37)	0.09177(37)	0.09191(37)
			z	0.13914(22)	0.13908(22)	0.13903(14)	0.13858(22)	0.13866(23)	0.13834(23)	0.13836(23)
			B_{iso} / Å^2*	0.035(9)	0.046(10)	0.192(11)	0.217(11)	0.304(7)	0.281(12)	0.380(13)
			R_p / %	12.0	12.3	13.0	13.1	7.99	13.4	13.9
			R_{wp} / %	13.8	14.2	15.0	14.7	9.54	15.1	15.8
			χ^2	16.3	15.7	17.0	16.1	5.84	14.7	16.4

Table 4.6 Metal-oxygen and metal-metal bond distances (Å) obtained from refined synchrotron x-ray diffraction results, with mean values <> shown for $MnFe_3O_5$ at 400 K and 13 K.

Bond	Distance	
	400 K	13 K
Mn1-O1 (x 2)	2.187(4)	2.154(3)
Mn1-O3 (x 4)	2.286(2)	2.262(2)
<Mn1-O>	2.253(3)	2.226(1)
Fe1-O1	1.901(2)	1.909(2)
Fe1-O2	2.220(4)	2.207(3)
Fe1-O2 (x 2)	2.067(3)	2.098(2)
Fe1-O3 (x 2)	2.077(3)	2.067(3)
<Fe1-O>	2.068(3)	2.074(1)
Fe2-O2 (x 4)	2.126(3)	2.082(2)
Fe2-O3 (x 2)	1.973(3)	1.982(3)
<Fe2-O>	2.075(3)	2.046(1)
Fe1-Fe1, Fe2-Fe2, Mn-Mn	2.933(1)	2.901(1)
Fe1-Fe2 (x2)	2.967(1)	2.979(1)
Fe1-Fe2(x 4)	3.127(1)	3.117(1)

4.2.4. Powder Neutron Diffraction study of $MnFe_3O_5$

Samples #9 and #11-13 were combined and ground to give a sample size of approximately 50 mg. The combined sample was packed into a vanadium can and high-resolution time-of-flight neutron diffraction data were collected at temperatures in the order of 300, 400, 5, 75 and 150 K on the WISH beamline at the ISIS facility, using a closed-cycle refrigerator (CCR) to control the temperature of the sample. The beam current for each temperature step was 88 μA (300 K), 117 μA (400 K), 148 μA (5 K), 110 μA (75 K) and 110 μA (150 K). Rietveld refinement of the structure using the obtained diffraction data was carried out using FullProf.[8] The peak shape was refined using the Ikeda-Carpenter function, as described in Section 2.2.4. The background of the diffraction patterns is fitted using linear interpolation between a set of background points with refinable heights.

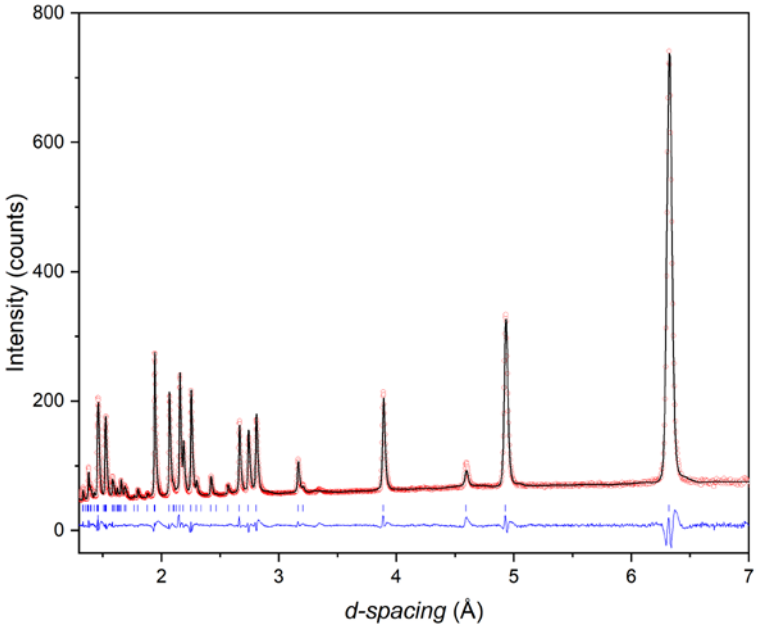

Figure 4.8 Rietveld refinement against the powder neutron diffraction data obtained from banks 3 and 8 at 400 K. (χ^2 = 12.4, R_{wp} = 9.5 % and R_p = 10.9%)

Rietveld fit to the 400 K diffraction patterns (**Figure 4.8**) confirmed the purity of the sample and the orthorhombic structure in the space group *Cmcm*. Occupancy refinements were carried out for the three cation sites in $MnFe_3O_5$, making use of the high neutron coherent scattering length contrast between Mn (-3.73 fm) and Fe (9.45 fm).[10] The results show that the octahedral sites were occupied exclusively by Fe, and that the trigonal prismatic site was predominantly Mn with 6.3(4) % substitution by Fe. Hence $MnFe_3O_5$ is Mn/Fe ordered and the overall $Mn_{0.94}Fe_{3.06}O_5$ composition of the present sample is close to the ideal stoichiometry. The small disordering of Fe/Mn in the triangular prismatic site could result from the similar ionic radii of high spin Fe^{2+} and Mn^{2+}. The Mn/Fe occupancy of the trigonal prismatic site was fixed to the refined 400 K values in the refinement profiles of patterns obtained below 400 K.

Crystal structure refinements confirmed that the unit cell symmetry remained orthorhombic *Cmcm* at all temperatures, consistent with the synchrotron x-ray results. Anisotropic thermal expansion in the lattice parameters, as reported in the synchrotron x-ray study, is also observed here. Details of the refined crystal structure model of $MnFe_3O_5$ from neutron diffraction are summarised in **Table 4.7**. Refinements of the thermal parameters of the atomic sites at 5 K led to some unrealistic values (negative parameters) for some of the sites. This could be due to the small sample size and the presence of multiple phases in the sample (nuclei and magnetic phases of $MnFe_3O_5$). Therefore, constraints were applied to the thermal factors of the cations and anions to obtain reasonable refined parameters that account for their thermal contributions. The large χ^2 found in the low temperature refinement profiles are likely resulted from the high counting statistics and the additional number of refined parameters from the magnetic phase.

Bond valence sums calculations was carried out on the three cation sites in $MnFe_3O_5$ using the accurate metal and oxygen positions obtained from high resolution neutron diffraction between 5 and 400 K (**Figure 4.9**). A standard method with linear interpolation to estimate mixed charge states between Fe^{2+} and Fe^{3+} for the Fe sites was used.[11,12] The M-O, M-M and BVS results are detailed in **Table 4.8**. A 2+ oxidation state is observed for the Mn site across the measured temperature range. As for the Fe sites, at 400 K the charge of Fe is disordered in the two different sites, with an estimated oxidation state of 2.56(12) and 2.35(10) for Fe1 and Fe2, respectively. The 5 K calculations show an uneven charge distribution between the two iron sites. The Fe1 site is found

to have an estimated oxidation state of 3.02(15), whilst the Fe2 site is 1.98(8). The effect of a Jahn-Teller distortion, Q_{JT}, (as described in Chapter 2) was calculated for the Fe1 and Fe2 sites and the results are consistent with the obtained BVS values, with compression observed in the Fe2 site. This localises the minority-spin electron in Fe^{2+} in the d_{xy} orbital to gain crystal field stabilisation energy.

Table 4.7 Refined structural parameters of $MnFe_3O_5$ in space group *Cmcm* from neutron diffraction data collected between 5 and 400 K. Estimated standard deviations in independent variables are shown in parentheses. Fe1 atoms are located at (½, *y*, *z*), Fe2 atoms with site symmetry 4*a* are located at (0, 0, 0), Mn atoms at (0, *y*, ¼), O1 atoms at (½, *y*, ¼), O2 atoms at (0, *y*, *z*) and O3 atoms at (0, *y*, *z*). The occupancy of the Mn site was fixed to a Mn/Fe ratio of 0.063/0.937.

T / K			5	75	150	300	400
Cell	*a* (Å)		2.9015(3)	2.9027(2)	2.9059(2)	2.9190(2)	2.9285(3)
	b (Å)		9.8923(7)	9.8937(6)	9.8911(6)	9.8986(6)	9.8665(8)
	c (Å)		12.6076(10)	12.6131(10)	12.6214(9)	12.6429(9)	12.6220(11)
	V (Å^3)		361.87(5)	362.23(5)	362.77(4)	364.56(4)	365.66(5)
Fe1	8*f*	*y*	0.2345(4)	0.2374(4)	0.2377(4)	0.2378(3)	0.2368(3)
		z	0.1131(3)	0.1136(3)	0.1150(2)	0.1150(2)	0.1150(2)
Mn	4*c*	*y*	0.4812(16)	0.4969(16)	0.4927(16)	0.4913(15)	0.4833(13)
O1	4*c*	*y*	0.3188(9)	0.3277(9)	0.3250(8)	0.3244(7)	0.3220(7)
O2	8*f*	*y*	0.3469(6)	0.3516(6)	0.3548(5)	0.3558(4)	0.3572(4)
		z	0.0473(7)	0.0490(6)	0.0455(4)	0.0450(4)	0.0447(4)
O3	8*f*	*y*	0.0992(6)	0.0899(6)	0.0917(6)	0.0940(5)	0.0959(5)
		z	0.1410(7)	0.1394(6)	0.1404(5)	0.1405(4)	0.1416(4)
B_{iso} / Å^2 (Mn, Fe1 and Fe2)			2.42(12)	2.00(11)	1.89(8)	2.13(8)	2.18(8)
B_{iso} / Å^2 (O1, O2 and O3)			3.00(15)	1.90(12)	1.96(10)	2.03(8)	2.00(9)
R_p / %			10.5	10.1	9.15	9.09	9.45
R_{wp} / %			11.1	10.8	9.49	9.23	9.40
χ^2			52.5	34.9	24.0	14.2	16.7

Table 4.8 Metal-oxygen, metal-metal bond distances (Å) and BVS obtained from refined neutron diffraction results, with mean values <> shown for $MnFe_3O_5$ at 5, 75, 150, 300 and 400 K.

Bond	Distance				
	5 K	75 K	150 K	300 K	400 K
Mn-O1 (x 2)	2.216(14)	2.102(17)	2.203(14)	2.200(13)	2.141(11)
Mn-O3 (x 4)	2.213(9)	2.293(11)	2.216(9)	2.235(8)	2.291(8)
<Mn-O>	2.214(5)	2.229(6)	2.212(5)	2.223(5)	2.241(4)
Fe1-O1	1.916(6)	1.939(6)	1.910(5)	1.909(5)	1.917(7)
Fe1-O2	2.178(10)	2.232(9)	2.223(6)	2.224(6)	2.242(10)
Fe1-O2 (x 2)	2.007(6)	2.012(6)	2.055(5)	2.066(4)	2.070(7)
Fe1-O3 (x 2)	2.005(6)	2.084(6)	2.073(6)	2.062(5)	2.052(6)
<Fe1-O>	2.020(3)	2.061(3)	2.065(2)	2.065(2)	2.067(3)
Fe2-O2 (x 4)	2.181(5)	2.155(5)	2.122(4)	2.118(3)	2.115(6)
Fe2-O3 (x 2)	2.032(9)	1.970(8)	1.991(7)	2.004(6)	2.012(8)
<Fe2-O>	2.131(3)	2.093(3)	2.078(2)	2.080(2)	2.081(3)
Fe1-Fe1,Fe2-Fe2,Mn-Mn	2.9015(3)	2.9027(3)	2.9059(3)	2.9190(3)	2.9289(3)
Fe1-Fe2 (x 2)	2.989(4)	2.975(5)	2.973(4)	2.971(4)	2.978(3)
Fe1-Fe2 (x 4)	3.087(4)	3.115(5)	3.121(4)	3.125(4)	3.118(3)
Mn BVS	1.65(3)	1.91(3)	1.94(2)	1.89(2)	1.84(2)
Fe1 BVS	3.02(15)	2.61(11)	2.57(9)	2.57(8)	2.56(12)
Fe2 BVS	1.98(8)	2.31(10)	2.39(9)	2.31(7)	2.35(10)

The changes in the calculated BVS and Q_{JT} for the Fe1 and Fe2 sites between 5 and 400 K are summarised in **Figure 4.9**. The origin of the $Fe^{2+/3+}$ charge ordering can be seen in the change in the Fe-O distance in the two octahedral sites upon cooling. The refined bond distances, shown in **Table 4.8**, indicate an increase in the average Fe2-O distance upon cooling, whilst the average Fe1-O distance decreases. The larger Fe2 site is therefore more Fe^{2+} selective, compared to the Fe1 site, resulting in an uneven distribution of Fe^{2+} and Fe^{3+} between the two octahedral sites.

The magnetic structures of $MnFe_3O_5$ were solved by Rietveld fitting the neutron diffraction patterns from an average of banks 1 to 4 and 7 to 10. A stack plot of the refined diffraction patterns between 5 and 400 K is presented in **Figure 4.10**, showing that $MnFe_3O_5$ exhibits magnetic ordering when cooled below 400 K. The results indicate the rise of magnetic reflections in the 300 K

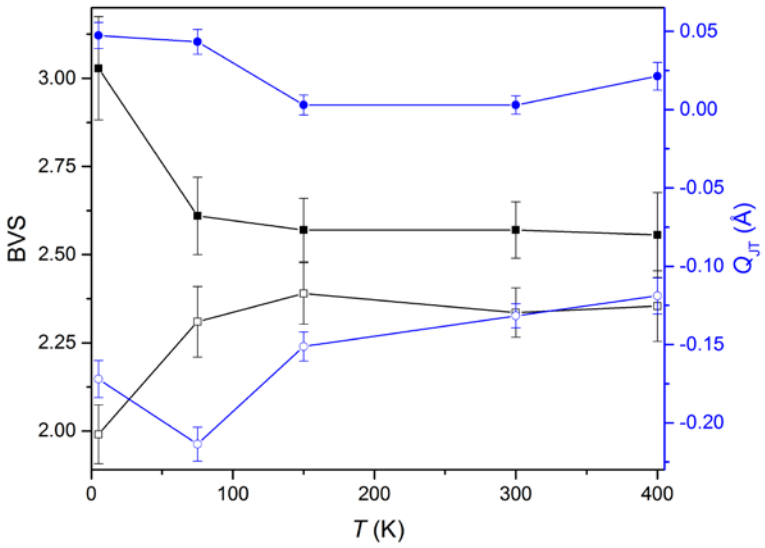

Figure 4.9 Temperature evolution of BVS and Q_{JT} obtained from neutron diffraction data, with closed/open symbols representing Fe1/Fe2 sites.

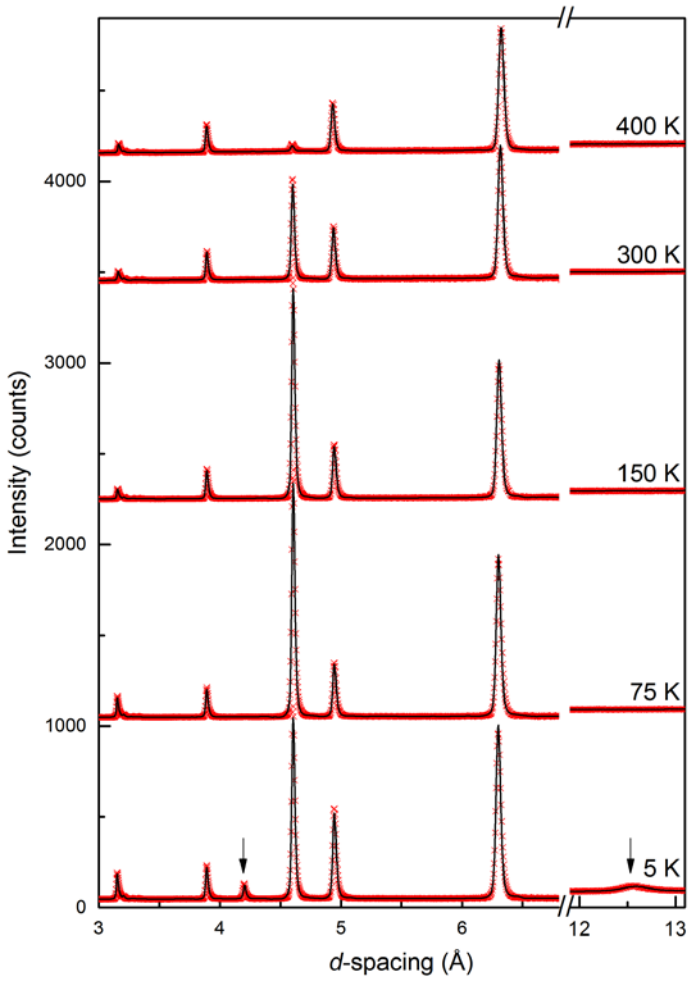

Figure 4.10 Temperature evolution of the neutron diffraction pattern of $MnFe_3O_5$. Magnetic contributions appear at 300 K, and arrows indicate additional magnetic peaks at 5 K, with *hkl* = (001) and (003) at d-spacing = 12.6 and 4.2 Å, respectively.

diffraction pattern. Below 75 K, additional magnetic reflections are observed. The new peaks were indexed as *hkl* = (001) and (003), which suggests the addition of spin components perpendicular to *c* in the low temperature magnetic structure. All the magnetic reflections in $MnFe_3O_5$ can be indexed with a magnetic propagation vector of [0 0 0]. Symmetry analysis was carried out using BasIreps (**Table 4.9**).[8] Good fits were obtained for the 150 and 300 K diffraction data by using operation $\Gamma_6\psi_9$ to describe the magnetic behaviour

Table 4.9 Irreducible representations (IrReps) and basis vectors (BV) for Fe1, Fe2 and Mn spin order in $MnFe_3O_5$ at 5 K, with propagation vector [0 0 0]. The magnetically independent atoms are Fe1 at (½, 0.2345, 0.1131), Fe2 at (0, 0, 0) and Mn1 at (0, 0.4812, ¼). The symmetry related positions are generated by the operators 1: (x, y, z), 2: (-x+½, -y+½, z+½), 3: (-x+1, y, -z+½), 4: (x-½, -y+½, -z+1), 5: (-x, -y, z+½) and 6: (-x, -y+1, z+½). The structure was solved using $\Gamma_2\psi_3$, $\Gamma_6\psi_8$ and $\Gamma_6\psi_9$ for Fe1 and Fe2, and $\Gamma_3\psi_4$, $\Gamma_6\psi_8$ and $\Gamma_7\psi_{11}$ for Mn1.

IrReps		Γ_1	Γ_2	Γ_3		Γ_4	Γ_5		Γ_6		Γ_7	Γ_8
	BV	ψ_1	ψ_2	ψ_3	ψ_4	ψ_5	ψ_6	ψ_7	ψ_8	ψ_9	ψ_{10}	ψ_{11}	ψ_{12}
Atoms		m_y	m_z	m_x	m_x	m_y	m_z	m_x	m_y	m_z	m_y	m_z	m_x
Fe1_1		+	+	+	+	+	+	+	+	+	+	+	+
Fe1_2		-	+	-	-	-	+	+	+	-	+	-	+
Fe1_3		+	-	-	+	-	+	-	+	-	-	+	+
Fe1_4		-	-	+	-	+	+	-	+	+	-	-	+
Fe2_1				+		+	+		+	+			+
Fe2_5				-		-	+		+	-			+
Mn1_1		+			+		+		+			+	+
Mn1_6		-			-		+		+			-	+

of the Fe ions at the Fe1 and Fe2 sites (with negative coefficients for Fe2). This marks the spin order of the Fe in $MnFe_3O_5$. The spins of the two independent Fe sites in $MnFe_3O_5$ are ordered antiferromagnetically in parallel to the *c*-axis, whilst the Mn spins remain disordered. This confirms that the Néel transition is observed at T_N = 350 K in the magnetisation measurements (**Figure 4.3**). The antiferromagnetism observed here results from direct exchange of the half-filled t_{2g} orbitals between the Fe1 and Fe2 ions through the edge sharing FeO_6 octahedra. The infinite ferromagnetic chains along the *a* axis originate from the 90° superexchange of Fe1/Fe2-O-Fe1/Fe2, competing with the direct exchange. The 150 K magnetic structure of $MnFe_3O_5$ is identical to the CA phase of $CaFe_3O_5$, as shown in **Figure 3.16**.

Spin ordering of the Mn site is observed when cooled below 150 K. Rietveld fits to the 75 K diffraction data, using additional magnetic operations of $\Gamma_6\psi_9$

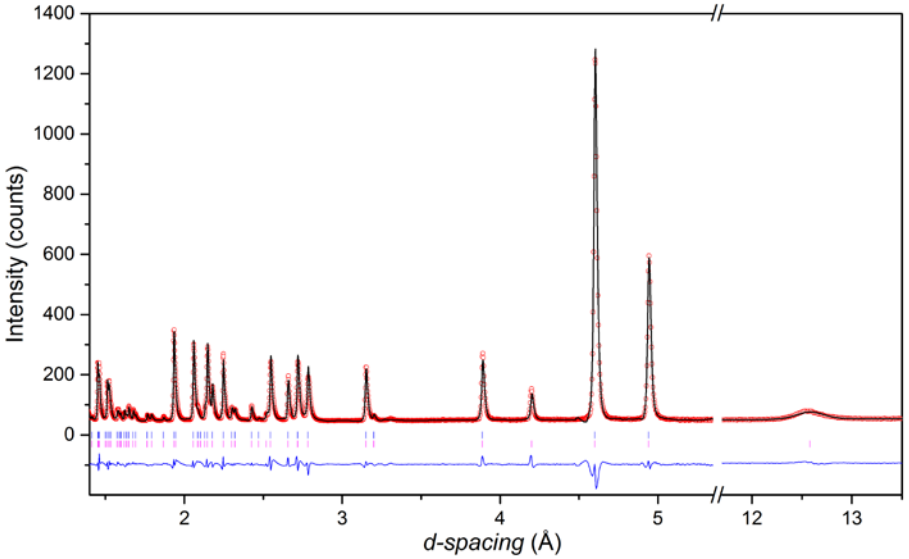

Figure 4.11 Rietveld refinement of the high-resolution neutron diffraction pattern of $MnFe_3O_5$ obtained at 5 K, with the upper tick marks indicating nuclear peaks and the lower indicating magnetic reflections. (χ^2 = 52.5, R_{wp} = 11.1 % and R_p = 10.5 %)

for Fe2 and $\Gamma_6\psi_8$ for Mn1, show the Mn spins align ferromagnetically along the *b*-axis. The Mn spin is coupled to the Fe1 and Fe2 spins via Mn–O–Fe bridges, and the frustration of the superexchange and direct exchange interactions leads to a perpendicular alignment of the Mn to the Fe moments. This frustration also causes the Fe1 spins to cant towards the *b*-axis, with antiferromagnetic coupling to the Mn spins, resulting in ferrimagnetism with a net magnetic moment of ~ 0.5 μ_B per $MnFe_3O_5$ formula unit. This observation is consistent with the increase in magnetisation when cooled below 300 K, as shown in **Figure 4.12**.

The additional magnetic reflections found in the 5 K neutron diffraction patterns mark another magnetic transition in $MnFe_3O_5$. The onset for this transition appeared to be the divergence between the zero-field cooled and field cooled susceptibilities at ~ 60 K in the susceptibility data (**Figure 4.4**). Rietveld fits to

the 5 K neutron diffraction pattern is shown in **Figure 4.11**. The ordered spin can be described by a combination of operations: $\Gamma_2\psi_3$, $\Gamma_6\psi_8$ and $\Gamma_6\psi_9$ for Fe1 and Fe2, and $\Gamma_3\psi_4$, $\Gamma_6\psi_8$ and $\Gamma_7\psi_{11}$ for Mn1. With the increase in the Mn moment on cooling further canting of all the spins is observed, with both the Fe1 and Fe2 sites becoming canted antiferromagnetically towards the *a* axis and ferromagnetically along *b*. The Mn spins are also canted antiferromagnetically to the *c* axis. The magnetic components of the Mn and the Fe2 sites on the *b* axis are antiparallel to that of the Fe1 and result in an enhancement in the magnetisation along the *b* axis to ~ 0.6 μ_B per $MnFe_3O_5$ formula unit. The spin reorientation at 60 K is likely to be driven by the charge ordering of Fe^{2+} and Fe^{3+} in $MnFe_3O_5$, where the spin components are altered by the change in the charge distribution in the lattice. The magnetic structures of the three magnetically ordered states exhibited by $MnFe_3O_5$ at 5, 75 and 300 K are presented in **Figure 4.12**, and the thermal evolution of the magnitude of the ordered moments is shown in **Figure 4.13**, with the refined values of the spin ordered components at 5 K, 75 K, 150 K and 300 K given in **Table 4.10**. The difference between the total magnetic moments obtained from the refined neutron data and the magnetisation measurements shown in **Figure 4.3** can be due to the insensitivity of neutrons to ferromagnetism, as ferromagnetic reflections have a propagation vector of [0 0 0] that lies on top of the nuclear peaks from the same lattice plane.

(A)

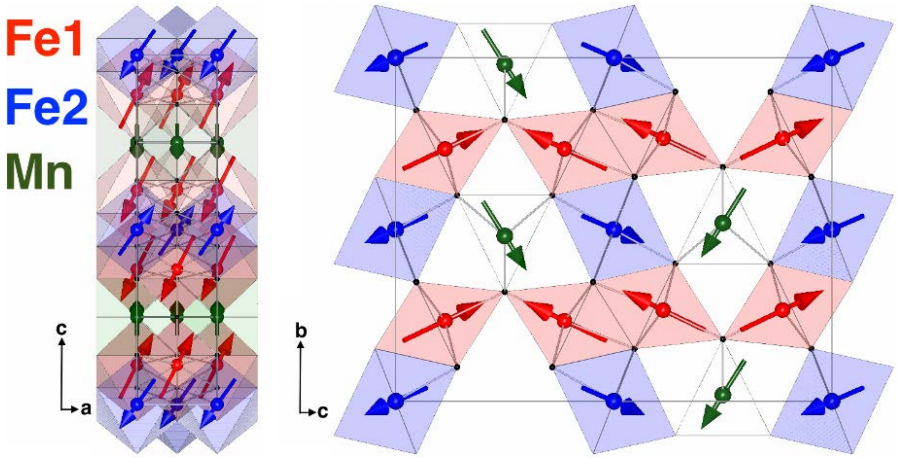

(B)

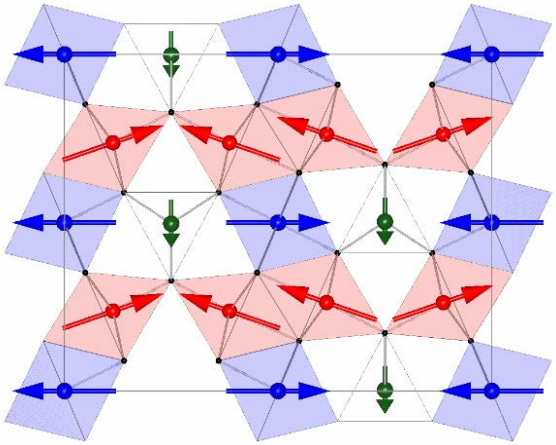

(C)

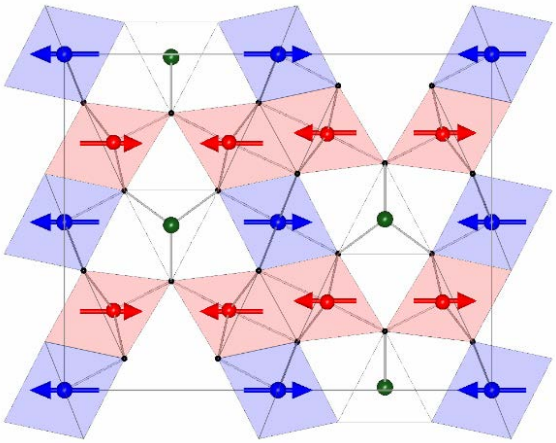

Figure 4.12 Magnetic structures of $MnFe_3O_5$ at (A) 5 K, (B) 75 K, and (C) 300 K. The network of FeO_6 octahedra is shown as red and blue for Fe1 and Fe2, respectively. Mn^{2+} in trigonal prismatic sites that form channels parallel to the *a*-axis is presented in green.

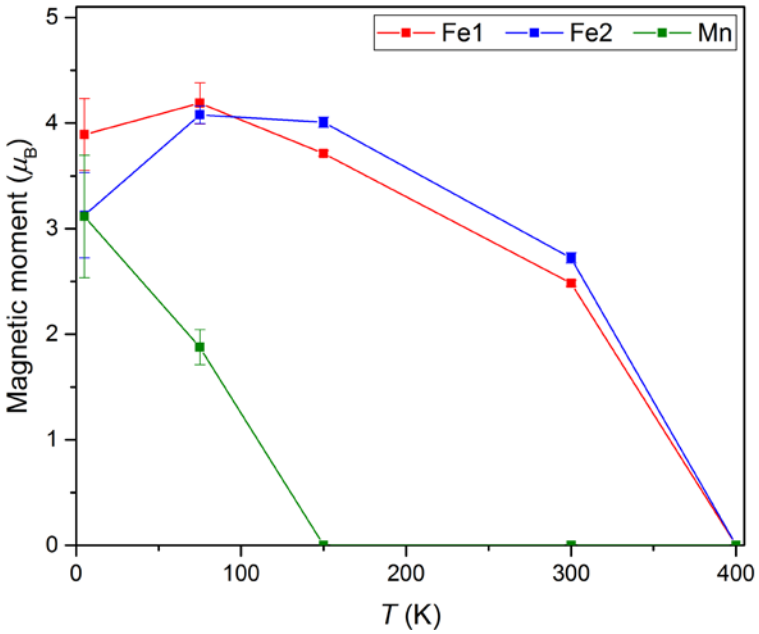

Figure 4.13 The temperature evolution of the ordered Mn, Fe1 and Fe2 magnetic moments in $MnFe_3O_5$.

Table 4.10 The magnetic components and total moment of each magnetic ion in $MnFe_3O_5$ between 5 and 300 K.

	Sites	5 K	75 K	150 K	300 K
Fe1 (μ_B)	Total	3.9(3)	4.2(2)	3.7(1)	2.4(1)
	x	1.6(1)	0	0	0
	y	1.5(2)	1.4(1)	0	0
	z	3.2(1)	3.9(1)	3.7(1)	2.4(1)
Fe2 (μ_B)	Total	3.1(4)	4.1(1)	4.0(1)	2.7(1)
	x	1.7(1)	0	0	0
	y	1.0(2)	0	0	0
	z	2.4(1)	4.1(1)	4.0(1)	2.7(1)
Mn (μ_B)	Total	3.1(6)	1.88(2)	0	0
	x	0	0	0	0
	y	2.6(3)	1.88(2)	0	0
	z	1.7(4)	0	0	0

4.3. Conclusion

Using high-pressure techniques, Mn^{2+} was stabilised at the triangular prismatic site of MFe$_3$O$_5$, leading to the discovery of a novel material – MnFe$_3$O$_5$. The synthesis of MnFe$_3$O$_5$ was carried out under a pressure of 10 GPa at 1200 °C. Initial characterisation using laboratory x-ray diffraction confirmed an orthorhombic structure in the space group *Cmcm*, isostructural to Fe$_4$O$_5$. The success in the synthesis of MnFe$_3$O$_5$ indicates that other cations with similar ionic radii can be stabilised the triangular prismatic site with pressure and that other analogues of the MFe$_3$O$_5$ family can be synthesised.

Magnetometry, resistivity measurements and synchrotron x-ray and neutron diffraction have been employed to characterise the physical properties as well as the crystal structure and magnetic behaviours of MnFe$_3$O$_5$. MnFe$_3$O$_5$ was found to exhibit complex magnetic states. Similar to Fe$_4$O$_5$, MnFe$_3$O$_5$ has a T_N above room temperature, at 350 K. This transition was confirmed by powder neutron diffraction as the spin order of the Fe sites. The Mn spin order was observed at 150 K, which also leads to the Fe1 site spin canting, resulting in a net moment of 0.72 μ_B per formula unit of MnFe$_3$O$_5$. Another magnetic transition was found at 60 K, where spins are reoriented across the three cation sites.

The Rietveld fitted powder synchrotron x-ray and neutron diffraction data shows no evidence of a change in crystal symmetry in MnFe$_3$O$_5$ within a temperature range of 5 to 400 K. However, like other members of the MFe$_3$O$_5$ family, anisotropic thermal expansion in the lattice parameters was observed

when cooled. BVS calculations were carried out using the refined neutron diffraction data indicating charge ordering of the Fe^{2+} and Fe^{3+} across the two different Fe sites at 60 K, supported by the Jahn-Teller distortion observed. This indicates that the magnetic transition observed at 60 K originates from the charge redistribution of the Fe ions. Cation charge ordering plays a very important role in many mixed valence transition metal oxides and is often found to be responsible for complex and sometimes competing ground states. This is demonstrated by Fe_3O_4, Fe_4O_5, and the recent discoveries in $CaFe_3O_5$ and $MnFe_3O_5$.

In summary, $MnFe_3O_5$ displays a rich variety of magnetically ordered states on cooling. Fe spins order antiferromagnetically below a Néel transition at 350 K. A second transition at 150 K marks Mn spin order that leads to spin canting of some of the Fe spins and ferrimagnetism. A further spin reorientation of all the cation sites at 60 K is driven by charge ordering of Fe^{2+} and Fe^{3+} over two inequivalent Fe sites. The discovery and characterisation of $MnFe_3O_5$ using property measurement systems and diffraction data collected on ID22 at the ESRF and WISH at ISIS has resulted in publications in Zeitschrift für Anorganische und Allgemeine Chemie (Synthesis, Crystal Structure, and Magnetic Properties of $MnFe_3O_5$)[13] and in the Journal of Materials Chemistry C – Royal Society of Chemistry (Cation, magnetic, and charge ordering in $MnFe_3O_5$).[14] This demonstrates the importance of this new family of the iron oxide system, particularly for the interest in studying the complex ground states of transition metal oxides.

4.4. References

1. B. Lavina, P. Dera, E. Kim, Y. Meng, R. T. Downs, P. F. Weck, S. R. Sutton, Y. Zhao. *Proc. Natl. Acad. Sci. USA* **2011,** *108,* 17281–17285.

2. R. D. Shannon, *Acta Cryst.* **1976**, *A32* 751-767.

3. M. Markkula, A, M. Arevalo-Lopez, A. Kusmartseva, J. A. Rodgers, C. Ritter, H. Wu, J. P. Attfield, *Phys. Rev. B* **2011**, *84*, 094450.

4. S. V. Ovsyannikov, M. Bykov, E. Bykova, K. Glazyrin, R. S. Manna, A. A. Tsirlin, V. Cerantola, I. Kupenko, A. V. Kurnosov, I. Kantor, A. S. Pakhomova, I. Chuvashova, A. I. Chumakov, R. Rüffer, C. McCammon, L. S. Dubrovinsky. *Nat. Chem.* **2016,** *8,* 501.

5. M. S. Senn, J. P. Wright, J. P. Attfield. *Nature* **2012**, *481,* 173–176.

6. C. Delacotte, F. Hüe, Y. Bréard, S. Hébert, O. Pérez, V. Caignaert, J. M. Greneche, D. Pelloquin. *Inorg. Chem.* **2014,** *53,* 10171–10177.

7. A. C. Larson, R. B. Von Dreele, *Los. Alamos National Laboratory Report LAUR,* **2004,** *748*, 86–748.

8. J. Rodriguez-Carvajal. *Physica B.* **1993** *192* ,55–69.

9. R.D. Shannon, *Acta Cryst.* **1976**, *A32* 751-767.

10. V. F. *Sears Neutron News,* **1992**, *3*, No. 3, 29-37.

11. J. P. Attfield, *Solid State Sci.* **2006**, *8*, 861–867.

12. I. D. Brown, *J. Appl. Crystallogr.* **1996**, *29*, 479–480.

13. K. H. Hong, G. M. McNally, M. Coduri, J. P. Attfield, *Zeitschrift für Anorg. und Allg. Chemie* **2016**, *642*, 1355–1358.

14. K. H. Hong, A. M Arevalo-Lopez, M. Coduri, G. M. McNally, J. P. Attfield, *J. Mater. Chem. C* **2018**, *6,* 3271–3275.

Chapter 5. High-Pressure Synthesis and Properties of $CoFe_3O_5$

5.1. Introduction

With the success in synthesising the high-pressure Mn analogue of the *M*Fe_3O_5 system (as described in Chapter 4), it was believed that cations with similar ionic radii and electronic properties could also be stabilised in the triangular prismatic site with pressure. The synthesis and characterisation of $CoFe_3O_5$ is detailed in this chapter. Co^{2+} has a slightly smaller ionic radius (0.75 Å) compared to both Mn^{2+} and Fe^{2+},[1] thus a higher pressure might be required to stabilise the $CoFe_3O_5$ phase. Furthermore, the similarity in ionic radii between Co^{2+} and Fe^{2+} means that Co^{2+} might be disordered and found in the octahedral sites, substituted for Fe^{2+}. If such Co/Fe cation disordering were to occur, it would result in an impact on the geometry of the octahedral sites, as Co^{2+} in the MO_6 coordination is known to undergo Jahn-Teller elongation to lower the crystal field energy of the d_{xz} and d_{yz} orbitals, in contrast to Jahn-Teller compression for Fe^{2+}. Different M-M and M-O distances would be expected for a cationic disordered phase, which in turn would result in different electronic exchange interactions.

The presence of the smaller Co^{2+} cation in $CoFe_3O_5$ would cause the lattice parameters to be smaller than those of the Mn and Fe analogues, and hence shorten the M-M distances between edge sharing octahedra along the *a* axis. The short M-M distance would favour the delocalisation of the minority electron

in Fe^{2+} with the cation sites along the axis and could lead to the suppression of $Fe^{2+/3+}$ charge ordering that was found in the low temperature structures of Fe_3O_4,[2,3] Fe_4O_5[4,5] and $MnFe_3O_5$ and the charge ordered phase of $CaFe_3O_5$, and instead would result in a structure similar to the charge averaged phase of $CaFe_3O_5$.

5.2. Experimental Methods and Results

5.2.1. Synthesis of $CoFe_3O_5$

The synthesis of $CoFe_3O_5$ was carried out using a solid-state high-pressure and high-temperature synthesis method, with conditions similar to those described for $MnFe_3O_5$. Polycrystalline CoO and Fe_3O_4 were ground together in a ratio of 1:1 using a mortar and pestle and the resulting mixture was packed into a in a Pt capsule. The capsule was then loaded inside the two-stage Walker-type module. The heating of the sample used the synthetic temperature of $MnFe_3O_5$, i.e. 1200 °C, for 20 minutes, and the pressure of the synthesis was explored between 10 and 12 GPa. Phase identification was carried out for the product using a Bruker D2 Phaser diffractometer, with x-ray

Table 5.1 Synthesis conditions of each batch of the $CoFe_3O_5$ sample.

Sample	*P* (GPa)	Set *T* (°C)	Phase presence
#1	10	1200	CoO and Fe_3O_4
#2	12	1200	$CoFe_3O_5$
#3	12	1200	$CoFe_3O_5$
#4	12	1200	$CoFe_3O_5$
#5	12	1200	$CoFe_3O_5$

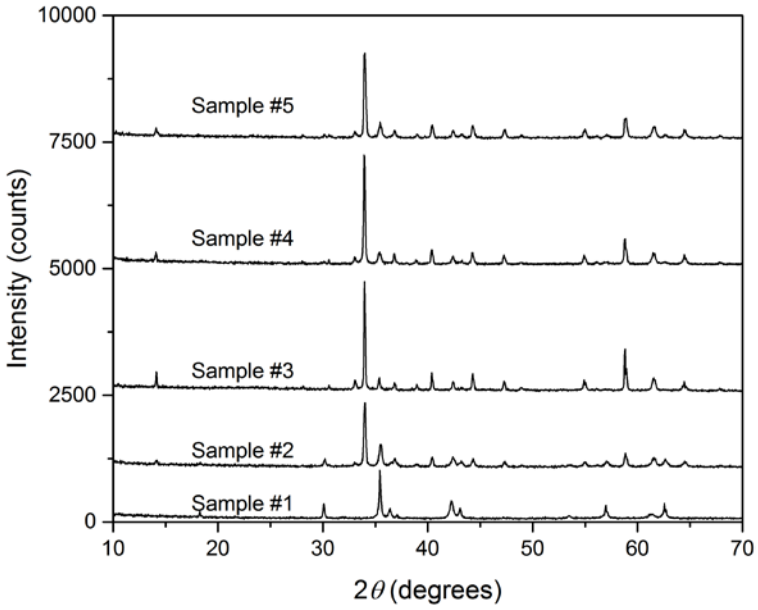

Figure 5.1 A stack plot of XRD patterns collected for the five batches of prepared $CoFe_3O_5$. Phase pure samples were obtained in samples #2 to #5

diffraction patterns collected using a Cu K_α/K_β radiation source (15 minutes scans of $5° \leq 2\theta \leq 70°$). The recorded diffraction patterns were Rietveld fitted using GSAS.[6]

A total of five batches of samples were synthesised, with synthesis conditions detailed in **Table 5.1**. A stack plot of diffraction patterns collected for each sample is shown in **Figure 5.1**. The pattern from sample #1 showed that the product only contains phases of the starting material, with all the Bragg reflections being indexed with the Fe_3O_4 and CoO profiles. The presence of starting materials suggests that no chemical reaction took place at 1200 °C under 10 GPa of pressure and that a higher pressure and/or temperature is required. However, from the experience of synthesising $MnFe_3O_5$, at temperatures above 1200 °C the formation of high-pressure impurities or sample melting is likely. Therefore, the temperature was fixed to 1200 °C and

a higher pressure of 12 GPa was used for sample #2. The Rietveld fit to the x-ray diffraction pattern collected for sample #2, as illustrated in **Figure 5.2**, shows a phase pure product of $CoFe_3O_5$, with an orthorhombic *Cmcm* symmetry corresponding to the $CaFe_3O_5$-type structure,[7] isostructural with other MFe_3O_5 (*M* = Ca, Fe and Mn) analogues. The refined room temperature lattice parameters of $CoFe_3O_5$ are a = 2.8982(4) Å, b = 9.767(2) Å and c = 12.567(1) Å, with a cell volume of V = 355.7(1) Å^3. The size of the unit cell is found to be consistent with the smaller ionic radius of Co^{2+}, when compared to Fe_4O_5[4,5] and $MnFe_3O_5$ (as detailed in Chapter 4). Due to the very similar electron densities of Fe and Co, refinement of the cation site occupancy was not possible with x-rays. The triangular prismatic site was fixed to be occupied exclusively by Co ions. In this chapter, the three cation sites in $CoFe_3O_5$ are labelled as M1 and M2 for the two octahedral sites and M3 for the triangular

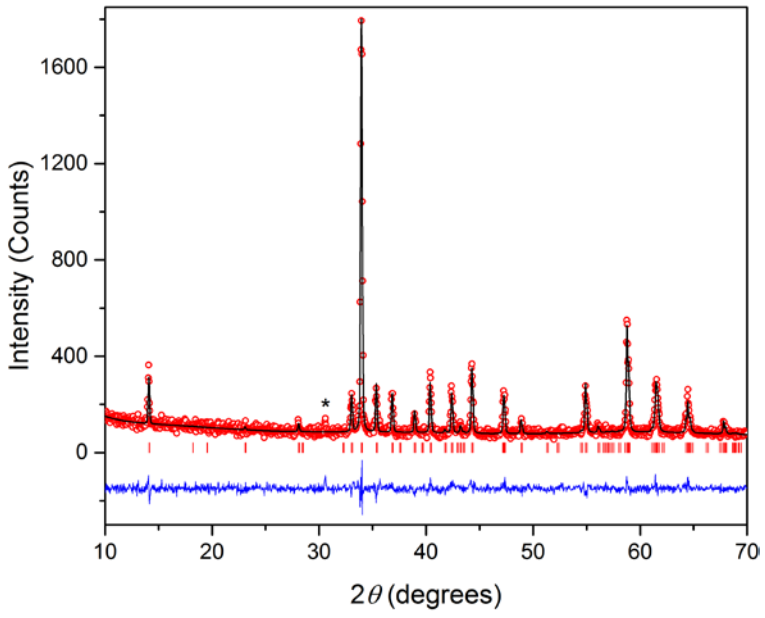

Figure 5.2 Rietveld fit to the powder x-ray diffraction pattern of $CoFe_3O_5$ (sample #2) obtained using a Bruker D2 diffractometer at room temperature, with an asterisk showing the reflection from Cu K_β radiation. (χ^2 = 1.3 %, R_{wp} = 10.8 % and R_p = 8.4 %.)

prism site. Extensive crystal structural studies were carried out using synchrotron x-ray diffraction techniques, as described later in Section 5.2.4.

No extra reflections that would indicate the presence of an impurity are observed in the diffraction pattern of sample #2. The same conditions were used for the synthesis of sample #3-5 and the x-ray patterns showed consistent purity in all the samples, as shown in **Figure 5.1**

5.2.2. Magnetic Properties of $CoFe_3O_5$

Magnetometry measurements were carried out on sample #2 (12.5 mg) with a Quantum Design MPMS XL SQUID magnetometer. An applied magnetic field of 5000 Oe was used to measure the magnetic susceptibility of the sample between 2 and 400 K under zero field cooled (ZFC) and field cooled (FC) conditions. As illustrated in **Figure 5.3**, the recorded data show a small susceptibility upturn upon cooling to $T_{C1} \approx 300$ K that evidences a weak ferromagnetic ordering. Another magnetic transition is found at $T_{C2} \approx 100$ K. Both transitions are found to be accompanied by divergence of the ZFC and FC measurements. Magnetisation versus field measurements were taken on the same sample with a magnetic field loop between -7 and 7 T, as shown in the inset of **Figure 5.3**. The 350 K data show a small remnant magnetisation of $M_r = 0.014\ \mu_B$ per formula unit of $CoFe_3O_5$. The small moment is likely due to traces of ferromagnetic spinel impurities that are beyond the detection limit of the x-ray diffraction pattern obtained. M_r increases to 0.06 μ_B on cooling from 350 to 200 K through T_{C1}, revealing an intrinsic weak ferromagnetism. A

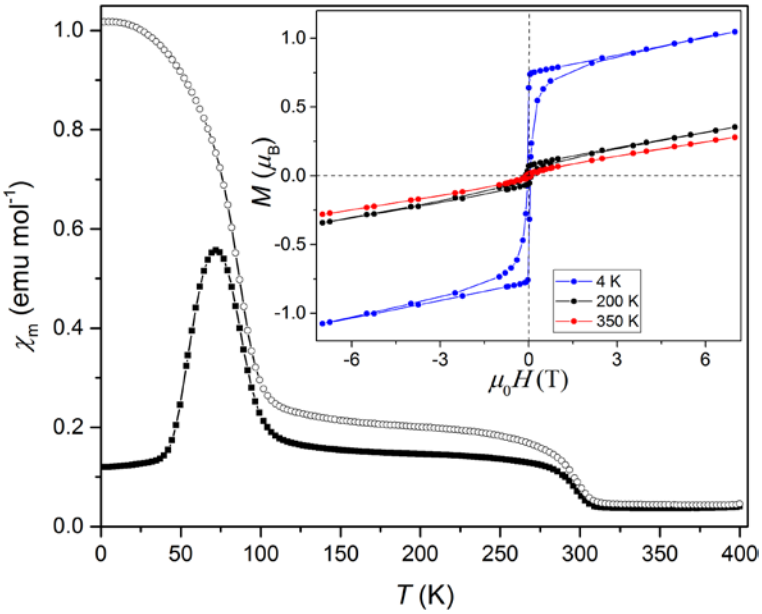

Figure 5.3 (a) Zero field cooled (closed symbols) and field cooled (open symbols) magnetic susceptibilities for $CoFe_3O_5$ in a 0.5 T field. Inset shows magnetization-field loops at 4, 200 and 350 K.

further increase in the magnetic moment of the sample is found when cooled bellow T_{C2}, with a moment of 0.75 μ_B observed at 4 K that is consistent with a ferrimagnetic order.

5.2.3. Electrical Properties Study of $CoFe_3O_5$

The electrical properties of $CoFe_3O_5$ were explored using a Quantum Design PPMS. Measurements were carried out on a polycrystalline pellet of $CoFe_3O_5$ from sample #3. The chosen sample had a cross section of 0.0011 cm^2 and a length of 0.095 cm between the furthest electrodes. The results show an increase in the resistivity of the sample when cooled from 400 to 120 K, demonstrating a semiconducting behaviour (**Figure 5.4**). The resistance of the $CoFe_3O_5$ sample was too great to be measured by the PPMS below 120 K. A

small deviation in the slope is observed at $T_{C1} \approx 300$ K. The high temperature activation energy for electron hopping, fitted as an Arrhenius $\rho = A \exp(E_a/k_B T)$ dependence (as shown in the insert in **Figure 5.4**), was $E_a = 14$ meV, reflecting the behaviours of a semiconductor. The Arrhenius fit to the slope of the low

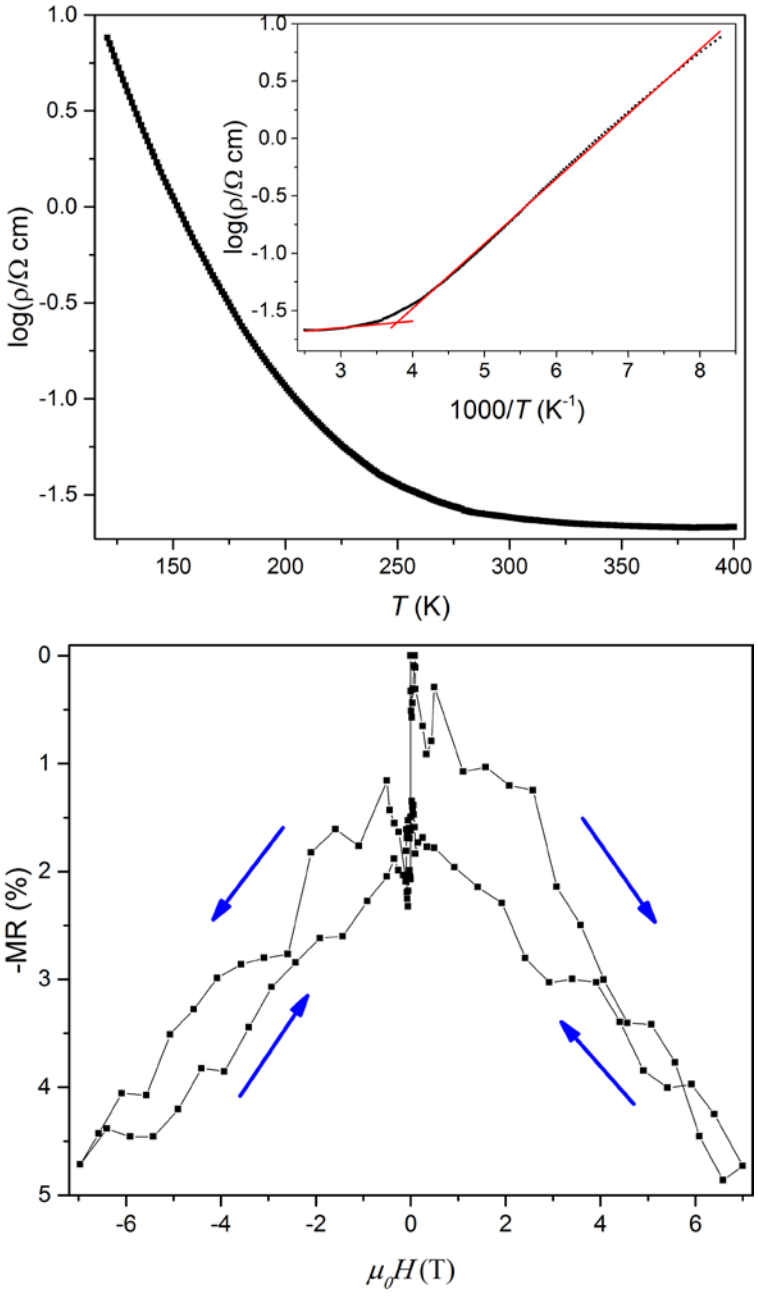

Figure 5.4 (Upper) Logarithmic plot of the electrical resistivity against temperature, with inset showing Arrhenius fits to the $\log_{10}$(resistivity) versus reciprocal temperature above and below $T_{C1} \approx 300$ K. (Lower) The magnetoresistance at 125 K.

temperature region between 130 and 245 K gives a substantially higher E_a = 112 meV, demonstrating a strong antiferromagnetic spin scattering contribution. The magnetoresistance of $CoFe_3O_5$ was studied by measuring the resistance of the same pellet with a magnetic field loop between -7 and 7 T. A small magnetoresistance effect of -5 % is observed in a 7 T field at 125 K, as shown in **Figure 5.4**, consistent with partial suppression of the spin scattering term. This also explains the larger magnetoresistance effect observed in $CoFe_3O_5$ compared to $CaFe_3O_5$, with its stronger ferrimagnetic behaviour at low temperature.

5.2.4. Synchrotron X-ray Diffraction Study of $CoFe_3O_5$

High resolution powder synchrotron x-ray diffraction data were collected using sample #2 at the ID22 beamline of the ESRF with incident wavelength 0.39994 Å. The sample was packed into a glass capillary with an outer diameter of 0.3 mm. Diffraction data were collected between 90 and 400 K using an Oxford Cryostream system, with the sample capillary spinning. A liquid helium cryostat system was used to collect patterns between 5 and 90 K. Data were collected from 50 to 90 K with the sample spinning, but stationary for the 5 and 25 K measurements due to technical issues. Rietveld refinements were carried out using FullProf,[8] with the peak shape refined using a pseudo-Voigt profile, as described in Section 2.2.4. The background of the diffraction patterns is fitted using linear interpolation between a set of background points with refinable heights. The Rietveld fit to the 300 K data (**Figure 5.5**) confirms the purity of

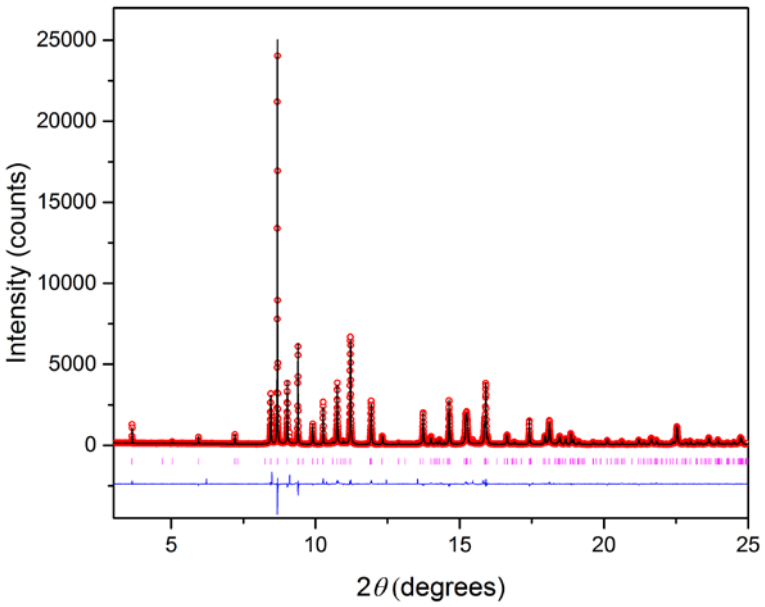

Figure 5.5 Rietveld fit to synchrotron powder diffraction profiles of $CoFe_3O_5$ at 300 K. (χ^2 = 8.5, R_{wp} = 12.3 % and R_p = 9.4 %)

the $CoFe_3O_5$ sample, with orthorhombic lattice parameters of *a* = 2.89825(2) Å, *b* = 9.76569(5) Å and *c* = 12.56384(7) Å, and a cell volume of 355.600(3) $Å^3$. The cation site occupancies were fixed to the Co/Fe ratios obtained from neutron diffraction, as discussed in Section 5.2.5.

The thermal evolution of the crystal structure of $CoFe_3O_5$ between 5 and 400 K, obtained from the refined diffraction patterns, was studied. The results show that the orthorhombic *Cmcm* structure is adopted throughout this temperature range. Anisotropic thermal expansion of the lattice parameters is observed when cooled below T_{C1} ≈ 300 K (**Figure 5.6**), with *a* and *c* contracting with decreasing temperature, whilst *b* expands. Another anomaly in the slope of the lattice parameters and cell volume is found at T_{C2} ≈ 100 K. These observations show that the changes in magnetic order are coupled to the lattice leading to magnetostrictive effects. The refinements of the crystal structure of $CoFe_3O_5$

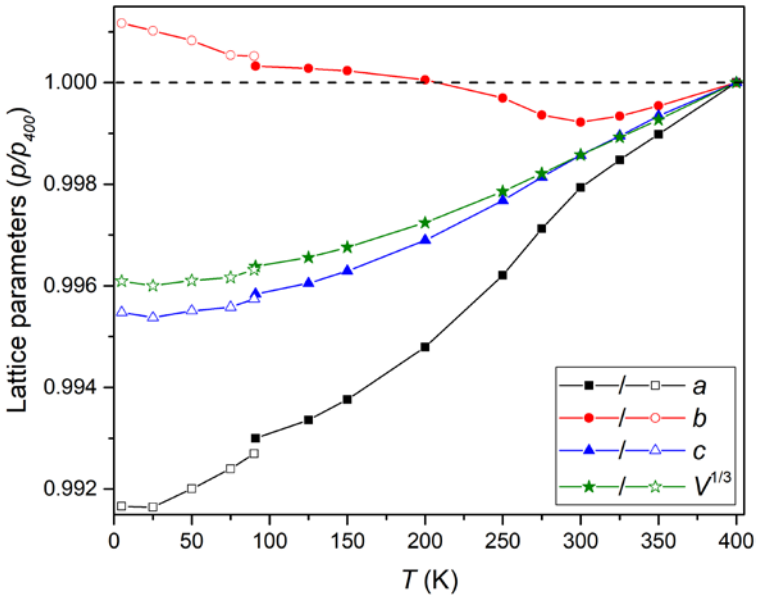

Figure 5.6 Changes in the lattice parameters relative to 400 K values obtained from synchrotron x-ray diffraction ($a_{400\ K}$ = 2.90423(3) Å, $b_{400\ K}$ = 9.77325(8) Å and $c_{400\ K}$ = 12.5817(1) Å). Open/closed points were collected using helium cryostat/nitrogen cryostream systems.

between 5 and 400 K show no evidence of a structural transition. Details of the refined crystallographic information are summarised in **Table 5.3** and **Table 5.4**. The refined thermal parameters from the synchrotron data were found to be smaller than usual, which are likely due to the absorption of x-rays by the sample. This also resulted in some unrealistic refined thermal factors (negative parameters), hence the thermal factors of all the atoms were constrained to be refined together to obtain a coefficient that accounts for their thermal contributions.

The M-O distances obtained from synchrotron x-ray data, as shown in **Table 5.2**, indicate a longer average M3-O distance at the trigonal prism site than the M1 and M2 sites. This suggests that the M3 site is likely to be occupied by Co or Fe cations with an oxidation state of 2+, due to their larger ionic radii in comparison to the 3+ cations. However, the weak interaction between x-rays

and oxygen could lead to less than accurate oxygen positions. Accurate M-O distances and cation site valence states were determined using neutron diffraction data, discussed in Section 5.2.5.

Table 5.2 Metal-oxygen bond lengths obtained from synchrotron x-ray diffraction data, with derived mean values < > and BVSs shown for $CoFe_3O_5$ at 400 K and 5 K.

Bond	Distance	
	400 K	5 K
M1-O1	1.922(3)	1.955(3)
M1-O2	2.243(4)	2.252(4)
M1-O2 (x 2)	2.088(3)	2.094(3)
M1-O3 (x 2)	2.078(1)	2.026(3)
<M1-O>	2.086(3)	2.075(1)
M2-O2 (x 4)	2.057(3)	2.040(3)
M2-O3 (x 2)	1.989(5)	2.021(3)
<M2-O>	2.034(2)	2.034(1)
M3-O1 (x 2)	2.123(5)	2.062(4)
M3-O3 (x 4)	2.229(4)	2.218(3)
<M3-O>	2.194(2)	2.166(1)

Table 5.3 Refined structural parameters of $CoFe_3O_5$ in space group *Cmcm* from synchrotron x-ray diffraction data between 5 and 90 K using a liquid helium cryostat system. Estimated standard deviations in independent variables are shown in parentheses. M1 atoms are located at (½, *y*, *z*), M2 atoms with site symmetry 4*a* are located at (0, 0, 0), M3 atoms at (0, *y*, ¼), O1 atoms at (½, *y*, ¼), O2 atoms at (0, *y*, z) and O3 atoms at (0, *y*, *z*). The 5 and 25 K diffraction data were collected without the use of cryostat spinner and resulted in a higher than usual *R*-factors and χ^2. The occupancy of the three cations sites were fixed to the values obtained from neutron diffraction, with Fe/Co ratios of 1/0, 0.78(1)/0.22 and 0.64(1)/0.36 for the M1, M2 and M3 site. * The thermal parameters for all the atoms are constrained to be refined together.

			T / K	5	25	50	75	90
Cell			*a* (Å)	2.8802(2)	2.87999(4)	2.88104(3)	2.88218(3)	2.88305(3)
			b (Å)	9.78467(7)	9.78329(12)	9.78138(10)	9.77855(10)	9.77841(11)
			c (Å)	12.52485(9)	12.52359(18)	12.52530(13)	12.52620(13)	12.52831(15)
			V (Å^3)	352.950(5)	352.861(8)	352.970(6)	353.033(6)	353.193(7)
M1	8*f*		*y*	0.23854(8)	0.23923(18)	0.23952(14)	0.23949(14)	0.23952(15)
			z	0.11656(5)	0.11558(10)	0.11644(8)	0.11656(8)	0.11674(9)
M3	4*c*		*y*	0.49295(11)	0.48984(20)	0.49309(17)	0.49351(16)	0.49332(17)
O1	4*c*		*y*	0.34373(50)	0.33625(81)	0.33618(69)	0.33726(68)	0.33649(72)
O2	8*f*		*y*	0.36258(35)	0.35926(57)	0.36030(48)	0.35087(47)	0.36046(50)
			z	0.04495(25)	0.04368(45)	0.04334(37)	0.04312(36)	0.04372(39)
O3	8*f*		*y*	0.09665(36)	0.10421(62)	0.09218(53)	0.09288(53)	0.09220(55)
			z	0.14355(23)	0.14858(40)	0.14180(33)	0.14164(33)	0.14249(36)
			B_{iso} / Å^{2}*	0.29(1)	0.72(4)	0.12(4)	0.08(4)	0.15(4)
			R_p / %	16.4	15.1	12.5	12.0	13.0
			R_{wp} / %	19.1	17.5	15.9	15.6	16.5
			χ^2	7.5	16.2	2.3	2.2	2.4

Table 5.4 Refined structural parameters of $CoFe_3O_5$ in space group *Cmcm* from synchrotron x-ray diffraction data between 90 and 275 K using an Oxford Cryostream system. Estimated standard deviations in independent variables are shown in parentheses. M1 atoms are located at (½, *y*, *z*), M2 atoms with site symmetry 4*a* are located at (0, 0, 0), M3 atoms at (0, *y*, ¼), O1 atoms at (½, *y*, ¼), O2 atoms at (0, *y*, *z*) and O3 atoms at (0, *y*, *z*). The occupancy of the three cations sites were fixed to the values obtained from neutron diffraction, with Fe/Co ratios of 1/0, 0.78(1)/0.22 and 0.64(1)/0.36 for the M1, M2 and M3 site. * The thermal parameters for all the atoms are constrained to be refined together.

			T / K	90	125	150	200	250	275
Cell			*a* (Å)	2.88391(2)	2.88497(2)	2.88613(2)	2.88312(2)	2.89324(2)	2.89590(2)
			b (Å)	9.77648(5)	9.77601(5)	9.77557(5)	9.77382(5)	9.77035(5)	9.76708(6)
			c (Å)	12.52947(7)	12.53214(7)	12.53519(7)	12.54280(7)	12.55262(7)	12.55842(7)
			V (Å^3)	353.262(3)	353.450(3)	353.663(3)	354.180(3)	354.837(3)	355.208(4)
M1	8*f*	*y*		0.23933(7)	0.23934(7)	0.23932(7)	0.23933(7)	0.23943(7)	0.23934(8)
		z		0.11654(4)	0.11650(4)	0.11644(4)	0.11636(4)	0.11626(4)	0.11617(5)
M3	4*c*	*y*		0.49368(8)	0.49350(8)	0.49351(8)	0.49326(9)	0.49292(9)	0.49287(9)
O1	4*c*	*y*		0.33654(38)	0.33681(38)	0.33661(38)	0.33645(40)	0.33623(41)	0.33633(41)
O2	8*f*	*y*		0.35927(27)	0.35957(27)	0.35944(28)	0.35975(28)	0.35972(29)	0.36001(29)
		z		0.04319(20)	0.04342(20)	0.04347(20)	0.04362(21)	0.04367(21)	0.04364(21)
O3	8*f*	*y*		0.09260(30)	0.09254(30)	0.09292(30)	0.09301(31)	0.09346(32)	0.09388(33)
		z		0.14160(18)	0.14164(18)	0.14159(18)	0.14155(18)	0.14172(19)	0.14194(19)
			B_{iso} / Å^{2}*	0.09(1)	0.11(11)	0.13(1)	0.20(1)	0.29(1)	0.30(1)
			R_p / %	9.7	8.7	8.8	9.0	9.1	9.3
			R_{wp} / %	11.6	11.7	11.7	12.1	12.3	12.5
			χ^2	7.5	7.5	7.3	7.5	8.15	8.8

Table 5.5 Refined structural parameters of $CoFe_3O_5$ in space group *Cmcm* from synchrotron x-ray diffraction data between 300 and 400 K using an Oxford Cryostream system. Estimated standard deviations in independent variables are shown in parentheses. M1 atoms are located at (½, *y*, *z*), M2 atoms with site symmetry 4*a* are located at (0, 0, 0), M3 atoms at (0, *y*, ¼), O1 atoms at (½, *y*, ¼), O2 atoms at (0, *y*, *z*) and O3 atoms at (0, *y*, *z*). The occupancy of the three cations sites were fixed to the values obtained from neutron diffraction, with Fe/Co ratios of 1/0, 0.78(1)/0.22 and 0.64(1)/0.36 for the M1, M2 and M3 site. * The thermal parameters for all the atoms are constrained to be refined together.

			T / K	300	325	350	400
Cell			*a* (Å)	2.89825(2)	2.89983(2)	2.90129(2)	2.90423(3)
			b (Å)	9.76569(5)	9.76687(5)	9.76881(5)	9.77325(8)
			c (Å)	12.56384(7)	12.56864(7)	12.57357(7)	12.58173(11)
			V (Å^3)	355.600(3)	355.973(4)	356.361(3)	357.117(5)
M1	8*f*	*y*		0.23925(7)	0.23931(8)	0.23922(8)	0.23928(12)
		z		0.11613(4)	0.11610(5)	0.11606(5)	0.11590(6)
M3	4*c*	*y*		0.49270(8)	0.49253(9)	0.49235(10)	0.49152(14)
O1	4*c*	*y*		0.33628(37)	0.33654(41)	0.33627(42)	0.33521(57)
O2	8*f*	*y*		0.36007(26)	0.36050(30)	0.36077(30)	0.35995(41)
		z		0.04355(19)	0.04354(22)	0.04367(22)	0.04482(31)
O3	8*f*	*y*		0.09388(29)	0.09425(33)	0.09405(34)	0.09223(46)
		z		0.14183(17)	0.14193(19)	0.14180(20)	0.14219(26)
			B_{iso} / Å^{2}*	0.34(1)	0.37(1)	0.43(1)	0.44(2)
			R_p / %	9.4	9.6	9.8	12.7
			R_{wp} / %	12.3	12.7	12.9	16.0
			χ^2	8.4	9.0	9.1	9.0

5.2.5. Powder Neutron Diffraction Study

High resolution time-of-flight powder neutron diffraction experiments were carried out to study the structural and magnetic behaviour of $CoFe_3O_5$ between 10 and 400 K. Samples #3-5 were combined and ground to give a combined sample size of approximately 50 mg. Diffraction data were collected between 10 and 400 K on warming, using a closed cycle refrigerator with a hot plate. Diffraction patterns with a long counting time were collected at 10 K (120 μA), 50 K (120 μA), 150 K (91 μA) and 400 K (134 μA), with lower count patterns (20 μA) taken at intermediate temperatures of 25, 75, 100, 125, 200, 250 and 375 K. The crystal and magnetic structures of $CoFe_3O_5$ were Rietveld-fitted using the FullProf Suite.[8] The peak shape was refined using the Ikeda-Carpenter function, as described in Section 2.2.4. The background of the diffraction patterns is fitted using linear interpolation between a set of background points with refinable heights.

The occupancies of the three cation sites were determined with the use of the high contrast between the neutron scattering lengths of Fe and Co (9.45 and 2.49 fm respectively) in the refinement of the 400 K diffraction data (**Figure 5.7**).[9] The results reveal that the M1 site is occupied exclusively by Fe while the other two cation sites contain a mixture of Fe/Co, with a ratio of 0.78(1)/0.22(1) and 0.64(1)/0.36(1) for the M2 and M3 sites, respectively. The overall refined composition of $Co_{0.58}Fe_{3.42}O_5$ is Co-deficient. The Rietveld fit to the 400 K diffraction data also shows the presence of a small amount of CoO and $CoFe_2O_4$ impurities, with refined amounts and compositions of 11.2(7) % by volume of $Co_{0.86(1)}Fe_{0.14(1)}O$ and 3.2(1) % $Co_{0.95(1)}Fe_{2.05(1)}O_4$, showing that

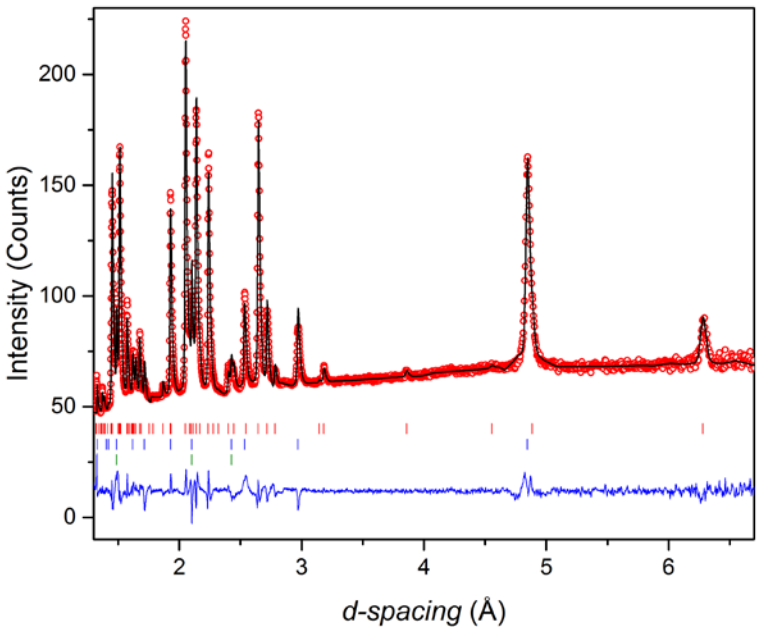

Figure 5.7 Rietveld analysis of the high resolution neutron diffraction pattern of $CoFe_3O_5$ obtained at 400 K, with red tick marks indicating the nuclear reflections of $Co_{0.58}Fe_{3.42}O_5$, blue tick marks indicating the nuclear reflections of $Co_{0.95}Fe_{2.05}O_4$, and green tick marks indicating the nuclear reflections of $Co_{0.86}Fe_{0.14}O$. (χ^2 = 13.1 %, R_{wp} = 10.7 % and R_p = 12.9 %)

these impurities are relatively Co rich. The composition of the three phases presence in the sample adds up to an overall formula of $CoFe_3O_5$. The Co/Fe occupancies of the three cation sites were fixed to the refined 400 K values in the refinement profiles of patterns obtained below 400 K.

The refined M-O distances (as shown in **Table 5.6**) were used to calculate the bond valence sums for each cation site with linear interpolation to estimate mixed charge states between Co^{2+}, Fe^{2+} and Fe^{3+}.[10,11] The M3 triangular prismatic site was found to be the largest cation site amongst the three and the M3 BVS shows that the site is occupied by divalent cations, in keeping with the other members of the MFe_3O_5 family. Similar average M-O distances were observed in the M1 and M2 octahedral sites and the BVSs indicate a mix of divalent and trivalent cations. Therefore, the site-specific composition, written

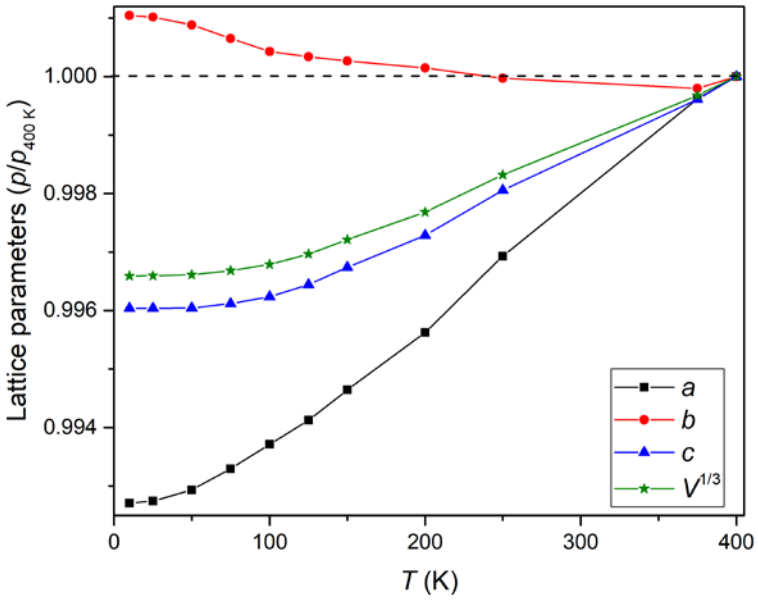

Figure 5.8 Changes to the lattice parameters relative to 400 K values obtained from powder neutron diffraction ($a_{400\ K}$ = 2.9048(2) Å, $b_{400\ K}$ = 9.7865(8) Å and $c_{400\ K}$ = 12.5884(6) Å).

as $(M3)(M1)_2(M2)O_5$ for comparison with the standard MFe_3O_5 formula, is thus $(Co^{2+}_{0.36}Fe^{2+}_{0.64})(Fe^{2+}_{0.33}Fe^{3+}_{0.67})_2(Co^{2+}_{0.22}\ Fe^{2+}_{0.11}Fe^{3+}_{0.67})O_5$ assuming that Fe is oxidised to the trivalent state in preference to Co.

Neutron diffraction patterns obtained below 400 K were refined using the site occupancy values obtained from the 400 K data. As illustrated in **Figure 5.8**, the change in lattice parameters in the measured temperature range shows similar features as the synchrotron x-ray data, with discontinuities in the lattice parameters due to magnetostrictive effects found at ≈ 300 and 100 K. The 300 K changes do not show clearly in the neutron data due to the lack of data points near the T_{C1} region. However, the data obtained between 100 and 250 K indicate anisotropic expansion in the lattice parameters, and that the rate of contraction in the *a* and *c* components decreases while the expansion along the *b* axis increases below T_{C2}. In keeping with the x-ray data, the refined

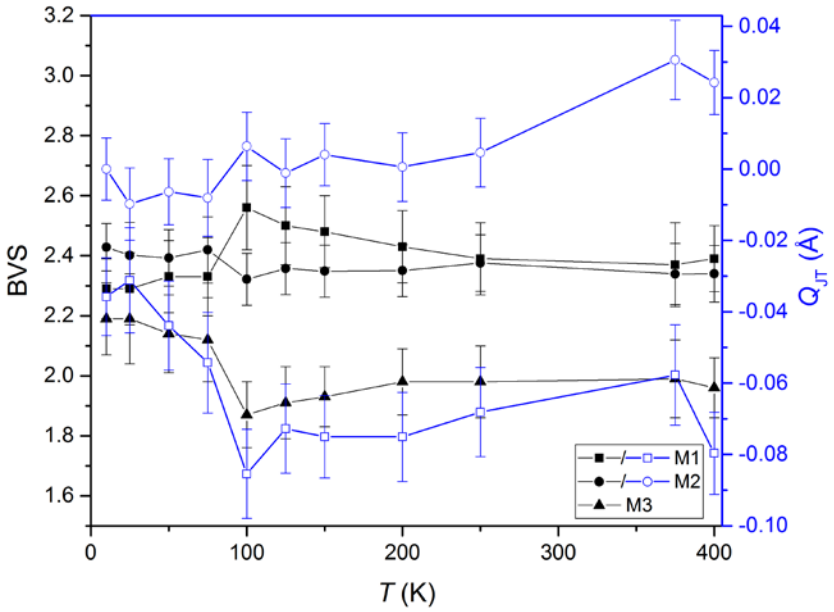

Figure 5.9 Temperature evolution of BVS (black points) and the tetragonal Jahn-Teller distortion parameter Q_{JT} for the octahedral cation sites in $CoFe_3O_5$, obtained from neutron diffraction data.

coordinates from neutron diffraction do not reveal any large changes of the crystal structure between 10 and 400 K. The temperature evolution of BVSs calculated for the three cations sites, as shown in **Figure 5.9**, indicates that the valence of the sites remains approximately constant throughout the measured temperature range. The tetragonal Jahn-Teller distortion parameter Q_{JT} (detailed in Chapter 2) was also calculated for the two octahedral sites (**Figure 5.9**) and shows small negative values for the M1 site and is almost 0 for the M2 site. The magnitudes of the obtained parameters are consistent with the Fe/Co occupancies and valences of the sites. The negative Q_{JT} values of the M1 site originate from the presence of Fe^{2+}, as Fe^{3+} has intrinsic $Q_{JT} = 0$ while orbitally-degenerate Fe^{2+} has negative Q_{JT}. Co^{2+} is also Jahn-Teller active and has positive Q_{JT}. Thus, the coexistence of Fe^{3+}, Fe^{2+} and Co^{2+} leads to a $Q_{JT} \approx 0$ at the M2 site. Small anomalies in the BVSs are observed around

Table 5.6 Metal-oxygen bond lengths with derived mean values < > and BVSs shown for $CoFe_3O_5$ at 400 K and 10 K.

Bond	Distance	
	400 K	10 K
M1-O1	1.943(7)	1.948(7)
M1-O2	2.257(9)	2.243(9)
M1-O2 (x 2)	2.038(7)	2.064(7)
M1-O3 (x 2)	2.120(8)	2.127(7)
<M1-O>	2.086(3)	2.096(3)
BVS(M1)	2.4(1)	2.5(1)
M2-O2 (x 4)	2.095(6)	2.071(5)
M2-O3 (x 2)	2.026(8)	2.040(8)
<M2-O>	2.072(3)	2.061(3)
BVS(M2)	2.4(1)	2.3(1)
M3-O1 (x 2)	1.967(9)	1.973(10)
M3-O3 (x 4)	2.245(7)	2.180(7)
<M3-O>	2.152(3)	2.111(3)
BVS(M3)	2.0(1)	2.2(1)

$T_{C2} \approx 100$ K accompanied by an increase in the Q_{JT} at the M1 site. The changes in the M1 site are consistent with intersite charge transfer, which leads to a small increase in the Fe^{3+}/Fe^{2+} ratio. There are traces of the charge ordering seen in other MFe_3O_5 materials, however the cation disorder in $CoFe_3O_5$ suppresses any clear charge and orbital ordering.

The M1 site in other MFe_3O_5 materials is found to have a higher BVS than the M2 site and complete Fe^{3+}/Fe^{2+} charge ordering over the M1/M2 sites is found in $MnFe_3O_5$ and the charge ordered phase of $CaFe_3O_5$. This is likely to be the driving force of the strong preference for Co^{2+} to substitute for Fe at the octahedral M2 site in $CoFe_3O_5$. Despite the Co disordering within the Co-deficient sample, no significant difference in the BVSs between the M1 and M2 sites is found. Details of the crystallographic information obtained from powder neutron diffraction are summarised in **Table 5.7** and **Table 5.8.** The thermal factors of the cation sites were constrained to be refined together to account

for the Co/Fe disorder in the structure. The presence of multiple phases in the sample led to the overlap of reflections also resulted in unrealistic values (negative parameters) for some of the thermal factors, hence constraints were applied to the thermal factors of the cations and anions during refinement to obtain coefficients that accounts for their thermal contributions.

Table 5.7 Refined structural parameters of $CoFe_3O_5$ in space group *Cmcm* from powder neutron diffraction data between 10 and 100 K. Estimated standard deviations in independent variables are shown in parentheses. M1 atoms are located at (½, *y*, *z*), M2 atoms with site symmetry 4*a* are located at (0, 0, 0), M3 atoms at (0, *y*, ¼), O1 atoms at (½, *y*, ¼), O2 atoms at (0, *y*, *z*) and O3 atoms at (0, *y*, *z*). The occupancy of the three cations sites were fixed to the values obtained from the 400 K neutron data, with Fe/Co ratios of 1/0, 078/0.22 and 0.64/0.36 for the M1, M2 and M3 site.

			T / K	10	25	50	75	100
Cell			*a* (Å)	2.88363(10)	2.88372(12)	2.88427(10)	2.88533(12)	2.88654(12)
			b (Å)	9.79675(25)	9.79649(30)	9.79517(27)	9.79290(31)	9.79074(33)
			c (Å)	12.53857(46)	12.53857(54)	12.53859(48)	12.53955(56)	12.54102(57)
			V (Å^3)	354.217(20)	354.219(24)	354.238(21)	354.314(24)	354.426(25)
M1	8*f*		*y*	0.241914(51)	0.24158(60)	0.24203(53)	0.24215(60)	0.24429(62)
			z	0.11760(28)	0.11726(34)	0.11744(30)	0.11731(35)	0.11675(33)
M3	4*c*		*y*	0.48344(84)	0.48374(100)	0.48388(87)	0.48349(98)	0.48462(93)
O1	4*c*		*y*	0.34599(112)	0.34461(133)	0.34404(118)	0.34379(137)	0.33964(135)
O2	8*f*		*y*	0.35868(74)	0.35816(90)	0.35752(79)	0.35760(91)	0.35443(81)
			z	0.04308(58)	0.04276(70)	0.04293(62)	0.04298(70)	0.04341(68)
O3	8*f*		*y*	0.08712(81)	0.08633(101)	0.08704(90)	0.08664(102)	0.09147(94)
			z	0.14783(62)	0.14858(78)	0.14777(68)	0.14717(78)	0.14491(70)
B_{iso} / Å^2 (M1, M2 and M3)				1.35(9)	1.18(12)	1.26(10)	1.23(11)	1.30(11)
B_{iso} / Å^2 (O1, O2 and O3)				0.75(9)	0.61(12)	0.62(10)	0.68(12)	0.66(12)
			R_p / %	9.5	11.0	9.2	11.7	12.2
			R_{wp} / %	9.0	9.5	8.7	9.7	10.0
			χ^2	14.2	2.6	12.9	2.6	2.7

Table 5.8 Refined structural parameters of $CoFe_3O_5$ in space group *Cmcm* from powder neutron diffraction data between 125 and 400 K. Estimated standard deviations in independent variables are shown in parentheses. M1 atoms are located at (½, *y*, *z*), M2 atoms with site symmetry 4*a* are located at (0, 0, 0), M3 atoms at (0, *y*, ¼), O1 atoms at (½, *y*, ¼), O2 atoms at (0, *y*, *z*) and O3 atoms at (0, *y*, *z*). The occupancy of the three cations sites were fixed to the values obtained from the 400 K neutron data, with Fe/Co ratios of 1/0, 078/0.22 and 0.64/0.36 for the M1, M2 and M3 site.

		T / K	125	150	200	250	375	400
Cell		*a* (Å)	2.88774(12)	2.88914(11)	2.89209(13)	2.89589(14)	2.90370(22)	2.90480(17)
		b (Å)	9.78984(33)	9.78915(30)	9.78796(38)	9.78625(49)	9.78454(99)	9.78653(79)
		c (Å)	12.54363(56)	12.54737(49)	12.55424(55)	12.56398(56)	12.58348(71)	12.58838(56)
		V (Å^3)	354.615(25)	354.880(22)	355.382(26)	356.062(30)	357.514(59)	357.861(39)
M1	8*f*	*y*	0.24384(61)	0.24367(52)	0.24340(59)	0.24303(60)	0.24332(72)	0.24377(55)
		z	0.11687(33)	0.11689(28)	0.11695(32)	0.11701(33)	0.11672(38)	0.11659(30)
M3	4*c*	*y*	0.48409(94)	0.48378(81)	0.48269(91)	0.48201(92)	0.48024(104)	0.47922(81)
O1	4*c*	*y*	0.34024(134)	0.34074(115)	0.34213(127)	0.34212(127)	0.34453(140)	0.34374(107)
O2	8*f*	*y*	0.35564(81)	0.35574(70)	0.35604(78)	0.35714(78)	0.35783(86)	0.35689(66)
		z	0.04288(67)	0.04351(58)	0.04324(66)	0.04366(66)	0.04493(75)	0.04470(59)
O3	8*f*	*y*	0.09059(93)	0.09025(80)	0.08913(89)	0.08903(87)	0.09098(94)	0.09021(79)
		z	0.14535(70)	0.14550(61)	0.14572(69)	0.14584(70)	0.14580(79)	0.14489(64)
B_{iso} / Å^2 (M1, M2 and M3)			1.32(11)	1.37(10)	1.56(11)	1.71(11)	1.98(12)	2.02(10)
B_{iso} / Å^2 (O1, O2 and O3)			0.70(11)	0.73(10)	0.81(11)	0.93(11)	0.88(12)	0.91(10)
		R_p / %	12.3	10.0	13.0	14.8	18.8	12.9
		R_{wp} / %	10.0	9.0	10.0	10.9	12.6	10.7
		χ^2	2.6	9.3	2.5	2.2	1.4	13.7

High resolution neutron diffraction data confirm the paramagnetic behaviour of $CoFe_3O_5$ at 400 K, with no magnetic peaks of the phase observed in the diffraction patterns above room temperature. Magnetic reflections of $CoFe_3O_5$ appear when cooled below $T_{C1} \approx 300$ K, as shown in **Figure 5.10**, with the green arrow indicating two of the most intense reflections, with *hkl* = (021) and (111). Additional magnetic reflections are found when cooled below $T_{C2} \approx 100$ K, just like what was observed in $MnFe_3O_5$ below 60 K. All of the magnetic peaks can be indexed with a magnetic propagation vector of [0 0 0] and magnetic irreducible representation analysis was carried out using BasIreps (**Table 5.9**).[8]

Rietveld fits to the 150 K diffraction patterns show an antiferromagnetic ordering of the M1 and M2 sites along the *c* axis. The spins of both sites can

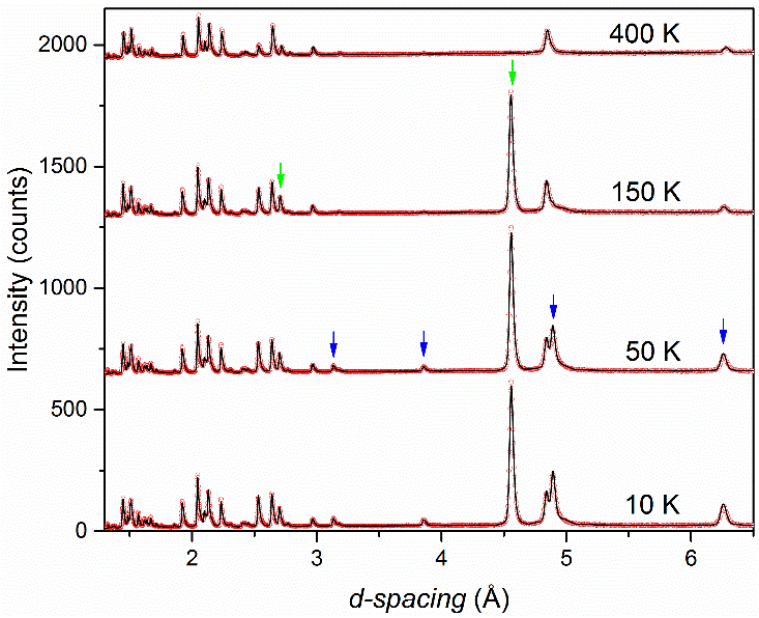

Figure 5.10 Temperature evolution of the neutron diffraction pattern of $CoFe_3O_5$. Magnetic contributions indicated by green arrows in the 150 K pattern are the (021) and (111) peaks, and those indicated by blue arrows at 50 K are the (002), (020), (022) and (004) peaks, in order of descending d-spacing.

Table 5.9 Irreducible representations (IrReps) and basis vectors (BV) for M1, M2 and M3 spin order in $CoFe_3O_5$ with propagation vector (0 0 0). The magnetically independent atoms are M1 at (½, 0.242, 0.118), M2 at (0, 0, 0) and M3 at (0, 0.483, ¼). The symmetry related positions are generated by the operators 1: (*x*, *y*, *z*), 2: (*x*-½, -*y*+½, -*z*+1), 3: (-*x*+1, *y*, -*z*+½), 4: (-*x*+½, -*y*+½, *z*+½), 5: (-*x*, *y*, -*z*+½) and 6: (*x*, -*y*+1, -*z*+1). The magnetic structures for 10-250 K were fitted using the basis vector $\Gamma_4\psi_6$ for the M1 and M2 spins. The magnetic structures for 10-75 K were fitted using basis vectors $\Gamma_3\psi_4$ and $\Gamma_4\psi_6$ for the M1 spins, $\Gamma_4\psi_6$ for the M2 spins, and $\Gamma_3\psi_4$ for the M3 spins.

IrReps	Γ_1	Γ_2		Γ_3	Γ_4		Γ_5		Γ_6	Γ_7		Γ_8
BV	ψ_1	ψ_2	ψ_3	ψ_4	ψ_5	ψ_6	ψ_7	ψ_8	ψ_9	ψ_{10}	ψ_{11}	ψ_{12}
Atoms	m_x	m_y	m_z	m_x	m_y	m_z	m_y	m_z	m_x	m_y	m_z	m_x
M1_1	+	+	+	+	+	+	+	+	+	+	+	+
M1_2	+	+	+	+	+	+	-	-	-	-	-	-
M1_3	-	-	+	+	+	-	+	-	+	-	+	-
M1_4	-	-	+	+	+	-	-	+	-	+	-	+
M2_1	+	+	+	+	+	+						
M2_5	-	-	+	+	+	-						
M3_1			+	+	+		+		+		+	
M3_6			+	+	+		-		-		-	

be described with operation $\Gamma_4\psi_6$, with a positive coefficient for the former site and negative one for the latter. The M3 site is found to remain spin disordered at 150 K as illustrated in **Figure 5.11A**. The 150 K magnetic structure is in keeping with the magnetic susceptibility measurements (**Figure 5.3**). The small moment of 0.06 μ_B that was observed in the magnetisation study suggests a very small canting in the M1 and M2 spins at a magnitude that is too small to be refined from the neutron data collected.

The rise of the new magnetic reflections below T_{C2} marks the spin order of the M3 site. A good fit was obtained to the 10 K diffraction data (**Figure 5.12**) by using the operation $\Gamma_3\psi_4$ with a negative coefficient to describe the magnetic behaviour of the Fe/Co cations at the M3 triangular prismatic site. The spins of the M3 site are aligned ferromagnetically along the *a* axis. The magnetic

Table 5.10 Refined components and total magnetic moments (μ_B) at the three cation sites in $CoFe_3O_5$ between 10 and 250 K.

Sites			M1	M2	M3
T (K)	m_x	m_z	m_{Total}	$m_z = m_{Total}$	$m_x = m_{Total}$
10	1.82(3)	3.94(4)	4.34(3)	3.31(6)	2.56(5)
25	1.80(4)	3.95(5)	4.34(5)	3.34(8)	2.51(7)
50	1.68(4)	3.89(4)	4.24(4)	3.42(7)	2.20(7)
75	1.33(6)	3.85(5)	4.07(5)	3.41(8)	1.59(10)
100	0	3.53(5)	3.53(5)	3.80(8)	0
125	0	3.52(5)	3.52(5)	3.62(8)	0
150	0	3.40(4)	3.40(4)	3.45(7)	0
200	0	3.09(5)	3.09(5)	3.00(8)	0
250	0	2.54(5)	2.54(5)	2.21(8)	0

behaviour of the M3 site is different from that of the $MnFe_3O_5$ analogue where the spins at the triangular prismatic site were aligned along *b*. This occurrence could be a consequence of the Co ions having a strong preference to an easy axis, due their magnetic anisotropy. Spin reorientation was also observed in the M1 site at 10 K. An additional operation of $\Gamma_3\psi_4$ was used to define the spin behaviour of M1. The M1 spins were found to tilt ferromagnetically toward the *a* axis, antiparallel to the M3 moment, as illustrated in **Figure 5.11B**. This results in an enhancement of the ferrimagnetic behaviour of $CoFe_3O_5$, consistent with the magnetisation study results, and leads to a net moment of approximately 1 μ_B per formula unit at 10 K. The thermal evolution of the magnitude of the ordered moments for each site and their spin ordered components are shown in **Figure 5.13**, with the refined values given in **Table 5.10**.

(A)

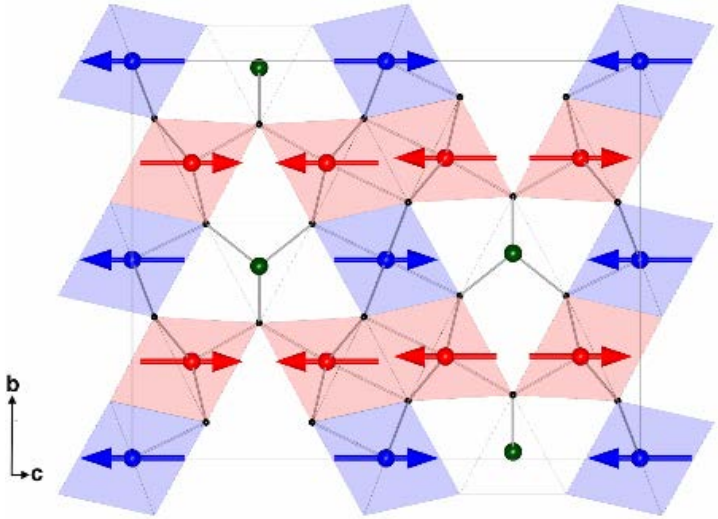

(B)

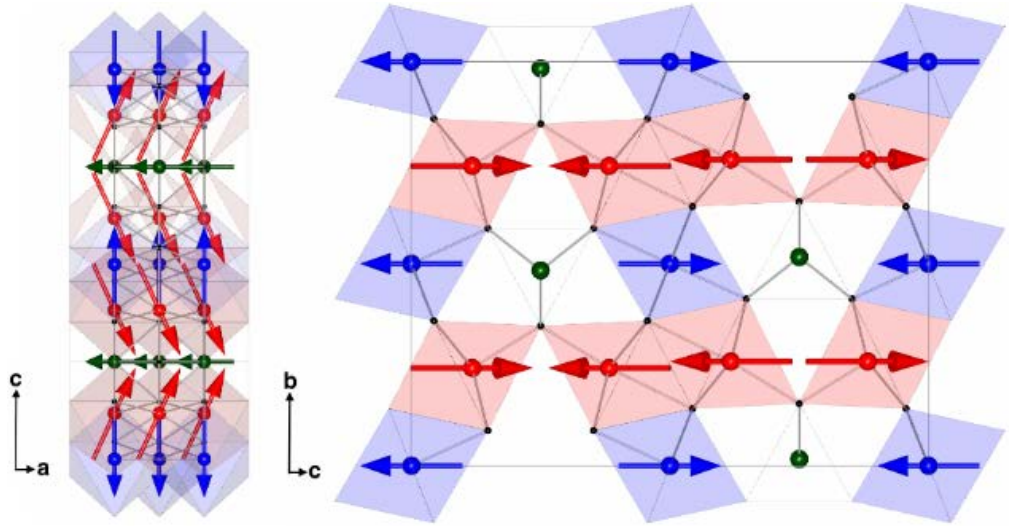

Figure 5.11 The magnetic structures of $CoFe_3O_5$ at (A) 150 K and (B) 10 K. Octahedral M1 and M2 and trigonal prismatic M3 sites and moments are shown in red, blue and green, respectively.

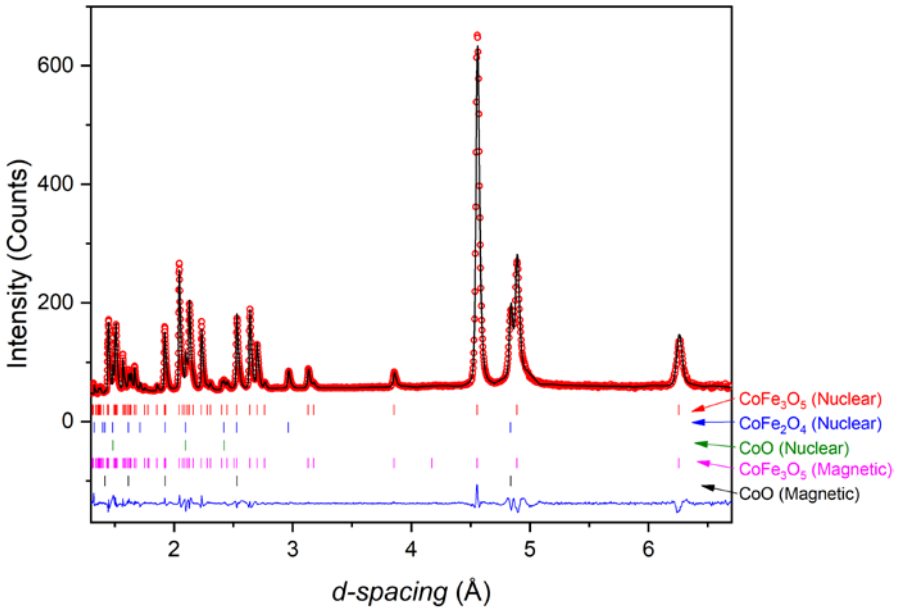

Figure 5.12 Rietveld fit to the 10 K neutron diffraction data. Tick marks, from top to bottom respectively, indicate the reflections from nuclear $CoFe_3O_5$, $CoFe_2O_4$ and CoO, and magnetic $CoFe_3O_5$ and CoO type phases. (χ^2 = 12.5, R_{wp} = 9.2% and R_p = 10.1%).

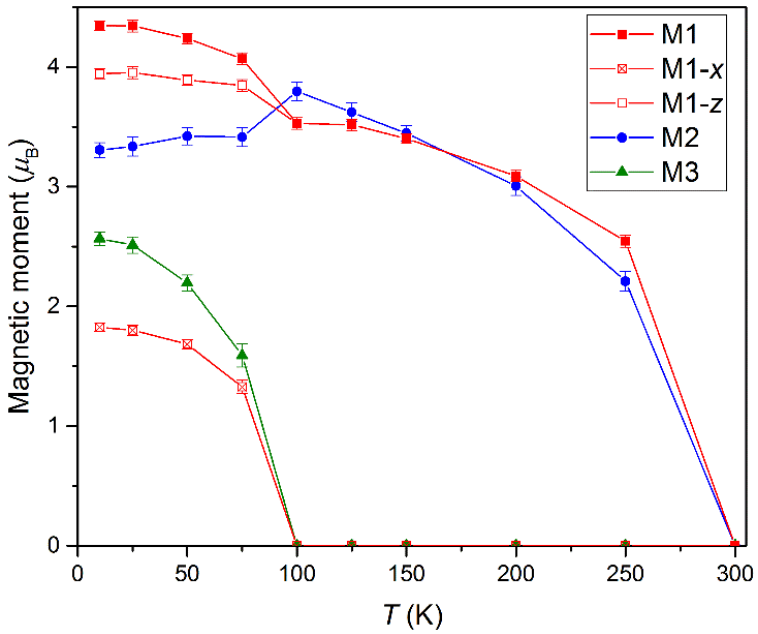

Figure 5.13 The temperature evolution of the ordered magnetic moments and the *x* and *z* components of the M1 spins.

5.3. Conclusions

$CoFe_3O_5$ was synthesised under 12 GPa of pressure, confirming that higher pressure is required to stabilise smaller cations (*M*) in the MFe_3O_5 system. Refinement of the cation site occupancy showed a Co-deficient $CoFe_3O_5$ phase ($Co_{0.58}Fe_{3.42}O_5$), suggesting that higher pressures may be required to stabilise the ideal stoichiometry. In the M^{2+} = Ca and Mn analogues, the larger M^{2+} cations were found to occupy only the trigonal prismatic sites, sometimes with a small amount of disordering. However, in $CoFe_3O_5$ the Co^{2+} was found to have a more disordered distribution over both the trigonal prismatic and octahedral sites. A strong preference of Co^{2+} for the M2 site was also revealed, which is likely due to the difference in the octahedral site potentials. However, despite this disorder of the Co cation within the structure, no significant impact on the BVSs of the octahedral sites was observed.

The crystal structure of $CoFe_3O_5$ was studied using powder synchrotron x-ray and neutron diffraction techniques. Discontinuities in the lattice parameters due to magnetostrictive effects were found at 100 and 300 K. The crystal symmetry of $CoFe_3O_5$ remained in the *Cmcm* space group throughout the measured temperature range of 10 to 400 K. BVS calculations showed the M3 site was occupied exclusively by cations with an oxidation state of 2+, and the M1 and M2 sites have a mixed 2+/3+ valance state . The BVSs of the three sites remained approximately constant between 10 and 400 K.

Just like other high-pressure MFe_3O_5 phases (*M* = Fe and Mn), $CoFe_3O_5$ displays complex magnetic behaviour. Magnetisation measurements revealed

two magnetic transitions between 2 and 400 K - a weak ferrimagnetic (canted antiferromagnetism) below T_{C1} ≈ 300 K, and an enhancement of the ferrimagnetic behaviour at T_{C2} ≈ 100 K. The magnetic structures were solved using neutron diffraction with results showing spin ordering at the M1 and M2 octahedral sites when cooled below T_{C1} and spin order of the M3 site at T_{C2} that leads to M1 spin reorientation, resulting in a second ferrimagnetic transition.

The synthesis of $CoFe_3O_5$ using high-pressure techniques, and its characterisation using property measurement systems and diffraction data collected on ID22 at the ESRF and WISH at the ISIS has resulted in a publication in ACS Inorganic Chemistry (Complex cation and spin orders in the high-pressure ferrite $CoFe_3O_5$).[12]

5.4. References

1. R. D. Shannon, *Acta Cryst.* **1976**, *A32* 751-767.

2. E. J. W. Verwey. *Nature* **1939**, *144*, 327–328.

3. M. S. Senn, J. P. Wright, J. P. Attfield. *Nature* **2012**, *481,* 173–176.

4. S. V. Ovsyannikov, M. Bykov, E. Bykova, K. Glazyrin, R. S. Manna, A. A. Tsirlin, V. Cerantola, I. Kupenko, A. V. Kurnosov, I. Kantor, A. S. Pakhomova, I. Chuvashova, A. I. Chumakov, R. Rüffer, C. McCammon, L. S. Dubrovinsky. *Nat. Chem.* **2016,** *8,* 501.

5. B. Lavina, P. Dera, E. Kim, Y. Meng, R. T. Downs, P. F. Weck, S. R. Sutton, Y. Zhao. *Proc. Natl. Acad. Sci. USA* **2011,** *108,* 17281–17285.

6. A. C. Larson, R. B. Von Dreele, *Los. Alamos National Laboratory Report LAUR,* **2004,** *748*, 86–748.

7. O. Evrard, B. Malaman, F. Jeannot, *J. Solid State Chem.* **1980,** *35,* 112–119.

8. J. Rodriguez-Carvajal, *Physica B.* **1993** *192* ,55–69.

9. V. F. *Sears Neutron News,* **1992**, *3*, No. 3, 29-37.

10. J. P. Attfield, *Solid State Sci.* **2006**, *8*, 861–867.

11. I. D. Brown, *J. Appl. Crystallogr.* **1996**, *29*, 479–480.

12. K. H. Hong, E. Solana-Madruga, M. Coduri, J. P. Attfield, *Inorg Chem.* **2018,** *57* (22), 14347-14352

Chapter 6. High-Pressure Synthesis and Properties of $NiFe_3O_5$

6.1. Introduction

Chapter 3 to 5, along with the reported discovery of Fe_4O_5, has demonstrated the versatility of the $M Fe_3O_5$ systems, where a variety of different cations can be incorporated into the structure.[1,2] Such flexibility has allowed the $M Fe_3O_5$ structure to host a plethora of different magnetic ground states through tuning the M-M distance, which resulted in different magnetic exchange interactions. The synthesis of $CoFe_3O_5$ detailed in Chapter 5 showed that it is possible to stabilise M^{2+} with ionic radius smaller than Fe^{2+} in the $M Fe_3O_5$ structure. This chapter described the synthesis and properties of $NiFe_3O_5$.

With the even smaller ionic radius of Ni^{2+} (0.69 Å) compared to Co^{2+} (0.75 Å), [3] a higher pressure is required to stabilise the M = Ni phase. With the similar ionic radii of Fe^{3+} (0.65 Å)[3] and Ni^{2+}, Ni/Fe disordering in the cation sites of the $M Fe_3O_5$ structure is expected, just like that found in $CoFe_3O_5$ (as detailed in Chapter 5). In terms of cell volume, $NiFe_3O_5$ would be the smallest known member of the $M Fe_3O_5$ family. This would mean smaller M-M separation distances compared to the others and hence stronger direct magnetic exchange interactions between cation sites, which can lead to competing magnetic ground states and the formation of magnetic structures that are not seen in related analogues.

6.2. Experimental Methods and Results

6.2.1. Synthesis of $NiFe_3O_5$

$NiFe_3O_5$ was synthesised using the high-pressure and high-temperature ceramic method. Polycrystalline NiO and Fe_3O_4, in a 1:1 ratio, were ground together using a mortar and pestle. The mixture was loaded into a Pt capsule and transferred into the two-stage Walker-type module. The synthesis of $NiFe_3O_5$ sample #1 was carried out under a pressure of 12 GPa with 20 minutes heating at 1200 °C, the same conditions used for $CoFe_3O_5$ described in Chapter 4. Initial phase characterisation was carried out using x-ray diffraction techniques. A diffraction pattern of the resulting sample (sample #1) was collected at room temperature using a Bruker D2 Phaser diffractometer, with Cu K_α radiation source (15 minutes scans of $5° \leq 2\theta \leq 70°$). A Rietveld fit

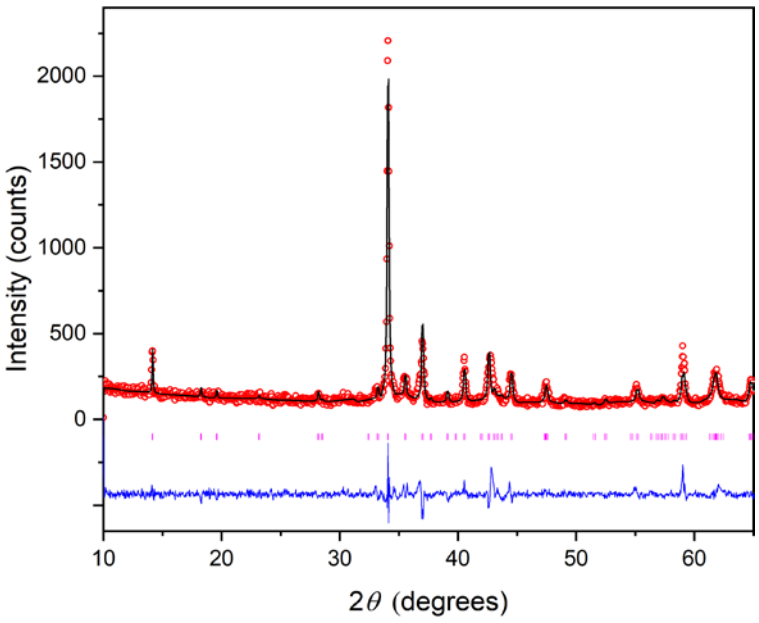

Figure 6.1 Rietveld fit to powder x-ray diffraction pattern of $NiFe_3O_5$ (sample #1) obtained using a Bruker D2 diffractometer at room temperature. (χ^2 = 2.3, R_{wp} = 28.8 % and R_p = 33.8 %.)

to the collected pattern using the FullProf Suite,[5] as shown in **Figure 6.1**, indicated the presence of the desired phase adopting the $CaFe_3O_5$-type structure.[4] $NiFe_3O_5$ was found to have an orthorhombic lattice parameters with a = 2.8897(4) Å, b = 9.7180(9) Å and c = 12.5254(13) Å at room temperature, smaller than the M^{2+} = Fe, Mn, Co and Ca analogues of MFe_3O_5,[1,2,4] consistent with the ionic size of M. In this chapter, the three cation sites in $NiFe_3O_5$ were labelled as M1 and M2 for the two octahedral sites and M3 for the triangular prism site. Refinement of the cation site occupancy was not possible with the obtained x-ray data, due to the similar Fe and Ni electron densities, and as such an accurate stoichiometry of $NiFe_3O_5$ could not be determined. During the refinement of the powder x-ray data, the M1 site was set to be occupied by Fe exclusively, whilst the M2 and M3 sites are occupied by both Ni and Fe with fixed ratios of 1:1, in keeping with the way the Co/Fe disordered in $CoFe_3O_5$. The crystal structure of $NiFe_3O_5$ was studied extensively using synchrotron x-ray and neutron diffraction techniques, as described later in Section 6.2.2 and 6.2.4.

The synthesis of $NiFe_3O_5$ was repeated for sample #2 using the same pressure and temperature conditions described above for #1, however only the reactants were found in the product, with no trace of the $NiFe_3O_5$ phase. The

Table 6.1 Synthesis conditions of each batch of the $NiFe_3O_5$ sample.

Sample	P (GPa)	Set T (°C)	Phase presence
#1	12	1200	$NiFe_3O_5$
#2	12	1200	NiO and Fe_3O_4
#3	13	1200	$NiFe_3O_5$
#4	13	1200	$NiFe_3O_5$
#5	13	1200	$NiFe_3O_5$
#6	13	1200	$NiFe_3O_5$

complete lack of the desired product indicated the pressure used was not high enough to stabilise the $NiFe_3O_5$ structure. Therefore, the synthesis pressure was increased to 13 GPa for Sample #3 - #6. Synthesis conditions of $NiFe_3O_5$ are detailed in **Table 6.1**.

6.2.2. Magnetisation measurements of $NiFe_3O_5$

The magnetic properties of $NiFe_3O_5$ were explored using a Quantum Design MPMS XL. The magnetic susceptibility of sample #1 (5 mg) was measured under zero field cooled (ZFC) and field cooled (FC) conditions between 2 and 400 K (upper panel of **Figure 6.2**), with an applied magnetic field of 2000 Oe. The sample was found to have a large magnetic susceptibility at 400 K. This indicated the presence of magnetically ordered components in the sample, which can originate from magnetic impurities. Divergence in the ZFC and FC data became more pronounced when cooled below 300 K. Discontinuities in both sets of data were observed at T_{N1} ~ 275 K, where the susceptibility of the ZFC measurement decreased with temperature, whilst a small increase was found in the FC data. The 275 K transition reassembled the antiferromagnetic transitions that were observed near room temperature in other analogues of MFe_3O_5 (*M* = Fe, Ca, Mn and Co). Small anomalies were found in the magnetisation data evident of a second magnetic transition at T_{N2} ~150 K, with the ZFC and FC measurements continued to diverge. Another magnetic transition was observed at T_{N3} ~20 K, with a sudden decrease in the ZFC susceptibility and a discontinuity in the FC data.

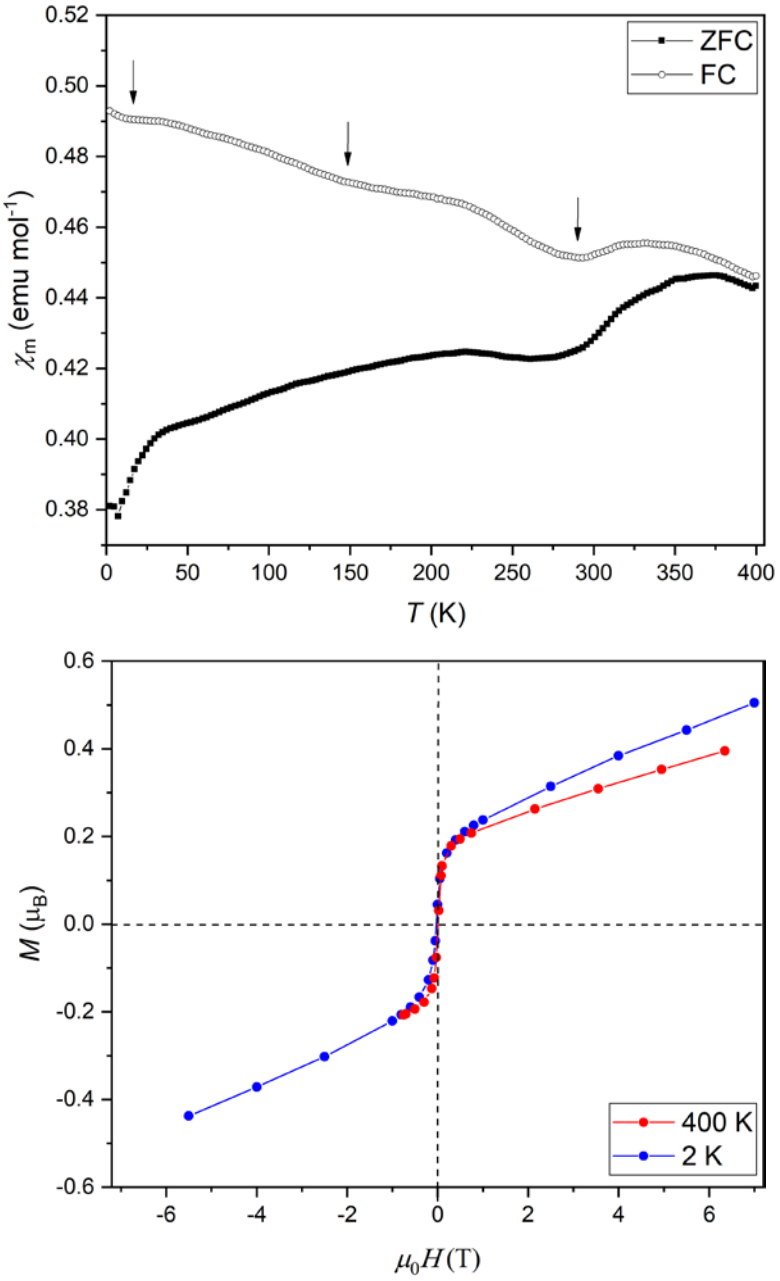

Figure 6.2 (Upper) Zero field cooled and field cooled magnetic susceptibilities for $NiFe_3O_5$ between 2 and 400 K, with arrows indicating magnetic transitions. (Lower) Magnetisation-field loops at 2 and 400 K.

Magnetisation versus field hysteresis measurements were also carried out on the $NiFe_3O_5$ sample, with an applied field between -7 and 7 T. As illustrated in the lower panel of **Figure 6.2**, a magnetisation of ~0.2 μ_B was observed in both the 2 K and 400 K data, with almost identical hysteresis loop feature in both temperatures. This suggested that the magnetisation likely came from the presence of magnetic impurities that are beyond the resolution of the D2 diffractometer. The three magnetic transitions found in the magnetic susceptibility data originated from the antiferromagnetic spin order of $NiFe_3O_5$. The magnetic structures of $NiFe_3O_5$ were studied using powder neutron diffraction and are discussed later in Section 6.2.4.

6.2.3. Synchrotron X-ray Diffraction Study of $NiFe_3O_5$

High resolution powder synchrotron x-ray diffraction data were collected for sample #1 at the ID22 beamline of the ESRF with an incident wavelength of 0.39996 Å. $NiFe_3O_5$ sample #1 (~8 mg) was packed into a glass capillary with an outer diameter of 0.3 mm. Diffraction data were collected, while the sample capillary was spinning, between 90 and 471 K on warming using an Oxford Cryostream system to control the sample environment. Rietveld refinement of the diffraction data was carried out using the FullProf Suite.[5] The peak shape was refined using a pseudo-Voigt profile, as described in Section 2.2.4. The background of the diffraction patterns is fitted using linear interpolation between a set of background points with refinable heights. A good Rietveld fit to 300 K data using the as shown in **Figure 6.3**, confirmed the presence of

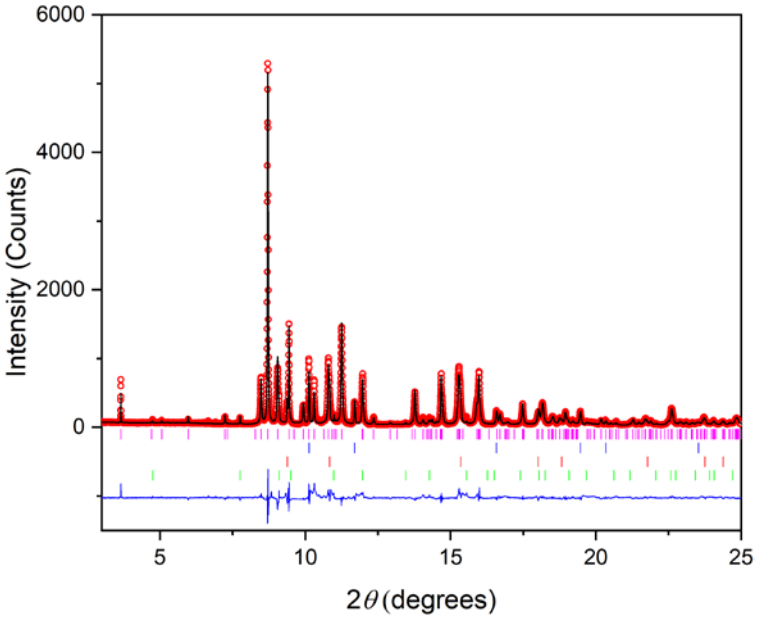

Figure 6.3 Rietveld fit of high resolution synchrotron x-ray diffraction pattern measured with λ = 0.399963 Å at 300 K, with pink tickmarks indicate the $NiFe_3O_5$ phase [92.3(6) % by volume], blue as Pt [1.56(1) %], red as NiO [3.72(6) %] and green as Fe_3O_4 [2.48(1) %]. (χ^2 = 12.9, R_{wp} = 20.9 % and R_p = 17.5 %)

$NiFe_3O_5$, with a 94.3(6) % by volume purity. A small amount of starting materials [NiO 3.77(6) % and Fe_3O_4 0.38(1) %], along with some Pt [1.58(2) %)] from the high-pressure capsule were found in the sample. The presence of magnetic spinel and NiO are likely the main contibutors to the magnetic features observed in the magnetisation measurements (**Figure 6.2**)

The $NiFe_3O_5$ sample has orthorhombic lattice parameters of *a* = 2.89126(7) Å, *b* = 9.71988(21) Å and *c* = 12.52694(27) Å, and a cell volume of 352.04(1) $Å^3$ at 300 K. Refinement of the Fe/Ni occupancy in the three cation sites was not possible using the x-ray data, due to the similar electron densities of Fe and Ni. Refinement of the 471 K diffraction pattern showed that $NiFe_3O_5$ started to thermally decompose back to NiO and Fe_3O_4. The results showed the purity

of the $NiFe_3O_5$ reduced from 92.3(5) % by volume at 300 K to 66.5(5) % at 471 K, as shown in **Figure 6.4**.

Refinement of the diffraction patterns obtained between 80 and 471 K showed that $NiFe_3O_5$ remained in the orthorhombic structure over the temperature range. The temperature revolution of the crystal structure of $NiFe_3O_5$, as shown in **Figure 6.5**, indicated isotropic thermal expansion in the lattice parameters when cooled below T_M ~ 300 K, where a small expansion in the *b* dimension was observed, while the *a* and *c* axis contracted. The changes in these lattice parameters were likely due to magnetostrictive effect.

The refined atomic positions allowed the M-O distances to be determined and to be used to estimate the occupancy of the cation sites. As shown in **Figure**

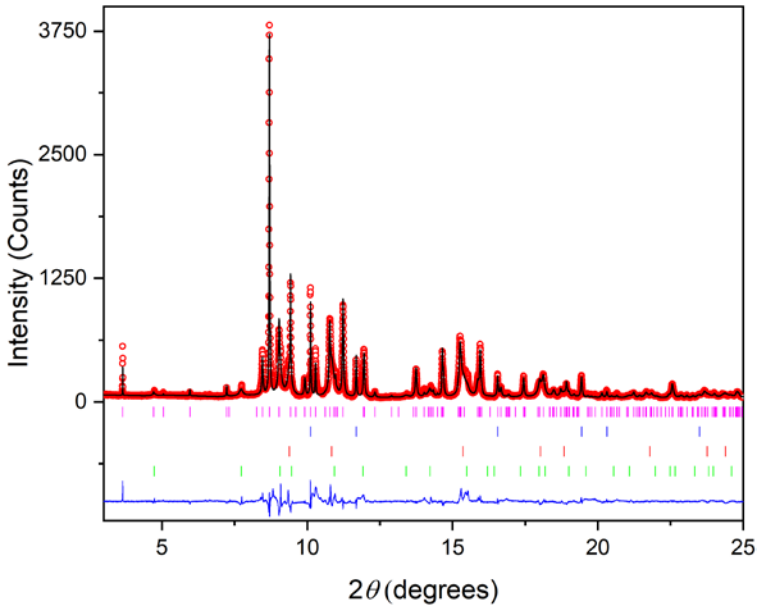

Figure 6.4 Rietveld fit of high resolution synchrotron x-ray diffraction pattern recorded at 471 K, with pink tickmarks indicate the $NiFe_3O_5$ phase [66.5(5) % by volume], blue as Pt [2.05(2) %], red as NiO [17.5(2) %] and green as Fe_3O_4 [13.9(2) %]. (χ^2 = 11.4 R_{wp} = 21.6 % and R_p = 19.2 %)

6.6, a longer average M3-O distance was found at the trigonal prismatic site, compared to those of M1-O and M2-O, just like what was found in the other MFe$_3$O$_5$ phases described in Chapter 3 to 5. It can be estimated that the M3 site is occupied predominantly by Fe^{2+}, which is the biggest cation in the system. Fe^{3+} and Ni^{2+} have similar ionic radii, so it is logical to assume Fe^{3+}/Ni^{2+} disordering in the M1 and M2. The slightly larger M1 site than M2 also suggested a higher proportion of Ni^{2+}. The similarity in the averaged M-O distance between 80 and 400 K indicated the charge distribution of $Fe^{2+/3+}$ remained more or less constant throughout the measured temperature range. The small anomalies at ~275 K are likely due to the magnetostrictive affect that are also found in similar temperature region in the lattice parameters

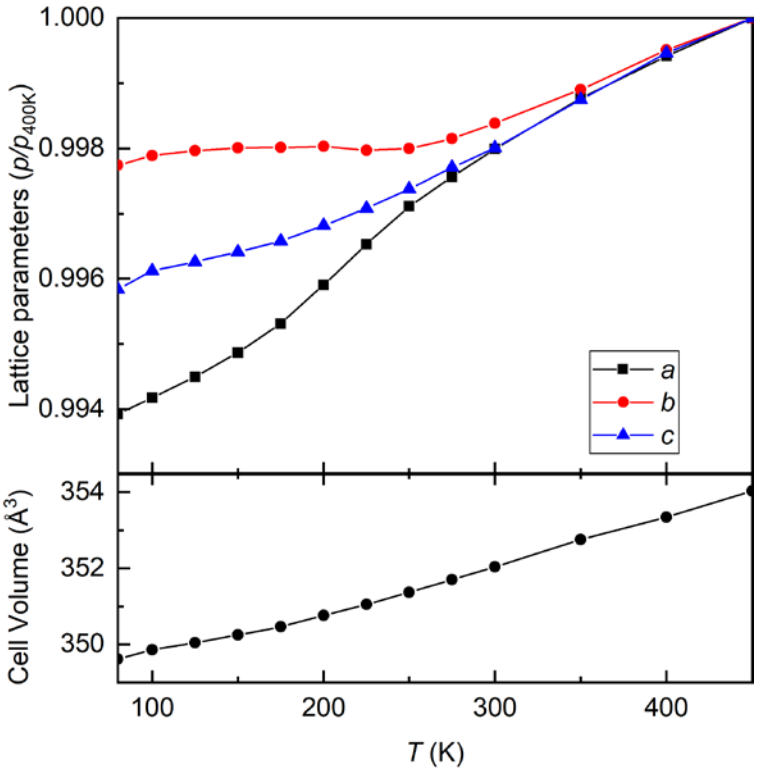

Figure 6.5 Changes in the lattice parameters relative to 450 K values [a_{450} = 2.89707(7), b_{450} = 9.73561(21) and c_{450} = 12.55195(27) Å].

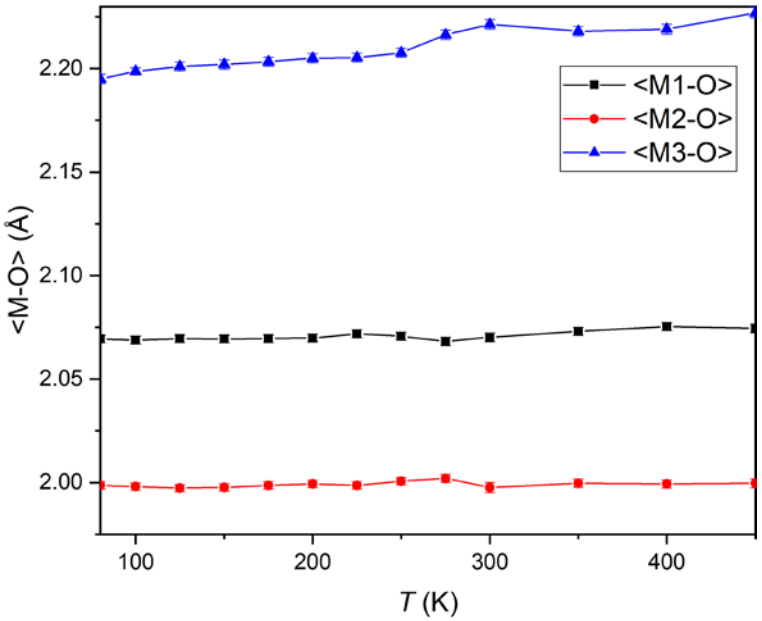

Figure 6.6 Temperature evolution of average metal-oxygen <M-O> distances between 80 and 450 K, obtained from powder synchrotron diffraction data.

(**Figure 6.5**). More accurate M-O distances were obtained using neutron diffraction data, discussed in Section 6.2.4.

Details of the refined crystallographic information from synchrotron x-ray diffraction are summarised in **Table 6.2** and **Table 6.3**. The refined thermal parameters from the synchrotron data were found to be smaller than usual, which are likely due to the absorption of x-rays by the sample. This also resulted in some unrealistic thermal factors (negative parameters), hence the thermal factors of the all the atoms were constrained to be refined together to obtain a coefficient that accounts for their thermal contributions.

Additional peaks with weak intensities were found in some of the diffraction patterns in the low scattering angle region. A stack plot of the collected patterns between 80 and 471 is shown in **Figure 6.7**, with arrows indicating the position of these reflections. The intensities of these reflection varied throughout the measured temperatures and were absent in the 225 K dataset, hence they are likely originated from spurious contributions from the instrument.

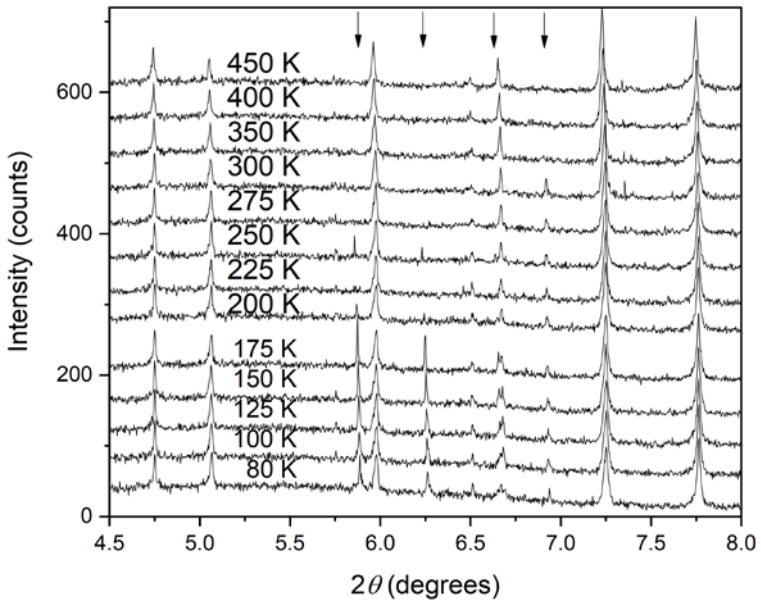

Figure 6.7 A stack plot of synchrotron x-ray diffraction patterns collected between 80 and 450 K. The figure shows reflections in the low scattering angle region (2θ = 4.5 – 8.0). Spurious peak positions are indicated with arrows.

Table 6.2 Refined structural parameters of $NiFe_3O_5$ in space group *Cmcm* from synchrotron x-ray diffraction data between 80 and 225 K using an Oxford Cryostream system. Estimated standard deviations in independent variables are shown in parentheses. M1 atoms are located at (½, *y*, *z*), M2 atoms with site symmetry 4*a* are located at (0, 0, 0), M3 atoms at (0, *y*, ¼), O1 atoms at (½, *y*, ¼), O2 atoms at (0, *y*, *z*) and O3 atoms at (0, *y*, *z*). The occupancy of the three cations sites were fixed to estimated values using the M-O distances, with M1 and M2 occupied by Fe/Ni ratios of 0.75/0.25 and 0.50/0.50, respectively, and the M3 site occupied exclusively by Fe. * The thermal parameters for all the atoms are constrained to be refined together.

			T / K	80	100	125	150	175	200	225
Cell			*a* (Å)	2.87948(5)	2.88020(5)	2.88112(5)	2.88220(6)	2.88349(6)	2.88521(6)	2.88702(6)
			b (Å)	9.71363(20)	9.71508(20)	9.71580(20)	9.71622(20)	9.71627(20)	9.71642(20)	9.71586(20)
			c (Å)	12.49975(23)	12.50330(23)	12.50501(23)	12.50692(24)	12.50901(24)	12.51198(24)	12.51530(25)
			V (Å^3)	349.62(1)	349.86(1)	350.05(1)	350.25(1)	350.46(1)	350.76(1)	351.05(1)
M1	8*f*	*y*		0.23846(14)	0.23830(14)	0.23832(14)	0.23851(15)	0.23851(15)	0.23843(15)	0.23842(15)
		z		0.11570(8)	0.11566(8)	0.11560(8)	0.11557(8)	0.11547(9)	0.11545(9)	0.11543(9)
M3	4*c*	*y*		0.49520(15)	0.49501(15)	0.49480(15)	0.49457(16)	0.49440(16)	0.49421(16)	0.49406(16)
O1	4*c*	*y*		0.33597(70)	0.33540(72)	0.33508(72)	0.33508(73)	0.33472(74)	0.33449(74)	0.33428(75)
O2	8*f*	*y*		0.36821(49)	0.36861(51)	0.36888(51)	0.36883(51)	0.36890(51)	0.36899(51)	0.36917(52)
		z		0.04555(35)	0.04573(37)	0.04578(37)	0.04562(37)	0.04590(38)	0.04598(38)	0.04591(39)
O3	8*f*	*y*		0.09781(53)	0.09828(55)	0.09847(55)	0.09836(56)	0.09852(56)	0.09869(56)	0.09843(57)
		z		0.13876(31)	0.13868(33)	0.13856(33)	0.13854(33)	0.13859(33)	0.13865(33)	0.13872(34)
			B_{iso} / Å^{2}*	0.17(1)	0.21(2)	0.22(2)	0.24(2)	0.27(2)	0.30(2)	0.32(2)
			R_p / %	14.2	14.8	15.0	15.1	15.2	15.3	15.5
			R_{wp} / %	16.7	17.5	17.6	17.7	17.8	17.9	18.3
			χ^2	8.6	9.7	9.7	9.9	9.9	10.0	10.4

Table 6.3 Refined structural parameters of $NiFe_3O_5$ in space group *Cmcm* from synchrotron x-ray diffraction data between 250 and 471 K using an Oxford Cryostream system. Estimated standard deviations in independent variables are shown in parentheses. M1 atoms are located at (½, *y*, *z*), M2 atoms with site symmetry 4*a* are located at (0, 0, 0), M3 atoms at (0, *y*, ¼), O1 atoms at (½, *y*, ¼), O2 atoms at (0, *y*, *z*) and O3 atoms at (0, *y*, *z*). The occupancy of the three cations sites were fixed to estimated values using the M-O distances, with M1 and M2 occupied by Fe/Ni ratios of 0.75/0.25 and 0.50/0.50, respectively, and the M3 site occupied exclusively by Fe. * The thermal parameters for all the atoms are constrained to be refined together.

			T / K	250	275	300	350	400	450	471
Cell			*a* (Å)	2.88870(6)	2.89001(6)	2.89126(7)	2.89350(6)	2.89538(6)	2.89707(7)	2.89739(9)
			b (Å)	9.71611(20)	9.71759(20)	9.71988(21)	9.72492(20)	9.73084(20)	9.73561(21)	9.73441(25)
			c (Å)	12.51901(25)	12.52317(26)	12.52694(27)	12.53626(26)	12.54515(26)	12.55195(27)	12.55047(33)
			V (Å^3)	351.37(1)	351.70(1)	352.04(1)	352.76(1)	353.34(1)	354.03(1)	353.98(2)
M1	8*f*		*y*	0.23847(15)	0.23808(16)	0.23857(17)	0.23835(16)	0.23845(16)	0.23838(19)	0.23828(25)
			z	0.11536(9)	0.11521(9)	0.11510(10)	0.11520(9)	0.11517(9)	0.11485(11)	0.11432(14)
M3	4*c*		*y*	0.49390(16)	0.49398(17)	0.49309(18)	0.49327(17)	0.49265(17)	0.49238(20)	0.49209(27)
O1	4*c*		*y*	0.33404(76)	0.33307(79)	0.33055(83)	0.33279(78)	0.33251(78)	0.33096(88)	0.33374(120)
O2	8*f*		*y*	0.36914(53)	0.36876(55)	0.36931(58)	0.36964(54)	0.36956(54)	0.36963(61)	0.37203(80)
			z	0.04606(39)	0.04683(41)	0.04642(43)	0.04629(41)	0.04619(41)	0.04654(46)	0.04661(62)
O3	8*f*		*y*	0.09885(58)	0.09928(60)	0.09833(64)	0.09892(59)	0.09835(59)	0.09839(68)	0.10132(92)
			z	0.13872(34)	0.13793(36)	0.13779(37)	0.13801(35)	0.13796(35)	0.13741(39)	0.13705(52)
			B_{iso} / Å^{2}*	0.35(2)	0.40(2)	0.45(2)	0.49(2)	0.56(2)	0.67(2)	0.73(3)
			R_p / %	15.6	16.2	17.5	16.0	16.0	17.5	19.2
			R_{wp} / %	18.4	19.4	20.9	19.0	18.9	20.7	21.6
			χ^2	10.5	11.7	12.9	10.9	10.3	12.0	11.4

6.2.4. Powder Neutron Diffraction Study

High intensity powder neutron diffraction experiments were carried out at the D20 beamline of the ILL to study the structural properties, as well as the magnetic behaviour of $NiFe_3O_5$. Diffraction data were collected on a ~45 mg $NiFe_3O_5$ sample (from Sample #4-6), using a neutron wavelength of 2.41 Å. Diffraction patterns were collected at 1.5 K, 110 K, 220 K, 300 K and 400 K, using a helium cryostat. Diffraction data of $NiFe_3O_5$ were Rietveld-fitted using the FullProf Suite.[5] The peak shape was refined using the Ikeda-Carpenter function, as described in Section 2.2.4. The background of the diffraction patterns is fitted using linear interpolation between a set of background points with refinable heights. Refinement of the 300 K diffraction data (**Figure 6.8**) showed an orthorhombic crystal structure (in the *Cmcm* space group) at room temperature, with lattice parameters of a = 2.8786 (3) Å, b = 9.6785(9) Å and

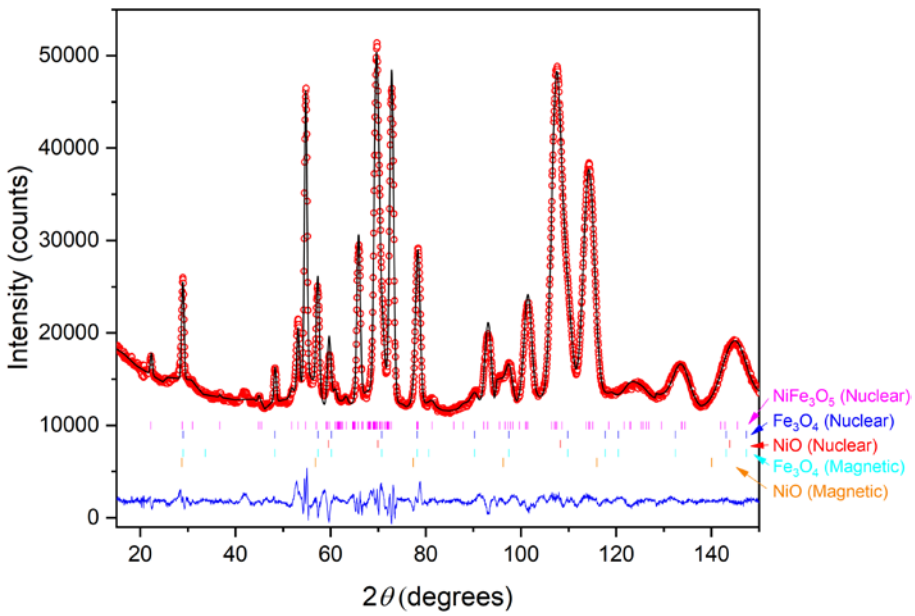

Figure 6.8 Rietveld fit to the 300 K neutron diffraction pattern of $NiFe_3O_5$, Tick marks from top to bottom respectively show reflections from nuclear $NiFe_3O_5$, Fe_3O_4 and NiO, and magnetic Fe_3O_4 and NiO type phases. (χ^2 = 11.6, R_{wp} = 7.8 % and R_p = 8.0 %)

c = 12.4708(10) Å, similar to what was obtained from synchrotron diffraction data.

The Rietveld fitted diffraction pattern showed a 77(2) % by volume pure sample, with the remaining compositions made up of components of the starting materials from high-pressure synthesis - Fe_3O_4 [10.7(2) % by volume] and NiO [12.7(3) %]. Refinement of the cation site occupancy was not possible, due to the similarity in the neutron scattering cross section between Fe (9.5 fm) and Ni (10.3 fm),[6] combining with the small sample size. Therefore, the stoichiometric composition of $NiFe_3O_5$ and the impurities in the sample cannot be determined.

Using the large neutron scattering length of oxygen, accurate M-O distances were determined using neutron diffraction techniques. The average M-O distances obtained from the refined diffraction patterns between 1.5 and 400 K are presented in **Table 6.4**. The 400 K M-O distances showed the M3 triangular prismatic is larger than the other two octahedral sites (M1 and M2). The neutron results support what was observed in the synchrotron data that the M3 site is likely occupied primarily by the larger Fe^{2+} ions and the M1 and M2 contain a mixture of Fe^{3+}/Ni^{2+}. The larger M1 site than M2 suggested a strong Ni^{2+} preference on M1. The M2-O average distance remained constant

Table 6.4 Mean values of metal-oxygen bond lengths (Å) with derived shown for $NiFe_3O_5$ at between 1.5 and 400 K.

T (K)	1.5	110	220	300	400
M1-O	2.051(3)	2.069(2)	2.105(3)	2.084(3)	2.108(3)
M2-O	2.000(2)	2.012(2)	1.984(2)	1.994(2)	1.977(2)
M3-O	2.209(3)	2.149(2)	2.148(3)	2.156(3)	2.139(3)

from 400 to 1.5 K, however, an increase in the difference in the size between M1 and M3 was found at 1.5 K, indicating possible charge redistribution below T_{N3} ~20 K. However, the effect of the nuclear and magnetic reflections overlapping must be taken into consideration, along with the limit in diffraction data resolution, which can result in less than accurate atomic positions.

Refinement of the lattice parameters and cell volume of $NiFe_3O_5$ showed a decrease in the lattice cell when cooled to 1.5 K. The magnetostrictive effects that were found in the synchrotron results data were not observed in the neutron data, due to the limited number of temperature steps. Details of the refined crystallographic information from neutron diffraction are summarised in **Table 6.5**. The overlapping of diffraction peaks from multiple phases in the sample, Ni/Fe disordering, combining with the limited resolution of the obtained diffraction patterns have resulted in unreliable, and some unrealistic (negative parameters) thermal factors. Therefore, the thermal parameters for all the atoms are constrained to be refined together to obtain a coefficient that accounts for their thermal contributions. The large χ^2 found in the 1.5 K refinement profiles is likely resulted from the additional number of refined parameters from the magnetic phase.

Table 6.5 Refined structural parameters of $NiFe_3O_5$ in space group *Cmcm* from powder neutron diffraction data between 1.5 and 400 K. Estimated standard deviations in independent variables are shown in parentheses. M1 atoms are located at (½, *y*, *z*), M2 atoms with site symmetry 4*a* are located at (0, 0, 0), M3 atoms at (0, *y*, ¼), O1 atoms at (½, *y*, ¼), O2 atoms at (0, *y*, *z*) and O3 atoms at (0, *y*, *z*). The occupancy of the three cations sites were fixed to estimated values using the M-O distances, with M1 and M2 occupied by Fe/Ni ratios of 0.75/0.25 and 0.50/0.50, respectively, and the M3 site occupied exclusively by Fe. * The thermal parameters for all the atoms are constrained to be refined together. ** The thermal parameters are fixed. *** Refinement was carried out without the Le Bail model of the $NiFe_3O_5$ magnetic phase with a *k*-vector = [0 0.38 0].

		T / K	1.5***	110	220	300	400
Cell		*a* (Å)	2.86957(17)	2.86635(10)	2.87280(12)	2.87870(12)	2.88232(13)
		b (Å)	9.66543(70)	9.67487(41)	9.673336(49)	9.67902(42)	9.68712(46)
		c (Å)	12.44070(69)	12.44286(38)	12.45288(50)	12.47219(47)	12.48444(51)
		V (Å^3)	345.05(4)	345.06(2)	346.6(3)	347.51(3)	348.58(3)
M1	8*f*	*y*	0.24679(96)	0.24987(50)	0.24612(65)	0.24496(62)	0.24738(62)
		z	0.11541(33)	0.11386(17)	0.11498(26)	0.11192(28)	0.11260(29)
M3	4*c*	*y*	0.48043(82)	0.48211(44)	0.48465(65)	0.48383(57)	0.47616(56)
O1	4*c*	*y*	0.33014(145)	0.34223(82)	0.33682(109)	0.32931(116)	0.33218(106)
O2	8*f*	*y*	0.36730(82)	0.36217(50)	0.36675(59)	0.36953(58)	0.37143(56)
		z	0.04676(66)	0.04526(36)	0.04111(45)	0.04151(41)	0.03902(42)
O3	8*f*	*y*	0.10402(92)	0.09095(68)	0.08780(102)	0.09005(105)	0.08470(97)
		z	0.13043(63)	0.14077(37)	0.14160(41)	0.14561(41)	0.14610(40)
		B_{iso} / Å^2	0.10**	0.15**	0.24(8)*	0.22(8)*	0.21(8)*
		R_p / %	10.1	4.9	8.4	8.0	8.4
		R_{wp} / %	10.8	5.5	8.2	7.8	8.3
		χ^2	24.5	8.4	13.1	11.6	13.2

The magnetic reflections observed in the 300 K diffraction pattern were indexed, as shown in (**Figure 6.8**) and were found to be originated from the impurities. Refined magnetic moments of the cation sites in Fe_3O_4 [2.0(1) and 1.4(1) μ_B per formula unit from the tetrahedral and octahedral sites, respectively] and NiO [3.33(8) μ_B per formula unit] indicated Fe/Ni disordering in both components. The lack of $NiFe_3O_5$ magnetic peaks in the diffraction pattern confirmed $NiFe_3O_5$ exhibits paramagnetic behaviour at room temperature and the magnetisation observed in the magnetic susceptibility study at 300 K (**Figure 6.2**) likely came from the magnetic spinel and NiO presence in the sample.

A stack plotting of the low scattering angle regions of neutron diffraction patterns collected between 1.5 and 400 K is shown in **Figure 6.9**, highlighting the temperature evolution of $NiFe_3O_5$ magnetic reflections. The 220 K data confirmed the magnetic transition observed in the magnetisation

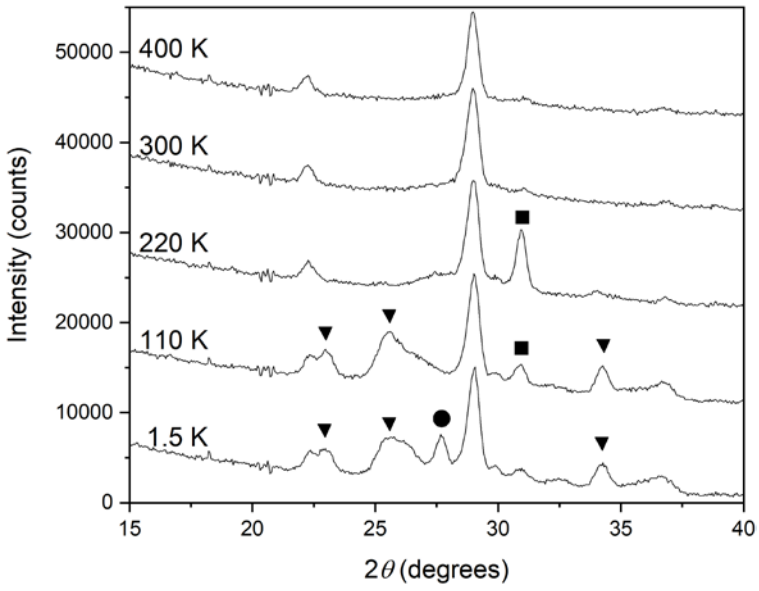

Figure 6.9 Temperature evolution of the neutron diffraction pattern of $NiFe_3O_5$. Magnetic peak contributions from magnetic structure with *k*-vector = [0 0 0], [0 0.38 0] and [½ ½ 0] are labelled by square, triangle and circle symbols, respectively.

Table 6.6 Irreducible representations (IrReps) and basis vectors (BV) for M1, M2 and M3 spin order in $NiFe_3O_5$ with *k*-vector [0 0 0]. The magnetically independent atoms are M1 at (½, 0.242, 0.118), M2 at (0, 0, 0) and M3 at (0, 0.483, ¼). The symmetry related positions are generated by the operators 1: (*x*, *y*, *z*), 2: (-*x*+½, -*y*+½, *z*+½), 3: (-*x*+1, *y*, -*z*+½), 4: (*x*-½, -*y*+½, -*z*+½) and 5: (-*x*, -*y*+1, *z*+½). Magnetic structures at 220 K were fitted using basis vector $\Gamma_5\psi_8$ for M1 and M2 spins.

IrReps	Γ_1	Γ_2		Γ_3		Γ_4	Γ_5		Γ_6	Γ_7	Γ_8	
BV	ψ_1	ψ_2	ψ_3	ψ_4	ψ_5	ψ_6	ψ_7	ψ_8	ψ_9	ψ_{10}	ψ_{11}	ψ_{12}
Atoms	m_x	m_y	m_z	m_y	m_z	m_x	m_y	m_z	m_x	m_x	m_y	m_z
M1_1	+	+	+	+	+	+	+	+	+	+	+	+
M1_2	-	-	+	-	+	-	+	-	+	+	+	-
M1_3	-	+	-	-	+	+	+	-	-	+	-	+
M1_4	+	-	-	+	+	-	+	+	-	+	-	-
M2_1	+			+	+		+	+		+		
M2_2	-			-	+		+	-		+		
M3_1		+			+	+	+			+		+
M3_5		-			+	-	+			+		-

measurements at T_{N1} = 275 K, revealing the spin order transition of the M1 and M2 octahedral sites in $NiFe_3O_5$. The observed magnetic reflection, with hkl values of (021), labelled with a square in **Figure 6.9**, was indexed with a with a magnetic propagation vector (*k*-vector) of [0 0 0]. Magnetic symmetry analysis was carried out using BasIreps (**Table 6.6**),[5] A Rietveld fit to the 220 K neutron diffraction pattern (**Figure 6.10A**) shows antiferromagnetic ordering of the M1 and M2 sites along the *c* axis, as illustrated in **Figure 6.10B**. The spin orientations of both cation sites are described by the symmetry operator $\Gamma_5\psi_8$, where a positive coefficient was used for the M1 cation and a negative value for that of M2. The M3 site is found to remain spin disordered at 220 K. The magnetic moment of M1 and M2 sites were constrained to be refined together and gave a refined moment of 1.15(2) μ_B per formula unit. The weak magnetic moment could be caused by local magnetic interactions that contributed to the diffused magnetic scattering found at $2\theta \sim 28$ degrees in the 220 K diffraction pattern.

(A)

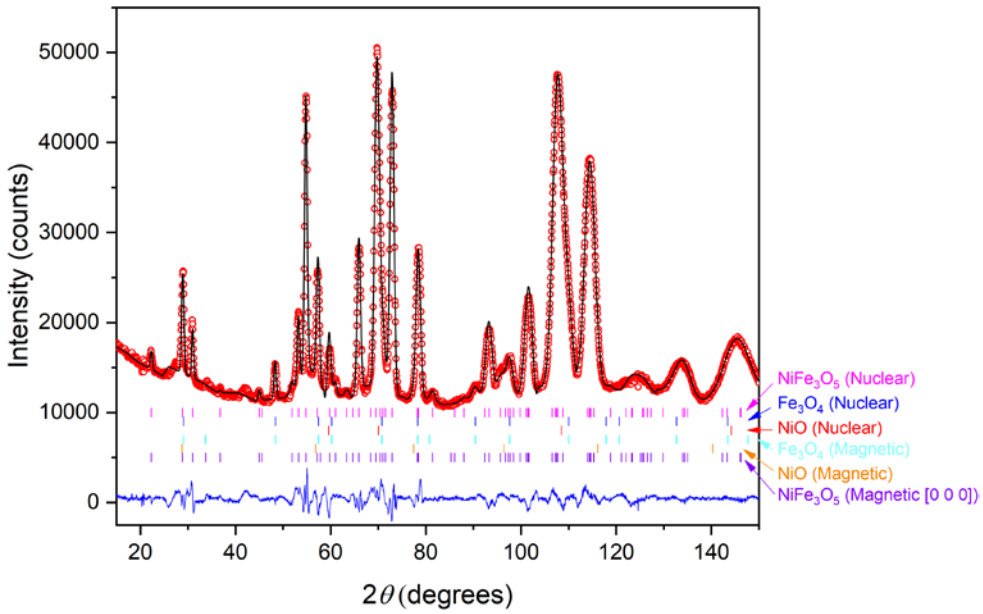

(B)

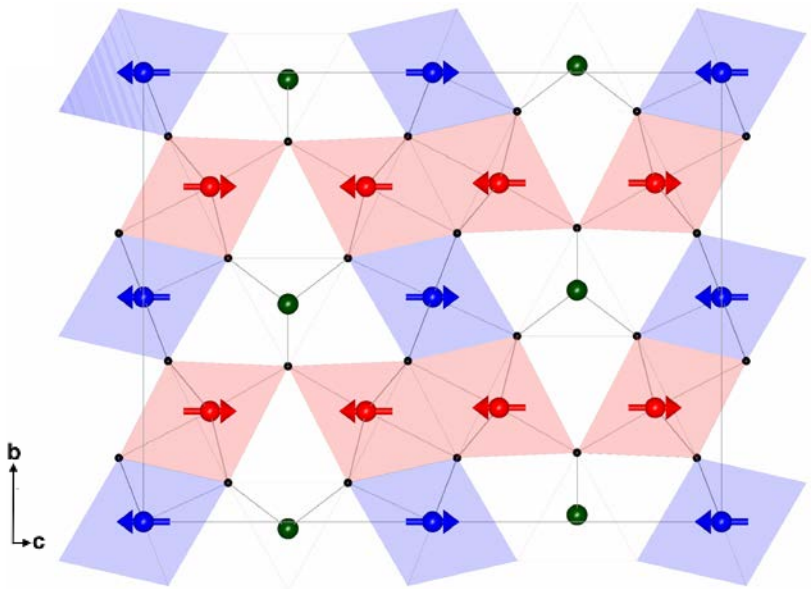

Figure 6.10 (A) Rietveld fit to the 220 K data. Markers from top to bottom respectively show reflections from nuclear $NiFe_3O_5$, Fe_3O_4 and NiO, and magnetic Fe_3O_4, NiO, $NiFe_3O_5$ [0 0 0] phases. (χ^2 = 13.1, R_{wp} = 8.2 % and R_p = 8.4 %). (A) Magnetic structure of $NiFe_3O_5$ at 220 K, with a *k*-vector = [0 0 0]. Red and blue MO_6 octahedra represent M1 and M2 sites respectively, channelled by M3 shown in green.

As illustrated in **Figure 6.7**, the intensity of (021) magnetic peak diminishes in the 110 K diffraction pattern, and new magnetic reflections (labelled with triangle in **Figure 6.9**) were observed. These new magnetic peaks have hkl values of (0 0.38 2), (0 2.38 1) and (0 0.38 3) and were indexed with an incommensurate *k*-vector of [0 0.38 0]. However, the incommensurate magnetic structure could not be solved with the collected diffraction data, due to the small sample size and the presence of impurities that overlapped with the magnetic reflections of $NiFe_3O_5$. Higher resolution diffraction data would be required for the incommensurate magnetic peaks to be fitted properly. A Rietveld fit to the 110 K pattern is shown in **Figure 6.11**, with the *k*-vector = [0 0.38 0] magnetic phase fitted with a Le Bail model.

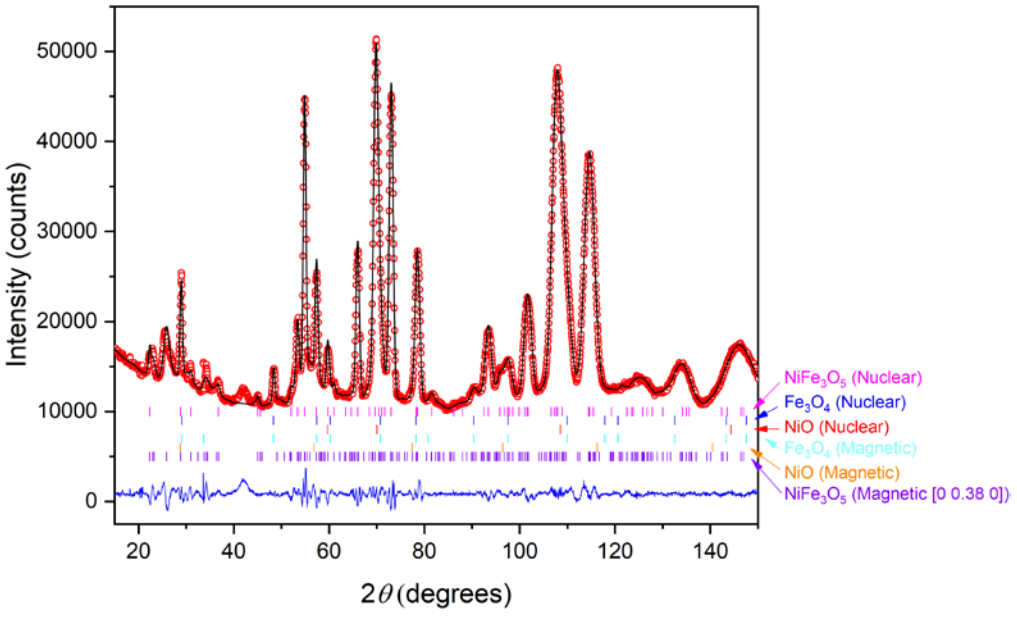

Figure 6.11 Rietveld plot for the 110 K data. Markers from top to bottom respectively show reflections from nuclear $NiFe_3O_5$, Fe_3O_4 and NiO, and magnetic Fe_3O_4, NiO, $NiFe_3O_5$ [0 0.38 0] phases. The magnetic phase of $NiFe_3O_5$ was fitted using a Le Bail model. (χ^2 = 8.4, R_{wp} = 5.5 % and R_p = 4.9 %).

Table 6.7 Irreducible representations (IrReps) and basis vectors (BV) for M1, M2 and M3 spin order in $NiFe_3O_5$ with *k*-vector [½ ½ 0]. The magnetically independent atoms are M1 at (½, 0.242, 0.118), M2 at (0, 0, 0) and M3 at (0, 0.483, ¼). The symmetry related positions are generated by the operators 1: (*x*, *y*, *z*), 2: (-*x*, -*y*, *z*+½), 3: (-*x*, -*y*, -*z*) and 4: (*x*, *y*, -*z*+½). Magnetic structures at 1.5 K were fitted using basis vector $\Gamma_2\psi_6$ for M1, M2 and M3 spins.

IrReps	Γ_1			Γ_2			Γ_3			Γ_4		
BV	ψ_1	ψ_2	ψ_3	ψ_4	ψ_5	ψ_6	ψ_7	ψ_8	ψ_9	ψ_{10}	ψ_{11}	ψ_{12}
Atoms	m_x	m_y	m_z	m_x	m_y	m_z	m_x	m_y	m_z	m_x	m_y	m_z
M1_1	+	+	+	+	+	+	+	+	+	+	+	+
M1_2	-	-	+	-	-	+	+	+	-	+	+	-
M1_3	-	-	-	+	+	+	-	-	-	+	+	+
M1_4	+	+	-	-	-	+	-	-	+	+	+	+
M2_1				+	+	+				+	+	+
M2_2				-	-	+				+	+	-
M3_1	+	+				+			+	+	+	
M3_2	-	-				+			-	+	+	

An additional magnetic peak was observed in the 1.5 K diffraction data (as shown in **Figure 6.9**, labelled with a circle symbol) that corresponded to the low temperature magnetic transition, shown in **Figure 6.2**, at T_{N3} ~20 K. The reflection originated from the hkl = (½ ½ 1) plane and was indexed with a *k*-vector of [½ ½ 0]. Magnetic symmetry analysis was carried out (**Table 6.7**) and the magnetic reflection was fitted using a the Γ_2 symmetry operator with a basis vector of ψ_6 for the spins of all three cation sites. Positive coefficients were used for the M1 and M2 cations and a negative value for the M3 site. The [½ ½ 0] magnetic structure, as presented in **Figure 6.12**, showed the M1 and M2 and M3 cations are ordered along *c* antiferromagnetically. The refined magnetic moments of the three cation sites of $NiFe_3O_5$ between 1.5 and 220 K are summarised in **Table 6.8**. The Rietveld fit to the 1.5 K diffraction pattern (**Figure 6.13**) was carried out without including the Le Bail model of the [0 0.38 0] magnetic phase, as the intensity fitting model can often compensate for the

intensity that originated from other phases in the overlapped areas, such as in this case with the magnetic contribution of the [½ ½ 0] phase. The coexistence of two magnetic structures in $NiFe_3O_5$ at 1.5 K is likely due to the presence of domains with different Fe/Ni disordering in the cation sites of $NiFe_3O_5$.

Table 6.8 Refined components and total magnetic moments (μ_B) at the three cation sites in $NiFe_3O_5$ between 1.5 and 220 K.

	Sites	M1	M2	M3
T (K)	k-vector	$m_z = m_{Total}$	$m_z = m_{Total}$	$m_x = m_{Total}$
1.5	[0 0.38 0] [½ ½ 0]	- 1.8(1)	- 1.6(2)	- 0.7(1)
110	[0 0.38 0]	-	-	-
220	[0 0 0]	1.15(2)	1.15(2)	0

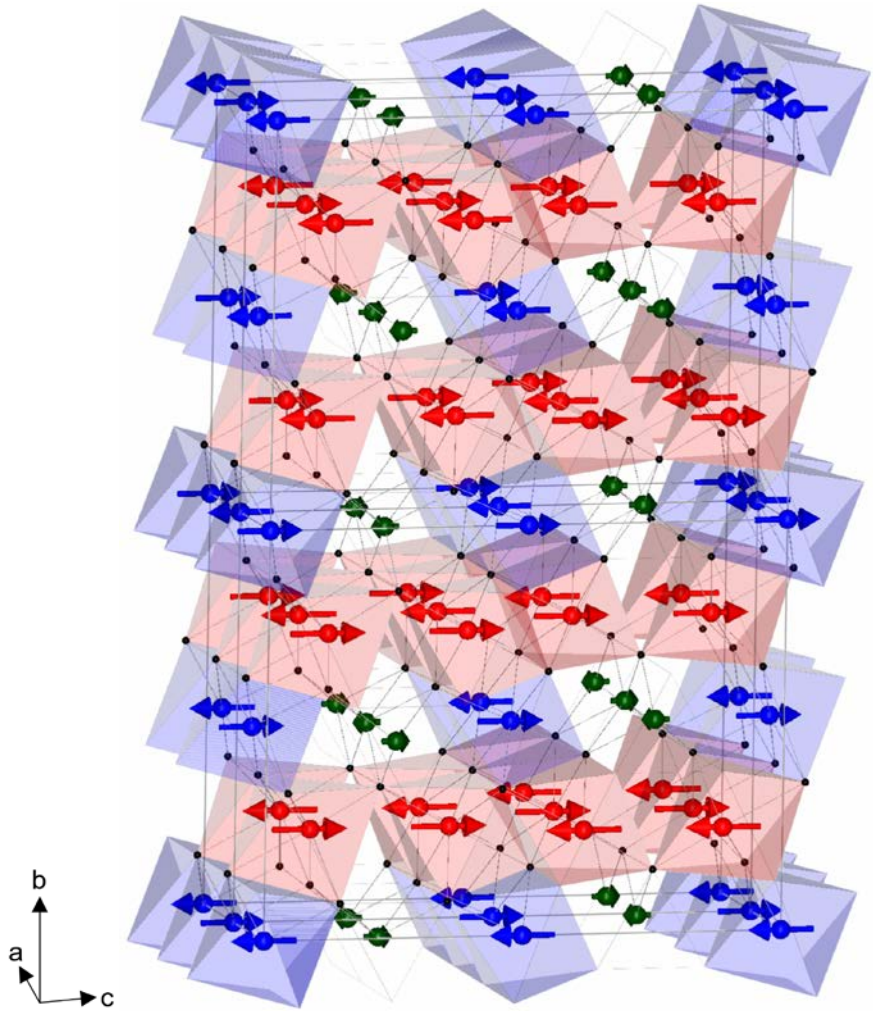

Figure 6.12 Magnetic structures of $NiFe_3O_5$ at 1.5 K with *k*-vector of [½ ½ 0]. Octahedral M1 and M2 and trigonal prismatic M3 sites and moments are shown as red, blue and green, respectively.

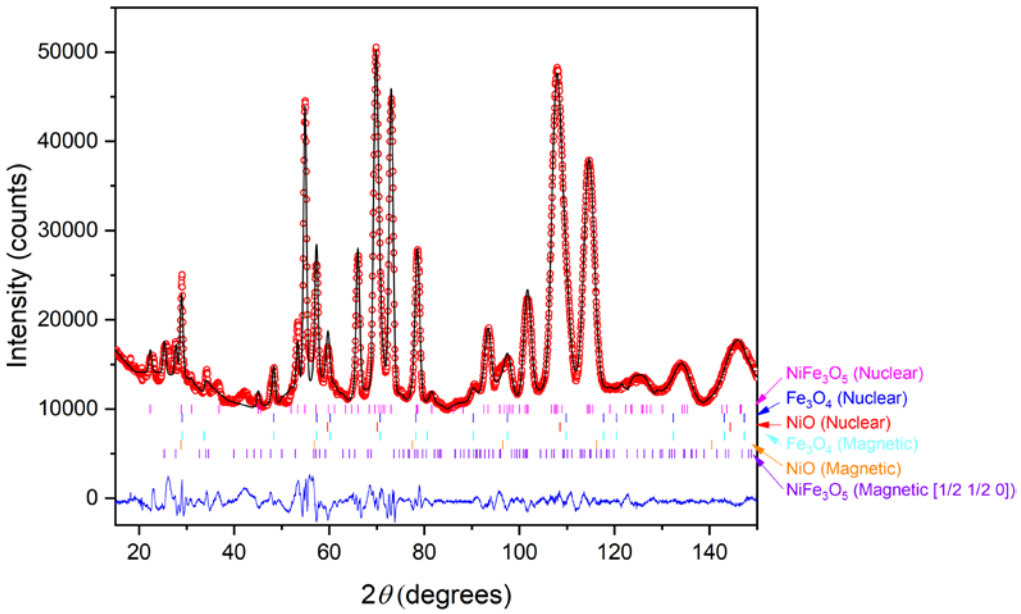

Figure 6.13 Rietveld plot for the 1.5 K data. Markers from top to bottom respectively show reflections from nuclear $NiFe_3O_5$, Fe_3O_4 and NiO, and magnetic Fe_3O_4, NiO, $NiFe_3O_5$ [½ ½ 0] phases. (χ^2 = 24.5, R_{wp} = 10.8 % and R_p = 10.1 %).

6.3. Conclusions

$NiFe_3O_5$ was synthesised under a pressure of 13 GPa at 1200 °C. Diffraction studies showed the presence of starting materials in the sample, suggesting a higher pressure may be required to stabilise the high-pressure phase, or a more rapid cooling method may be used to avoid the reformation of more thermodynamically favourable phases. As with the other analogues of the MFe_3O_5 system, $NiFe_3O_5$ crystallised into the $CaFe_3O_5$-type structure, adopting an orthorhombic structure, with a *Cmcm* space group. The Fe/Ni disordering in the cation sites of $NiFe_3O_5$ is expected due to their similar ionic radii, despite the fact that the occupancy of the sites could not be refined due to the similarity in electron densities of Fe and Ni in x-ray diffraction and the limited quantity of sample in neutron diffraction, estimates were made using

the size of the cation sites obtained from the refined average M-O distances. The magnetisation study and magnetic neutron diffraction revealed multiple magnetically ordered states that are exhibited by $NiFe_3O_5$. Spin order of the M1 and M2 sites of $NiFe_3O_5$ with a *k*-vector of [0 0 0] was observed at T_{N1} ~275 K, where the spins of the two sites are ordered antiferromagnetically along the *c* axis. An incommensurate magnetic transition was found below T_{N2} ~150 K, however, due to the small sample size and the presence of multiple magnetic impurities in the sample, the incommensurate magnetic structure could not be solved. An additional magnetically ordered state, on top of the incommensurate magnetic structure, was observed when cooled below T_{N3} ~20 K. In the low temperature magnetic structure, the magnetic moments were found to propagate through the lattice with a *k*-vector = [½ ½ 0], doubling the *a* and *b* lattice parameters, with the spins of the three cation sites of $NiFe_3O_5$ ordered antiferromagnetically along *c*.

6.4. References

1. B. Lavina, P. Dera, E. Kim, Y. Meng, R. T. Downs, P. F. Weck, S. R. Sutton, Y. Zhao. *Proc. Natl. Acad. Sci. USA* **2011,** *108,* 17281–17285.

2. S. V. Ovsyannikov, M. Bykov, E. Bykova, K. Glazyrin, R. S. Manna, A. A. Tsirlin, V. Cerantola, I. Kupenko, A. V. Kurnosov, I. Kantor, A. S. Pakhomova, I. Chuvashova, A. I. Chumakov, R. Rüffer, C. McCammon, L. S. Dubrovinsky. *Nat. Chem.* **2016,** *8,* 501.

3. R. D. Shannon, *Acta Cryst.* **1976**, *A32* 751-767.

4. O. Evrard, B. Malaman, F. Jeannot, *J. Solid State Chem.* **1980,** *35,* 112–119.

5. J. Rodriguez-Carvajal, *Physica B.* **1993** *192* ,55–69.

6. V. F. *Sears Neutron News,* **1992**, *3*, No. 3, 29-37.

Chapter 7. Conclusions

The first part of this Thesis (Chapter 3) set out to synthesise $CaFe_3O_5$, the first discovered member of the MFe_3O_5 system.[1] $CaFe_3O_5$ was prepared by reacting powder samples of $CaFe_2O_4$ with Fe and Fe_2O_3 under a vacuum, and a temperature of 1100 °C. The results of this study revealed an electronic phase separation in $CaFe_3O_5$ when cooled below a magnetic transition temperature of T_M = 302 K, forming a charge ordered and a charge averaged phase; this is similar to what was reported in manganite perovskites that is responsible for the colossal magnetoresistance phenomena. DFT studies carried out on $CaFe_3O_5$ show that the two low temperature phases are energetically similar. These two phases exhibit different antiferromagnetically ordered states. Trimeron formations are found in the charge ordered phases, where direct Fe-Fe interactions can be found between face sharing MO_6 octahedra, which localise the minority spin electrons from the Fe^{2+} in these trimeric Fe clusters throughout the lattice.

Chemical modifications of MFe_3O_5 can lead to discoveries of novel electronically ordered states, and typical physical property trends can be altered by changing the composition. Such knowledge would be valuable for functionalising this materials for applications. Therefore, the second part of this Thesis (Chapter 4-6) aimed to explore and characterise novel members of the MFe_3O_5 family.

Cations, with an oxidation state of 2+, that are electronically similar to Fe were substituted as *M* in the MFe_3O_5 structure. The *M* = Mn, Co and Ni analogues are described in Chapter 4, 5 and 6 of this Thesis, respectively. These materials were prepared from polycrystalline *M*O and Fe_3O_4, with solid-state synthesis carried out using high-pressure and high-temperature ceramic methods. The results show pressure is necessary to stabilise MFe_3O_5 with small cation *M* and the required pressure varies indirectly with the ionic radius of *M*, as shown in **Figure 7.1**. In the *M* = Ca, Mn and Fe analogues, the *M* species are found predominantly occupying the triangular prismatic site,[2] the largest out of the three cation sites. As the ionic radius of *M* becomes comparable or smaller than that of Fe^{2+}, cation disordering between the three cation sites occurs, such as those in the *M* = Co and Ni structures. This is likely

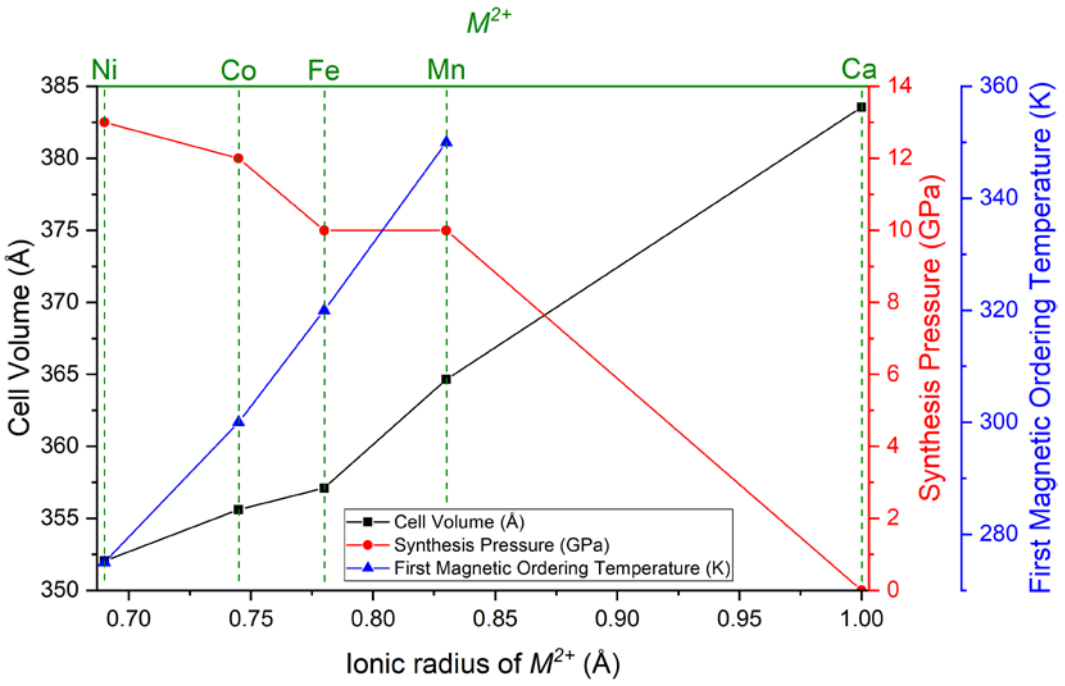

Figure 7.1 Trends in the synthesis pressure, cell volume and the temperature of the first magnetic transition in MFe_3O_5 (with *M* = Ni, Co, Fe, Mn and Ca), in respect to the ionic radius of M^{2+}.

due to the fact that it is more difficult to stabilise smaller cations in a large site. Consistent changes in the cell volume, with respect to the size of *M*, were found across the analogues investigated, as shown in **Figure 7.1**. All the known members of the MFe_3O_5 family have magnetic transitions near room temperature. A trend in the magnetic ordering temperatures is observed between analogues with *M* species that are electronically similar (*M* = Mn, Fe,[3] Co and Ni), where the transition temperature varies directly with the size of *M*, as illustrated in **Figure 7.1**. The *M* = Ca (charge averaged phase), Mn, Co and Ni analogues adopt the same magnetic structure below their first magnetic transition temperature. The transition involves spin ordering of the octahedral sites of the MFe_3O_5 structure, with moments ordered antiferromagnetically along *c*, propagating through the lattice with a *k*-vector of [0 0 0], whilst the triangular prismatic site remain disordered.

MFe_3O_5 analogues with *M* that are magnetically active exhibit rich magnetically ordered ground states. In $MnFe_3O_5$ and $CoFe_3O_5$, spin order of the triangular prismatic site occurs at 150 and 75 K, respectively. The spins of the triangular prismatic site are orientating ferromagnetically along *b* in $MnFe_3O_5$ and *a* in $CoFe_3O_5$, perpendicular to those on the octahedral sites, giving rise to a net magnetisation to the structure. The rise of the triangular prismatic site moment also leads to spin orientation transitions in both materials at low temperature. The tilting of the moments is likely to originate from the interaction between the moment on the triangular prismatic site with those on the octahedral sites and results in spin canting out of the original axis.

The magnetic structure of $NiFe_3O_5$ becomes incommensurate with a new *k*-vector of [0 0.38 0], below the antiferromagnetic transition at ~150 K. An additional antiferromagnetic structure is also found at even lower temperature (~20 K), which could originate from a separate domain with different Fe/Ni disordering. The extra magnetic structure has a *k*-vector of [½ ½ 0], with spins of the three cation sites ordered antiferromagnetically along *c*.

Only the commensurate magnetic structures of $NiFe_3O_5$ are determined, due to limited sample size and purity of the $NiFe_3O_5$ sample prepared for this Thesis. Higher quality samples may be prepared in the future using better heating control systems that minimise the thermal gradient in the sample, or perhaps using higher pressures. This could provide higher resolution neutron data which could be used to solve the incommensurate magnetic structure.

There are other novel MFe_3O_5 analogues that have not been explored, this includes the *M* = Mg structure, where the synthesis route was recently reported.[4] However, its structure has not yet been studied. Success in synthesising $CaFe_3O_5$, $MnFe_3O_5$, Fe_4O_5,[2] $CoFe_3O_5$ and $NiFe_3O_5$ suggests that electronically similar M^{2+} (e.g. Zn^{2+}), can be incorporated in the MFe_3O_5 structure, with conditions estimated using the trends shown in **Figure 7.1**. Furthermore, the reported pressure study of Fe_4O_5 has shown that $Fe^{2+/3+}$ charge ordering can be tuned with pressure. It is expected for homologues of Fe_4O_5, with the same structure type and comparable electronic properties to react to pressure in a similar manner. Future studies concerning electronic behaviours of other MFe_3O_5 under pressure may allow the physical properties

of these materials to be modified and be adopted for applications, especially in $CaFe_3O_5$ where electronic phase separation is sensitive to small chemical and physical perturbations.

7.1. References

1. O. Evrard, B. Malaman, F. Jeannot, *J. Solid State Chem.* **1980,** *35,* 112–119.

2. B. Lavina, P. Dera, E. Kim, Y. Meng, R. T. Downs, P. F. Weck, S. R. Sutton, Y. Zhao. *Proc. Natl. Acad. Sci. USA* **2011,** *108,* 17281–17285.

3. S. V. Ovsyannikov, M. Bykov, E. Bykova, K. Glazyrin, R. S. Manna, A. A. Tsirlin, V. Cerantola, I. Kupenko, A. V. Kurnosov, I. Kantor, A. S. Pakhomova, I. Chuvashova, A. I. Chumakov, R. Rüffer, C. McCammon, L. S. Dubrovinsky. *Nat. Chem.* **2016,** *8,* 501.

4. L. Uenver-Thiele, A. B. Woodland, N. Miyajima, T. B. Ballaran, D. J. Frost. *Contrib. Mineral. Petrol.* **2018,** *173,* 1−16.

PUBLICATIONS

The following publications have resulted from the work described in this Thesis.

Synthesis, Crystal Structure, and Magnetic Properties of $MnFe_3O_5$

K. H. Hong, G. M. McNally, M. Coduri, J. P. Attfield

Reprinted with permission from *Zeitschrift für Anorg. und Allg. Chemie* **2016**, *642*, 1355–1358.

Cation, magnetic, and charge ordering in $MnFe_3O_5$

K. H. Hong, A. M Arevalo-Lopez, M. Coduri, G. M. McNally, J. P. Attfield

Reprinted with permission from *J. Mater. Chem. C* **2018**, *6,* 3271–3275.

Long range electronic phase separation in $CaFe_3O_5$

K. H. Hong, A. M. Arevalo-Lopez, J. Cumby, C. Ritter, J. P. Attfield

Reprinted with permission from *Nat. Commun.* **2018,** *9,* 2975.

Complex Cation and Spin Orders in the High-Pressure Ferrite $CoFe_3O_5$

K. H. Hong, E. Solana-Madruga, M. Coduri, J. P. Attfield

Reprinted with permission from *Inorg Chem.* **2018,** *57* (22), 14347-14352

Journal of Inorganic and General Chemistry
ZAAC
Zeitschrift für anorganische und allgemeine Chemie
www.zaac.wiley-vch.de
ARTICLE

DOI: 10.1002/zaac.201600365

Synthesis, Crystal Structure, and Magnetic Properties of $MnFe_3O_5$

Ka H. Hong,[a] Graham M. McNally,[a] Mauro Coduri,[b] and J. Paul Attfield*[a]

Dedicated to Professor A. K. Cheetham on the Occasion of his 70th Birthday

Keywords: High pressure synthesis; Iron oxides; Structural properties; Manganese

Abstract. $MnFe_3O_5$ was synthesized under a pressure of 10 GPa at 1400 °C. $MnFe_3O_5$ has an orthorhombic structure (space group *Cmcm*, a = 2.9137(1), b = 9.8565(7) and c = 12.6143(6) Å at 300 K) and is isostructural with Fe_4O_5. Magnetic measurements reveal an antiferromagnetic transition at 350 K and a broad Curie transition at 150 K, similar to the spin ordering temperatures of Fe_4O_5. Variable temperature synchrotron X-ray diffraction shows that the structure undergoes anisotropic thermal expansion below 350 K, but no long range charge ordering is observed in the crystal structure.

Introduction

Magnetite (Fe_3O_4) has been one of the most intensively studied transition metal oxide systems since the discovery of the low temperature Verwey transition in 1939.[1] However, due to the difficulties in obtaining experimental evidence to test Verwey's charge ordering hypothesis, the ground state structure was only recently solved.[2] This revealed a complex charge and orbital ordered arrangement with weak Fe–Fe bonding interactions giving rise to trimerons, linear orbital molecule clusters of three Fe ions.

Fe_3O_4 may be described as the n = 3 member of the $MFe_{n-1}O_{n+1}$ family (with M^{2+} = Fe), and other members have recently been explored.[3] Fe_4O_5 was synthesized using high pressure and high temperature methods,[4] and a structural study revealed anisotropic thermal expansion in the lattice parameters when cooled below room temperature. An incommensurate charge order is observed at T_{CO} = 150 K, below which dimeron and trimeron like groups of Fe ions are formed.[5] Two magnetic transitions were also found, an antiferromagnetic ordering at 320 K and a further spin canting transition at 85 K. Subsequent work has shown that a related series of Fe_nO_{n+1} homologues can be made for larger n, also at pressure.[6] Phases with n = 4, 5, and 6 were also reported in an early study of the M = Ca system,[7] and a coupled structural and magnetic transition is observed at 360 K in $CaFe_5O_7$, associated with Fe^{2+} and Fe^{3+} charge order and accompanying orbital and spin orders.[8]

* Dr. J. P. Attfield
Fax: +44-131-651-7049
E-Mail: j.p.attfield@ed.ac.uk
[a] Centre for Science at Extreme Conditions and School of Chemistry
University of Edinburgh
Mayfield Road
Edinburgh EH9 3JZ, UK
[b] European Synchrotron Radiation Facility
71 avenue des Martyrs
38000 Grenoble, France

The n = 4 $MFe_{n-1}O_{n+1}$ phases adopt the orthorhombic $Sr_2Tl_2O_5$ type structure, in which M^{2+} cations occupy triangular prismatic sites within a network of corner and edge-sharing FeO_6 octahedra, as shown in Figure 1. As M = Fe and Ca phases are already known, it seems likely that an M = Mn analogue should also be accessible at pressure. High pressure is known to stabilize high spin Mn^{2+} ion in unusual coordination environments, for example, at the A cation sites of the ABO_3 perovskite structure in $MnVO_3$;[10] double perovskites Mn_2FeSbO_6,[11] Mn_2ScSbO_6,[12] Mn_2FeReO_6,[13,14] and Mn_2MnReO_6 (Mn_3ReO_6);[15] 134 types ζ-Mn_2O_3[16] and $MnCu_3V_4O_{12}$;[17] and the new "double double" cation ordered phases $MnRMnSbO_6$ (R = La, Pr, Nd, Sm).[18] We report herein the synthesis and initial characterization of the structure and magnetic properties of $MnFe_3O_5$.

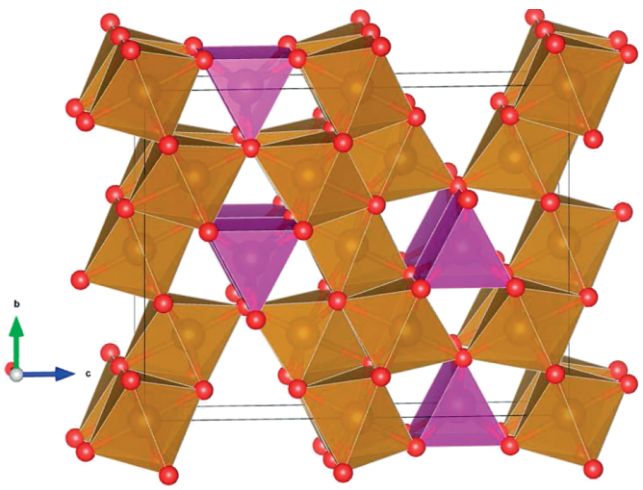

Figure 1. The *Cmcm* structure of $MnFe_3O_5$ with FeO_6 edge sharing octahedra shown in brown, MnO_6 triangular prisms in purple and the oxygens represented by red spheres.[9]

Results and Discussion

A polycrystalline sample of $MnFe_3O_5$ was synthesized using a high pressure solid-state synthetic method as described in the Experimental Section. Laboratory powder X-ray diffraction confirmed that $MnFe_3O_5$ is isostructural with previous MFe_3O_5 phases (M = Ca, Fe) and has an orthorhombic structure with space group *Cmcm*. The room temperature lattice parameters of $MnFe_3O_5$ (a = 2.9137(1), b = 9.8565(7), and c = 12.6143(6) Å) are larger than those for Fe_4O_5 (a = 2.8906(1), b = 9.8024(3), and c = 12.5804(4) Å),[5] consistent with the relative ionic sizes of Mn^{2+} and Fe^{2+}. There are two iron sites in $MnFe_3O_5$ which form edge-sharing FeO_6 octahedra in layers perpendicular to the c axis. Layers are interleaved by channels of Mn^{2+} ions in triangular prisms that share faces along the a axis (Figure 1).

Synchrotron powder X-ray diffraction data were recorded between 90 and 400 K. No structural phase transition was observed in this range. Rietveld fitting of the room temperature synchrotron diffraction data is shown in Figure 2. A small amount of platinum from the capsule used in the high pressure synthesis was also observed. The changes in lattice parameters and cell volume with temperature are shown in Figure 3a and b, respectively. Similar to Fe_4O_5, anisotropic thermal expansion is observed in $MnFe_3O_5$,[5] with a and c contracting with decreasing temperature, whilst b expands. The onset of the anisotropic behavior is close to the 350 K magnetic ordering transition described later, and thus the lattice distortion appears to be magnetostrictive. However, no long range structural change accompanying possible charge order is seen down to 90 K in $MnFe_3O_5$, which may reflect the presence of some Mn/Fe cation disorder although this cannot be quantified in our X-ray structure refinements.

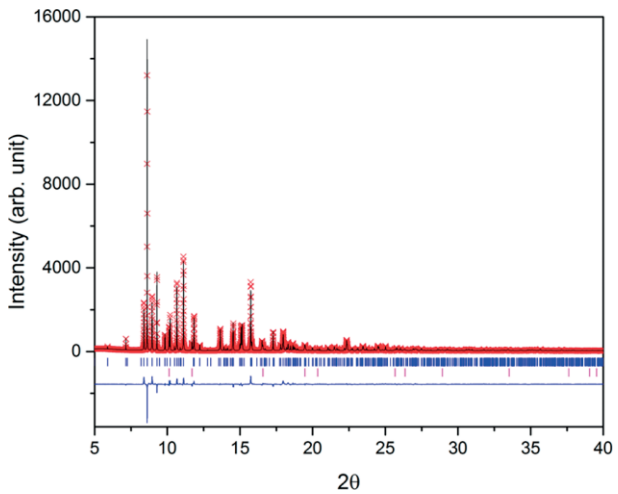

Figure 2. Rietveld fit to synchrotron powder diffraction profiles for $MnFe_3O_5$ at 300 K, with upper tick marks indicating the $MnFe_3O_5$ phase and lower for platinum.[19]

Details of the refined structure models for $MnFe_3O_5$ at 90 and 400 K are summarized in Table 1 and Table 2. The average Mn–O bond length is greater than that for the two Fe sites, confirming that the former site is occupied principally by Mn. Fe–O bond lengths for the two Fe sites are very similar. The

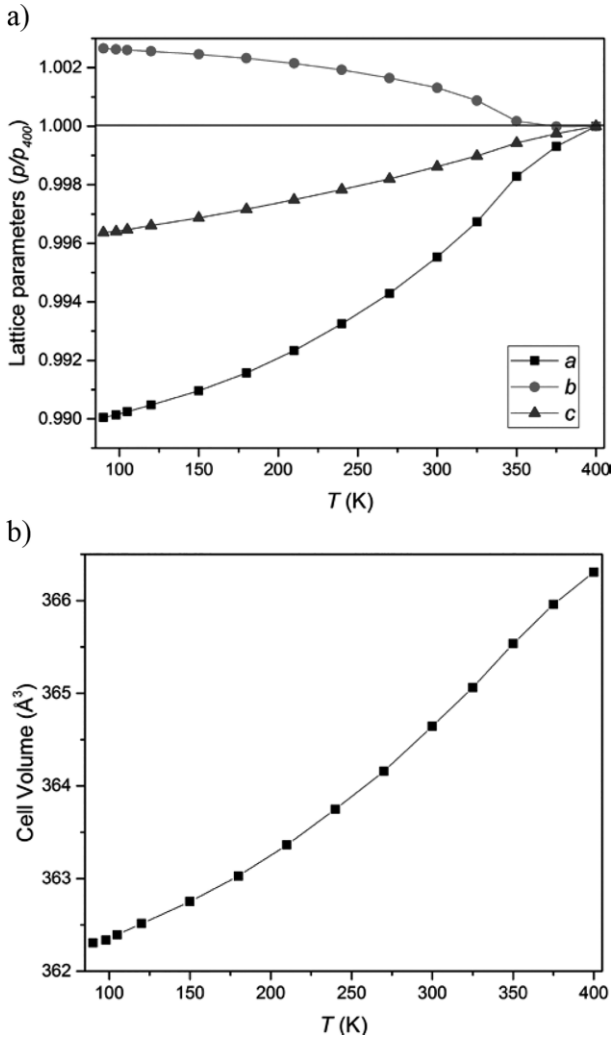

Figure 3. Changes in the (a) lattice parameters relative to 400 K values (which are shown in Table 1) and (b) cell volume of $MnFe_3O_5$ between 90 and 400 K.

Bond Valence Sum (BVS) for each cation site was calculated using the standard Mn^{2+} parameter for the M = Mn1 site, and an interpolation method for the mixed Fe^{2+}/ Fe^{3+} sites Fe1 and Fe2.[20,21] The BVS's of Mn1, Fe1, and Fe2 were estimated to be +1.65, +2.55, and +2.44, respectively, at 400 K, confirming Mn^{2+} at the trigonal prismatic M = Mn1 site. However, it was not possible to refine the Fe/Mn populations of the cation sites directly given the very similar electron densities of the two elements, and neutron diffraction will be needed to confirm the overall composition and cation distribution. The similarity of the two Fe site BVS's shows that there is no long range charge ordering between Fe1 and Fe2. Both Fe sites are occupied by Fe^{2+} and Fe^{3+} according to the average formal charge state of $Fe^{2.67+}$.

It is notable that the Fe–Fe distances within edge-sharing octahedral chains parallel to the a axis shrink significantly on cooling from 400 to 90 K (this is equivalent to the a axis contraction shown in Figure 3a), whereas the other short Fe1–Fe2 distance expands. This suggests that some weak Fe–Fe bond-

Table 1. Lattice parameters, atomic coordinates, and isotropic thermal displacements from synchrotron refinements in *Cmcm* space group of $MnFe_3O_5$ at 400 K (upper values) and 90 K (lower values). Estimated standard deviations in independent variables are shown in parentheses. *R* factors are R_{wp} = 15.9 and 13.9 %, and R_p = 14.5 and 12.8 % at 400 and 90 K, respectively.

a /Å		*b* /Å	*c* /Å		Volume /Å^3
2.93332(2)		9.86510(7)	12.65855(9)		366.307(5)
2.90413(2)		9.89136(5)	12.61259(8)		362.307(4)
Atom	Site	*x*	*y*	*z*	B_{iso} /Å^2
Fe1	8*f*	½	0.23790(9)	0.11496(6)	0.38(1)
			0.23668(7)	0.11522(6)	0.03(1)
Fe2	4*a*	0	0	0	0.38
					0.03
Mn1	4*c*	0	0.48660(13)	¼	0.38
			0.48655(11)		0.03
O1	4*c*	½	0.32230(50)	¼	0.38
			0.32141(42)		0.03
O2	8*f*	0	0.35507(36)	0.04488(28)	0.38
			0.35691(31)	0.04536(24)	0.03
O3	8*f*	0	0.09194(38)	0.13836(24)	0.38
			0.09230(32)	0.14017(21)	0.03

Table 2. Metal-oxygen bond lengths /Å, with mean values < > shown for $MnFe_3O_5$ at 400 K (upper values) and 90 K (lower values).

Bond	Distance	Bond	Distance
Mn1–O1 (×2)	2.187(4)	<Fe1–O>	2.068(3)
	2.186(3)		2.065(2)
Mn1–O3 (×4)	2.286(2)	Fe2–O2 (×4)	2.126(3)
	2.263(2)		2.107(2)
<Mn1–O>	2.253(3)	Fe2–O3 (×2)	1.973(3)
	2.237(2)		1.990(3)
Fe1–O1	1.901(2)	<Fe2–O>	2.075(3)
	1.895(2)		2.068(2)
Fe1–O2 (×2)	2.067(3)	Fe1–Fe2	2.967(1)
	2.073(2)		2.983(1)
Fe1–O2	2.220(4)	Fe1–Fe1, Fe2–Fe2	2.933(1)
	2.227(3)		2.904(1)
Fe1–O3 (×2)	2.077(3)		
	2.061(2)		

ing may occur within the chains of the magnetically ordered phase, as observed in the dimeron and trimeron units found in Fe_4O_5 and the trimerons of Fe_3O_4.[2,5]

Magnetic susceptibility measurements (shown in Figure 4a) reveal two magnetic transitions for $MnFe_3O_5$ at similar temperatures to those in Fe_4O_5. The susceptibility maximum at 350 K evidences an antiferromagnetic transition, as observed at 320 K in Fe_4O_5. A broad susceptibility upturn below 150 K evidences spin canting or some other ferro- or ferri-magnetic transition. This is close to the 150 K charge ordering and 85 K spin rearrangement transition temperatures of Fe_4O_5.

Magnetic hysteresis loops (shown in Figure 4b) reveal a small moment of 0.025 μ_B per formula unit at 300 K, which is probably due to traces of a magnetic impurity such as Fe_3O_4, below the limit of X-ray detection. Cooling through the 150 K transition confirms that $MnFe_3O_5$ adopts a ferrimagnetic spin order with a magnetization of 1.0 μ_B fu^{-1} at 2 K. This value is consistent with a collinear order of two up-spin S = 5/2 d^5 ions (Mn^{2+} or Fe^{3+}) and down-spin S = 5/2 and S = 2 d^6 Fe^{2+} ions, leading to a resultant magnetization of 1 μ_B fu^{-1}. Neutron diffraction will be needed to confirm the spin orders below the

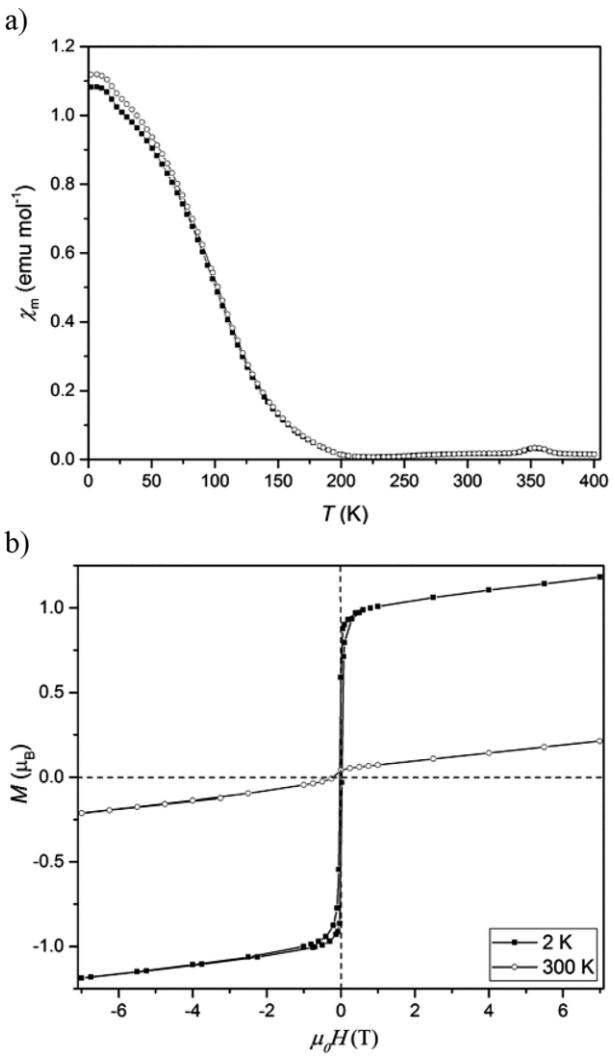

Figure 4. (a) ZFC (closed symbols) and FC (open symbols) magnetic susceptibilities for $MnFe_3O_5$. (b) Magnetization-field measurements at 2 and 300 K.

350 and 150 K transitions, and also to provide contrast between Mn and Fe to determine whether any disorder occurs across the three cation sites.

Conclusions

The above results demonstrate that $MnFe_3O_5$ can be synthesized under high pressure and temperature conditions, suggesting that other $MFe_{n-1}O_{n+1}$ homologues may also be accessible. $MnFe_3O_5$ adopts the orthorhombic $Sr_2Tl_2O_5$ type structure of Fe_4O_5, and undergoes similar anisotropic thermal expansion below an antiferromagnetic ordering transition at 350 K. An additional spin canting transition consistent with formation of a collinear ferrimagnetic state is observed at 150 K. However, no long range structural transition associated with charge ordering is observed down to 90 K. Neutron diffraction will be needed to confirm the spin orders and to determine the Mn/Fe order across the three cation sites.

Experimental Section

MnO and Fe_3O_4 were ground together in a 1:1 ratio and pressed into a pellet. The pellet was sealed inside an evacuated quartz tube and heated at 1100 °C for 12 h. The resulting product was heated at 1400 °C in a Pt capsule for 20 min under 10 GPa pressure, using a two-stage Walker-type module. Laboratory X-ray diffraction data were collected with a Bruker D2 diffractometer using Cu-K_α radiation.

High resolution powder X-ray diffraction data were collected at the ID22 beamline of the ESRF with incident wavelength 0.39996 Å. The powder was packed into a glass capillary with an outer diameter of 0.3 mm and spun during acquisition. Data were collected at temperatures from 90 to 400 K using an Oxford Cryostream system.

Magnetic measurements were carried out with a Quantum Design MPMS XL SQUID magnetometer. Magnetic susceptibility was recorded in zero field cooled (ZFC) and field cooled (FC) conditions between 2 and 400 K with an applied magnetic field of 5000 Oe. Hysteresis loops were also measured at 2 and 300 K.

Acknowledgements

We acknowledge financial support from European Research Council (ERC) and Science and Technology Facilities Council (STFC), and assistance provided by *Dr. Angel M. Arevalo-Lopez*.

References

[1] E. J. W. Verwey, *Nature* **1939**, *144*, 327–328.
[2] M. S. Senn, J. P. Wright, J. P. Attfield, *Nature* **2011**, *481*, 173–176.
[3] Y. Garcia, G. Subias, *J. Phys. Condens. Matter* **2004**, *16*, R145.
[4] B. Lavina, P. Dera, E. Kim, Y. Meng, R. T. Downs, P. F. Weck, S. R. Sutton, Y. Zhao, *Proc. Natl. Acad. Sci. USA* **2011**, *108*, 17281–17285.
[5] S. V. Ovsyannikov, M. Bykov, E. Bykova, D. P. Kozlenko, A. A. Tsirlin, A. E. Karkin, V. V. Shchennikov, S. E. Kichanov, H. Gou, A. M. Abakumov, R. Egoavil, J. Verbeeck, C. McCammon, V. Dyadkin, D. Chernyshov, S. van Smaalen, L. S. Dubrovinsky, *Nat. Chem.* **2016**, 1–8.
[6] B. Lavina, Y. Meng, *Sci. Adv.* **2015**, *1*, e1400260.
[7] O. Evrard, B. Malaman, F. Jeannot, *J. Solid State Chem.* **1980**, *35*, 112–119.
[8] C. Delacotte, S. Hébert, V. Hardy, Y. Bréard, R. Maki, T. Mori, D. Pelloquin, *Solid State Sci.* **2016**, *54*, 54–58.
[9] K. Momma, F. Izumi, *J. Appl. Crystallogr.* **2011**, *44*, 1272–1276.
[10] M. Markkula, A. M. Arévalo-López, A. Kusmartseva, J. A. Rodgers, C. Ritter, H. Wu, J. P. Attfield, *Phys. Rev. B* **2011**, *84*, 094450.
[11] A. J. Dos Santos-García, E. Solana-Madruga, C. Ritter, D. Ávila-Brande, O. Fabelo, R. Sáez-Puche, *Dalton Trans.* **2015**, *44*, 10665.
[12] E. Solana-Madruga, A. J. Dos Santos-García, A. M. Arévalo-López, D. Ávila-Brande, C. Ritter, J. P. Attfield, R. Sáez-Puche, *Dalton Trans.* **2015**, *44*, 20441.
[13] A. M. Arevalo-Lopez, G. M. McNally, J. P. Attfield, *Angew. Chem. Int. Ed.* **2015**, *54*, 12074.
[14] M.-R. Li, M. Retuerto, Z. Deng, P. W. Stephens, M. Croft, Q. Huang, H. Wu, X. Deng, G. Kotliar, J. Sanchez-Benitez, J. Hadermann, D. Walker, M. Greenblatt, *Angew. Chem. Int. Ed.* **2015**, *54*, 12069.
[15] A. M. Arévalo-López, F. Stegemann, J. P. Attfield, *Chem. Commun.* **2016**, *52*, 5558.
[16] S. V. Ovsyannikov, A. M. Abakumov, A. A. Tsirlin, W. Schnelle, R. Egoavil, J. Verbeeck, G. Van Tendeloo, K. Glazyrin, M. Hanfland, L. Dubrovinsky, *Angew. Chem. Int. Ed.* **2013**, *52*, 1494.
[17] S. K. Shiro, I. Yamada, N. Ikeda, K. Ohgushi, M. Mizumaki, R. Takahashi, N. Nishiyama, T. Inoue, T. Irifune, *Inorg. Chem.* **2013**, *52*, 11538–11543.
[18] E. Solana-Madruga, Á. M. Arévalo-López, A. J. Dos Santos-García, E. Urones-Garrote, D. Ávila-Brande, R. Sáez-Puche, J. P. Attfield, *Angew. Chem. Int. Ed.* **2016**, *55*, 9340–9344.
[19] J. Rodriguez-Carvajal, *Phys. B* **1993**, *192*, 55.
[20] J. P. Attfield, *Solid State Sci.* **2006**, *8*, 861–867.
[21] I. D. Brown, *J. Appl. Crystallogr.* **1996**, *29*, 479–480.

Received: September 29, 2016
Published Online: November 22, 2016

Journal of Materials Chemistry C

PAPER

View Article Online
View Journal | View Issue

Cite this: J. Mater. Chem. C, 2018, 6, 3271

Cation, magnetic, and charge ordering in $MnFe_3O_5$†

K. H. Hong,[a] A. M. Arevalo-Lopez,[b] M. Coduri,[c] G. M. McNally[a] and J. P. Attfield *[a]

Received 4th January 2018,
Accepted 16th January 2018

DOI: 10.1039/c8tc00053k

rsc.li/materials-c

The recently-discovered high pressure material $MnFe_3O_5$ displays a rich variety of magnetically ordered states on cooling. Fe spins order antiferromagnetically below a Néel transition at 350 K. A second transition at 150 K marks Mn spin order that leads to spin canting of some of the Fe spins and ferrimagnetism. A further transition at 60 K is driven by charge ordering of Fe^{2+} and Fe^{3+} over two inequivalent Fe sites, with further canting of all spins. Electrical resistivity measurements reveal semiconducting behaviour in $MnFe_3O_5$ with a change in activation energy at 285 K.

Introduction

The variable $3d^n$ configurations of Mn and Fe cations in spinel-type and other oxides give rise to many important applications as energy materials[1] and in magnetism. Many manganese oxides are used as cathode materials in rechargeable batteries, *e.g.* $LiMn_2O_4$-spinel, Li_2MnO_3, and $NaMnO_2$. The phosphate $LiFePO_4$ has been commercialised as a lithium battery cathode and iron oxides such as Fe_2O_3 and magnetite, Fe_3O_4, have been explored as anode materials.[2] Manganese and iron based spinels are also active catalysts for oxygen reduction/evolution reactions (ORR/OER) in fuel cells, metal–air batteries, and water-splitting cells.[3]

The spinel magnetite is also notable as the original magnetic material, and Fe_3O_4 has been studied intensively since Verwey's observation of a metal–insulator transition accompanied by a structural distortion.[4] The low temperature structure has a complex charge and orbital ordering and weak Fe–Fe bonding interactions that form trimerons – linear orbital molecule clusters of three Fe ions.[5,6] A related iron oxide, Fe_4O_5, was recently discovered using high temperature and high pressure synthesis,[7] and has an incommensurate charge order at 150 K, below which dimeron and trimeron-like groups of Fe ions are formed.[8] Subsequent work has shown that Fe_nO_{n+1} homologues with $n > 4$ can also be made at pressure.[9] $M^{2+}Fe_{n-1}O_{n+1}$ analogues of these materials with M^{2+} = Ca were reported previously,[10] and recent detailed studies of $CaFe_5O_7$ revealed a coupled structural and magnetic transition at 360 K accompanied by Fe^{2+}/Fe^{3+} charge ordering.[11–13]

We recently reported the synthesis at high pressures of the first $n > 3$ M = Mn material in this family, the $n = 4$ member $MnFe_3O_5$.[14] $MnFe_3O_5$ is isostructural with Fe_4O_5 and adopts the orthorhombic $Sr_2Tl_2O_5$-type structure (space group *Cmcm*) in which divalent cations occupy triangular prismatic sites within triangular channels in a network of corner and edge-sharing octahedra. $MnFe_3O_5$ showed two magnetic transitions – an antiferromagnetic transition at 350 K and a broad ferromagnetic transition at 150 K – indicating that complex spin–spin interactions are present. We report here a high resolution powder neutron diffraction study of $MnFe_3O_5$, revealing the Mn/Fe chemical order and the temperature evolution of the magnetic behaviour between 5 and 400 K, supported by low temperature powder synchrotron X-ray diffraction and the electrical resistivity measurements.

Experimental

$MnFe_3O_5$ was synthesised using high pressure and high temperature solid state synthesis. Powders of MnO and Fe_3O_4 were ground together in a 1 : 1 ratio, and were heated at 1400 °C in a Pt capsule for 20 min under 10 GPa pressure, using a two-stage Walker-type module. Products were characterised by laboratory X-ray diffraction data collected with a Bruker D2 diffractometer using Cu-K_α radiation.

Magnetic measurements were carried out with a Quantum Design MPMS XL SQUID magnetometer. Magnetic susceptibility was recorded in zero field cooled (ZFC) and field cooled (FC) conditions between 2 and 400 K with an applied magnetic field of 5000 Oe. Hysteresis loops were measured at 2, 75, 300 and 400 K. Electrical resistivity measurements were carried out with a Quantum Design PPMS, between 260 and 380 K.

[a] Centre for Science at Extreme Conditions and School of Chemistry, University of Edinburgh, Mayfield Road, Edinburgh EH9 3JZ, UK. E-mail: j.p.attfield@ed.ac.uk
[b] Univ. Lille, CNRS, Centrale Lille, ENSCL, Univ. Artois, UMR 8181 – UCCS – Unité de Catalyse et Chimie du Solide, F-59000 Lille, France
[c] European Synchrotron Radiation Facility, 71 avenue des Martyrs, Grenoble, 38000, France

† Electronic supplementary information (ESI) available: Tables of crystallographic results and powder synchrotron profile fit. See DOI: 10.1039/c8tc00053k

High resolution time-of-flight neutron diffraction data were collected at the WISH beamline of the ISIS facility, with 50 mg of powder from several high pressure runs packed into a vanadium can. Diffraction patterns were collected at 5, 75, 150, 300 and 400 K using a closed cycle refrigerator (CCR) with a hot stage. High resolution powder X-ray diffraction data were collected at the ID22 beamline of the ESRF with incident wavelength 0.39994 Å. A glass capillary with an outer diameter of 0.3 mm was used to contain the polycrystalline sample. Low temperature diffraction data were collected from 13 to 120 K using a liquid helium cryostat system.

Results and discussion

Crystal and magnetic structures

High resolution time-of-flight neutron diffraction experiments were carried out to determine the structure and magnetic behaviour of $MnFe_3O_5$. Crystal structure refinements show that the unit cell symmetry remains orthorhombic *Cmcm* at all temperatures. Occupancy refinements for the three cation sites, making use of the high neutron scattering contrast between Mn and Fe, showed that octahedral sites are occupied exclusively by Fe, and the trigonal prism site is predominantly Mn with 6.3(4)% substitution by Fe. Hence $MnFe_3O_5$ is Mn/Fe ordered and the overall $Mn_{0.94}Fe_{3.06}O_5$ composition of the present sample is close to the ideal stoichiometry.

Magnetisation measurements (Fig. 1) show a maximum at 350 K and a broad magnetic upturn signifying a ferro- or ferri-magnetic ordering at 150 K as reported previously.[14] This is corroborated by the saturated magnetisations observed in hysteresis loops at 2 and 75 K.

The neutron diffraction patterns shown in Fig. 2 reveal the appearance of magnetic reflections when cooled below 400 K. The magnetic structures in the different regimes were solved and Rietveld fitted to the neutron diffraction patterns, as shown for the 5 K pattern in Fig. 3. The magnetic reflections from all the magnetic phases of $MnFe_3O_5$ were indexed with a propagation vector of (000), and the structures obtained at 5, 75 and 300 K are presented in Fig. 4a. At 150 and 300 K, the spins at the two independent Fe sites in $MnFe_3O_5$ are both found to be ordered antiferromagnetically parallel to the *c*-axis, whilst the Mn spins remain disordered. This confirms that a Néel transition is observed at T_N = 350 K in the magnetisation measurements (Fig. 1).

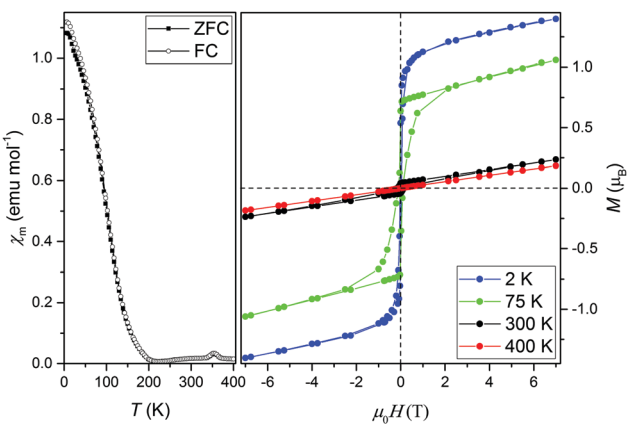

Fig. 1 (left) Zero-field cooled and field cooled magnetisation measurements between 2 and 400 K. (right) Magnetisation-field hysteresis loops for $MnFe_3O_5$ measured at 2, 75, 300 and 400 K.

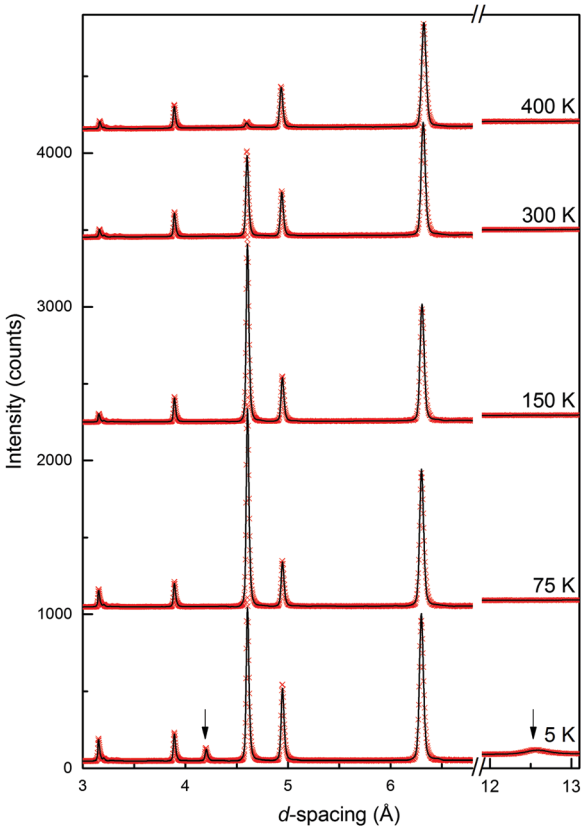

Fig. 2 Temperature evolution of the neutron diffraction pattern of $MnFe_3O_5$. Magnetic contributions appear at 300 K, and arrows indicate additional magnetic peaks at 5 K, with *hkl* = (001) and (003) at *d*-spacing = 12.6 and 4.2 Å, respectively.

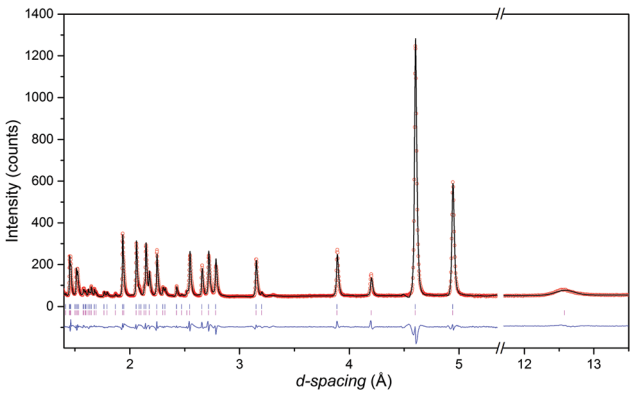

Fig. 3 Rietveld refinement of high resolution neutron diffraction patterns of $MnFe_3O_5$ obtained at 5 K, with upper tick marks indicating nuclear peaks and lower presenting magnetic reflections. (R_{wp} = 12.9% and R_p = 12.6%).

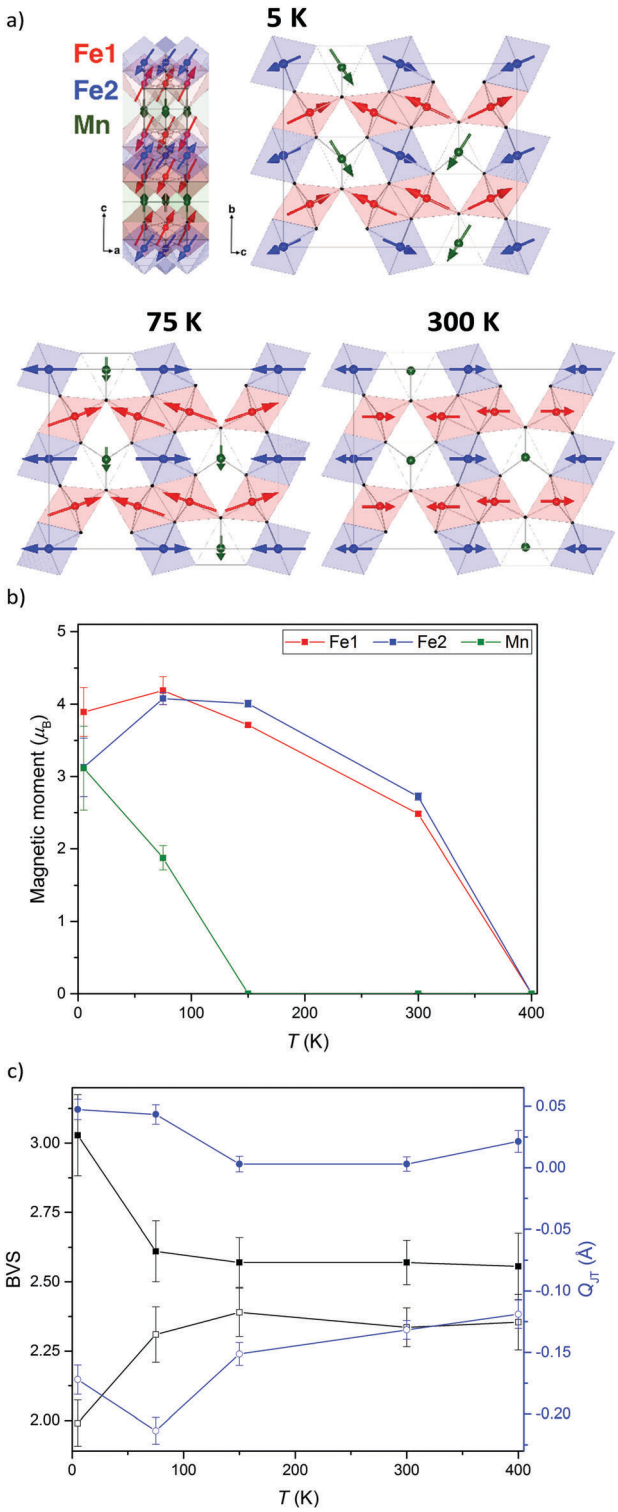

Fig. 4 (a) Magnetic structures of $MnFe_3O_5$ at 5, 75 and 300 K. The network of FeO_6 octahedra is shown, with Mn^{2+} in trigonal prismatic sites within channels parallel to the *a*-axis. (b) The temperature evolution of the ordered Mn, Fe1 and Fe2 magnetic moments. (c) Temperature evolution of BVS and Q_{JT}, with closed/open symbols representing Fe1/Fe2 sites.

Fits to the 75 K diffraction data showed additional spin ordering of the Mn site, with moments aligned ferromagnetically along the *b* axis below T_{Mn} = 150 K. The order of the Mn site moment leads the spins of the nearest Fe site – Fe1 to cant towards the *b* axis. The *b*-components of Fe1 spins are antiparallel to those of Mn, resulting in a net magnetisation of $\sim$0.5 μ_B per $MnFe_3O_5$ formula unit, which is consistent with the increase in magnetisation on cooling from 300 to 75 K shown in Fig. 1. A similar spin canting was reported in Fe_4O_5.[8]

The additional magnetic reflections observed in the 5 K neutron diffraction patterns reveal another change in the magnetic structure in $MnFe_3O_5$. The onset for this third magnetic transition appears to be the divergence between zero-field cooled and field cooled susceptibilities at $\sim$60 K in the susceptibility data (Fig. 1). An increase in the ordered Mn moment leads to further canting of all the spins, with both of the Fe sites canted antiferromagnetically towards the *a* axis and ferromagnetically along *b*. In addition, the Mn spins become canted antiferromagnetically to the *c* axis. The magnetic components of the Mn and the Fe2 sites on the *b* axis are antiparallel to Fe1, as shown in Fig. 4a. This enhances the magnetisation along the *b* axis to $\sim$0.6 μ_B per $MnFe_3O_5$ formula unit. The thermal evolution of the magnitude of the ordered moments in $MnFe_3O_5$ are shown in Fig. 4b, and the values of the ordered components and other refinement results are given in ESI.†

The 300 K magnetic structure reveals dominant antiferromagnetic Fe1–Fe2 interactions; from direct exchange *via* overlap of half-filled t_{2g} orbitals through edge-sharing of FeO_6 octahedra, and through superexchange mediated by Fe–O–Fe connections at shared corners. Each Mn spin is coupled to 4 Fe1 and 4 Fe2 spins *via* Mn–O–Fe bridges, and frustration of both of these interactions leads to an almost perpendicular alignment of the Mn moments at 75 K, although Fe1 spin canting occurs such that their components in the *b*-direction are antiferromagnetically coupled to the Mn spins. Further canting occurs at 5 K as the Mn spins become more fully ordered and Fe1 and Fe2 spins cant out of the *bc*-plane. This magnetic order breaks the mirror-plane symmetries of the lattice perpendicular to the *a* and *c* axes, so an exchange-strictive distortion might be expected but is not observed within the resolution of the present data.

The possibility of internal electronic distortions was investigated by using the Bond Valence Sum (BVS) method to estimate oxidation states for the Fe sites *via* a standard interpolation method[15,16] with bond distances derived from the neutron refinements. The BVS results in Fig. 4c show that both Fe1 and Fe2 sites have mixed Fe^{2+}/Fe^{3+} charge states at 75–400 K, but charge ordering is evident at 5 K with Fe1 and Fe2 respectively tending to Fe^{3+} and Fe^{2+} states. The effect of Jahn Teller distortion (Q_{JT}) is also calculated for both Fe sites. Charge localisation as Fe^{2+} is expected to lead to Jahn Teller compression of the $Fe2O_6$ octahedron (negative values of the Q_{JT} parameter reported in ref. 5), and although no large changes are observed on cooling below 75 K, the negative Q_{JT} for Fe2 (Fe^{2+}) and near zero value for Fe1 (Fe^{3+}) corroborate the BVS charge ordering results. Hence a Fe^{2+}/Fe^{3+} charge ordering transition occurs at T_{CO} = 60 K in $MnFe_3O_5$, with concomitant spin canting. As the Fe^{2+} and Fe^{3+} states respectively localise at inequivalent Fe2 and Fe1 sites there

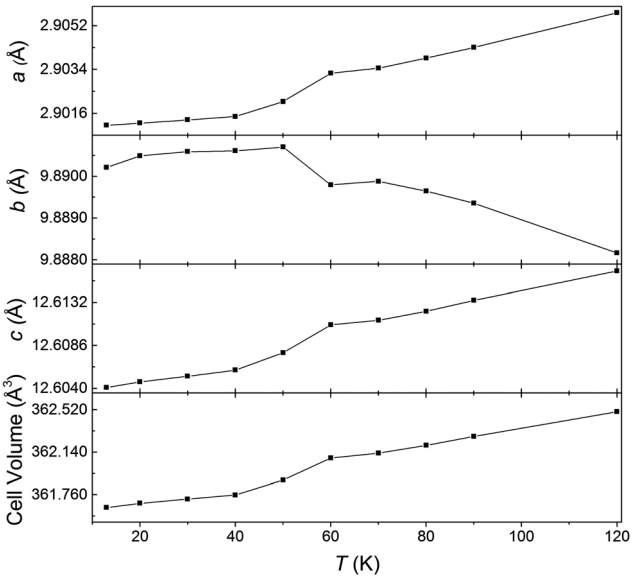

Fig. 5 Changes in the lattice parameters and cell volume obtained from powder synchrotron X-ray diffraction experiments.

is no symmetry-breaking distortion associated with the charge order, or with the Fe^{2+} orbital order, although the associated 5 K spin order does break the *Cmcm* lattice symmetry as noted above.

Our previous study of the crystal structure using powder synchrotron X-ray diffraction data showed that anisotropic thermal expansion of the lattice parameters is observed over the temperature range 90–400 K. Further data collected between 15 and 120 K here confirm that the orthorhombic *Cmcm* structure persists to low temperatures. A discontinuity in the refined lattice parameters and cell volume is observed at 60 K, (Fig. 5) corresponding to the divergence in the ZFC and FC magnetisation measurements. This likely marks the onset of the charge ordering observed in the 5 K but not the 75 K neutron diffraction data.

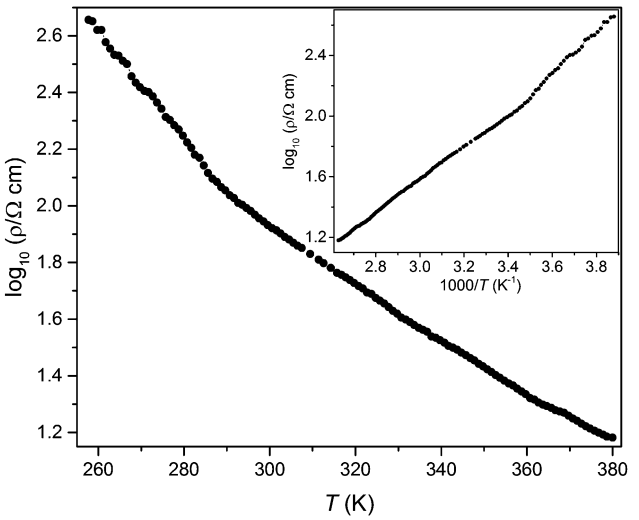

Fig. 6 Log of electrical resistivity of $MnFe_3O_5$ measured between 260 and 380 K, with insert showing the plot against reciprocal temperature.

Electrical properties

Electrical resistivity measurement of a polycrystalline pellet of $MnFe_3O_5$ shows semiconducting behaviour, with the resistivity increasing when cooled (Fig. 6). The sample resistance was too great to be measured below 260 K. Two linear regions are observed in the inset plot of log(resistivity) *vs.* inverse temperature, with a change of slope near 285 K. Fitting the Arrhenius equation $\rho = A\exp(E_a/k_BT)$ to the two linear regions gives the activation energy E_a as 210 meV above and 280 meV below the 285 K crossover. This temperature does not match any of the observed magnetic transition temperatures, and may correspond to a change from defect-dominated to intrinsic bandgap conduction.

The presence of structural channels within a framework of redox-active FeO_6 octahedra, and moderate electrical conductivity, suggests that $MnFe_3O_5$ would be worth investigating as a battery electrode material. Full reduction of Fe^{3+} to Fe^{2+} through lithium insertion would give $Li_2MnFe_3O_5$, and as cycling between this and the parent phase does not involve oxidation of Mn^{2+} then structural degradation from formation of Jahn–Teller active Mn^{3+} is avoided. However, alternative methods to high pressure synthesis are likely to be needed to make sufficient quantities of $MnFe_3O_5$ for practical battery research.

Conclusions

$MnFe_3O_5$ is found to have a rich magnetic ordered behaviour between 5 and 400 K. On cooling from high temperatures, the moments at the iron sites order with an antiferromagnetic arrangement at T_N = 350 K, but additional order of Mn moments below T_{Mn} = 150 K leads to canting of Fe1 spins and a significant ferrimagnetic moment. A similar canting of Fe (and Re) spins due to low temperature order of Mn^{2+} moments was reported in the double perovskite Mn_2FeReO_6.[17] Fe^{2+}/Fe^{3+} charge ordering drives a further transition at T_{CO} = 60 K with additional canting of all spins. Similar charge and orbital orders are observed in Fe_3O_4 and Fe_4O_5. Electrical resistivity measurements reveal semiconducting behaviour in $MnFe_3O_5$ and a small change in the activation energy at 285 K may correspond to a crossover from defect to intrinsic conduction regimes. $MnFe_3O_5$ is worth further investigation as a potential lithium battery electrode material.

Conflicts of interest

There are no conflicts to declare.

Acknowledgements

We acknowledge financial support from European Research Council (ERC), Engineering and Physical Sciences Research Council (EPSRC) and Science, Technology Facilities Council (STFC) and the ESRF for provision of beamtime. We would also like to thank Andy Fitch (ESRF), Pascal Manuel (ISIS) and

James Cumby, Alexander J. Browne, Giuditta Perversi and Paul M. Sarte (Edinburgh) for assistance provided.

References

1 N. Yabuuch and S. Komaba, *Sci. Technol. Adv. Mater.*, 2014, **15**, 043501.
2 L. Zhang, H. B. Wu and X. W. Lou, *Adv. Energy Mater.*, 2013, **4**, 1300958.
3 Q. Zhao, Z. Yan, C. Chen and J. Chen, *Chem. Rev.*, 2017, **117**, 10121–10211.
4 E. J. W. Verwey, *Nature*, 1939, **144**, 327–328.
5 M. S. Senn, J. P. Wright and J. P. Attfield, *Nature*, 2012, **481**, 173–176.
6 G. Perversi, J. Cumby, E. Pachoud, J. P. Wright and J. P. Attfield, *Chem. Commun.*, 2016, **52**, 4864.
7 B. Lavina, P. Dera, E. Kim, Y. Meng, R. T. Downs, P. F. Weck, S. R. Sutton and Y. Zhao, *Proc. Natl. Acad. Sci. U. S. A.*, 2011, **108**, 17281–17285.
8 S. V. Ovsyannikov, M. Bykov, E. Bykova, D. P. Kozlenko, A. A. Tsirlin, A. E. Karkin, V. V. Shchennikov, S. E. Kichanov, H. Gou, A. M. Abakumov, R. Egoavil, J. Verbeeck, C. McCammon, V. Dyadkin, D. Chernyshov, S. van Smaalen and L. S. Dubrovinsky, *Nat. Chem.*, 2016, 1–8.
9 B. Lavina and Y. Meng, *Sci. Adv.*, 2015, **1**, e1400260.
10 O. Evrard, B. Malaman and F. Jeannot, *J. Solid State Chem.*, 1980, **35**, 112–119.
11 C. Delacotte, F. Hüe, Y. Bréard, S. Hébert, O. Pérez, V. Caignaert, J. M. Greneche and D. Pelloquin, *Inorg. Chem.*, 2014, **53**, 10171–10177.
12 C. Delacotte, Y. Bréard, V. Caignaert, V. Hardy, J. M. Greneche, S. Hébert, E. Suard and D. Pelloquin, *Key Eng. Mater.*, 2014, **617**, 237–240.
13 C. Delacotte, Y. Bréard, V. Caignaert, V. Hardy, J. M. Greneche, S. Hébert, E. Suard and D. Pelloquin, *J. Solid State Chem.*, 2017, **247**, 13–19.
14 K. H. Hong, G. M. McNally, M. Coduri and J. P. Attfield, *Z. Anorg. Allg. Chem.*, 2016, **642**, 1355–1358.
15 J. P. Attfield, *Solid State Sci.*, 2006, **8**, 861–867.
16 I. D. Brown, *J. Appl. Crystallogr.*, 1996, **29**, 479–480.
17 A. M. Arévalo-López, G. M. McNally and J. P. Attfield, *Angew. Chem., Int. Ed.*, 2015, **54**, 12074–12077.

nature COMMUNICATIONS

Corrected: Correction

ARTICLE

DOI: 10.1038/s41467-018-05363-6 OPEN

Long range electronic phase separation in $CaFe_3O_5$

Ka. H. Hong [1], Angel M. Arevalo-Lopez[2], James Cumby [1], Clemens Ritter[3] & J. Paul Attfield [1]

Incomplete transformations from ferromagnetic to charge ordered states in manganite perovskites lead to phase-separated microstructures showing colossal magnetoresistances. However, it is unclear whether electronic matter can show spontaneous separation into multiple phases distinct from the high temperature state. Here we show that paramagnetic $CaFe_3O_5$ undergoes separation into two phases with different electronic and spin orders below their joint magnetic transition at 302 K. One phase is charge, orbital and trimeron ordered similar to the ground state of magnetite, Fe_3O_4, while the other has Fe^{2+}/Fe^{3+}charge averaging. Lattice symmetry is unchanged but differing strains from the electronic orders probably drive the phase separation. Complex low symmetry materials like $CaFe_3O_5$ where charge can be redistributed between distinct cation sites offer possibilities for the generation and control of electronic phase separated nanostructures.

[1] Centre for Science at Extreme Conditions and School of Chemistry, University of Edinburgh, Mayfield Road, Edinburgh EH9 3JZ, UK. [2] Univ. Lille, CNRS, Centrale Lille, ENSCL, Univ. Artois, UMR 8181 - UCCS - Unité de Catalyse et Chimie du Solide, Lille F-59000, France. [3] Institut Laue-Langevin, 71 avenue des Martyrs, Grenoble 38000, France. Correspondence and requests for materials should be addressed to J.P.A. (email: j.p.attfield@ed.ac.uk)

Manganites such as $La_{0.7}Ca_{0.3}MnO_3$ and magnetite, Fe_3O_4, share similar physics as both have a spin-polarised conducting state near ambient temperature due to double exchange between ferromagnetically aligned Mn^{3+} and Mn^{4+} or Fe^{2+} and Fe^{3+} spins, respectively. Both undergo charge ordering on cooling, which for magnetite is accompanied by a lattice distortion below the much-studied Verwey transition at 125 K[1]. This was recently found to result from a complex ordering of Fe^{2+}/Fe^{3+} charge states, Fe^{2+} orbitals, and three-Fe trimeron groups[2]. However, long range phase segregation is observed below charge ordering transitions in many manganites[3–5] and related perovskites but has not been found in magnetite or related ferrite spinels.

Here, following recent studies of spin and charge ordering in non-spinel $MFe_{n-1}O_{n+1}$ ($n \geq 4$) ferrites with $M = Fe$[6,7], Mn[8,9] and Ca[10,11], we investigate $n = 4$ $CaFe_3O_5$ and discover long range electronic phase separation between a magnetite-like charge ordered phase and a charge averaged phase.

Results

Preparation and characterisation of $CaFe_3O_5$. $CaFe_3O_5$ was synthesised and characterised as described in Methods. The orthorhombic crystal structure consists of FeO_6 octahedra sharing edges to form infinite chains parallel to the *a*-axis and ribbons of three octahedra parallel to the *bc*-plane as shown in Fig. 1a. Magnetisation measurements (Fig. 1b) reveal a sharp magnetic ordering transition at $T_M = 302$ K and a small net magnetisation of 0.05 μ_B per $CaFe_3O_5$ unit with a moderate coercivity of 0.3 T at 2 K. Ceramic pellets of $CaFe_3O_5$ are semiconducting with a small magnetoresistance of −1% at 200 K (Fig. 1c), likely reflecting the small net magnetisation of the sample.

Evidence for electronic phase separation in $CaFe_3O_5$. A single high temperature (HT) crystalline phase of $CaFe_3O_5$ is observed above $T_M = 302$ K, but both powder synchrotron X-ray (Fig. 2a, b) and neutron diffraction data (Fig. 2c, d) reveal long range phase separation as diffraction peaks broaden or split into two components below the magnetic ordering transition as shown in Fig. 2a, c. The shift of the X-ray (002) peak to lower 2θ at 300 K evidences a small bulk lattice distortion due to spin ordering before separation into two phases at lower temperatures. Both low temperature phases have the same *Cmcm* space group symmetry as the HT parent. Crystallographic results are shown in Supplementary Tables 1–5. Magnetic neutron diffraction peaks observed below T_M (Supplementary Fig. 1) show that one phase has magnetic propagation vector (½ 0 0) while the other has (0 0 0) (Fig. 2c), and a good fit to the data (Fig. 2d) was obtained using the magnetic structure models shown in Fig. 3. No additional broadening of magnetic peaks was observed showing that both magnetic orders have correlation lengths of at least ~200 nm. Both phases have collinear antiferromagnetic orders with moments parallel to the *c*-axis, but an important difference is that the (½ 0 0) phase has ferromagnetic (FM) alignment of spins within the three-atom ribbons parallel to the *bc*-plane, while the (0 0 0) has FM spin chains parallel to the *a*-axis. Although both orders are antiferromagnetic, the observation of a small net magnetisation below T_M suggests that one or both of the spin structures are canted. The fractions of the two phases are found to be different in the synchrotron and neutron diffraction experiments (Fig. 2a), consistent with a strain-driven phase separation being dependent on the thermal history of the sample.

Thermal evolution of lattice parameters from neutron and X-ray fits are, respectively, shown in Fig. 4a and Supplementary Fig. 2, and variations of internal structural quantities from both studies are shown in Fig. 4b–d to emphasise the reproducibility of

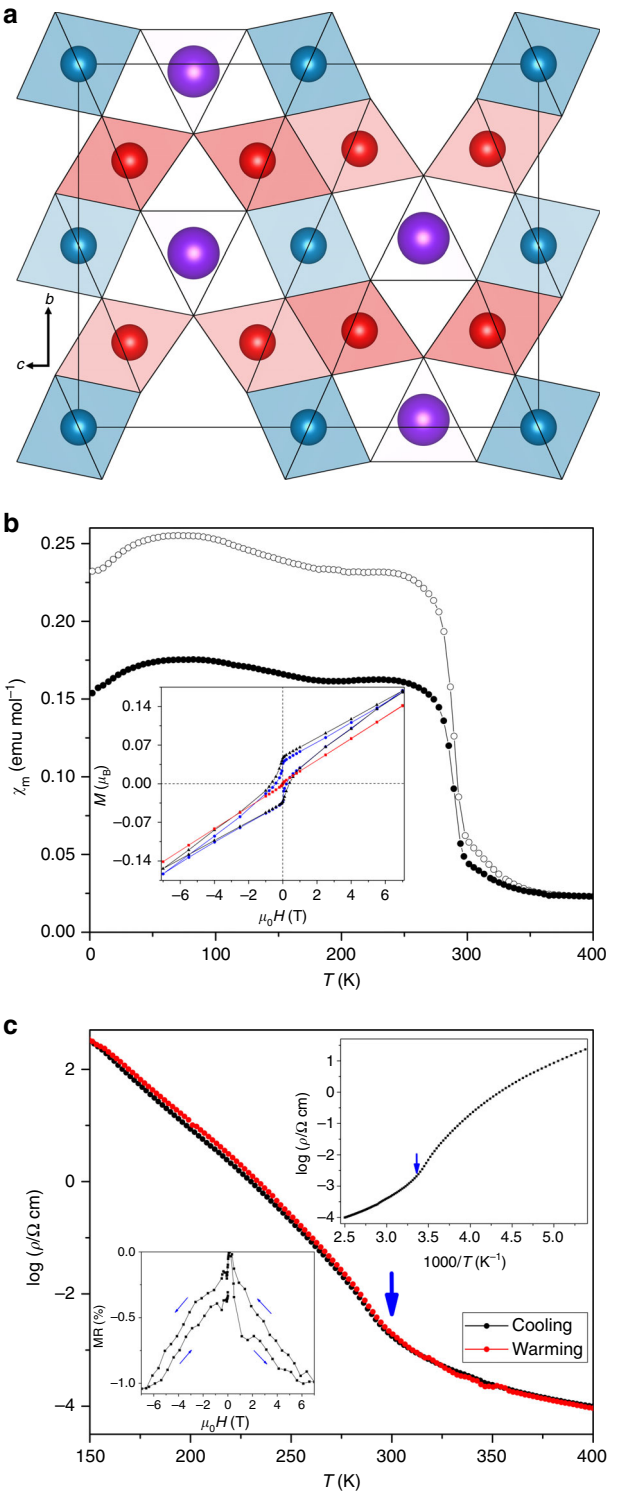

Fig. 1 Crystal structure and magnetisation studies of $CaFe_3O_5$. **a** Polyhedral projection of the $CaFe_3O_5$ structure showing FeO_6 octahedra in red/blue for symmetry inequivalent Fe1/Fe2 sites, and Ca within trigonal prismatic tunnels in purple. **b** ZFC (closed symbols) and FC (open symbols) magnetic susceptibilities for $CaFe_3O_5$, with insert showing magnetisation-field measurements at 2, 230 and 300 K (blue, black and red points respectively). **c** Log_{10} plot of the electrical resistivity of a sintered pellet of $CaFe_3O_5$ against temperature on cooling and warming, with the discontinuity at 302 K marked. Inset in the top right shows the plot against reciprocal temperature with a change in activation energy from 0.61 eV below T_M to 0.26 eV above the transition. Inset in lower left displays the magnetoresistance MR at 200 K

discovered structural differences between the two phases. Two inequivalent iron sites Fe1 and Fe2 are present in a 2:1 ratio in $CaFe_3O_5$, and in the HT phase they have respective Bond Valence Sums (BVSs) of 2.43 and 2.22, equivalent to formal charges of +2.75 and +2.50 when renormalized to the average of +2.67. Differing charge redistributions occur below the 302 K magnetic and phase segregation transition (Fig. 4b). In the phase with magnetic propagation vector (½ 0 0), the Fe1 and Fe2 BVSs diverge to very different values of 2.67(6) and 2.03(4) at 4 K, consistent with charge order (CO) of Fe^{3+} and Fe^{2+} respectively. The coexisting phase with (0 0 0) magnetic order shows the opposite behaviour as the Fe1 and Fe2 BVSs converge to similar values of 2.44(8) and 2.29(7) at 4 K showing that the electronic states at the two sites are not significantly different, hence this phase is charge averaged (CA).

Degenerate $3d^6$ Fe^{2+} states are subject to Jahn–Teller distortion which leads to tetragonal octahedral compression in magnetite[2], corresponding to negative values of the Q_{JT} distortion parameter. The Fe2 site in $CaFe_3O_5$ has a large negative Q_{JT} value due to intrinsic distortions within the HT structure (Fig. 4c), but below $T_M = 302$ K Q_{JT} becomes more negative for the CO phase, consistent with localisation of Fe^{2+} states, while the magnitude of Q_{JT} decreases in keeping with the observed increase in Fe2 site valence for the CA phase. Jahn–Teller distortion at the Fe2 site in the CO phase leads to order of the t_{2g} orbital with minority spin electron density directed towards the two neighbouring Fe1 sites. Hence this localised orbital has the correct orientation to form a trimeron, a linear unit of three Fe ions formed by delocalisation of the minority spin electron in the ordered orbital of the central Fe^{2+} ion[2], as shown in Fig. 3c. Trimeron formation requires FM alignment of the three magnetic moments, Fe^{3+}–Fe^{2+}–Fe^{3+} CO, orbital order at the central Fe^{2+} in the plane of the three atoms, and shortening of the Fe–Fe distances within the trimeron[2]. All these conditions are observed in the Fe1–Fe2–Fe1 ribbons in the CO phase with shortening of Fe1–Fe2 distances below T_M observed in Fig. 4d, but none are fulfilled in the CA structure, so the observed spin orders and structural distortions in $CaFe_3O_5$ demonstrate that trimeron order is observed only in the CO phase. However, a slight shortening of Fe–Fe distances in the FM chains parallel to the *a*-axis is observed in the CA phase (Fig. 4d), consistent with a weak bonding effect from extended band states of the minority spin electrons. Fe1–Fe1 and Fe2–Fe2 distances are constrained to be equal (to *a*/2) and this is the likely driver for the observed averaging of charge states between the two sites in the CA phase so that their minority spin populations become more equal.

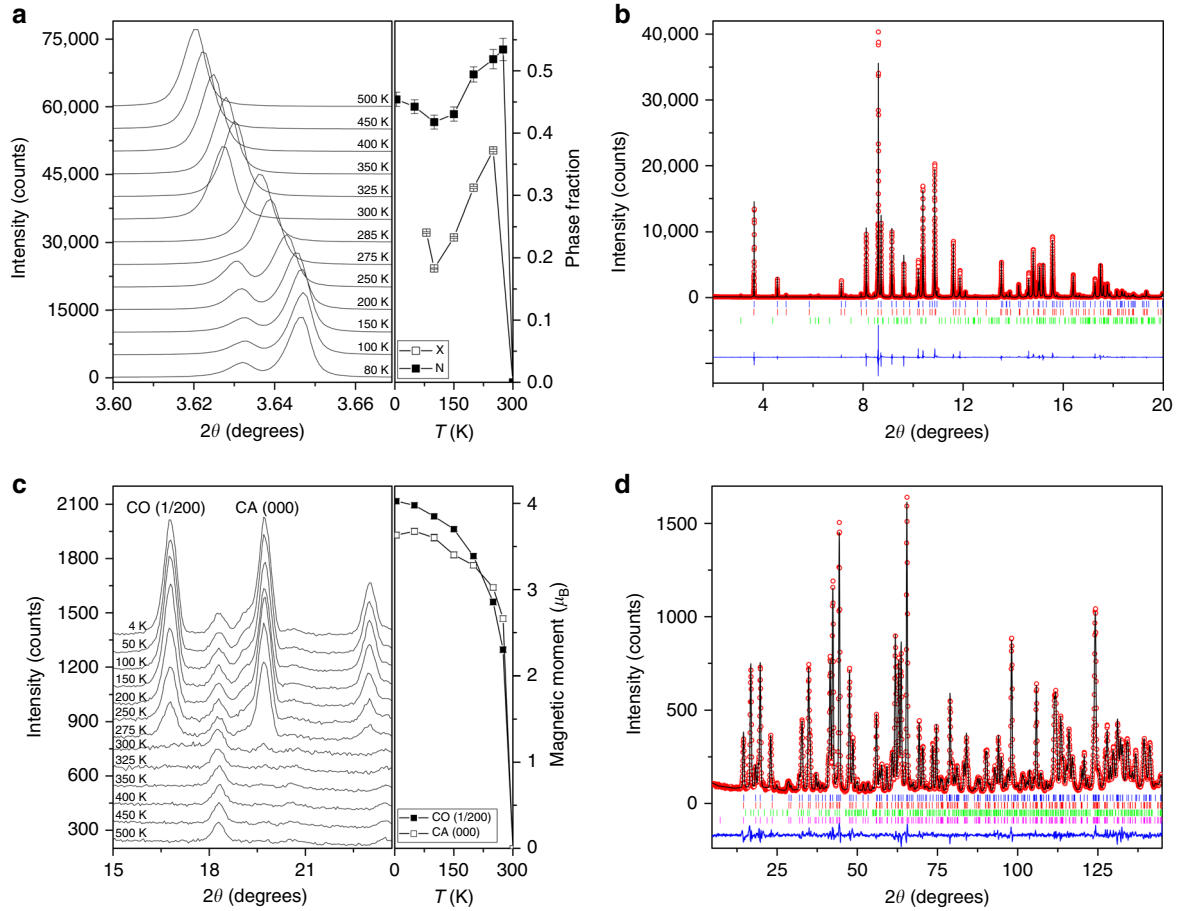

Fig. 2 Electronic phase separation of $CaFe_3O_5$. **a** Evolution of the X-ray (002) peak which shifts to lower 2θ when cooled to 300 K, just below the $T_M = 302$ K transition, with separation into two components at lower temperatures. The phase fractions of the charge averaged (CA) phase, obtained from synchrotron (X) and neutron (N) diffraction data are shown in the right-hand panel. Error bars are the estimated standard deviations calculated during profile fitting. **b** Rietveld fit to synchrotron powder diffraction profiles for $CaFe_3O_5$ at 80 K (R-factors $R_p = 9.35$ %, $R_{wp} = 11.0$ %), with blue and red tick marks indicating the two low temperature phases and green marks 2.3% of $Ca_2Fe_2O_5$ impurity. **c** The appearance of the magnetic reflections with propagation vectors of (000) for the CO phase and (½00) for the charge averaged (CA) phase below 302 K and the temperature evolution of their magnetic moments. **d** The Rietveld fit to neutron powder diffraction profiles for $CaFe_3O_5$ at 4 K (R-factors $R_p = 6.14$ %, $R_{wp} = 7.28$ %), with structural phases indicated with blue and red tick marks. The green and pink tick marks represent the magnetic phases with propagation vectors of (½00) and (000)

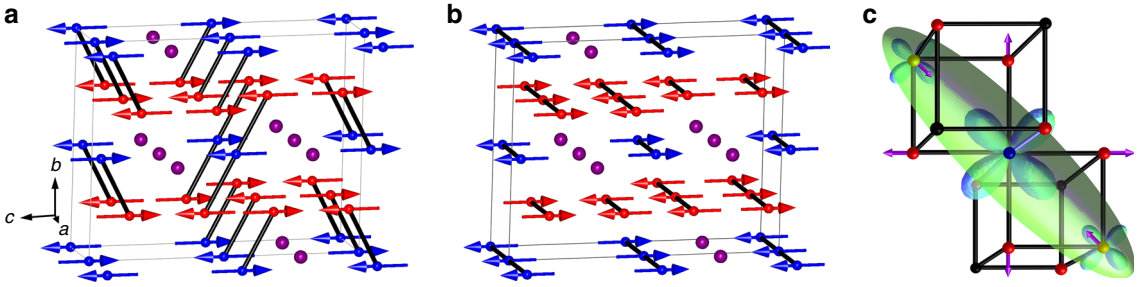

Fig. 3 Magnetic structures for the two phases of $CaFe_3O_5$. Fe1/Fe2 spins are shown in red/blue and Ca ions in purple. **a** Magnetic structure of the charge ordered (CO) phase $CaFe_3O_5$ with propagation vector (½ 0 0), with lines showing ferromagnetic order within trimerons. **b** Magnetic structure of the charge averaged (CA) phase, with (0 0 0) propagation and lines showing the ferromagnetic chain parallel to the *x* axis. **c** A trimeron unit as found in the CO structure (**a**) with bonding electron density represented as an ellipsoid. The size of the t_{2g} orbitals approximates the atomic populations. The atomic displacement arrows indicate the elongation of the four Fe–O bonds perpendicular to the Jahn–Teller contracted axis and the shortening of the cation–cation distances due to weak Fe–Fe bonding interactions

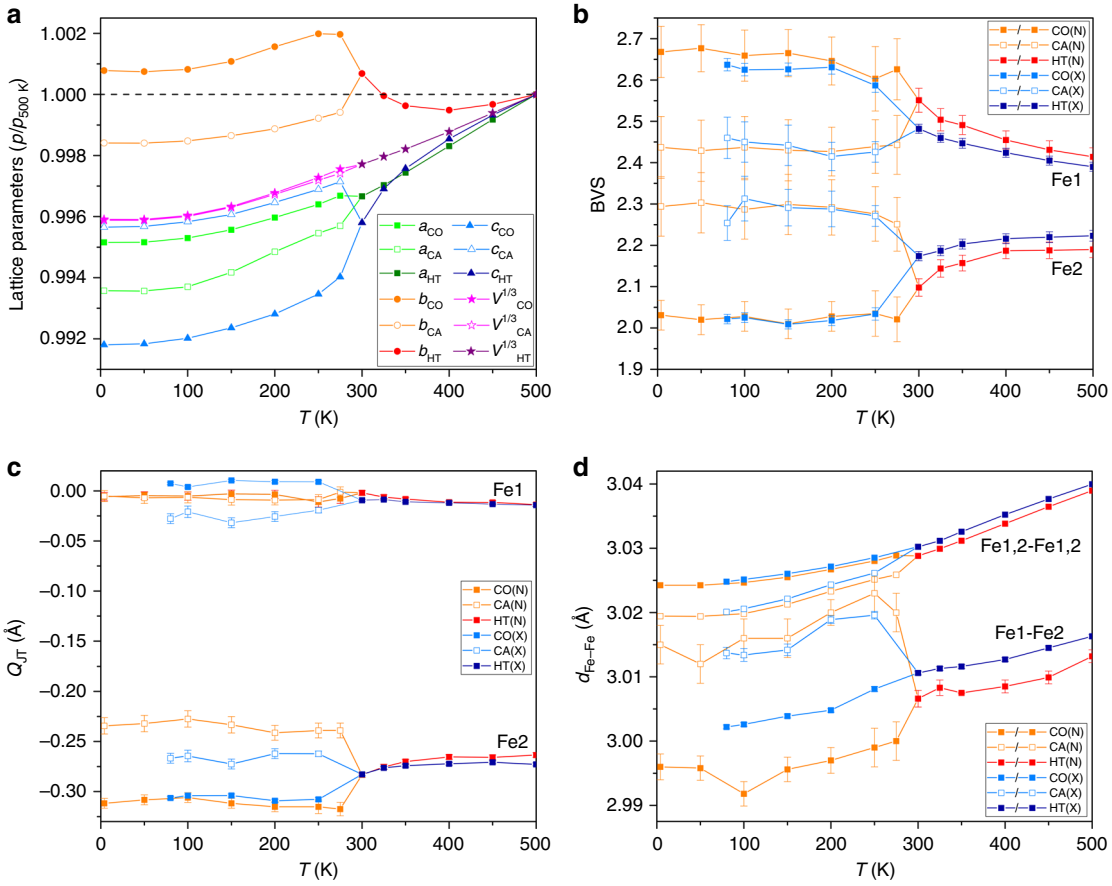

Fig. 4 Crystal structure parameters of $CaFe_3O_5$. **a** Changes in the lattice parameters relative to 500 K values obtained from PND ($a_{500\ K} = 3.03896(1)$, $b_{500\ K} = 10.01355(5)$ and $c_{500\ K} = 12.67039(7)$ Å). Temperature dependence of the **b** BVS and **c** the amplitude of Jahn–Teller distortion (Q_{JT}) of the FeO_6 octahedra for the two sites in the high temperature (HT), charge ordered (CO) and charge averaged (CA) phases, obtained from neutron (N) and synchrotron X-ray (X) diffraction data. **d** The evolution of the Fe1-Fe2 bonding distance with temperature, with the lattice parameter (Fe1,2-Fe1,2) as reference. Error bars are the estimated standard deviations calculated during profile fitting

The electronic orders in the two phases of $CaFe_3O_5$ do not change the structural symmetry, but they lead to different cell distortions (Fig. 4a) as trimeron formation shortens the *c*-axis parameter in the CO phase, with *a* and *b* expanding to compensate, while the *a*-axis shortening in the CA phase leads to expansion of *c*. Although the overall cell volumes for the two components remain identical within error at low temperatures, the differing spontaneous strains from these lattice distortions are the likely driver for the long range separation as proposed for perovskite manganites[12–14]. Short range phase and strain fluctuations in the HT phase are evidenced indirectly below 350 K through divergence of zero field- and field- cooled susceptibilities in Fig. 1b, and changes in the slopes of *b* and *c* lattice parameters in Fig. 4a.

Charge ordering in one of the two low temperature phases is clearly a key driver for the long range electronic phase separation in $CaFe_3O_5$ and perovskite type oxides[15] although in $CaFe_3O_5$ this leads to the formation of orbital molecules[16], more complex

electronic objects than simple localised-charge ions. However, phase separation in $CaFe_3O_5$ occurs without a change of lattice symmetry in either component, demonstrating that strain variations within a given lattice are sufficient to drive long range segregation. Band structure calculations (shown in Supplementary Fig. 4 and Supplementary Table 6) confirm that these distortions are sufficient to stabilise CO in one structure but not the other for a realistic value of the Hubbard U-parameter. Phase separation in manganites usually results from an incomplete phase transition where a metallic HT FM phase is partially transformed to a charge ordered insulator, and the high and low temperature phases coexist to base temperature. A notable example is $Nd_{0.5}Sr_{0.5}MnO_3$ which on cooling was observed to order as a single FM phase at 250 K, then to phase separate into a mixture of FM and A-type antiferromagnetic (AFM-A) phases below 220 K, and finally to undergo a further phase separation into a mixture of FM, AFM-A and charge ordered AFM-CE phases below 150 K, with all three phases extant down to the lowest measured temperature of 15 K[17]. $CaFe_3O_5$ undergoes a genuine electronic phase separation in the sense that both of the two low temperature CA and CO phases are electronically and magnetically distinct from the HT paramagnetic state, and so is analogous to e.g. the separation of a fluid into a liquid and gas below a critical transition. Both low temperature $CaFe_3O_5$ phases are magnetically ordered and it is remarkable that they appear to share a common magnetic ordering temperature as shown in Fig. 2c although the spin-spin exchange interactions within the two magnetic structures will not be identical.

Another important difference is that phase separation in manganites is associated with substantial intrinsic disorder due to cation mixing, and a recent study has demonstrated that chemical ordering of cations in $(La_{1-y}Pr_y)_{1-x}Ca_xMnO_3$ suppresses long range phase separation[18]. $CaFe_3O_5$ is in principle a stoichiometric material although small strain variations due to the 4% substitution of Fe for Ca observed in our polycrystalline sample may tip the local balance between the energies of the two ground states leading to phase coexistence. The resulting disorder in magnetic interactions could also be important in stabilising the phase coexistence in a Griffiths-type model[19]. All Mn sites are electronically equivalent in the HT aristotype manganite perovskite structure but $CaFe_3O_5$ has a further electronic degree of freedom as charge can be redistributed between structurally inequivalent Fe1 and Fe2 sites, leading to the observed extremes of charge ordering (CO) in one phase and charge averaging (CA) in the other. This charge redistribution mechanism is akin to electronic separation models originally proposed for manganites[20,21], although couplings of both the charge redistribution degree of freedom and trimeron formation associated with charge and orbital ordering to the lattice appear to be important factors that drive phase segregation in $CaFe_3O_5$.

Discussion

In conclusion, the present study demonstrates that phase separation of a single HT paramagnetic state into two distinct low temperature phases with different long range spin and electronic orders occurs in $CaFe_3O_5$ when cooled below 302 K. Although both phases are antiferromagnetic overall, the formation of different FM units within them is coupled to the electronic orders; one phase has full Fe^{2+}/Fe^{3+} CO associated with trimeron formation, but CA stabilises FM chains in the other phase. Weak Fe–Fe bonding driven by the FM orders introduces different lattice strains into the two phases although no change of structural symmetry occurs, and strain variations within the polycrystalline sample tip the local balance between the energies of the two phases leading to phase coexistence. $CaFe_3O_5$ thus links the trimeron-ordering of magnetite to the microstructural physics of perovskite manganites. $CaFe_3O_5$ also demonstrates new possibilities for more complex 'electronically soft matter'[22] than in perovskites where orbital molecule formation and redistribution of charge between distinct cation sites offer additional degrees of freedom for generation and potential control of electronic phase-segregated nanostructures.

Methods

Sample preparation and characterisation. Polycrystalline $CaFe_3O_5$ was prepared from stoichiometric quantities of $CaFe_2O_4$, Fe_2O_3, and Fe powders pressed into pellets, sealed in evacuated quartz tubes, and heated at 1100 °C for 12 h. (The $CaFe_2O_4$ was synthesised at ambient pressure using the ceramic technique outlined by Wan et al[23]. where $CaCO_3$ and Fe_2O_3 powders were ground together in 1:1 ratio, pressed into pellets, heated at 850 °C for 4 h, reground and repelleted, and finally reheated at 1100 °C for 12 h.) Thermogravimetric analysis heating the sample in air at 10 °C min^{-1} to 900 °C, as shown in Supplementary Fig. 3, gave a mass increase of 2.789%, in agreement with the calculated value of 2.781% for oxidation of $CaFe_3O_5$. Powder X-ray diffraction confirmed that $CaFe_3O_5$ adopts an orthorhombic $Sr_2Tl_2O_5$ type structure with space group *Cmcm* as reported previously[10].

Magnetic and electrical measurements. Magnetic measurements were carried out with a Quantum Design MPMS XL SQUID magnetometer. Magnetic susceptibility was recorded in zero field cooled (ZFC) and field cooled (FC) conditions between 2 and 400 K with an applied magnetic field of 1000 Oe. Hysteresis loops were also measured at 2, 230 and 300 K. Electrical resistivity measurements were carried out with a Quantum Design PPMS, between 180 and 400 K. Magnetoresistance hysteresis loops were also measured at 200 K.

Powder synchrotron X-ray and neutron diffraction studies. High resolution powder X-ray diffraction data were collected at the ID22 beamline of the ESRF with incident wavelength 0.3999 Å. The powder was packed into a glass capillary with an outer diameter of 0.7 mm and spun during data acquisition with temperatures from 80 to 500 K controlled using an Oxford Cryostream system. High resolution neutron diffraction data were collected at the D2B beamline of the ILL with incident wavelength 1.5940 Å. 5 g of powder samples were packed into a vanadium can and diffraction patterns were collected at temperatures from 4 to 500 K. Crystal and magnetic structures of $CaFe_3O_5$ were Rietveld-fitted using the FullProf Suite[24]. A small amount of Fe at the Ca site was found from both synchrotron X-ray [4.4(3)% Fe] and neutron [4.0(8)% Fe] refinements of cation site occupancies at 500 K. Crystal structure refinements of the two phases formed below 302 K in $CaFe_3O_5$ was possible with both the synchrotron X-ray and neutron powder diffraction data except at temperatures just below the transition (275 and 285 K). Magnetic irreducible representation analysis was carried out using BasIrReps. Bond valence sums for each iron site were calculated using a standard method with linear interpolation to estimate mixed charge states between Fe^{2+} and Fe^{3+}[25,26]. The crystal structure projection in Fig. 1a was generated using VESTA[27] and the magnetic structures in Fig. 3a, b were made using FullProf Studio.

Electronic structure calculations. DFT+U electronic structure calculations were performed using CASTEP[28] (v16 and 17) utilising planewaves (650 eV cutoff) and on-the-fly pseudopotentials, within the PBE approximation to exchange and correlation. Band structures (shown in Supplementary Fig. 4 and Supplementary Table 6) predict metallic charge averaged ground states for both the refined CO and CA structures at small values of the Hubbard *U* energy, and insulating charge ordered states for both phases at large *U*. However, values in the range $2.0 < U < 4.0$ eV simultaneously predict the charge averaged state for the CA structure and the charge ordered state for the CO structure, and hence confirm that this range is realistic for Fe oxides.

Data availability. Data that support the findings of this study have been deposited at https://doi.org/10.7488/ds/2378.

Received: 3 March 2018 Accepted: 25 June 2018
Published online: 30 July 2018

References

1. Verwey, E. J. W. Electronic conduction of magnetite (Fe_3O_4) and its transition point at low temperatures. *Nature* **144**, 327–328 (1939).
2. Senn, M. S., Wright, J. P. & Attfield, J. P. Charge order and three-site distortions in the Verwey structure of magnetite. *Nature* **481**, 173–176 (2012).
3. Dagotto, E., Hotta, T. & Moreo, A. Colossal magnetoresistant materials: the key role of phase separation. *Phys. Rep.* **344**, 1–153 (2001).

4. Uehara, M., Mori, S., Chen, C. H. & Cheong, S. W. Percolative phase separation underlies colossal magnetoresistance in mixed-valent manganites. *Nature* **399**, 560–563 (1999).
5. Tokura, Y. Critical features of colossal magnetoresistive manganites. *Rep. Prog. Phys.* **69**, 797–851 (2006).
6. Lavina, B. et al. Discovery of the recoverable high-pressure iron oxide Fe_4O_5. *Proc. Natl Acad. Sci. USA.* **108**, 17281–5 (2011).
7. Ovsyannikov, S. V. et al. Charge-ordering transition in iron oxide Fe_4O_5 involving competing dimer and trimer formation. *Nat. Chem.* **8**, 501–508 (2016).
8. Hong, K. H., McNally, G. M., Coduri, M. & Attfield, J. P. Synthesis, crystal structure, and magnetic properties of $MnFe_3O_5$. *Z. für Anorg. und Allg. Chem.* **642**, 1355–1358 (2016).
9. Hong, K. H., Arevalo-Lopez, A. M., Coduri, M., McNally, G. M. & Attfield, J. P. Cation, magnetic, and charge ordering in $MnFe_3O_5$. *J. Mater. Chem. C.* **6**, 3271–3275 (2018).
10. Evrard, O. et al. Mise en évidence de $CaFe_4O_6$ et détermination des structures cristallines des ferrites de calcium $CaFe_{2+n}O_{4+n}$ (n =1, 2, 3): nouvel exemple d'intercroissanc. *J. Solid State Chem.* **35**, 112–119 (1980).
11. Delacotte, C. et al. Structural transition at 360 K in the $CaFe_5O_7$ ferrite: toward a new charge ordering distribution. *Inorg. Chem.* **53**, 10171–10177 (2014).
12. Ahn, K. H., Lookman, T. & Bishop, A. R. Strain-induced metal-insulator phase coexistence in perovskite manganites. *Nature* **428**, 401–404 (2004).
13. Burgy, J., Moreo, A. & Dagotto, E. Relevance of cooperative lattice effects and stress fields in phase-separation theories for CMR manganites. *Phys. Rev. Lett.* **92**, 3–6 (2004).
14. Guzmán-Verri, G. G., Brierley, R. T., Littlewood, P. B. Elastic interactions and control of the Mott transition. Preprint at arXiv:1701.02318 (2017).
15. Shenoy, V. B. & Rao, C. N. R. Electronic phase separation and other novel phenomena and properties exhibited by mixed-valent rare-earth manganites and related materials. *Philos. Trans. R. Soc. A* **366**, 63–82 (2008).
16. Attfield, J. P. Orbital molecules in electronic materials. *APL Mater.* **3**, 1–7 (2015).
17. Woodward, P. M., Cox, D. E., Vogt, T., Rao, C. N. R. & Cheetham, A. K. Effect of compositional fluctuations on the phase transitions in $(Nd_{1/2}Sr_{1/2})MnO_3$. *Chem. Mater.* **11**, 3528–3538 (1999).
18. Zhu, Y. et al. Chemical ordering suppresses large-scale electronic phase separation in doped manganites. *Nat. Commun.* **7**, 1–6 (2016).
19. Magen, C. et al. Observation of a Griffiths-like phase in the magnetocaloric compound $Tb_5Si_2Ge_2$. *Phys. Rev. Lett.* **96**, 167201 (2006).
20. Yunoki, S. et al. Phase separation in electronic models for manganites. *Phys. Rev. Lett.* **80**, 845–848 (1998).
21. Moreo, A., Yunoki, S. & Dagotto, E. Phase separation scenario for manganese oxides and related materials. *Science* **283**, 2034–2040 (1999).
22. Milward, G. C., Calderon, M. J. & Littlewood, P. B. Electronically soft phases in manganites. *Nature* **433**, 607–610 (2005).
23. Wan, R., Jia, C. & Zhang, W. Preparation and photoelectric properties of p-$CaFe_2O_4$/n-WO_3 composites. *J. Alloy Compd.* **544**, 1–5 (2012).
24. Rodriguez-Carvajal, J. Recent advances in magnetic structure determination by neutron powder diffraction. *Physica B.* **192**, 55–69 (1993).
25. Attfield, J. P. Charge ordering in transition metal oxides. *Solid State Sci.* **8**, 861–867 (2006).
26. Brown, I. D. VALENCE: a program for calculating bond valences. *J. Appl. Crystallogr.* **29**, 479–480 (1996).
27. Momma, K. & Izumi, F. VESTA 3 for three-dimensional visualization of crystal, volumetric and morphology data. *J. Appl. Crystallogr.* **44**, 1272–1276 (2011).
28. Clark, S. J. et al. First principles methods using CASTEP. *Z. Krist.* **220**, 567–570 (2005).

Acknowledgements

The authors acknowledge financial support from European Research Council (ERC), Engineering and Physical Sciences Research Council (EPSRC) and Science and Technology Facilities Council (STFC). The authors also thank Andy Fitch for help at ESRF and Gary Nichol, Graham McNally, Alex Browne and Giuditta Perversi for local support.

Author contributions

K.H.H. and J.P.A. designed the concept for this study. K.H.H., A.M.A.-L., and C.R. performed the experimental work and data analysis, and J.C. performed the band structure calculations. K.H.H. and J.P.A. wrote the manuscript with inputs from all authors.

Additional information

Supplementary Information accompanies this paper at https://doi.org/10.1038/s41467-018-05363-6.

Competing interests: The authors declare no competing interests.

Reprints and permission information is available online at http://npg.nature.com/reprintsandpermissions/

Publisher's note: Springer Nature remains neutral with regard to jurisdictional claims in published maps and institutional affiliations.

Inorganic Chemistry
Cite This: Inorg. Chem. 2018, 57, 14347−14352
Article
pubs.acs.org/IC

Complex Cation and Spin Orders in the High-Pressure Ferrite $CoFe_3O_5$

Ka H. Hong,[†] Elena Solana-Madruga,[†] Mauro Coduri,[‡] and J. Paul Attfield*[,†]

[†]Centre for Science at Extreme Conditions and School of Chemistry, University of Edinburgh, West Mains Road, Edinburgh EH9 3FD, United Kingdom

[‡]European Synchrotron Radiation Facility, 71 avenue des Martyrs, Grenoble 38000, France

Supporting Information

ABSTRACT: A ferrite in the $Sr_2Tl_2O_5$-type MFe_3O_5 family with M = Co has been synthesized at 12 GPa pressure. Neutron diffraction shows the sample to be Co deficient with composition $Co_{0.6}Fe_{3.4}O_5$. The Co/Fe cation distribution is found to be profoundly different from those of MFe_3O_5 analogs and lies between normal and inverse limits, as Co^{2+} substitutes across trigonal prismatic and one of the two octahedral sites. $CoFe_3O_5$ shows complex magnetic behavior with weak ferromagnetism below $T_{C1} \approx 300$ K and a second transition to ferrimagnetic order at $T_{C2} \approx 100$ K. Spin scattering of carriers leads a substantial increase in the hopping activation energy below T_{C1}, and a small negative magnetoresistance is observed at low temperatures.

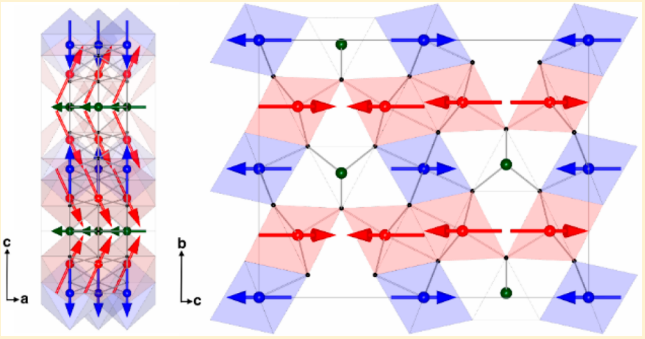

INTRODUCTION

Iron oxide spinels and related magnetic materials are important for many applications and also for fundamental interest in couplings between spin, charge, orbital, and lattice degrees of freedom. Magnetite, Fe_3O_4, has been studied intensively since 1939 when Verwey reported a metal−insulator transition accompanied by a structural distortion.[1] The low-temperature structure has a complex charge and orbital ordering that leads to the formation of trimerons−linear orbital molecule clusters of three Fe ions.[2] Further notable magnetic and electronic orders have subsequently been discovered in the underexplored Fe_nO_{n+1} and substituted $MFe_{n-1}O_{n+1}$ homologous series. The $n = 4$ phase Fe_4O_5, prepared using high-pressure high-temperature (HPHT) synthesis,[3] has an incommensurate charge order at 150 K below which dimeron and trimeron-like groups of Fe ions are formed,[4] and higher Fe_nO_{n+1} homologues with $n > 4$ have also been made at pressure.[5] Studies of $n = 6$ $CaFe_5O_7$ have revealed a coupled structural and magnetic transition at 360 K accompanied by charge ordering.[6−8]

In addition to Fe_4O_5, other $n = 4$ MFe_3O_5 phases have also been found to have notable properties. $CaFe_3O_5$, which was first reported in 1980 and can be prepared at ambient pressure,[9] has recently been shown to have long-range electronic phase separation. Magnetic ordering below 302 K leads to segregation into Fe^{2+}/Fe^{3+} charge averaged and charge ordered phases with formation of trimerons in the latter.[10] $MnFe_3O_5$, discovered under HPHT conditions, shows a rich variety of magnetic ordered states on cooling below $T_N = 350$ K, and Fe^{2+}/Fe^{3+} charge ordering at 60 K leads to spin reorientation.[11,12] $MgFe_3O_5$ was also reported in a study of the Fe_4O_5-$Mg_2Fe_2O_5$ solid solution, but the crystal structure and magnetic properties were not reported.[13]

The MFe_3O_5 phases adopt the orthorhombic $Sr_2Tl_2O_5$-type structure with space group *Cmcm*.[14] This has three independent cation sites M1, M2, and M3 in a 2:1:1 ratio, where M1 and M2 form edge-sharing MO_6 octahedra channeled by triangular prisms containing the M3 site, as shown in Figure 1. The M3 site is occupied by large M^{2+} = Ca, Mn, and Fe cations in the above MFe_3O_5 materials. However, it is unclear whether transition metals smaller than iron will also occupy trigonal prismatic M3 sites or will prefer octahedral M1 and M2. These alternative distributions are analogous to the much-studied normal and inverse cation arrangements in spinels. Hence we report here the HPHT synthesis of $CoFe_3O_5$, the crystal structure including the cation distribution, and the electrical and magnetic properties.

EXPERIMENTAL SECTION

HPHT Synthesis. CoO and Fe_3O_4 powders were ground together in a 1:1 ratio and were heated under pressure at 1200 °C in a Pt capsule for 20 min in a two-stage Walker-type module. Reaction at 10 GPa pressure was unsuccessful, but 12 GPa gave a polycrystalline product of apparent composition $CoFe_3O_5$. Several batches of material were synthesized under the latter conditions.

Magnetic and Electrical Property Measurements. A Quantum Design MPMS XL SQUID magnetometer was used to carry out magnetization measurements. Electrical resistivity measurements were carried out with a Quantum Design PPMS.

Received: August 30, 2018
Published: November 1, 2018

DOI: 10.1021/acs.inorgchem.8b02458
Inorg. Chem. 2018, 57, 14347−14352

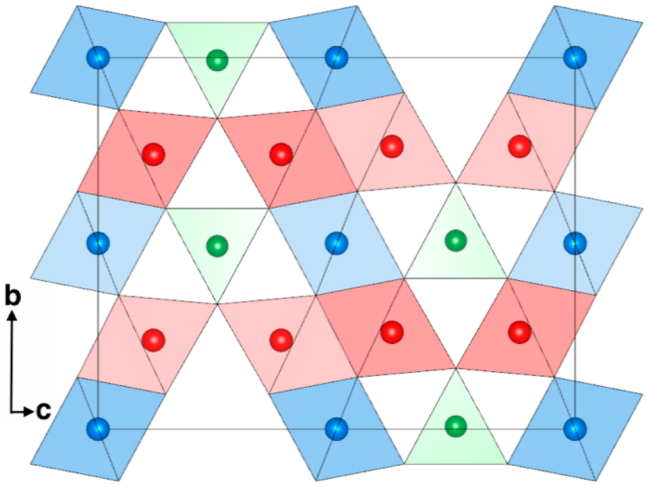

Figure 1. Polyhedral projection of the *Cmcm* structure of $CoFe_3O_5$ at 300 K with M1 site octahedra shown in red, M2 octahedra in blue, and M3 triangular prisms in green. Oxygens are located at the corners of polyhedra.

Crystal and Magnetic Structures. HPHT reaction products were initially characterized by powder X-ray diffraction collected with a Bruker D2 diffractometer using Cu K_α radiation. High-resolution powder synchrotron X-ray diffraction (PSXRD) data were collected at the ID22 beamline of the ESRF with incident wavelength 0.39994 Å. A glass capillary with an outer diameter of 0.3 mm was used to contain the polycrystalline sample of approximately 8 mg. Low-temperature diffraction data were collected from 5 to 90 K using a liquid helium cryostat system and from 90 to 400 K with an Oxford Cryosystems nitrogen cryostream. High-resolution time-of-flight powder neutron diffraction (PND) data were collected at the WISH beamline of the ISIS facility, with 50 mg of powder from several high-pressure syntheses packed into a vanadium can. Diffraction patterns were collected between 10 and 400 K using a closed cycle refrigerator (CCR) with a hot stage. The crystal and magnetic structures of $CoFe_3O_5$ were Rietveld-fitted using the FullProf Suite and General Structure Analysis System (GSAS),[15,16] and images were generated using VESTA.[17]

RESULTS AND DISCUSSION

Synthesis. Phase formation was confirmed using laboratory powder X-ray diffraction. A Rietveld fit to the diffraction pattern (Figure S1) confirms an orthorhombic *Cmcm* phase isostructural with the MFe_3O_5 (M = Ca, Fe, and Mn) analogs. The room-temperature lattice parameters of $CoFe_3O_5$ are a = 2.8982(4), b = 9.767(2), and c = 12.567(1) Å, with a cell volume of V = 355.7(1) Å^3. Further structural results are described later.

Magnetic and Electrical Properties. Magnetic susceptibilities in Figure 2a reveal two magnetic transitions for $CoFe_3O_5$. A small magnetic upturn is observed at $T_{C1} \approx 300$ K, and a second transition is seen at $T_{C2} \approx 100$ K. Both are accompanied by divergence of zero-field cooled (ZFC) and field cooled (FC) measurements indicating ferromagnetic contributions. Magnetization-field loops, shown in the inset of Figure 2a, show a small remnant magnetization of M_r = 0.014 μ_B per formula unit at 350 K, mostly likely due to traces of ferromagnetic spinel impurities. M_r increases to 0.06 μ_B on cooling from 350 to 200 K through T_{C1}, revealing an intrinsic weak ferromagnetism, and increases further on cooling through T_{C2} to 0.75 μ_B at 4 K, consistent with a ferrimagnetic order. Two similar magnetic transitions were reported for $MnFe_3O_5$ at 350 and 60 K.[12]

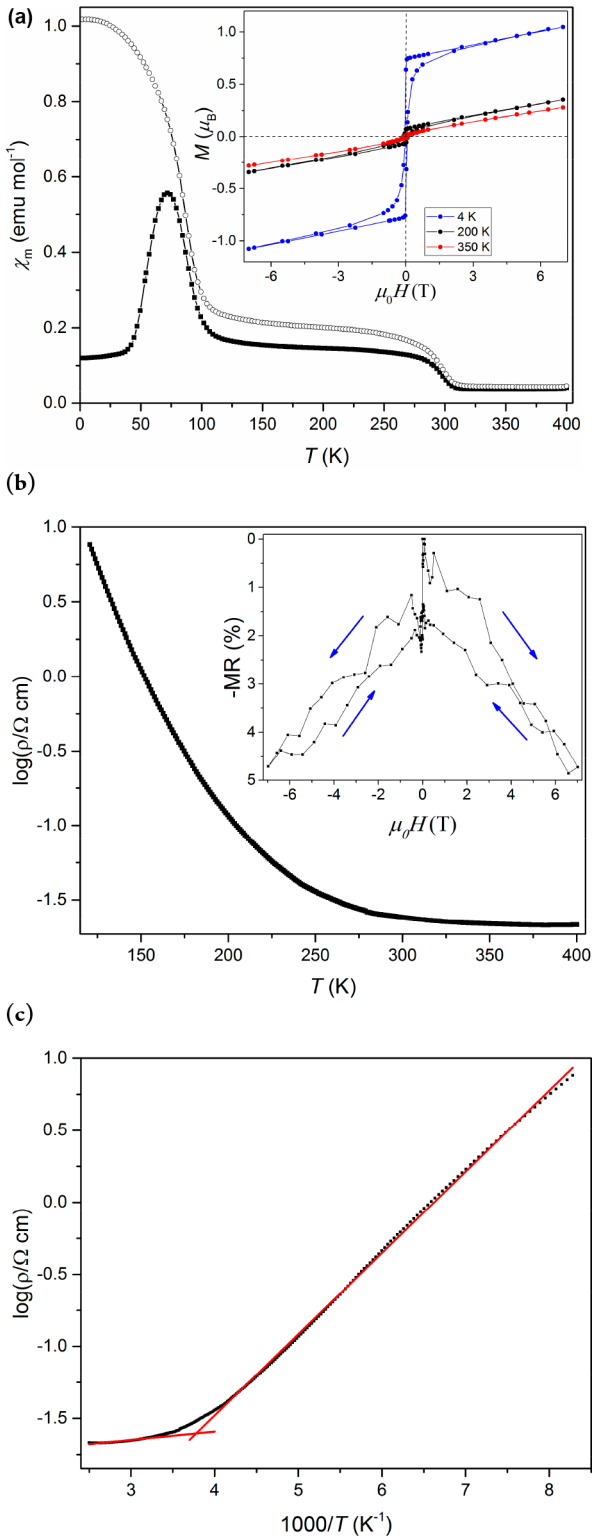

Figure 2. (a) ZFC (closed symbols) and FC (open symbols) magnetic susceptibilities for $CoFe_3O_5$ in a 0.2 T field. Inset shows magnetization-field loops at 4, 200, and 350 K. (b) Log_{10} of the electrical resistivity against temperature. Inset shows magneto-resistance at 125 K. (c) Log_{10}(resistivity)−reciprocal temperature plot showing Arrhenius fits above and below $T_{C1} \approx 300$ K.

The electrical resistivity of a polycrystalline pellet of $CoFe_3O_5$ shows semiconducting behavior (Figure 2b), and the resistance was too great to be measured below 120 K. The

DOI: 10.1021/acs.inorgchem.8b02458
Inorg. Chem. 2018, 57, 14347−14352

high-temperature activation energy for electron hopping, fitted as an Arrhenius $\rho = A \exp(E_a/k_BT)$ dependence in Figure 2c, is E_a = 14 meV showing that the material behaves as a highly doped semiconductor. The slope deviates on cooling below $T_{C1} \approx 300$ K ($1000/T_{C1} \approx 3.3$), and the 130−245 K region has a substantially higher E_a = 112 meV revealing a strong antiferromagnetic spin scattering contribution. A small magnetoresistance effect of $MR = -5\%$ in a 7 T field at 125 K is observed, as shown in the inset to Figure 2b, consistent with partial suppression of the spin scattering term. $CoFe_3O_5$ has a larger $-MR$ than $CaFe_3O_5$ due to a higher magnetization at low temperature.

Crystal Structure Determination. The high contrast between the neutron scattering lengths of Fe and Co (9.45 and 2.49 fm respectively) enabled occupancies of the three cation sites to be determined from refinement against the high-resolution neutron diffraction data obtained at 400 K (Figure S2). This reveals that the M1 site is occupied exclusively by Fe, while the M2 and M3 sites contain Fe/Co mixtures as shown in Table 1. The overall refined composition of $Co_{0.58}Fe_{3.42}O_5$ is Co deficient. Refined amounts and compositions of CoO rock salt and $CoFe_2O_4$ spinel-type secondary phases were 11.2(7)% $Co_{0.86}Fe_{0.14}O$ and 3.2(1)% $Co_{0.95}Fe_{2.05}O_4$, showing that these impurities are relatively Co rich. Further details are in Table S1. M−O bond distances and derived values for the bond valence sum (BVS), estimated by a standard interpolation method,[18,19] are shown in Table 2.

Table 1. Lattice Parameters, Atomic Coordinates, Site Occupancies, and Isotropic Thermal Displacements from Neutron Refinements in *Cmcm* Space Group of $CoFe_3O_5$ at 400 K (Upper Values) and 10 K (Lower Values)[a]

a (Å)	*b* (Å)	*c* (Å)	volume (Å^3)
2.9048(2)	9.7865(8)	12.5884(6)	357.86(4)
2.8836(1)	9.7968(3)	12.5385(5)	354.21(2)

atom	*x*	*y*	*z*	Occ[b] Fe/Co	B_{iso} (Å^2)
M1	1/2	0.2438(6)	0.1166(3)	1/0	2.0(1)
		0.2419(5)	0.1176(3)		1.4(1)
M2	0	0	0	0.78(1)/0.22	2.0
					1.4
M3	0	0.4792(8)	1/4	0.64(1)/0.36	2.0
		0.4834(8)			1.4
O1	1/2	0.3437(11)	1/4	1	0.9(1)
		0.3460(11)			0.8(1)
O2	0	0.3569(7)	0.0447(6)	1	0.9
		0.3587(7)	0.0431(6)		0.8
O3	0	0.0902(8)	0.1449(6)	1	0.9
		0.0872(8)	0.1478(6)		0.8

[a]Estimated standard deviations in independent variables are shown in parentheses. χ^2 = 13.1 and 11.8, R_{wp} = 10.7 and 8.7%, and R_p = 12.9 and 10.1% at 400 and 10 K, respectively. [b]Variable occupancies were refined against 400 K neutron data and were fixed in lower temperature refinements.

The long average M3−O distance and the M3 BVS show that this trigonal prismatic site is occupied by divalent cations, in keeping with other $Sr_2Tl_2O_5$-type materials, while the similar average distances and BVSs for the octahedral M1 and M2 sites indicate that they have a mix of divalent and trivalent cations. The estimated bond valence sums (BVSs) of the three cation sites in $CoFe_3O_5$ are similar to those of Fe_4O_5 at room temperature. The site-specific composition, written as $(M3)_2(M1)_2(M2)O_5$ for comparison with the standard MFe_3O_5 formula, is thus $(Co^{2+}_{0.36}Fe^{2+}_{0.64})(Fe^{2+}_{0.33}Fe^{3+}_{0.67})_2(Co^{2+}_{0.22}Fe^{2+}_{0.11}Fe^{3+}_{0.67})O_5$ assuming that Fe is oxidized to the trivalent state in preference to Co. The cation distribution reveals that this Co-deficient sample lies between the postulated normal and inverse MFe_3O_5 distributions with around 60% of the substituted Co^{2+} at the trigonal prismatic sites (normal distribution) and the remaining 40% at the octahedral sites (inverse distribution).

Table 2. Metal−Oxygen Bond Lengths with Derived Mean values ⟨ ⟩ and BVSs Shown for $CoFe_3O_5$ at 400 K (Upper Values) and 10 K (Lower Values)

bond	distance (Å)	bond	distance (Å)
M1−O1	1.943(7)	M2−O2 (×4)	2.095(6)
	1.948(7)		2.071(5)
M1−O2	2.257(9)	M2−O3 (×2)	2.026(8)
	2.243(9)		2.040(8)
M1−O2 (×2)	2.038(7)	⟨M2−O⟩	2.072(3)
	2.064(7)		2.061(3)
M1−O3 (×2)	2.120(8)	BVS(M2)	2.4(1)
	2.127(7)		2.3(1)
⟨M1−O⟩	2.086(3)	M3−O1 (×2)	1.967(9)
	2.096(3)		1.973(10)
BVS(M1)	2.4(1)	M3−O3 (×4)	2.245(7)
	2.5(1)		2.180(7)
		⟨M3−O⟩	2.152(3)
			2.111(3)
		BVS(M3)	2.0(1)
			2.2(1)

A surprisingly strong preference for Co to substitute for Fe at the octahedral M2 but not the M1 site is also discovered in $CoFe_3O_5$. The M1 site is found to have a higher BVS than M2 in other MFe_3O_5 materials, and a complete Fe^{3+}/Fe^{2+} charge ordering over M1/M2 sites is observed in one phase of $CaFe_3O_5$.[10] Hence the tendency for cobalt to substitute as Co^{2+} rather than Co^{3+} probably drives the M2 octahedral site preference, although the disorder within our Co-deficient sample does not lead to a significant difference between the M1 and M2 site BVSs.

Temperature Evolution of Crystal Structure. The thermal evolution of the crystal structure of $CoFe_3O_5$ between 5 and 400 K has been studied using high-resolution PSXRD (Figure 3) and PND experiments. Rietveld fits showed that the orthorhombic *Cmcm* structure is adopted throughout this temperature range. Anisotropic thermal expansion of the lattice parameters is observed when cooled below $T_{C1} \approx 300$ K (Figures 4 and S3), with *a* and *c* contracting with decreasing temperature, while *b* expands. Another anomaly in the slope of the lattice parameters and cell volume is found at $T_{C2} \approx 100$ K. These observations show that the changes in magnetic order are coupled to the lattice leading to magnetostrictive effects.

Refined coordinates do not reveal any large changes in the crystal structure between 10 and 400 K. BVS's shown in Figure 5 remain approximately constant on cooling, although slight anomalies are seen around $T_{C2} \approx 100$ K accompanied by an increase in the tetragonal Jahn−Teller distortion parameter Q_{JT} at site M1. The latter is consistent with intersite charge transfer increasing the Fe^{3+}/Fe^{2+} ratio, as Fe^{3+} has intrinsic $Q_{JT} = 0$, while orbitally degenerate Fe^{2+} has negative Q_{JT}. Hence there are traces of the charge ordering seen in other MFe_3O_5

DOI: 10.1021/acs.inorgchem.8b02458
Inorg. Chem. 2018, 57, 14347−14352

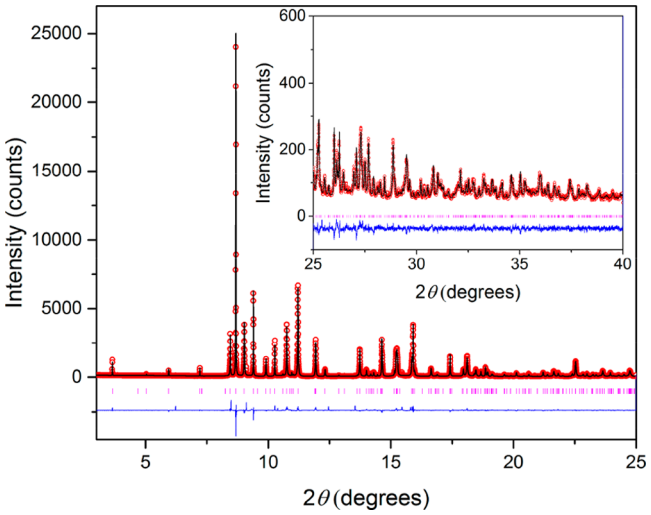

Figure 3. Rietveld fit to synchrotron powder diffraction profiles for $CoFe_3O_5$ at 300 K, with inset showing high-angle fitting (χ^2 = 8.5, R_{wp} = 12.3% and R_p = 9.4%).

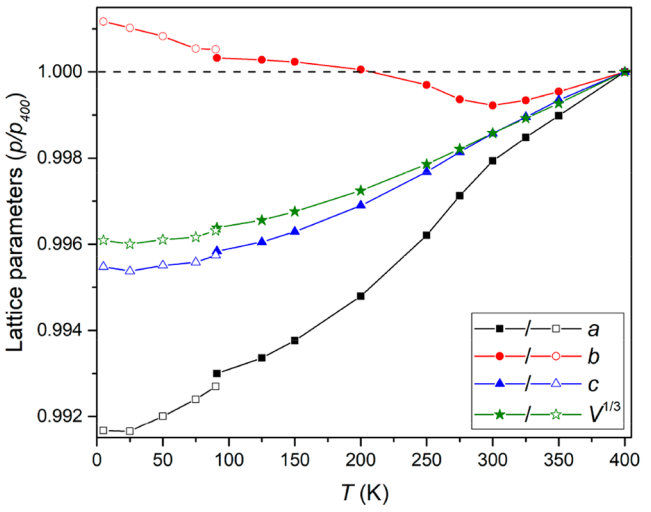

Figure 4. Changes in the lattice parameters relative to 400 K values obtained from PSXRD ($a_{400\ K}$ = 2.90423(3), $b_{400\ K}$ = 9.77325(8), and $c_{400\ K}$ = 12.5817(1) Å). Open/closed points were collected using helium cryostat/nitrogen cryostream systems.

materials, but the cation disorder in $CoFe_3O_5$ suppresses any clear charge and orbital ordering.

Magnetic Structures. High-resolution PND patterns collected at 10, 50, 150, and 400 K and additional short scans at intermediate temperatures were used to determine the magnetic structures of $CoFe_3O_5$ and to study their thermal evolution. Plots in Figure 6a reveal the appearance of magnetic reflections when $CoFe_3O_5$ is cooled below $T_{C1} \approx 300$ K, and additional magnetic peaks are observed below $T_{C2} \approx 100$ K. All of the magnetic reflections in both regimes were indexed by propagation vector [0 0 0], and analysis of the resulting irreducible representations for the spin order is shown in Table S2 with refined moment components in Table S3. The refined magnetic structures gave good fits to the data, as shown in Figure 6b. The magnetic contribution of the rock salt $Co_{0.86}Fe_{0.14}O$ phase, where spins order antiferromagnetically below ~300 K with a propagation vector of [1/2 1/2 1/2], was also included in the refinements.

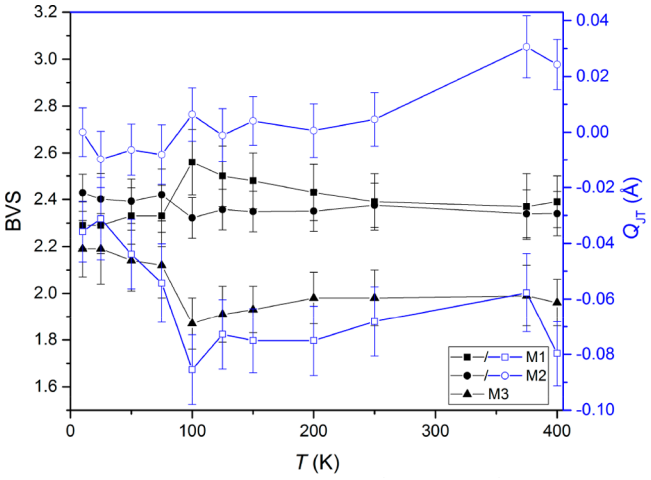

Figure 5. Temperature evolution of BVS (black points) and the tetragonal Jahn–Teller distortion parameter Q_{JT} (blue points) for the octahedral cation sites in $CoFe_3O_5$, obtained from PND data.

The magnetic structures adopted by $CoFe_3O_5$ below T_{C1} and T_{C2} are presented in Figure 7a,b, respectively, and the thermal evolutions of the ordered moments are shown in Figure 7c. On cooling below $T_{C1} \approx 300$ K, the spins at the octahedral M1 and M2 sites order antiferromagnetically parallel to the *c* axis, while the M3 spins remain disordered. Canting of the spins toward the *b*-axis is allowed by symmetry, although the ordered component is too small to refine, and this weak ferromagnetism is the likely cause of the small net magnetization observed at 200 K in Figure 2a. The additional magnetic reflections below $T_{C2} \approx 100$ K are fitted by a ferromagnetic order of the M3 spins along the *a*-axis with canting of the M1 spins so that they gain a ferromagnetic *x*-component antiparallel to the M3 spins. Further low-temperature spin reorientations reported in Fe_4O_5 and $MnFe_3O_5$ are driven by Fe^{2+}/Fe^{3+}charge ordering. However, cation disorder in $CoFe_3O_5$ suppresses any charge ordering, and hence no further spin canting is observed at lower temperatures. The total ordered M1 moment at 10 K of 4.3 μ_B is consistent with near-Fe^{3+}spins, while smaller M2 and M3 moments of 3.3 and 2.6 μ_B reflect the Fe/Co disorder. The predicted net ferrimagnetic moment of 1.1 μ_B per formula unit at 10 K is comparable to the remnant magnetization of 0.75 μ_B observed at 2 K (Figure 2a).

The antiferromagnetic spin ordering of $CoFe_3O_5$ formed below T_{C1} is the same as those reported in $MnFe_3O_5$ and in the charge averaged phase of $CaFe_3O_5$.[10,12] This is favored by dominant antiferromagnetic M1–M2 interactions through direct exchange and M–O–M superexchange between edge and corner sharing $M1O_6$ and $M2O_6$ octahedra. Weaker antisymmetric Dzyaloshinskii–Moriya (DM) interactions lead to canting and the observed weak ferromagnetism. Spins at the trigonal prismatic M3 sites are coupled to equal numbers of antiparallel M1 and M2 moments through M–O–M bridges, and so their long-range order is frustrated. Weaker DM interactions thus result in ferromagnetic order of M3 moments, perpendicular to the antiferromagnetic spins, below T_{C2}. Symmetric superexchange interactions between M3 and M1 spins lead to a canting of the latter such that they gain ferromagnetic components aligned antiparallel to the M3 spins. A similar coupled order of M3 and antiparallel M1 spin components is observed in the intermediate temperature spin

DOI: 10.1021/acs.inorgchem.8b02458
Inorg. Chem. 2018, 57, 14347–14352

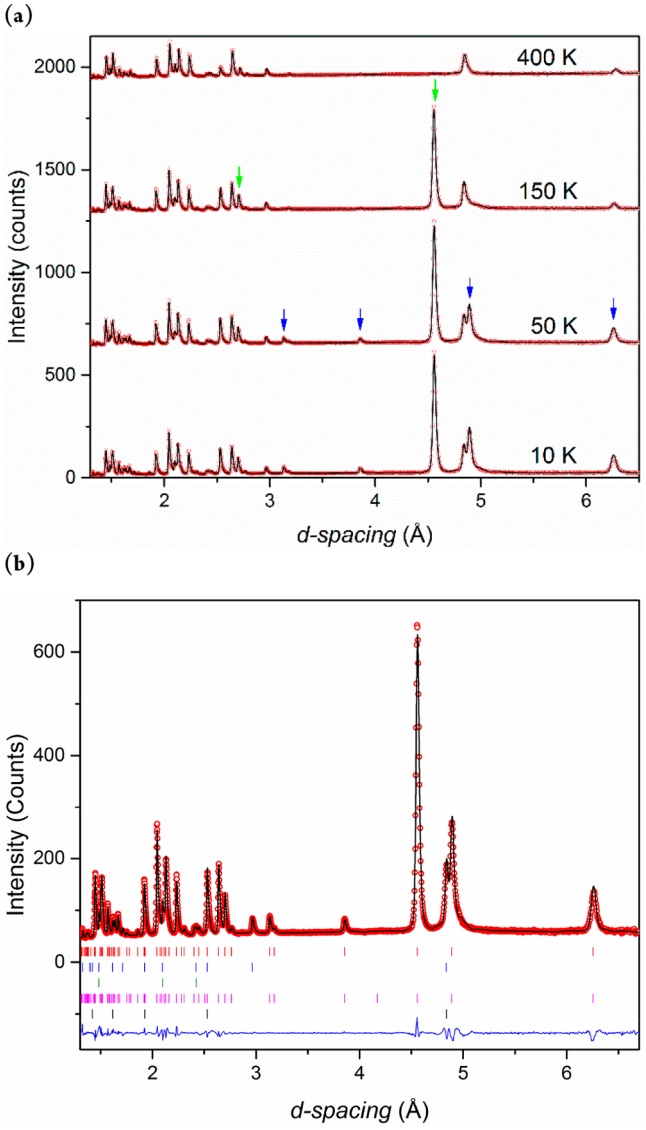

Figure 6. (a) Temperature evolution of the neutron diffraction pattern of $CoFe_3O_5$. Magnetic peak contributions indicated by green arrows in the 150 K pattern are (021) and (111), and those indicated by blue arrows at 50 K are (002), (020), (022), and (004), in order of descending *d*-spacing. Rietveld fits to the profiles are shown. (b) Full Rietveld plot for the 10 K data. Markers from top to bottom, respectively, show reflections from nuclear $CoFe_3O_5$, $CoFe_2O_4$, and CoO and magnetic $CoFe_3O_5$ and CoO type phases (χ^2 = 12.5, R_{wp} = 9.2% and R_p = 10.1%).

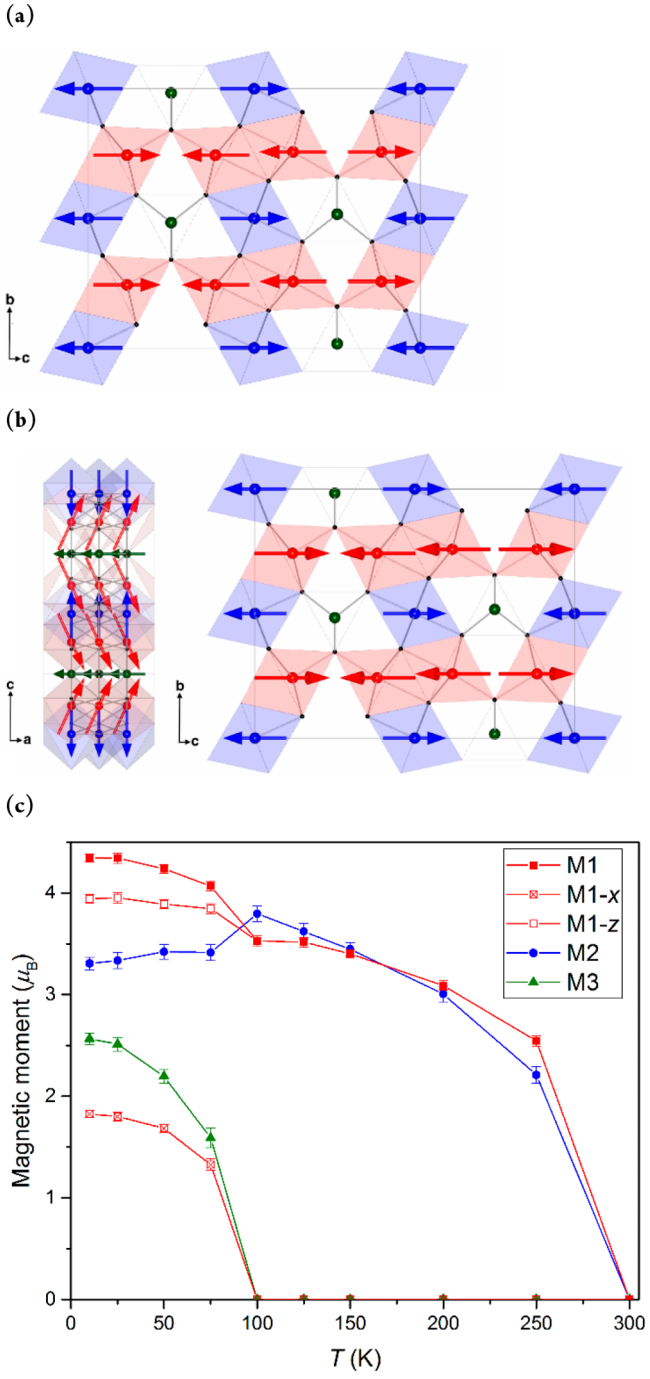

Figure 7. Magnetic structures of $CoFe_3O_5$ at (a) 150 and (b) 10 K. Octahedral M1 and M2 and trigonal prismatic M3 sites and moments are shown as red, blue, and green, respectively. (c) The temperature evolution of the ordered magnetic moments and the *x* and *z* components for the M1 spins.

structure of $MnFe_3O_5$,[12] but with spins in the *b*-direction, whereas those for $CoFe_3O_5$ are in the *a*-direction. The strong electronic anisotropy of Co^{2+} is likely to be responsible for the latter difference.

CONCLUSION

The above results demonstrate that the series of orthorhombic $Sr_2Tl_2O_5$-type MFe_3O_5 ferrites can be extended to M = Co, although a Co-deficient $Co_{0.6}Fe_{3.4}O_5$ phase was obtained from synthesis at 12 GPa, suggesting that higher pressures may be required to stabilize the ideal stoichiometry.

The cation distribution determined from neutron diffraction is found to be profoundly different from those in previously studied MFe_3O_5 derivatives of Fe_4O_5. Materials with M^{2+} = Ca and Mn cations larger than Fe^{2+} adopt normal cation distributions with M^{2+} only at the trigonal prismatic sites. The present study shows that Co^{2+} substitutes more evenly across trigonal prismatic and octahedral sites, so the cation distribution lies between normal and inverse MFe_3O_5 limits. A surprisingly strong preference for Co to substitute at just one of the two octahedral sites is also revealed. This likely reflects differing site potentials, although the disorder within our sample does not lead to a significant difference between octahedral site bond valence sums.

DOI: 10.1021/acs.inorgchem.8b02458
Inorg. Chem. 2018, 57, 14347−14352

$CoFe_3O_5$ shows complex magnetic behavior with weak ferromagnetism (canted antiferromagnetism) below $T_{C1} \approx 300$ K and a second transition to ferrimagnetic order at $T_{C2} \approx 100$ K. Spin scattering of carriers leads a substantial increase in the hopping activation energy below T_{C1}, and a small negative magnetoresistance is observed at low temperatures.

■ ASSOCIATED CONTENT

Supporting Information

The Supporting Information is available free of charge on the ACS Publications website at DOI: 10.1021/acs.inorgchem.8b02458.

Additional data and experimental details (PDF)

Accession Codes

CCDC 1866328−1866335 contain the supplementary crystallographic data for this paper. These data can be obtained free of charge via www.ccdc.cam.ac.uk/data_request/cif, or by emailing data_request@ccdc.cam.ac.uk, or by contacting The Cambridge Crystallographic Data Centre, 12 Union Road, Cambridge CB2 1EZ, UK; fax: +44 1223 336033.

■ AUTHOR INFORMATION

Corresponding Author

*E-mail: j.p.attfield@ed.ac.uk.

ORCID

J. Paul Attfield: 0000-0001-9763-3987

Funding

We acknowledge financial support from European Research Council (ERC) and Engineering and Physical Sciences Research Council (EPSRC) UK.

Notes

The authors declare no competing financial interest.

Data that support the findings of this study have been deposited at https://datashare.is.ed.ac.uk/handle/10283/838.

■ ACKNOWLEDGMENTS

We acknowledge Science and Technology Facilities Council (STFC) UK and the ESRF for provision of beamtime. We would also like to thank Pascal Manuel (ISIS) and Angel M. Arevalo-Lopez, Paul M. Sarte, Alexander J. Browne, Giuditta Perversi, and James Cumby (Edinburgh) for assistance provided.

■ REFERENCES

(1) Verwey, E. J. W. Electronic conduction of magnetite (Fe3O4) and its transition point at low temperatures. *Nature* **1939**, *144*, 327−328.

(2) Senn, M. S.; Wright, J. P.; Attfield, J. P. Charge order and three-site distortions in the Verwey structure of magnetite. *Nature* **2012**, *481*, 173−176.

(3) Lavina, B.; Dera, P.; Kim, E.; Meng, Y.; Downs, R. T.; Weck, P. F.; Sutton, S. R.; Zhao, Y. Discovery of the recoverable high-pressure iron oxide Fe4O5. *Proc. Natl. Acad. Sci. U. S. A.* **2011**, *108*, 17281−5.

(4) Ovsyannikov, S. V.; Bykov, M.; Bykova, E.; Kozlenko, D. P.; Tsirlin, A. A.; Karkin, A. E.; Shchennikov, V. V.; Kichanov, S. E.; Gou, H.; Abakumov, A. M.; Egoavil, R.; Verbeeck, J.; McCammon, C.; Dyadkin, V.; Chernyshov, D.; van Smaalen, S.; Dubrovinsky, L. S. Charge-ordering transition in iron oxide Fe4O5 involving competing dimer and trimer formation. *Nat. Chem.* **2016**, *8*, 501−508.

(5) Lavina, B.; Meng, Y. Unraveling the complexity of iron oxides at high pressure and temperature: Synthesis of Fe5O6. *Sci. Adv.* **2015**, *1*, e1400260.

(6) Delacotte, C.; Hüe, F.; Bréard, Y.; Hébert, S.; Pérez, O.; Caignaert, V.; Greneche, J. M.; Pelloquin, D. Structural Transition at 360 K in the CaFe5O7 Ferrite: Toward a New Charge Ordering Distribution. *Inorg. Chem.* **2014**, *53*, 10171−10177.

(7) Delacotte, C.; Bréard, Y.; Caignaert, V.; Hardy, V.; Greneche, J. M.; Hébert, S.; Suard, E.; Pelloquin, D. Transmission Electron Microscopy Study of CaFe5O7: Evidence of a Monoclinic Superstructure at Room Temperature. *Key Eng. Mater.* **2014**, *617*, 237−240.

(8) Delacotte, C.; Bréard, Y.; Caignaert, V.; Hardy, V.; Greneche, J. M.; Hébert, S.; Suard, E.; Pelloquin, D. Morin-like spin canting in the magnetic CaFe5O7 ferrite: A combined neutron and Mössbauer study. *J. Solid State Chem.* **2017**, *247*, 13−19.

(9) Evrard, O.; Malaman, B.; Jeannot, F.; et al. Mise en évidence de CaFe4O6 et détermination des structures cristallines des ferrites de calcium CaFe2+*n*O4+*n* (*n* = 1, 2, 3): nouvel exemple d'intercroissanc. *J. Solid State Chem.* **1980**, *35*, 112−119.

(10) Hong, K. H.; Arevalo-Lopez, A. M.; Cumby, J.; Ritter, C.; Attfield, J. P. Long range electronic phase separation in CaFe3O5. *Nat. Commun.* **2018**, *9*, 2975.

(11) Hong, K. H.; McNally, G. M.; Coduri, M.; Attfield, J. P. Synthesis, crystal structure, and magnetic properties of MnFe3O5. *Z. Anorg. Allg. Chem.* **2016**, *642*, 1355−1358.

(12) Hong, K. H.; Arevalo-Lopez, A. M.; Coduri, M.; McNally, G. M.; Attfield, J. P. Cation, magnetic, and charge ordering in MnFe3O5. *J. Mater. Chem. C* **2018**, *6*, 3271−3275.

(13) Uenver-Thiele, L.; Woodland, A. B.; Miyajima, N.; Ballaran, T. B.; Frost, D. J. Behaviour of Fe4O5−Mg2Fe2O5 solid solutions and their relation to coexisting Mg−Fe silicates and oxide phases. *Contrib. Mineral. Petrol.* **2018**, *173*, 1−16.

(14) Berastegui, P.; Eriksson, S.; Hull, S.; García García, F. J.; Eriksen, J. Synthesis and crystal structure of the alkaline-earth thallates $M_nTl_2O_{3+n}$ (M = Ca, Sr). *Solid State Sci.* **2004**, *6*, 433−441.

(15) Rodriguez-Carvajal, J. Recent advances in magnetic structure determination by neutron powder diffraction. *Phys. B* **1993**, *192*, 55−69.

(16) Larson, A. C.; Von Dreele, R. B. General Structure Analysis System (GSAS). *Los Alamos National Laboratory Report LAUR 86-748*; Los Alamos National Laboratory: Los Alamos, NM, 2004.

(17) Momma, K.; Izumi, F. VESTA 3 for three-dimensional visualization of crystal, volumetric and morphology data. *J. Appl. Crystallogr.* **2011**, *44*, 1272−1276.

(18) Attfield, J. P. Charge ordering in transition metal oxides. *Solid State Sci.* **2006**, *8*, 861−867.

(19) Brown, I. D. VALENCE: a program for calculating bond valences. *J. Appl. Crystallogr.* **1996**, *29*, 479−480.

DOI: 10.1021/acs.inorgchem.8b02458
Inorg. Chem. 2018, 57, 14347−14352